République Algérienne Démocratique et Populaire
وزارة التعليم العالي و البحث العلمي
Ministère de l'enseignement supérieur et de la recherche scientifique

Université Mohamed Khider – Biskra
Faculté des Sciences et de la technologie
Département : Génie Electrique
Ref : 04/G.E/2025

جامعة محمد خيضر بسكرة
كلية العلوم و التكنولوجيا
قسم :الهندسة الكهربائية
المرجع : 04/G.E/2025

Thèse présentée en vue de l'obtention du diplôme de :

Doctorat LMD en Electrotechnique

Spécialité (Option) : **Réseaux Electriques**

Intitulé de la Thèse :

Contribution à l'optimisation de l'intégration des énergies renouvelables et des systèmes FACTS dans les réseaux électriques : Cas d'étude Réseau Electrique Algérien

Présentée par :

Zahia DJEBLAHI

Soutenue publiquement le 21/01/2025

Devant le jury composé de :

Abdelhafid ROUINA	**MCA**	**Président**	**Université de Biskra**
Belkacem MAHDAD	**Professeur**	**Rapporteur**	**Université de Biskra**
Kamel SRAIRI	**Professeur**	**Co- Rapporteur**	**Université de Biskra**
Laid ZELLOUMA	**Professour**	**Examinateur**	**Université de El-Oued**
Mohamed Toufik BENCHOUIA	**Professeur**	**Examinateur**	**Université de Biskra**

Année Universitaire 2024/2025

République Algérienne Démocratique et Populaire
وزارة التعليم العالي والبحث العلمي
Ministère de l'enseignement supérieur et de la recherche scientifique

University Mohamed Khider – Biskra
Faculty of Science and Technology
Department of Electrical Engineering
Ref : 04/G.E/2025

جامعة محمد خيضر بسكرة
كلية العلوم و التكنولوجيا
قسم :الهندسة الكهربائية
المرجع : 04/G.E/2025

A thesis submitted for the fulfillment of the degree of :

LMD Doctorate in Electrotechnics

Specialty (Option): **Electrical Networks**

Thesis Title:

Contribution to the optimization of the integration of the renewable energies and the FACTS systems into electrical grids: A case study of the Algerian electrical network

Presented by:

Zahia DJEBLAHI

The public thesis defense on 21/01/2025

Board of Examiners:

Abdelhafid ROUINA	**MCA**	**Chairperson**	**Université de Biskra**
Belkacem MAHDAD	**Professor**	**Supervisor**	**Université de Biskra**
Kamel SRAIRI	**Professor**	**Co- Supervisor**	**Université de Biskra**
Laid ZELLOUMA	**Professor**	**Examiner**	**Université de El-Oued**
Mohamed Toufik BENCHOUIA	**Professor**	**Examiner**	**Université de Biskra**

University Year 2024/2025

Acknowledgement

First, our heartfelt thanks go to Allah Almighty, who has granted us health, courage, and given me the strength and confidence to complete this thesis. By the bounty and mercy of Allah, I have been able to achieve this work. After that, first and foremost, I would like to express my sincere gratitude to my supervisor, **Professor Belkacem MAHDAD** for their invaluable direction and supervision work and his support, and encouragement throughout my PhD studies. His constant support and expertise have been crucial in bringing this project to fruition, enabling us to reach this point and achieve our goals. I really appreciate all the time he devoted to discussing all the topics of this dissertation. His dedication to helping me develop my research skills has been indispensable. His insightful advice not only enhanced the quality of this thesis but also helped shape my academic growth and approach to research.

I would like to express my gratitude and thanks to **Professor Kamel SRAIRI**, my co-supervisor, who guided me with patience and dedication throughout the four years of my PhD studies. He encouraged me to grow and explore my potential. A special thanks to **Pr. Mohamed Yassine HAMOUDI**, for his advices to realize this modest work. I would like to express my sincere thanks to **Dr. Yassine HIMEUR** from Dubai University.

I would like to thank committee members, **Pr. ROUINA Abdelhafid**, **Pr. ZELLOUMA Laid** from University of **El Oued**, and **Pr. BENCHOUIA Mohamed Toufik** from University of Biskra for their valuable and constructive comments.

Next, I would like to thank the director of the Laboratory **Pr. MOUMEHREZ Mohamed**, for the best conditions he has reserved for us to finish this work.

Finally, special thanks for my mother, who encouraging me when everything seemed weak, for my brothers, especially Adel, my sister Elkamla, and my best friends (Touti Fatma zohra and, Bensahla Imen) for their endless love and support that have made the hard times so much easier. I would like to express my deepest gratitude to everyone who has contributed, directly or indirectly, to the completion of this project.

Sincerely

Zahia Djeblahi 2024

Dedication

Dedications

I thank Allah for giving me the strength to accomplish this work and to go further.

I dedicate this work to my parents; my father (الله يرحمه), and my mother for her encouragement and prayers.

I dedicate it to my sister and my brothers.

I dedicate it to all the people who have supported me throughout my university career.

To all my dear family.

To all my friends with whom I have shared moments of joy and happiness.

Thank you very much indeed.

ZAHIA

ملخص

تتمثل المساهمة الرئيسية لهذه الأطروحة في تعزيز أداء الشبكات الكهربائية الحديثة من خلال تحسين دمج مصادر الطاقة المتجددة، وأجهزة مرنة للنقل بالتيار المتناوب (FACTS) باستخدام طرق التحسين الميتا-استدلالية الحديثة. أين كان الهدف من هذه الدراسة هو حل مشاكل تدفق الأمثل للطاقة ذات الهدف الواحد والمتعددة الأهداف. تم تحليل وظائف مختلفة، من بينها تقليل تكلفة الوقود، انبعاثات الغازات، فقدان الطاقة، وانحرافات الجهد، على كل من شبكة النقل الكهربائية (IEEE 30-bus) وكذلك على الشبكة الكهربائية الجزائرية (DZA-114 bus) . قمنا أيضًا في هذه الأطروحة بتركيب أجهزة مرنة للنقل بالتيار المتناوب لتحسين أداء نظام الطاقة. تم استعمال أربع خوارزميات هجينة مستوحاة من الطبيعة، واحدة منها تم استخدامها لأول مرة في هذه الأطروحة، لحل مشكلة أمثلية الطاقة أحادية الهدف في أنظمة الطاقة الحديثة المدمجة بالطاقات المتجددة. الهدف من استعمال خوارزميات هجينة هو تحسين الحل الأمثل. تم استخدام المنهجيات المقترحة لتحديد أفضل موقع لأنظمة تحسين التوتر المرنة لتقليل تكلفة الإنتاج، التقليل من ضياع الطاقة، وتحسين الجهد الكهربائي، لضمان تشغيل فعال للشبكات الكهربائية. لاختبار فعالية ونجاعة الخوارزميات المقترحة وأثر الأجهزة المرنة للنقل بالتيار المتناوب (FACTS) قمنا بتطبيق البرنامج على الشبكة الكهربائية (IEEE 30-bus) المدمجة بطاقة الرياح، وعلى الشبكة الكهربائية الجزائرية (DZA-114 bus) المدمجة بطاقة الرياح وكذلك الطاقة الشمسية. تؤكد النتائج التي تم الحصول عليها فعالية الطرق المقترحة لحل مشكلة التدفق الأمثل للطاقة في وجود مختلف أجهزة النقل المرنة (FACTS) .

كلمات مفتاحية: مصادر الطاقة المتجددة، التدفق الأمثل للطاقة، أجهزة مرنة للنقل بالتيار المتناوب (FACTS)، طرق التحسين الميتا-اســتدلالية، الشــبكة الكهربائية (IEEE 30-bus) ، الشــبكة الكهربائية الجزائرية (DZA-114 bus)، الخوارزميات الهجينة، الأمثلة متعددة الأهداف، أنظمة الطاقة الحديثة، الطاقات المتجددة، الأنظمة المرنة للنقل بالتيار المتناوب، تكلفة الإنتاج

Abstract

The main contribution of this thesis is to enhance the performance of modern electrical networks by optimizing the integration of renewable energy sources and Flexible Alternating Current Transmission Systems (FACTS) through recent metaheuristic optimization methods. Where the objective of this study was to solve single and multi-objective optimal power flow problems. Various functions were analyzed, including the minimization of fuel cost, gas emissions, energy losses, and voltage deviations, on both the IEEE 30-bus electrical transmission network and the Algerian electrical network (DZA-114 bus). In this thesis, we also installed FACTS devices to improve the performance of the power system. Four nature-inspired hybrid algorithms were used, one of which was employed for the first time in this thesis, to solve the single-objective energy optimization problem in modern power systems integrated with renewable energies. The aim of using hybrid algorithms is to improve the optimal solution. The proposed methodologies were used to determine the best location for flexible voltage regulation systems to reduce production costs, decrease energy losses, and improve voltage levels, ensuring efficient operation of electrical networks. To test the effectiveness and efficiency of the proposed algorithms and the impact of flexible alternating current transmission systems (FACTS), we applied the program to the IEEE 30-bus electrical network integrated with wind energy, and to the Algerian electrical network DZA-114 bus integrated with both wind and solar energy. The results obtained confirm the effectiveness of the proposed methods for solving the optimal power flow problem in the presence of various flexible transmission devices (FACTS).

Keywords: Renewable energy sources, Flexible Alternating Current Transmission Systems (FACTS), optimal power flow, metaheuristic optimization methods, IEEE 30-bus electrical network, Algerian electrical network DZA-114 bus. hybrid algorithms, multi-objective optimization, modern power systems

Résumé

La contribution principale de cette thèse consiste à améliorer la performance des réseaux électriques modernes en optimisant l'intégration des sources d'énergie renouvelables et des Systèmes Flexibles de Transmission en Courant Alternatif (FACTS) à l'aide des méthodes d'optimisation métaheuristiques récentes. Où l'objectif de cette étude était de résoudre des problèmes de flux optimal de puissance à objectif unique et multi-objectifs. Diverses fonctions ont été analysées, notamment minimisation du coût du carburant, les émissions de gaz, les pertes d'énergie et les déviations de tension, tant sur le réseau de transmission électrique sur le réseau de transport électrique (IEEE 30-bus) ainsi que sur le réseau électrique algérien (DZA-114 bus). Dans cette thèse, nous avons également installé des dispositifs flexibles de transport en courant alternatif pour améliorer la performance du système énergétique. Quatre algorithmes hybrides inspirés de la nature ont été utilisés, dont l'un pour la première fois dans cette thèse, pour résoudre le problème d'optimisation de l'énergie à objectif simple dans les systèmes énergétiques modernes intégrant des énergies renouvelables. L'objectif de l'utilisation d'algorithmes hybrides est d'améliorer la solution optimale. Les méthodologies proposées ont été utilisées pour déterminer le meilleur emplacement des systèmes flexibles de régulation de tension afin de réduire les coûts de production, diminuer les pertes d'énergie et améliorer la tension électrique, assurant ainsi un fonctionnement efficace des réseaux électriques. Pour tester l'efficacité et la performance des algorithmes proposés et l'impact des dispositifs flexibles de transport en courant alternatif (FACTS), nous avons appliqué le programme sur le réseau électrique (IEEE 30-bus) intégré à l'énergie éolienne, ainsi que sur le réseau électrique algérien (DZA-114 bus) intégré à l'énergie éolienne et solaire. Les résultats obtenus confirment l'efficacité des méthodes proposées pour résoudre le problème de flux de puissance optimal en présence de divers dispositifs de transport flexibles (FACTS).

Mots clés : sources d'énergie renouvelables, flux optimal de puissance, méthodes d'optimisation métaheuristique, algorithmes hybrides, optimisation multi-objectifs, systèmes énergétiques modernes, énergies renouvelables, dispositifs flexibles de transport en courant alternatif, coût du carburant, réseau électrique IEEE 30-bus, réseau électrique algérien DZA-114 bus

Table of contents

List of Publications and Conferences

1. Journal Publications

Djeblahi, Z., Mahdad, B., & Srairi, K. (2024). Solving the Energy Management Problems Using Thermal Exchange Optimization.

Djeblahi, Z., Mahdad, B., & Srairi, K. (2024). Optimized the locations and sizes of FACTS devices on electrical network involving wind power using a new hybrid stochastic algorithm. *Engineering Research Express*, *6*(3), 035339.

2. Conference internationals:

2.1. Djeblahi, Z., Mahdad, B., & Srairi, K. Optimal Power Flow Management of the Algerian Electric Transmission System Using Moth Flame Optimizer Algorithm. In: Artificial Intelligence and Heuristics for Smart Energy Efficiency in Smart Cities: Case Study: Tipasa, Algeria. Springer International Publishing, 2022. p. 66-77.

2.2. Djeblahi, Z., Mahdad, B., & Srairi, K. (2022, May). Solving Energy Management Optimization Using Various Global Metaheuristics Methods. In 2022 19th International Multi-Conference on Systems, Signals & Devices (SSD) (pp. 2028-2034). IEEE.

2.3. Djeblahi, Z., Mahdad, B., & Srairi, K. Dandelion Optimizer (DO) algorithm for Parameters Extraction of Photovoltaic Solar Cell. In 2023 1st International Conference on Renewable Solutions for Ecosystems: Towards a Sustainable Energy Transition (ICRSEtoSET) (pp. 1-6). IEEE.

2.4. Djeblahi, Z., Mahdad, B., & Srairi, K. (2023, jun). Global MPPT Techniques for Solar Photovoltaic under Partial Shading, Energy Alliance for Realistic and Profitable Energy Transition Relié – juin 2024.

2.5.Djeblahi, Z., Mahdad, B., & Srairi, K. Multi-objective Salp Swarm Algorithm (MSSA) for solving the energy management problem of the Algerian electric 114-nod, The International Conference On Applied Science And Engineering (ICASE-22), oron, Dec 2023.

2.6.Djeblahi, Z., Mahdad, B., & Srairi, K. M. Y., Hamoudi, Veysel Murat İstemihan Genç (2023, nov). Parameters Estimation of Photovoltaic Solar Cell Using A Stochastic Optimization Approach, In *International Conference on Artificial Intelligence in Renewable Energetic Systems* (pp. 39-53). Cham: Springer Nature Switzerland.

2.7. Djeblahi, Z., Mahdad, B., & Srairi, K. Comparison Between Global MPPT Techniques for Solar Photovoltaic under Partial Shading, ICSEHS’22: International Conference on Solar Energy and Hybrid Systems, University Amar Telidji of Laghouat, Algeria Laghouat, Algeria, May 3-4, 2023

3. Conferences nationals:

3.1. Djeblahi, Z., Mahdad, B., & Srairi, K, A comprehensive Studies Between Maximum Power Peak using Stochastic Techniques for PV Systems under PSC, The First National Conference on New Educational Technologies and Informatics, NCNETI23

3.2. Mimoune, K., Hamoudi., Mimoune, M. Y., S. M., **Djeblahi, Z.**, H-infinity Control of Nonlinear Systems Using Non-Quadratic Lyapunov Function LMI approach’, The First National Conference on New Educational Technologies and Informatics, NCNETI23.

3.3. Djeblahi, Z., Mahdad, B., & Srairi, K, A New Hybrid Metaheuristic Optimization Algorithm for Parameters Estimation of Photovoltaic Models, NC skikda October 2023

3.4. Djeblahi, Z., Mahdad, B., & Srairi, K Maximum Power Peak Tracking for Solar panel Under Partial Shading Conditions Via Moth Flame Optimizer Approach, Djelfa, Dec 2023

List of figures

List of tables

List of acronyms

Symbol	Explanation
OPF	Optimal Power Flow
MOOPF	Mult-objective Optimal Power Flow
FACTS	Flexible Alternating Current Transmission Systems.
SVC	Static Var Compensator.
STATCOM	Synchronous Static Compensator.
TCSC	Thyristor-Controlled Series Compensator.
TCSR	Thyristor Controlled Series Reactor
TSSC	Thyristor Switched Series Capacitor.
SSSC	Static Synchronous Series Compensator
IPFC	Interline Power Flow Controller.
TCPAR	Thyristor-Controlled Phase-Angle Regulator.
UPFC	Unified Power Flow Controller.
TCPS	Thyristor-Controlled Phase Shifter
RESs	Renewable Energy Resources
PV	Photovoltaic Sources.
DC	Direct current
AC	Alternating Current.
SDM	Single Diode Model
DDM	Double Diode Model
TFC	Total Fuel Cost
TEG	Total Emission Gas
APL	Total Active Power losses
TVD	Voltage Deviation
GA	Genetic Algorithm
PSO	Particle Swarm Optimisation
DO	Dandelion Optimizer algorithm
SSA	Salp swarm algorithm
TEO	Thermal exchange optimization
FBD-AEO	Fitness Distance Balance based Artificial Ecosystem Optimization Algorithm:

FBD-AOA	Fitness Distance Balance based Archimedes Optimization Algorithm:
MOPSO	Multi-objective particle swarm optimization
MOGA	Multi-objective genetic algorithm
MOAGDE	Multi-Objective Adaptive Guided Differential Evolution
MOTEO	Multi-objective version of thermal exchange optimization algorithm
IMOMRFO	Improved multi-objective manta-ray foraging optimization
DSC-MOAGDE	Dynamic Switched Crowding Mult objective- Adaptive Guided Differential Evolution Algorithm
MSSA	Multi-objective salp swarm algorithm
RMSE	Root Mean Square Error.
SPE	Société Algérienne de Production de l'Électricité (Algerian Electricity Production Company)
SKTM	Shariket Kahraba wa Taket Moutadjadida (Company for Electricity and Renewable Energy)
Fuelvlv cost	Thermal generation cost involving the valve cost
Valveff cost	Valve Cost
Thermal gen cost	Thermal generation cost
Tgen cost	Totat generation cost without valve cost
Wind gen cost	Wind generation cost
Solar gen cost	Solar generation cost

List of Symbols

Symbol	Explanation
$\boldsymbol{B_{svc}}$	the susceptance of the SVC.
$\boldsymbol{B_{svc}^{\min}}$	the minimum limits of the susceptance SVC.
$\boldsymbol{B_{svc}^{\max}}$	maximum limits of the susceptance SVC.
$\boldsymbol{Q_{SVC}}$	The amount of reactive power supplied by SVC
$\boldsymbol{C_{TSSC}}$	The capacitor of TSSC
$\boldsymbol{X_{TCSC}}$	Controllable reactance of TCSC.
$\boldsymbol{X_{mn}}$	Reactance of the line inductive (*m n*).
$\boldsymbol{\delta_{mn}}$	Phase angle of the line inductive (*m n*).
$\boldsymbol{C_T}$	The total capacitance of $TCSC$
$\boldsymbol{R_S}$	The series resistance of SDM
$\boldsymbol{I_{ph}}$	The photocurrent
$\boldsymbol{I_{sd}}$	The saturation current
$\boldsymbol{n}$	The ideality factor
$\boldsymbol{R_{Sh}}$	The shunt resistance
$\boldsymbol{K}$	The Boltzmann constant
$\boldsymbol{q}$	The electron charge.
$\boldsymbol{T}$	The cell temperature
$\boldsymbol{I_{sd1}}$	The diffusion current of the first diode of the DDM
$\boldsymbol{n_1}$	indicates ideality factor.
$\boldsymbol{n_2}$	complex diode ideality
$\boldsymbol{I_{sd2}}$	The capacity current of the second diode of the DDM
$\boldsymbol{N_G}$	Generator number
$\boldsymbol{N_{TG}}$	Number of thermal Generators
$\boldsymbol{P_{G_i}}$	The active generator's power at i^{th} thermal generating units
$\boldsymbol{P_{G_i}^{min}, P_{G_i}^{max}}$	The minimum and maximum real power limit of the i^{th} generator
$\boldsymbol{Q_{G_i}}$	The reactive generator's power at i^{th} thermal generating units
$\boldsymbol{Q_{G_i}^{min}, Q_{G_i}^{max}}$	The minimum and maximum reactive power limit of the i^{th} generator
$\boldsymbol{S_{D_i}}$	The apparent power demand in i^{th} bus
$\boldsymbol{P_{D_i}}$	The real power demand in i^{th} bus

D_{D_i}	The reactive power demand in i[th] bus
a_i; b_i and c_i	The price coefficients for the i[th] thermal power generating Units.
α_i;β_i; γ_i; ω_i and μ_i:	The emission coefficients concerning the i^{th} thermal generating unit.
G_{ij}, B_{ij}	The conductance and susceptance of the transmission line between the i[th] and j[th] buses.
V_{ij} , θ_{ij}	The voltage phase angle difference between the i[th] and j[th] buses
N_b	The total number of buses,
V_i , V_j	The voltage magnitudes at the i[th] and j[th] buses.
$V_{G_i}^{min}$, $V_{G_i}^{max}$	refer to the lower and upper limits of voltage of generators bus
N_G	The total numbers of thermal and wind generations.
$S_{L,i}$, $S_{L,i}^{max}$	The power limits of the i[th] transmission line.
L_i	the i[th] load bus.
N_{STL}	The number of transmission lines in the power system
$V_{L,i}^{min}$, $V_{L,i}^{max}$	The voltage limits of the i[th] load bus $V_{L,i}$
NPQ	The total number of load bus
$T_{Tr,i}^{min}$, $T_{Tr,i}^{max}$	The limits of the i[th] tap setting transformer $T_{Tr,i}$
N_{Tr}	The tap changers number.
$Q_{C,i}$	Shunt Capacitor at i[th] bus
$Q_{C,i}^{min}$, $Q_{C,i}^{max}$	The limits of the i[th] shunt compensator $Q_{C,i}$
n_C	The number of the capacitors linked to the power system.
N_{TCSC}	The numbers TCSC
N_{TCPS}	The numbers of TCPS
N_{SVC}	Number of SVC
C_{gen}	The total generation Cost
P_{loss}	Reel power losses
C_{gross}	Gross cost which continent the total generation cost involves losses cost

General Introduction

General Introduction

In modern times, electrical energy is crucial for most activities that would be nearly impossible without it. Recently, the use of electrical power has surged due to the growing global demand. Ensuring stable, reliable, and continuous power quality with minimal loss is a significant challenge for energy systems. This increase in demand poses challenges, particularly in maintaining a delicate balance between production and consumption. Complicating matters is the immediate need to consume electricity upon production due to the limited and inefficient current storage options. Not long ago, conventional energy sources were the primary means of electricity production, based on fuel-fossil thermal power plants, met the most of the demand for electricity. However, electricity generation from these plants are neither eco-friendly nor sustainable. Nowadays, renewable energy sources (RES) have been widely integrated into energy systems to meet the rising demand for electricity and provide a sustainable, eco-friendly alternative to fossil fuel-based energy sources. Consequently, the generation of electricity from sustainable energy sources has gained increasing significance.

The primary challenges facing modern power systems that integrate renewable (such as wind and solar power) and non-renewable energy sources into the main electrical grid are their fluctuating nature and the resulting power quality issues. This intermittency creates unpredictable scenarios for the power grid operator, who must continuously ensure that production and consumption are balanced at all times. This necessitates additional means to optimize the monitoring, protection, and management of power flow within electrical transmission and distribution networks [1].

Several technologies have been utilized to enhance power quality in electrical networks, which is paramount for present and future power systems. In these situations, Flexible Alternating Current Transmission System (FACTS) controllers play a crucial role in managing power system security. These intelligent power electronic devices offer a promising solution due to their significant capacity to control voltage levels and power flow in real time. They are very promising under high penetration of renewable energies, which is expected to occur within a few decades. As well alleviate electrical network congestion during power grid overloads [2]. Electric power system operators are always on the lookout for exploring new approaches to tackle operational planning hurdles, aiming to maintain service continuity while reducing damage to electrical equipment. In today's power system operations, every fluctuation in demand necessitates precise adjustments in power generation to maintain the balance between supply and demand, ensuring grid stability. This can be locally achieved through effective power management.

The Optimal Power Flow (OPF) is crucial for planning future growth and operating power systems. Its main goal is to ensure network safety by optimizing specific objectives while adhering to inequality and equality constraints, adapting to load demand changes by updating control variable settings within grid operating conditions and various constraints. This makes it a complex optimization issue characterized by high non-linearity, large-scale dimensions, multidimensionality, and non-convexity. The classical objectives of OPF focus on conventional thermal generating units. However, the integration of large-scale, unpredictable renewable energy sources like wind and solar into the electrical network requires additional considerations, including security and operational constraints. OPF scheduling now also needs to account for the forecast uncertainty of these renewables, making it essential to reassess OPF strategies to accommodate the diversity of energy sources [3].

Over the past decade, with the rise emergence of the recent optimization techniques, such as metaheuristic methods, alongside the deregulation of electricity markets and the incorporation of renewable energy sources (RES) and FACTS devices, has substantially complicated the study of OPF. This complexity has significantly heightened the objectives of OPF, requiring special efforts to establish optimal planning and operations management for electric power systems. This is attributed to the diverse functions derived from the variability and uncertainty inherent in its problem formulation [4]. In this context, developing of new strategies to address this challenge has garnered significant interest in academic and research circles, particularly with the rise of computational intelligence. Where this field has become immensely popular among scientific and engineering communities for its capability to tackle complex problems.

This thesis focuses on applying artificial intelligence methods to solve engineering optimization problems, such as optimizing the electrical parameters of PV models and solving the single and multi-objective optimal power flow in the IEEE 30-bus system and the Algerian electrical network DZA-114 bus.

In the second part based on the work of **Pr. MAHDAD Belkacem** in the field of power flow optimization, and referring to his published articles[5][6][7][8], also, and the work of **Dr. Partha Biswass**, and his published articles as basic references [8][9], when integrate the renewables energies in the electrical transmission network 30 bus, with optimal placement of FACTS devices. And referring in the scientific papers of **DR. Mouassa Souhil** as basic references [10], when integrate the renewables energies such as, wind and solar in the electrical transmission network Algerian DZA-114 bus. Here, one of this research contributes is that it only takes into account wind and solar energies resources into the modified electrical network DZA-114 bus, with optimal placement of FACTS devices.

The subject of our thesis is the optimization of the electrical network with presence of FACTS; case study electrical network Algeria. This thesis titled " **Contribution à l'optimisation de l'intégration des énergies renouvelables et des systèmes FACTS dans les réseaux électriques: Cas d'étude Réseau Electrique Algérien** " was conducted within the Laboratory of Modeling of Energy Systems (LMSE) at the University of Biskra. It represents a contribution to the improvement of some recent intelligent optimization methods for solving the OPF in the transmission electrical network in the test network IEEE 30-bus, the reel transmission electrical network Algeria DZA-114 bus with presence of renewables energies and FACTS devices.

CHAPTER 1: Overview of the thesis.

1.1. Introduction

The expansion of modern power systems, including increased loads, lines, and generators, coupled with a surge in demand and environmental concerns, necessitates the use of more efficient elements and procedures. The challenge of managing long-distance power flows and evolving system demands has spurred the development of methods that satisfy economic and technical criteria, a problem commonly addressed as Optimal Power Flow (OPF). OPF analysis is essential in both the planning and real-time operation of power grid.

Numerous approaches have been suggested to address the OPF problems with including both thermal and RESs, where the incorporation of power electronics has significantly advanced the integration process. By employing FACTS controllers, it's possible to adjust power flow for optimal accuracy, precision, and speed, thus enhancing the utilization of existing and future electrical networks. To solve OPF problems involving thermal generators and FACTS devices alongside RESs, various metaheuristic algorithms have been proposed. These solutions aim to maintain reasonable electricity prices, thereby preserving consumer loyalty. However, applying these strategies to improve load control and ensure system security presents ongoing challenges. Demand side management schemes benefit from various optimization algorithms, leading to improved outcomes by accommodating flexible load models tailored to individual lifestyles, ultimately enhancing user comfort. The culmination of this work is the efficient scheduling of power in the modern electrical network, employing unconventional optimization techniques and considering two pricing schemes to optimize comfort and efficiency [11].

This chapter presents an overview about our thesis, defense plans used to prevent major outages. Our focus lies specifically on Flexible Alternating Current Transmission Systems (FACTS) and the integration of renewable energies.

1.2. State of art

Starting in 1919, research engineers began to take an interest in the optimal functioning of power systems. In 1958, Kirchmayer's book "Economic Operation of Power Systems," introduced a nonlinear programming formulation of the economic dispatch problem, leading to the development of the first algorithms for solving power flow. The majority of traditional optimization methods rely on sensitivity analysis and gradient-based methodologies. In 1961 to 1962: Squires and Carpentier began optimal power flow (OPF) research. Although some researchers credit Dommel and Tinney (1968) with developing the OPF methodology to address the economic dispatch problem. Since then, the OPF approach has been adapted to various challenges and has become the foundation for managing and controlling power networks. Today, it is widely used to allocate available power plant generation while optimizing specific objective functions or multiple objectives simultaneously [12].

In previous years, conventional and intelligent optimization algorithms can be addressed the OPF problems. In this connection, quite a few mathematical programming methodologies that have been implemented for handling the OPF problems such as newton-based technique. In [13], a linear programming (LP) approach was tested on IEEE-14, 57, and 118 bus systems, demonstrating its effectiveness through numerical simulations. In [14] used quadratic programming (QP) used for solving Economic Dispatch problems, tested on IEEE-5, 14, 30, 57, and 118 bus systems. Nonlinear programming (NLP) [15], employed to solve OPF problems by locating reactive power support among competing generators in a deregulated environment. Performance was analyzed using a modified IEEE-118 bus system. Interior point (IP) methods, implemented in [16] on IEEE 30-bus system to minimize generation cost, with results compared to the lambda iterative method, showing very close outcomes but slight differences in active losses. Furthermore, the OPF problem has traditionally been solved using conventional methods. However, these approaches have significant limitations, they are limited to specific OPF problems and continuous problems that use derivatives and gradients, providing optimal solutions only under certain conditions involving simple and differentiable objective functions. However, in modern power systems, the OPF problem is consistently a nonlinear optimization challenge that may also be non-differentiable. This complex nature poses a significant challenge for conventional techniques within practical power grids. To overcome these limitations, metaheuristic methods have been considered as alternative approaches to solving the complex OPF optimization problem [17].

The emergence of "metaheuristics" began in the 1980s, particularly with Glover's work in 1986. Advancements in computer science have since led to the development of various intelligent optimization approaches to tackle OPF challenges, especially in systems with thermal generators [17]. One prominent example is the Genetic Algorithm (GA), recognized for its efficiency in finding optimal solutions. The feasibility of GA was demonstrated using the IEEE 30-bus system, where it was compared with other techniques from the literature, showing the effectiveness of the proposed method [18]. An Enhanced GA (EGA) was also developed to address the OPF problem, incorporates an incremental power flow model based on sensitivities, significantly reducing CPU time [19]. The Particle Swarm Optimization (PSO) introduced by Eberhart and Kennedy in 1995, it has proven effective in solving OPF challenges, as demonstrated on the IEEE-30 bus system [20], The Differential Evolution (DE) algorithm inspired by evolutionary strategies and GA, DE is effective for continuous variable problems, as tested on IEEE-14, 30, 57, and 118 bus systems, showing strong results for nonlinear objectives and constraints [21]. The Artificial bee colony has been tested on IEEE-9, 30, and 57 bus systems, showing effectiveness in solving large-scale OPF problems [22]. Gravitational search algorithm (GSA) Based on Newtonian gravity, GSA has been applied to IEEE-30 and 57 bus systems, demonstrating robust and high-quality results [23]. Other notable algorithms include Tabu Search (TS) [24], self-adaptive differential evolution (SADE) [25], modified differential evolution algorithm (MDEA) [26], adaptive real coded biogeography-based optimization (ARCBOA) [27], Grey Wolf Optimizer GWO [28], moth swarm algorithm (MSA) [29]. In [30], Moth Swarm Algorithm (MSA) The MSA and four other algorithms are applied to solve the OPF on the IEEE 30-bus, 57-bus, and 118-bus power systems, the results demonstrate the MSA's effectiveness and superiority over many recent OPF solutions. stud krill herd algorithm (SKHA) [31], Developed grey wolf optimization (IGWO) [32], salp swarm algorithm (SSA) [33], whale optimization algorithm (WOA) [34]. the Peafowl Optimization Algorithm (POA) [35] was applied the solve the OPF in the standard electrical network IEEE 14-bus and 57-bus, the results clearly shown the superiority of this algorithm in tacking this challenges' Grey Wolf Optimization (GWO) [36], … etc... In addition to these, hybrid Particle Swarm Optimization and Differential Evolution (HPSO-DE) [37], and the hybrid Particle Swarm Optimization and Gravitational Search Approach (HPSO-GSA) [38], In [39], a hybrid method designed and applied to tackle the OPF problems, which is Fitness-distance balance based artificial ecosystem optimization (FDB-AEO), the main advantage of this approach is more efficiently reaches the global optimum., …etc. These methods demonstrate the vast potential of intelligent optimization in solving complex OPF problems.

With the integration of large-scale renewable power into power systems, OPF scheduling now requires to account for the forecast uncertainty of renewable energy. To address these challenges, numerous approaches have been developed for OPF problems involving both thermal and renewable energy sources (RES). Some of these optimization methods employ approximate techniques to manage the complexity of incorporating renewable energy into OPF scheduling, such as the Fitness–Distance Balance based (FBD-AGDEA) adaptive guided differential evolution algorithm [40]. Chaotic Bonobo Optimizer (CBO) algorithm [41], has been employed to tackle the OPF problem in systems featuring thermal and RES generators. The algorithm is verified on modified IEEE-30 and IEEE-57 bus test systems. The results prove the efficiency, the superiority and robustness of CBO for finding the best solution to the OPF problem with stochastic RESs. In [42] Conditional Value at Risk (CVaR) have been employed to tackle the OPF problem in systems featuring thermal and RESs generators, as well as wind generation units, is used as a management tool to enhance the security level of each operational constraint. A hybrid optimization algorithm, the Particle Swarm with Gray Wolf Optimizer (HPS-GWO) [43], has been used to address the OPF problem on the IEEE 30-bus system, including renewable energy sources. Simulation results confirm its strong exploitation and exploration capabilities for tacking this challenge. The hybrid algorithm PSO with an Aging Leader and Challengers (ALC-PSO) was implemented in [44] which has been used to identify high-quality solutions to OPF problems in systems equipped with FACTS components. adaptive fitness-distance balance-based (AFBD-SFSA) stochastic fractal search algorithm [45], was implanted for solving OPF problems in systems equipped with FACTS components, …. Etc

The incorporating FACTS devices into modern electrical systems significantly increases the complexity of OPF problems, and making it more challenging to obtain optimal solutions. A brief overview of the metaheuristic approaches utilized to address the OPF problems of a system that involves thermal generators is given, such as, Genetic Algorithm (GA) has been used to solve FACTS allocation within the context of the OPF problem. Specifically, the allocation of the TCPST was managed using GA and OPF equations. GA handled OPF to solve the power balance equations and adjust the voltage regulators (VRs) [46]. The cross-entropy approach was implemented for minimizing both power loss and voltage deviation for best location of SVC and TCPS [47]. The particle swarm optimization (PSO) [48], The optimal placement and rating of two TCSCs in transmission network IEEE 30-bus was performed by utilizing adaptive parallel seeker optimization (APSOA) algorithm [49], was applied to optimize the coordination and placement of TCSC, SVC, TCPS, and UPFC in IEEE 30-bus, Incorporating the unpredictability of loads, the properties of transmission lines, and the cost associated with TCSCs were all included in the problem formulation. A Hybrid Particle Swarm Optimization and adaptive (PSO-GSA) used for optimizing the allocation and rating of TCSC and SVC concepts [50]. Non-dominated sorting particle swarm optimization algorithm (NSPSO) was applied for enhancing the higher voltage stability of the electrical grid by utilizing both SVC and TCSC and optimizing their location and size [51]. In [52], the Moth Swarm Algorithm (MSA) was employed to find the correct position TCSC on the electrical network IEEE 30-bus test system, … etc. In certain other studies, the placement and sizing were optimized for single or multi-types of FACTS devices along with the primary aims being to improve the voltage stability and/or the load capacity of a power grid comprising thermal generators.

To solve OPF problems in energy systems featuring thermal generators, renewable energy sources (RES), and FACTS devices, several intelligent optimization algorithms have been proposed for solving this problem. In [53] some of proposed techniques were evaluated against established methods, including Particle Swarm Optimization (PSO), Moth Flame Optimization (MFO), and Grey Wolf Optimizer (GWO), using the IEEE 30-bus test system, with the presence and absence of FCTAS, renewable energy sources. The results showed that MPA, SMA, JS, and AEO algorithms are more effective in solving OPF problems compared to PSO, GWO, and MFO, ... etc.

Currently, there is a limited amount of research using metaheuristic optimization techniques for solving OPF problems in networks with integrated renewable energy and FACTS devices. Moreover, there is a few studies comparing novel metaheuristic optimization techniques or analyzing the impact of renewable energy sources, such as wind and solar, on network efficiency and optimization methods. In [9], a recent study by Biswas et al. addressed OPF for the IEEE 30-bus network, focusing on the optimal location and sizing of various FACTS devices, including VAR compensator (SVC), TCSC (thyristor-controlled series compensator), and TCPS (thyristor-controlled phase shifter), using the Success History-based Adaptive Differential Evolution (SHADE) method. This study concentrated on single-objective OPF problems related to electricity production costs and power loss, and included fixed-location wind turbine generators as renewable energy sources but neglected solar energy units. Additionally, the developed Runge Kutta optimizer (DRKO) was used for OPF analysis in systems with wind/PV/TCSC [54]. The modified krill herd algorithm (MKHA) was applied to the best allocation and rating of FACTS devices in the IEEE 30-bus grid with wind power [55]. In [56], An improved Hunter-prey optimization (HPO) method was also used to enhance search capabilities for OPF problems involving FACTS devices and wind power integration, The Hunter-Prey Optimization (HPO) method has been utilized to enhance search capabilities for solving the Optimal Power Flow (OPF) problem, incorporating FACTS devices and wind power energy integration. Furthermore, in [57], the Chaos Game Optimization Approach conducted to study the OPF in the IEEE 30-bus network.

Based on this historical overview about the OPF, and the previous studies primarily dealt with OPF issues in electrical networks supported by FACTS, integrating wind turbines and PV generator units in smaller grids, this thesis focuses on the integrating those stochastic generation units to determine optimal placements for FACTS devices and address more complex OPF challenges in large-scale electrical networks, which is the reel electric Algerian transmission network DZA-114 bus.

1.3. Problem statement

Power systems are operating at near full capacity, posing risks to the security of the electrical grid. There is a consensus on the need to reinforce and upgrade the electrical transmission infrastructure by adding new lines, substations, and equipment. However, this solution is difficult, expensive, time-consuming, and controversial.

The optimal power flow (OPF) is gaining paramount importance in the operation and planning phases of the electrical network. Several optimization methods face challenges in handling the stochastic nature of OPF problems, especially within practical electric grids. Unlike conventional thermal generators, the integration of renewable energy sources (RES), which adds significant complexity due to these generators cannot be scheduled predictably, as their output depends on variable climatic factors like solar irradiation and wind speed. This variability poses a major challenge for operating hybrid generation systems and integrating RES into power grids on a large scale. The uncertainty associated with climatic conditions further complicates maintaining a stable and reliable power supply. This highlights the need for innovative solutions and optimization techniques that can accommodate the dynamic and unpredictable nature of renewable energy in OPF calculations Additionally, the variability of renewable energy sources introduces power quality challenges in the grid, necessitating the application of advanced technologies. FACTS controllers are effective technical solutions for these challenges, offering significant benefits in power system security management and mitigating the inherent drawbacks of renewable energy integration [3][10][11].

Over the past two decades, numerous optimization methods have been used to determine optimal control variables for power flow problems, both single and multi-objective, with and without renewable energy sources (RES). Despite some success results, the effectiveness of these methods has been limited by the complex nature of the OPF problem. especially in large-scale power grids with conflicting objectives, and selecting the right optimization approach remain challenging for Identifying optimal solutions. Solving the OPF problem in the presence of RES and FACTS devices is crucial for the efficient and reliable operation of modern power systems. It requires sophisticated optimization approaches that can handle the system's complexity and uncertainties. Advanced optimization techniques such as metaheuristic algorithms, machine learning, and robust optimization are employed to find a global optimum solution that balances all objectives while satisfying constraints with reasonable computational effort.

1.4. Major contributions of the thesis

This doctoral thesis focuses to address the issue OPF in electrical transmission networks by optimizing a specific objective function using metaheuristic optimization methods. The main objectives and effects and contributions of the dissertation can be outlined in the following points:

- Different metaheuristics algorithms were proposed to identify the best optimal electrical parameters of PV models.

- Recent intelligence artificial optimization algorithms were proposed to deal with different single and multi-objective optimal power flow problem in the electrical transmission network IEEE 30-bus test system, and in large-scale power systems, which is the real electric network Algerian DZA-114 bus.

• Our thesis motivation is to showcase the current state of power systems integrated with intelligent techniques, particularly for renewable resources and FACTS devices.

• The stochastic wind and solar power plants are modeled, analyzed, and calculated using Weibull PDF (probability density function).

• Study of the impact of some FACTS devices on the electrical transmission network. Our research focuses on optimizing the placement and sizing of FACTS devices (two TCPSs, two TCSCs, and two SVCs) in the modified electrical transmission network IEEE 30-bus test system, and the modified electrical transmission network Algerian DZA-114 bus.

The optimization process was conducted using recent optimization algorithms in order to explore the advantages of each with a view to improving the quality of the solution obtained and the execution time. A novel algorithm was proposed and developed specifically for the **first time** known as the **FDB-AOA**. in this thesis for resolving this issue in the electrical network involving both renewable and thermal power generators, and finally achieve the best solution of the OPF problem. Making decisions about the dimensions of a search agent is a crucial step. there are 27 decision variables control for the modified IEEE 30-bus, and 57 decision variables for the modified DZA-114 bus.

1.5. Outline of the thesis

Including this introductory chapter, this thesis is organized into six chapters:

In the second chapter, the overviews for FACTS devices are presented, along with their advantages to the power grid. To validate the impact of integrating these devices on improving the efficiency of transmission networks.

In the third chapter, we will present the renewable energies, their classification, and detailed some interesting in our thesis like the wind and solar power plants, and their modulation. In the fourth chapter, we presented the formulation of the optimal power flow problem, which summarizes the objective functions addressed in our thesis, namely the minimization of fuel cost, emission gases, active power losses, and voltage deviation.

In Chapter 5, basics of some metaheuristic methods was detailed, the concept of inspiration, and its operational principles. We will focus on those we have studied in the context of this thesis presented the most commonly optimization methods used in solving the OPF problem.

The simulation results as well as the corresponding analysis and discussion of these results will be also presented in the Chapter 6. Finally, conclusions, the thesis concludes with a general conclusion, synthesizing the main contributions presented in this work. and perspectives that could be further developed, envisaged to address the multi-objectives problem of electrical network planning in the presence of renewable sources and in coordination with FACTS systems, while considering the real models of renewable sources characterized by probabilistic aspects, thus opening new avenues and proposals aimed at improving this work and initiating future research, will also be provided.

1.6. Conclusion

This chapter presented a detailed overview of the contents of this thesis. It began with an exploration of the state of the art in Optimal Power Flow (OPF) and the various optimization methods used in this domain. Following this, the outlined the problem statement, highlighting the key challenges and research gaps that this thesis aims to address. Subsequently, the contributions of this thesis were discussed, detailing the novel approaches and findings that this research will offer to the field. Finally, the chapter concluded with an outline of the thesis, providing a roadmap for the subsequent chapters and the overall structure of the research.

CHAPTER 2: FACTS Modeling and Integration in Power System.

2.1. Overview of FACTS devices

The increase in electrical energy demand has led to more complex electrical power transmission networks, making them more susceptible to issues such as power transfer challenges and increased stress on transmission lines. … etc. It has become challenging to ensure reliable control of energy transfer’s process. The most obvious solution to address these challenges is the construction of new transmission lines. However, this approach has significant disadvantages, including high costs and lengthy implementation periods. The conventional means of controlling or enhancing the performance of electrical network, and system parameters such as; power flow, transmission line impedances, voltage magnitude, and phase angle of the bus, necessitate a more strategic use of existing alternating current (AC) links. This emerging trend has been provided through modern technologies to overcome these current challenges in electrical transmission systems. One such innovative framework is the Flexible Alternating Current Transmission System (FACTS), which offers advanced solutions to ensure better performance and improved reliability in electrical transmission networks [58][59].

This chapter focused on an overview of the FACTS system; the main objective is to assess the impact of FACTS devices on the operation of the electrical network.

2.2. Flexible Alternating Current Transmission Systems (FACTS)

According to the IEEE (Institute of Electrical and Electronics Engineers) FACTS devices can be defined: “FACTS is a system based on power electronics and other static equipment that control one or more parameters of the AC transmission system to enhance controllability and increase the power transfer capability of the electrical network”. FACTS devices achieve this by the modification of the apparent impedance of a transmission line to control the active and reactive power flow and regulate the voltage levels by injecting (or absorbing) reactive power at bus (busbars). They can also improve the overall quality of the electricity transmitted [60].

2.3. State of art about FACTS devices

The FACTS technology was introduced by the Electric Power Research Institute (EPRI) in 1986, and their inception of the concept of FACTS devices was defined by Hingorani in 1988 [61]. The first generation of FACTS technology is begun with theoretical research and studies exploring the potential of power electronics in power systems for controlling, and enhancing the electrical networks operation [62]. These devices have been developed in the 1980s and 1990s, focused on controlling reactive power flow in transmission lines. These devices significantly improved power system stability, increased power transfer capacity, and reduced voltage fluctuations. The second generation, developed in the late 1990s and early 2000s, advanced to manage both reactive and active power flow. Since then, extensive research has been conducted to explore the impact of FACTS devices on power systems, particularly on steady-state performance and both dynamic and transient stability. These devices can be installed at multiple locations throughout a power system, allowing for more precise control over power flow and voltage stability. Overall, each generation of FACTS devices has built upon the previous generation's capabilities, providing increasingly sophisticated methods for controlling power flow in transmission systems [63].

The first use of FACTS devices in transmission networks can be traced back early 1990s. One of the pioneering implementations was the installation of a Static Var Compensator (SVC) in the United States in the late 1980s. In 2002, Algeria decided to install a total of three Static Var Compensators (SVCs) in the electrical transmission network: one at the Naama substation and two at Bechar. All three SVCs have a rating of (-10 / +40 MVAR) at 220 kV [12]. The **figure (2.1)** Static Var Compensators (SVCs) installed in the Algerian transmission network.

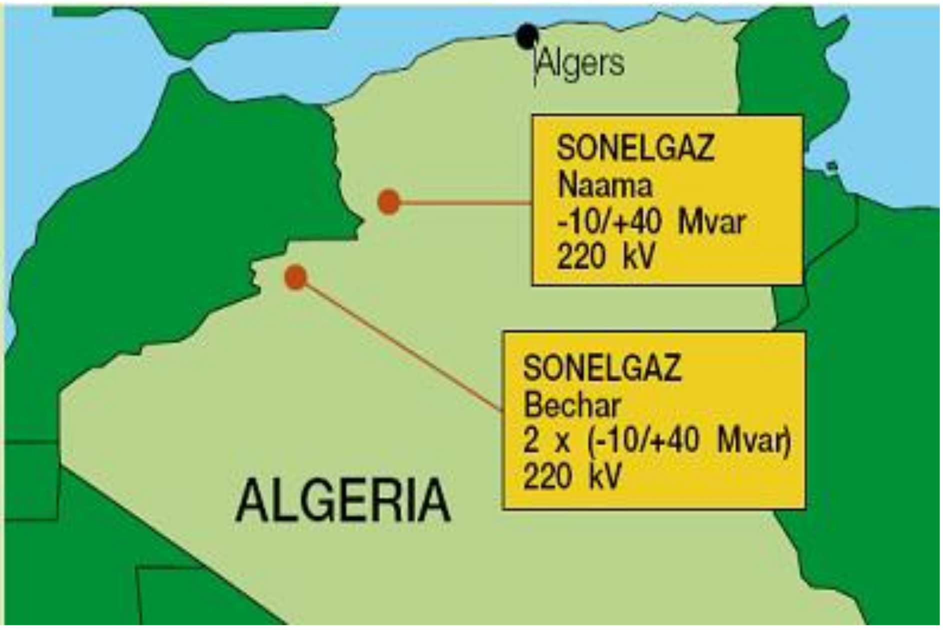

Fig. 2.1: Static Var Compensators (SVCs) installed in the Algerian transmission network.

2.4. Classification of FACTS devices

FACTS systems are mainly classified into three categories, each distinguished by its structure. The first category employs conventional control systems such as transformers with load-adjustable taps, phase-shifting transformers, and banks of capacitors or inductors, all controlled by conventional thyristors. The other two categories use static converters based on power semiconductors, controllable by Gate Turn-Off thyristors (GTOs). The most recent classification of FACTS controllers, based on their arrangement within the power system, is depicted in the **figure (2.2)** [64].

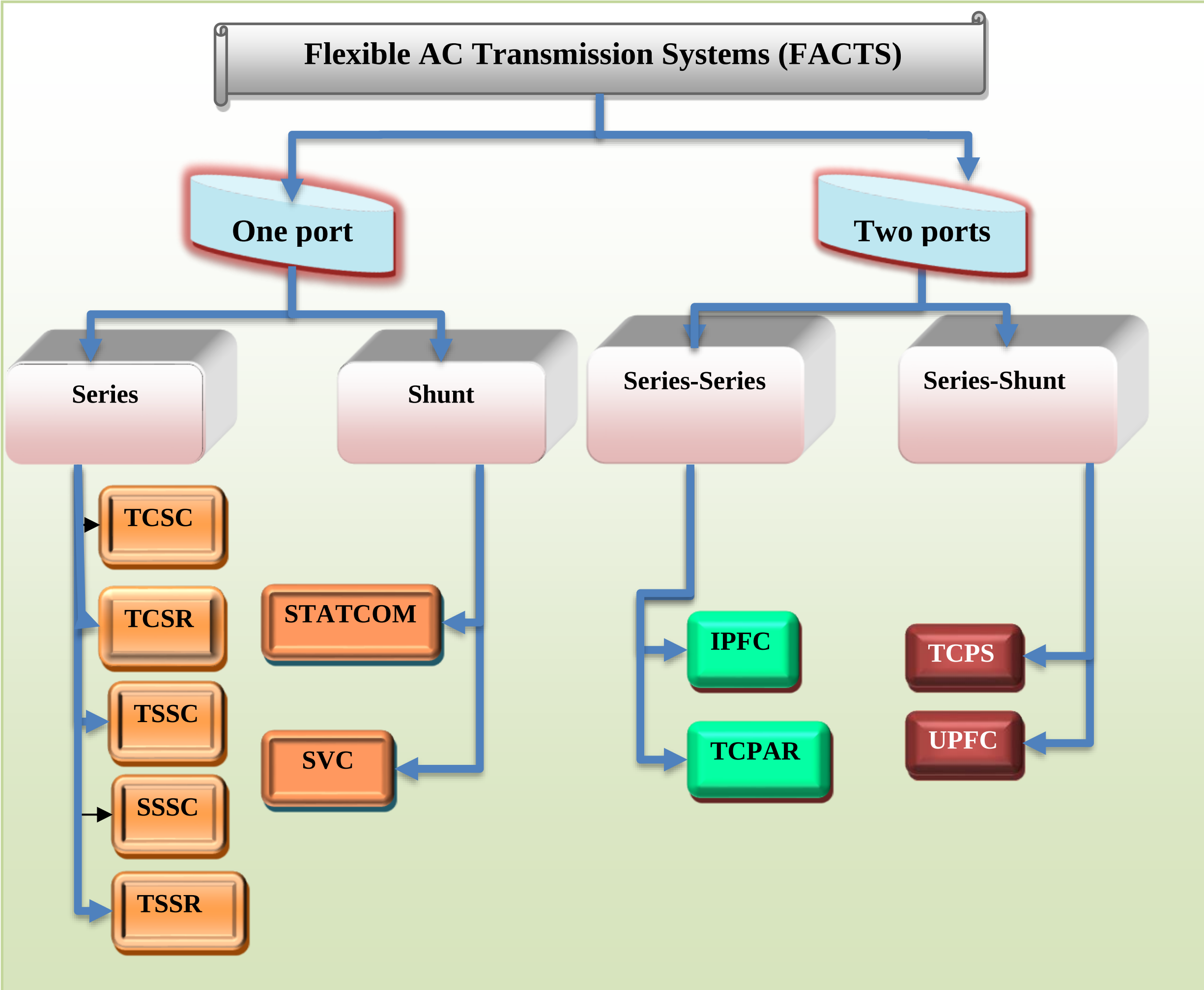

Fig. 2.2: Classification of FACTS devices.

2.4.1. Shunt FACTS compensator

A shunt compensator is a device used in power systems to manage and improve the quality of electrical power. It functions as a variable impedance, variable source, or the both. The most common types of shunt devices include:

2.4.1.1. Static Var Compensator (SVC)

A Static Var Compensator (SVC) is a device that generates or absorbs reactive power, it connected in parallel at critical points within the transmission network. The SVC is capable of providing compensation for inductive and capacitive loads by varying its reactive power output based on system needs, with the role to control busbar voltage. The basic structure of SVC is illustrated in **figure (2.3 (a))**, and their susceptance model is illustrated in **figure. (2.3 (b))** [64][65].

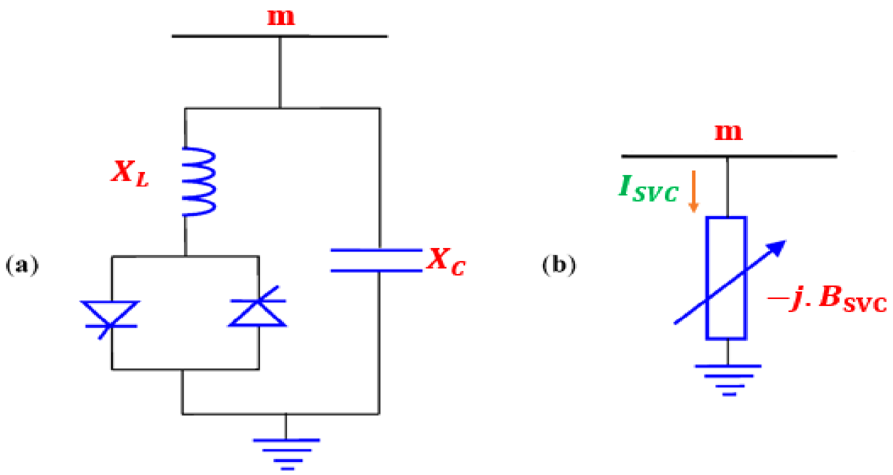

Fig. 2.3. (a): Basic equivalent circuit structure of SVC, (b): Model of SVC.

the SVC consists of a thyristor-controlled reactor $(X_L = \omega L)$ paired with a capacitor $(X_C = 1/\omega C)$. The reactance is adjusted by controlling the firing angle of the thyristors (θ_m), The equivalent susceptance of SVC represents by equation (2.1):

$$B_{\mathrm{SVC}} = B_C + B_L(\theta_m) \tag{2.1}$$

Where; $B_C = \omega C$ (2.2)

and $B_L(\theta_m) = \frac{1}{\omega L}\left(1 - \frac{2\gamma}{\pi} - \frac{\sin 2(\theta_m)}{\pi}\right)$ (2.3)

The current consumed by the SVC is given by equation (2.4):

$$I_{SVC} = jB_{SVC}V_m \tag{2.4}$$

Where, B_{svc} is the susceptance of the SVC, and V_m is the voltage at bus m. When conducting a power flow analysis, the amount of reactive power (Q_{SVC}) supplied by SVC can be represented in the following manner (2.5) [63]:

$$Q_{SVC} = Q_m = -V_m^2 \cdot B_{\mathrm{SVC}} \tag{2.5}$$

Where, the variable susceptance B_{SVC} is taken as a state variable. θ_m is the firing angle of the thyristor.

With $B_{svc}^{\min} \leq \boldsymbol{B}_{SVC} \leq \boldsymbol{B}_{svc}^{\max}$ (2.6)

Where $B_{svc}^{\min}$ and $\boldsymbol{B}_{svc}^{\max}$ are the minimum and maximum limits of the susceptance SVC.

2.4.1.2. Synchronous Static Compensator (STATCOM)

The STATCOM is defined as a device used in alternating current electricity transmission networks to control reactive power. It operates as a static synchronous generator connected in parallel to the network, with its capacitive or inductive output current controllable independently from the system voltage [8][65]. The figure (**2.4**) shows the basic schematic diagram model of a STATCOM. Generally, the STATCOM is modeled as a controllable voltage source in series with impedance, acting as a source or sink of reactive power [10]. It performs a similar function to a Static Var Compensator (SVC) but offers greater robustness, delivering reactive power even when busbar voltage is low. Ideally, a STATCOM should not exchange active power with the grid [66].

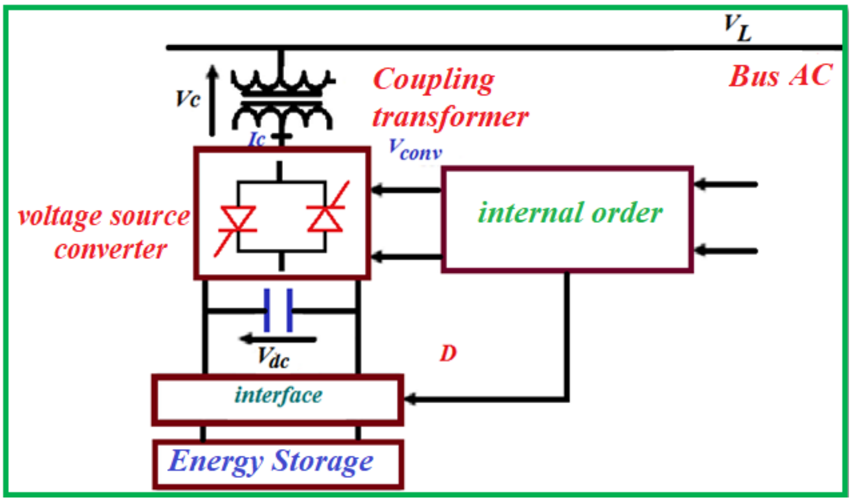

Fig. 2.4: Basic schematic diagram of STATCOM.

2.4.2. Serie FACTS compensators

Series compensation devices are integrated into transmission lines through a transformer and function as controllable voltage sources. Their main purpose is to regulate power by acting as variable impedances. This capability helps enhance voltage levels, transient stability, and power oscillation damping [28]. Notable examples of series FACTS devices include:

2.4.2.1. Thyristor-Controlled Series Compensator (TCSC)

The TCSC (Thyristor-Controlled Series Capacitor) consists of an inductor paired with a thyristor-controlled capacitor and is placed in series along the transmission line. It features a fixed series capacitor (XC) in parallel with a thyristor-controlled reactor (XL) branch. This configuration allows the TCSC to control and enhance the power transfer capacity of the transmission line by adjusting its reactance, providing either capacitive or inductive compensation [67]. The equivalent circuit of the TCSC is shown in **figure (2.5)** [68].

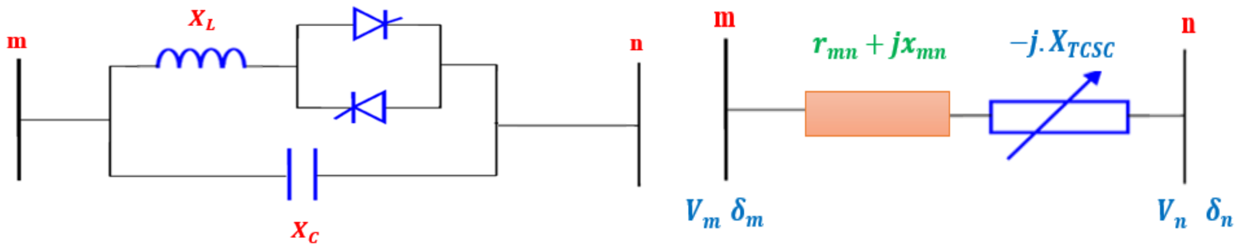

(a) (b)

Fig. 2.5 (a): schematic diagram of the TCSC; (b): equivalent circuit of TCSC model'.

It is crucial to note that the reactance value $X_C < X_L$, enabling the TCSC to function as an adjustable capacitive impedance by altering the firing angle of the thyristors (γ). The combined reactance of a TCSC, represented by X_C and X_L can be mathematically written as (2.7):

$$X_{TCSC}(\gamma) = \frac{X_C X_L(\gamma)}{X_L(\gamma)} \tag{2.7}$$

The controllable reactance X_{TCSC} is used directly as a control variable and can be given by (2.8):

$$X_{\mathrm{TCSC}} = \frac{X_C X_L}{\frac{X_C}{\pi}[2(\pi-\alpha)+\sin{(2\alpha}]-X_L} \tag{2.8}$$

The modified equivalent reactance (Xeq) of the transmission line, after incorporating a TCSC can be stated as (2.9):

$$X_{eq} = (1-\tau)X_{mn} \tag{2.9}$$

where $\tau = \frac{X_{TCSC}}{X_{mn}}$

which indicated the degree of compensation of the series, where X_{mn} and δ_{mn} represent the reactance and the phase angle of the line inductive ($m\ n$) [64,65,67]. The specific equations that describe the active and reactive power flow from the appropriate buses and line can be formulated as follow [69]:

$$P_{mn} = V_m^2 G_{mn} - V_m V_n (G_{mn}\cos\ \delta_{mn} + B_{mn}\sin\ \delta_{mn}) \tag{2.10}$$

$$Q_{mn} = -V_m^2(B_{mn} + B_{sh}) - V_m V_n (G_{mn}\sin\ \delta_{mn} - B_{mn}\cos\ \delta_{mn}) \tag{2.11}$$

$$P_{nm} = V_n^2 G_{nm} - V_n V_m (G_{nm}\cos\ \delta_{nm} - B_{nm}\sin\ \delta_{nm}) \tag{2.12}$$

$$Q_{nm} = -V_n^2(B_{mn} + B_{sh}) + V_n V_m (G_{mn}\sin\ \delta_{mn} + B_{mn}\cos\ \delta_{mn}) \tag{2.13}$$

$$G_{mn} = \frac{R}{R^2+(X_{mn}-X_{Tcsc})^2} \quad \text{and} \quad B_{mn} = \frac{-X_{mn}-X_{Tcsc}}{R^2+(X_{mn}-X_{Tcsc})^2} \tag{2.14}$$

2.4.2.2. Thyristor Controlled Series Reactor (TCSR)

This device is an inductive reactance compensator designed to replace mechanically controlled phase-shifting transformers with on-load tap changers. It comprises two transformers: one in series with the line, controlled by thyristors in anti-parallel and regulated by a firing angle (α) from 90° to 180°, and the other in parallel with a thyristor-switched reactor. These transformers are interconnected via thyristors to provide smooth variable inductive reactance. When the firing angle is 180°, the reactor stops conducting, acting as a fault current limiter. If the firing angle is below 180°, the net inductance decreases, thus controlling the voltage in the network. The **figure (2.6)** shows the diagram of a TCSR [70].

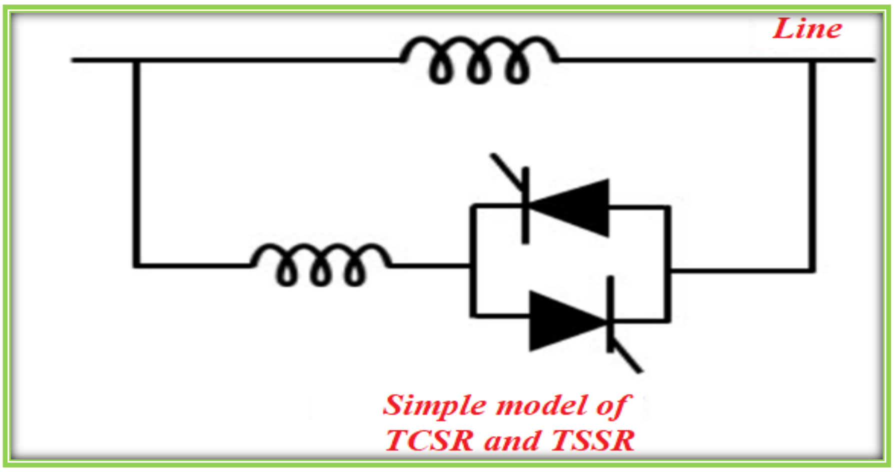

Fig. 2.6: Diagram of the principle of a TCSR.

2.4.2.3. Thyristor Switched Series Capacitor (TSSC)

The TSSC consists of several series capacitors, each controlled by two anti-parallel thyristors, as shown in the **figure (2.7)** [71], Each capacitor is shunted by a bypass valve made up of reverse parallel connected thyristors, allowing the system to quickly adapt to changing conditions by bypassing or engaging specific capacitors as needed. All capacitors have the same value, C_{TSSC} [72].

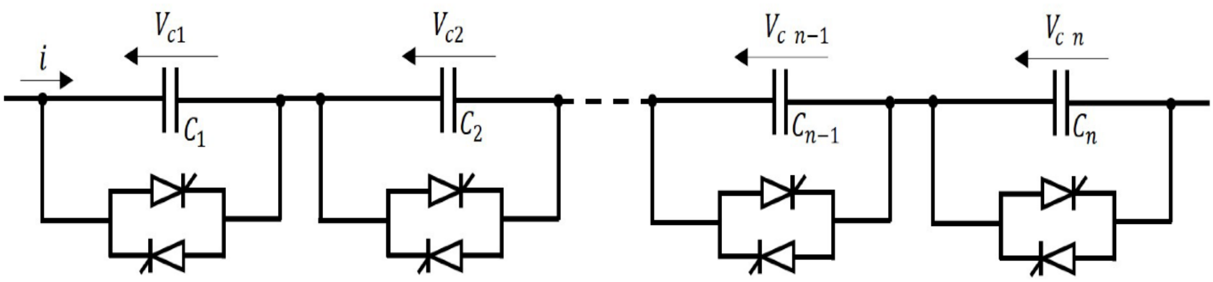

Fig. 2.7: Thyristor Switched Series Capacitor.

The overall capacitance of the circuit is controlled by conducting or blocking each thyristor pair. When a thyristor pair conducts, the capacitor C_{TSSC} is short-circuited. When a thyristor pair is open, the value C_{TSSC} is added to the total capacitance C_T. The total capacitance is given by equation (2.15):

$$C_T = \frac{C_{TSSC}}{m} \tag{2.15}$$

Where; m is the number of active capacitors.

In this mode, the compensating capacitive reactance is chosen to provide maximum nominal series compensation [72][73].

2.4.2.4. Static Synchronous Series Compensator (SSSC)

The SSSC is a series-connected FACTS device that provides inductive or capacitive voltage independently of the transmission line current within its rated limits. It consists of a three-phase inverter coupled in series with the power line via a transformer and includes parallel elements to control power flow and adjust reactance. By injecting a voltage in quadrature with the transmission line, the SSSC controls active power flow without consuming reactive power from the grid, utilizing energy stored in capacitor banks. It can exchange both active and reactive power with the AC system. Its basic configuration includes a voltage source converter connected to a DC voltage source and coupled to the AC system through a series transformer, as shown in **figure** (**2.8**) [72].

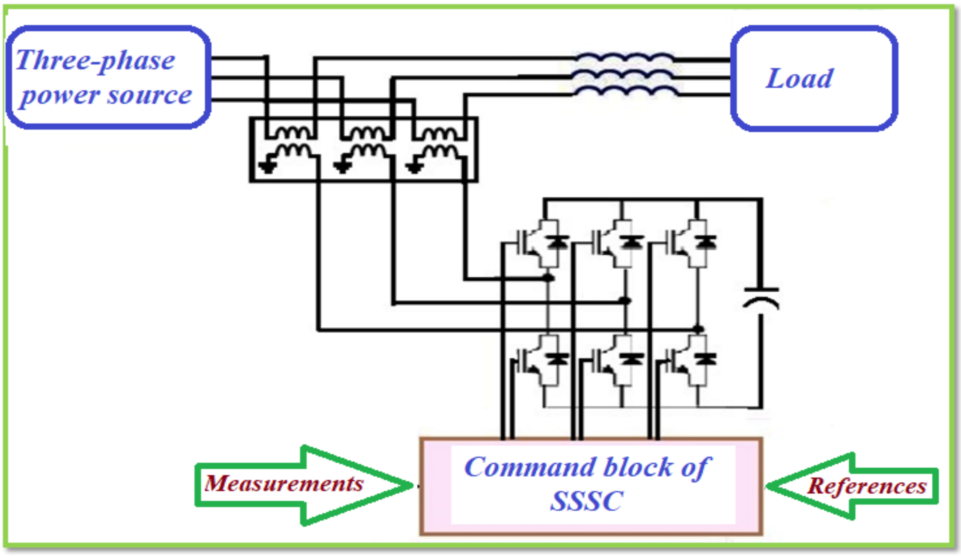

Fig. 2.8: Schematic representation of SSSC.

2.4.3. Combined Series-Series Controllers

This system combines separate series controllers that are coordinately controlled across multiple transmission lines. It could be an Interline Power Flow Controller (IPFC).

2.4.3.1. The Interline Power Flow Controller (IPFC)

The IPFC is designed to manage the transfer of real power among transmission lines while independently controlling reactive compensation for each line [74]. Typically, the IPFC employs multiple DC-to-AC converters, each providing series compensation for different lines. The simplest IPFC configuration includes two back-to-back DC-to-AC converters, where each SSSC adds series power to its respective transmission line [75]. These converters are connected via a DC capacitor and directly attached to the AC network through transformers as shown in the **figure (2.9).**

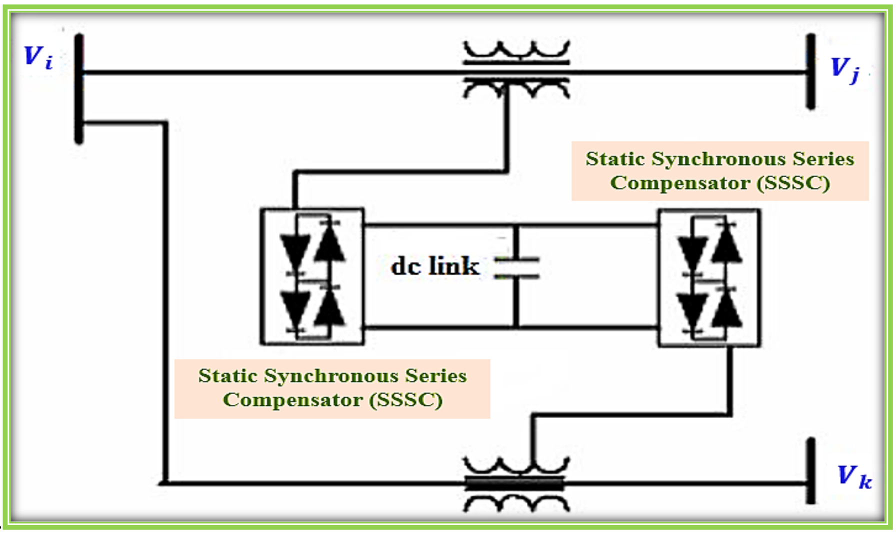

Fig. 2. 9: Schematic diagram of IPFC.

By this, it not only provides reactive power addition, but also any of the converters can be manipulated to inject the optimal real power to the dc joint from its own transmission. Through the bidirectional link facilitates active power exchange between voltage sources [76].

V_i, V_j and V_k are the complex bus voltages at the buses i, j and k respectively, defined as:

$$V_x = V_x \angle \theta_x \ (x = i, j \text{ and } k). \tag{2.16}$$

2.4.3.2. Thyristor-Controlled Phase-Angle Regulator (TCPAR)

TCPARs are usually installed to facilitate operation and maintenance. Therefore, the line shunt impedance should be placed on the right side of the TCPAR. For simplicity in problem formulation, the shunt impedance is moved to the left side of the TCPAR, as depicted in **figure (2.10).** In practice, this approximation has minimal impact on computational accuracy.

The TCPAR is equipment that can control power flow in transmission lines of power system by regulating the phase angle of the bus voltage. Environment restrictions usually restrict opportunities of reinforcement through the consideration of new routes. In such a situation, the

TCPAR play an important role in increasing load ability of the existing system and controlling the congestion in the network. FACTS device like TCPAR can be used to regulate the power flow in the tie-lines of interconnected power system. When TCPAR is equipped with power regulator and frequency [77]. Its operating principle is to inject into the three phases of the line a voltage ΔV in quadrature with the voltage to be phase shifted. It has the advantage of not generating harmonics. The amplitude of the injected voltage is a combination of the secondaries of the parallel transformer whose transformation ratios are n1, n2, n3.

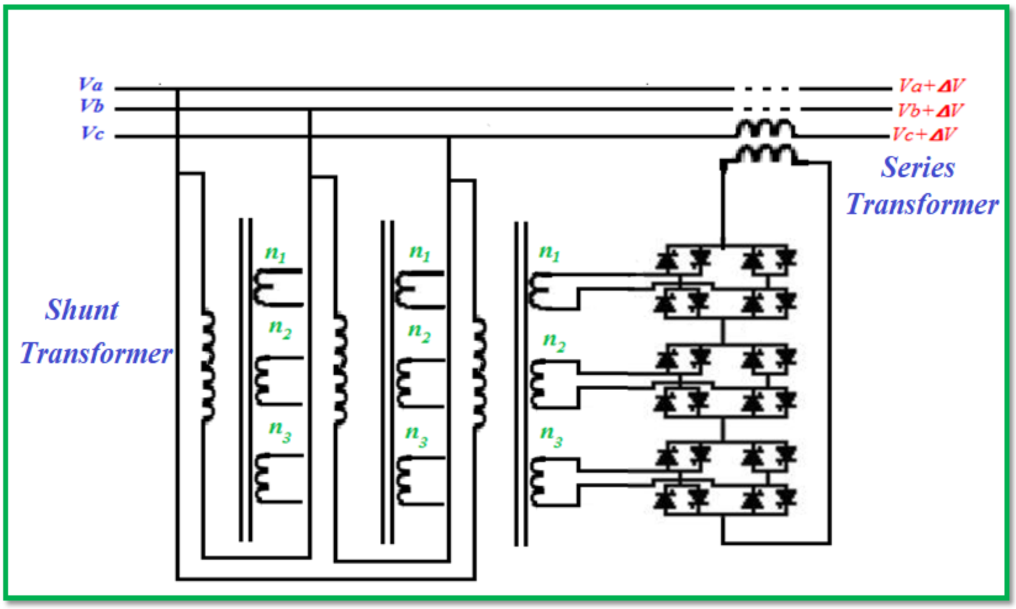

Fig. 2.10: Equivalent circuit of TCPAR.

2.4.4. Combined Series-Shunt Controllers

These controllers have combined both shunt and series controllers, with advanced control mechanisms. When used together, the shunt and series controllers facilitate real power exchange through their common DC link.

2.4.4.1. The Unified power flow controller (UPFC)

The UPFC, a series-shunt controller, is mainly used to enhance voltage stability and control the power flow. It can independently or concurrently manage various parameters and switch control schemes in real-time. The UPFC is placed at the beginning of the transmission line connecting bus k and m. The UPFC combines STATCOM (shunt) and SSSC (series) via a d.c. link. The converters are connected to the line through transformers. This configuration offers flexible operation within a power system network. The **figure (2.11)** illustrates the UPFC schematic [17],[78].

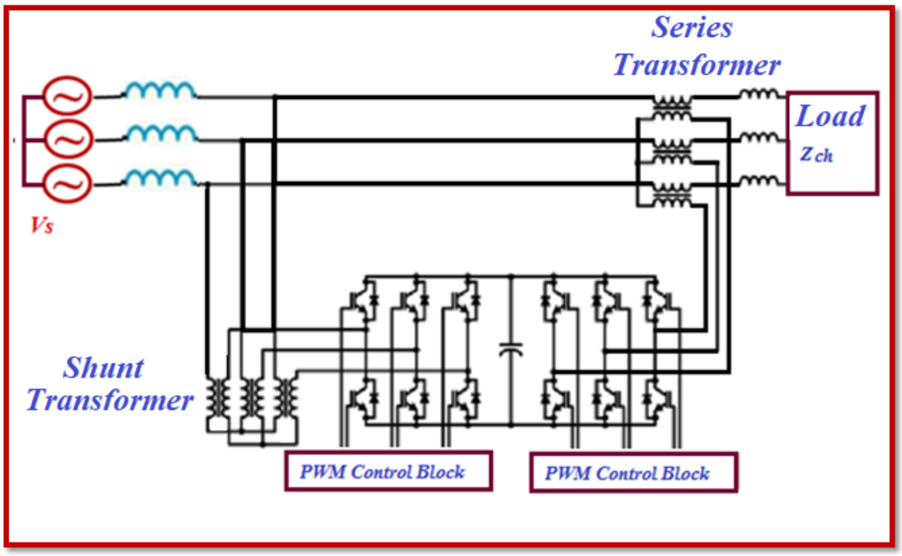

Fig. 2.11: schema diagram of an UPFC.

2.4.4.2. Thyristor-controlled phase shifter (TCPS)

The TCPST is essential for managing and adjusting the phase angle of the bus voltage between two points on a transmission line. It does this by introducing a perpendicular voltage component, which can either increase or decrease the phase angle. The TCPST can be depicted as a voltage compensation series or an ideal phase shifter. The **figure (2.12)** illustrates the equivalent circuit of the TCPST placed between buses m and n.

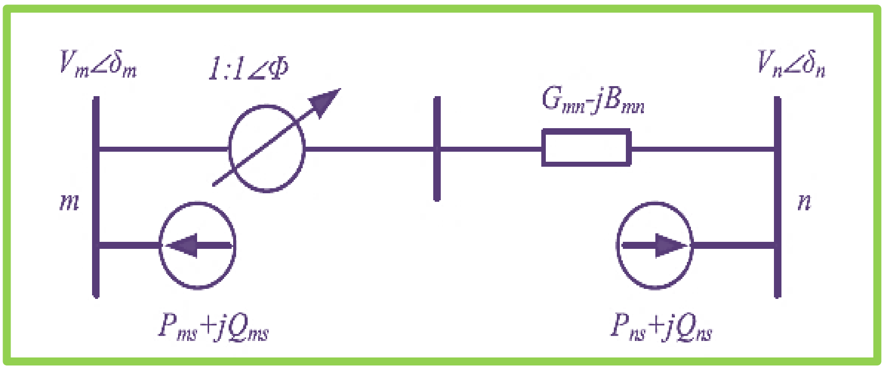

Fig. 2.12: Basic equivalent circuit of TCPS.

When taking into account the phase angle alteration caused by TCPS, the power flow equations of the line can be written as follows [79]:

$$P_{mn} = \frac{V_m^2 G_{mn}}{\cos^2\Phi} - \frac{V_m V_n}{\cos\Phi}\left[G_{mn}\cos\left(\delta_m - \delta_n + \Phi\right) + B_{mn}\sin\left(\delta_m - \delta_n + \Phi\right)\right] \quad (2.17)$$

$$Q_{mn} = -\frac{V_m^2 B_{mn}}{\cos^2\Phi} - \frac{V_m V_n}{\cos\Phi}\left[G_{mn}\sin\left(\delta_m - \delta_n + \Phi\right) - B_{mn}\cos\left(\delta_m - \delta_n + \Phi\right)\right] \quad (2.18)$$

$$P_{nm} = V_n^2 G_{mn} - \frac{V_m V_n}{\cos\Phi}\left[G_{mn}\cos\left(\delta_m - \delta_n + \Phi\right) - B_{mn}\sin\left(\delta_m - \delta_n + \Phi\right)\right] \quad (2.19)$$

$$Q_{nm} = -V_n^2 B_{mn} + \frac{V_m V_n}{\cos\Phi}[G_{mn}\sin(\delta_m - \delta_n + \Phi) + B_{mn}\cos(\delta_m - \delta_n + \Phi)] \quad (2.20)$$

The active and reactive power injected into the transmission line can be expressed using the following equations [68]:

$$P_{ms} = \& - G_{mn} V_m^2 \tan^2 \Phi - V_m V_n \tan \Phi[G_{mn}\sin(\delta_m - \delta_n) - B_{mn}\cos(\delta_m - \delta_n)] \quad (2.21)$$

$$Q_{ms} = B_{mn} V_m^2 \tan^2 \Phi + V_m V_n \tan \Phi[G_{mn}\cos(\delta_m - \delta_n) + B_{mn}\sin(\delta_m - \delta_n)] \quad (2.22)$$

$$P_{ns} = -V_m V_n \tan \Phi[G_{mn}\sin(\delta_m - \delta_n) + B_{mn}\cos(\delta_m - \delta_n)] \quad (2.23)$$

$$Q_{ns} = -V_m V_n \tan \Phi[G_{mn}\cos(\delta_m - \delta_n) - B_{mn}\sin(\delta_m - \delta_n)] \quad (2.24)$$

2.5. Conclusion

This chapter provides a comprehensive introduction to FACTS (Flexible AC Transmission Systems) devices, presenting their definition, role, classification, various categories, as well as their structure and operating principles, illustrated by diagrams detailing each device. The first part focuses on a general overview of FACTS devices, highlighting their importance and operation within electrical networks. The second part addresses the modeling of certain FACTS devices integrated into the electrical network. These devices modeling aims to use for controlling the voltage levels at busbar and the power flow in electric power transmission networks. In the following chapter, we will present the renewable energies sources, detailing some of them.

CHAPTER 3: Renewable Energies Sources

3.1. Introduction

Due to the high increasing energy demand worldwide, and the constrained reserves of resources fossil fuel-based energy. At the same time, the use of conventional energy sources has significant environmental impacts, such as climate change, and greenhouse gas emissions, these issues present formidable challenges that must be addressed. Nowadays, experts from various fields are collaborating working to create clean energy-harvesting environment, that have low-carbon technology, aiming to reduce pollution [80]. To achieve this transition, many governments have encouraged research in the field of renewable energy, and investing in ways how to incorporate these sources into the electrical grids looking to diversify production sources, and ensure a stable, environmentally friendly energy supply for the future [81].

This chapter focuses on renewable energy sources, covering their classification, definition, and exploration. It particularly interests on solar and wind power plants, along with the prevalent modeling techniques and simulations used for these energy sources.

3.2. Definition of Renewable Energy Sources

Renewable energy sources (RESs), defined as those naturally replenished on a timescale. They characterized by their cyclical recovery, vast availability, and have minimal environmental impact compared to fossil fuels. However, their intermittent nature, requiring careful planning for integration into the electrical network [82].

3.3. Classification of renewable energy sources

The classifications are based on the type of energy source used [83], such as solar, wind, hydro, and geothermal, … etc, are essential for a sustainable future due to their ability to provide an inexhaustible supply of clean energy. The main classification of renewable energy sources can be illustrated in figure **(3.1)**.

In this part we present a brief overview about the renewable energies' sources, definition, and the main renewable energies sources. In the next part, we will present the details of those interesting in our thesis, which are the solar and wind power plants. Below are the details of these two energies sources and their modulizations.

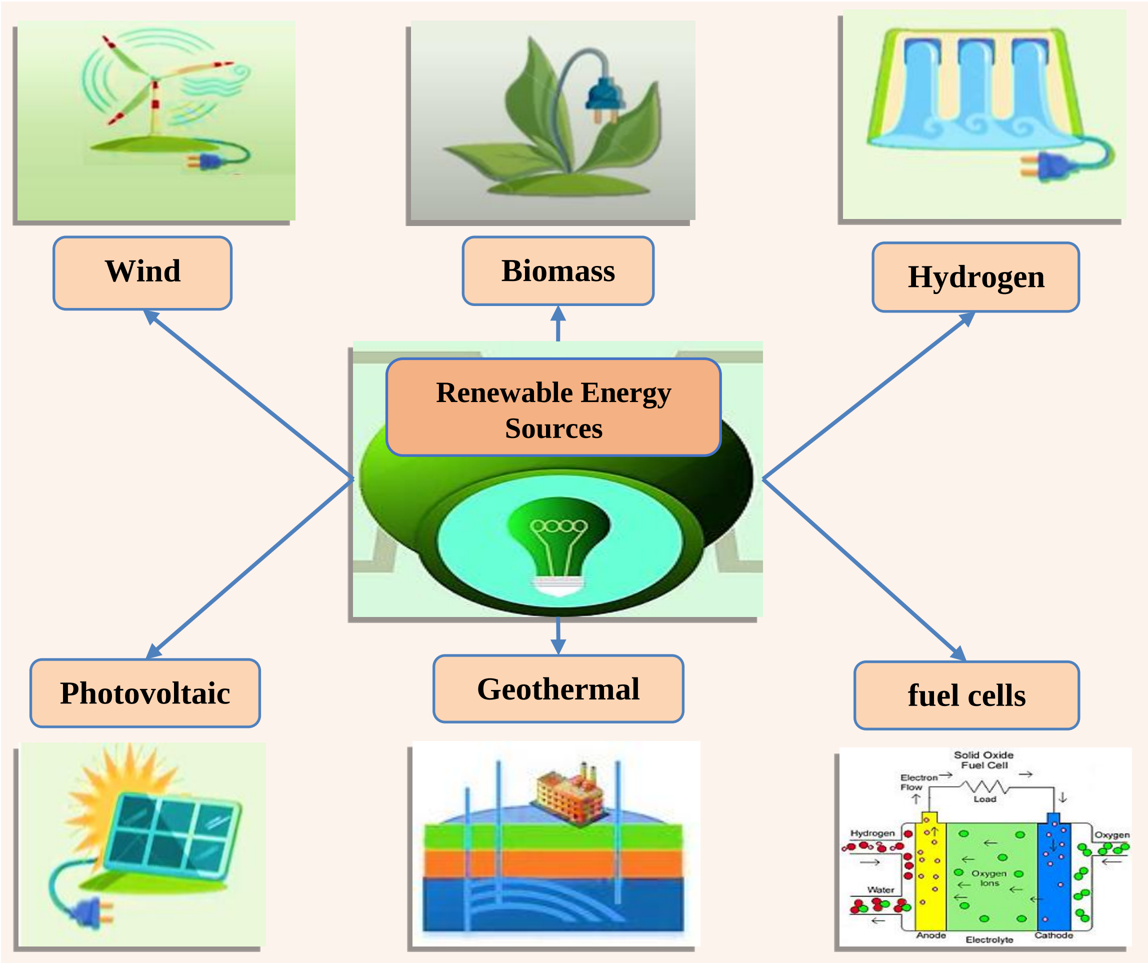

Fig. 3.1: Classification of renewable energy sources.

3.3.1. Photovoltaic (PV) Sources

3.3.1.1. Overviews about Photovoltaic (PV) Sources

Solar energy systems are of particular interest for their significant future impact. These systems use photovoltaic (PV) panels to convert sunlight directly into electricity through the photovoltaic effect of semiconductors. Solar production is affected by weather conditions, making storage batteries necessary to stabilize output. Solar energy harvesting has emerged as the most favorable choice among all renewable energy sources due to its usability, cleanliness, widespread availability, and lower maintenance costs [35].

3.3.1.2. State of art about photovoltaic

The photovoltaic (PV) effect, discovered by Becquerel in 1839, began to see commercial development for power generation in the mid-1950s, primarily for spacecraft applications until the mid-1970s. the cost of PV power was prohibitively high, which was about $100/W in 1962 and decreased to \$2.50/W by 1988, limited its competitiveness with traditional power sources for most terrestrial uses. Despite this, the PV industry grew significantly, from a cumulative capacity of about 5 MW in 1980 to around 160 MW. PV technology has become economically viable for remote corrosion protection and communications, with potential for significant market expansion at \$2/W and utility-scale adoption at \$1/W. Cost reductions, alongside efficiency and lifespan improvements, are expected to increase PV capacity to between 5,000 and 20,000 MW by the year 2000. A more conservative estimate by the Commission of European Communities in 1982 predicted annual world sales of 100 MW by 1990, reaching at least 200 MW/year by 2000.

This context underscores the importance of exploring PV applications and estimating system performance beyond monitored prototype systems, with PV systems being configured in various ways to accommodate diverse electrical loads [85].

3.3.1.3. Modeling a photovoltaic (PV) system

In a photovoltaic (PV) system, PV modules capture solar energy and convert it into direct current (DC) electricity. These modules are interconnected to form a PV solar panel system. An inverter is typically connected to this system to convert the DC into alternating current (AC), enabling its use in an independent power system or integration into the electrical grid, the **figure (3.2)** represents the diagram of a photovoltaic solar energy conversion chain [85].

Fig. 3.2: Diagram of a photovoltaic solar energy conversion chain.

- **The photovoltaic cell models**

PV cell models are classified into various equivalent circuits, the most widely used models are the Single Diode Model (SDM) and the Double Diode Model (DDM). These models provide frameworks for understanding and analyzing the performance of PV solar cells [86]:

A. Single-Diode Model (SDM)

The SDM is favored for its simplicity and high accuracy in describing the static properties of photovoltaic (PV) solar cells. It comprises a current source and a diode, with shunt resistance indicates leakage current, and the series resistance (R_S), reflects load current losses. The **figure (2.3 (a))** depicts the equivalent circuit of a SDM, which has five parameters: the photocurrent (I_{ph}), the saturation current (I_{sd}), the ideality factor (n), and the shunt resistance (R_{sh}).

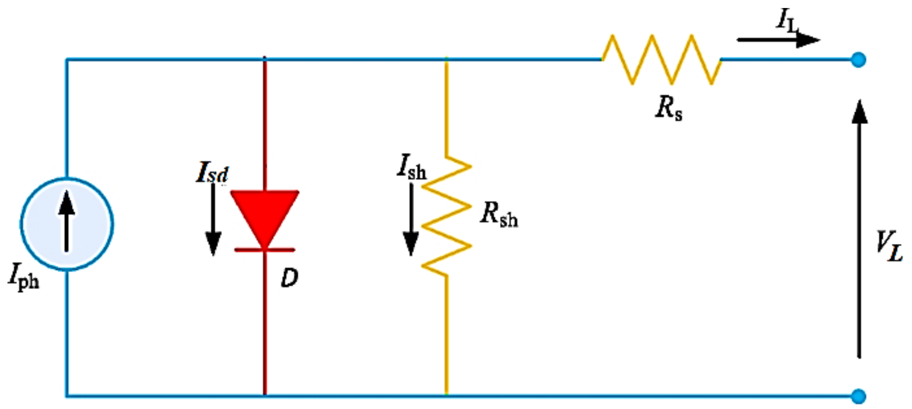

Fig. 3.3 (a): the equivalent circuit of a single-diode model (SDM).

uses the follow equation to express the output current (I_L), demonstrating its approach to modeling PV cell behavior [86].

$$I_L = I_{ph} - I_{sd}\left(\exp\left(\frac{V_L+R_SI_L}{n\frac{kT}{q}}\right) - 1\right) - \frac{V_L+R_SI_L}{R_{sh}} \tag{3.1}$$

Where, $V_L$and I_L refer to the measured I-V data of the PV cell, k denotes the Boltzmann constant, and electron charge are indicated by q, respectively; T refers to the cell temperature (K).

B. Double-diode model (DDM)

To improve the accuracy of PV cell modeling by accounting for current losses due to recombination in the depletion region, a factor not fully addressed by the Single Diode Model (SDM), an additional recombination diode is introduced. This addition incorporates two new parameters: n_2 and I_{sd2}. The Double Diode Model (DDM) is depicted in the **figure (2.3 (b))** and includes seven parameters: $I_{ph}, I_{sd1}, n_1, I_{sd2}, n_2, R_s$ *and* R_{sh}. The mathematical representation for the output current (I_L) in this model is expressed by equation (2):

$$I_L = I_{ph} - I_{sd1}\left(\exp\left(\frac{V_L+R_SI_L}{n_1\frac{kT}{q}}\right) - 1\right) - I_{sd2}\left(\exp\left(\frac{V_L+R_SI_L}{n_2\frac{kT}{q}}\right) - 1\right) - \frac{V_L+R_SI_L}{R_{sh}} \tag{3.2}$$

where I_{sd1} refers to the diffusion current and n_1 indicates ideality factor; n_2 and I_{sd2} refer to complex diode ideality issue and capacity current, respectively [80].

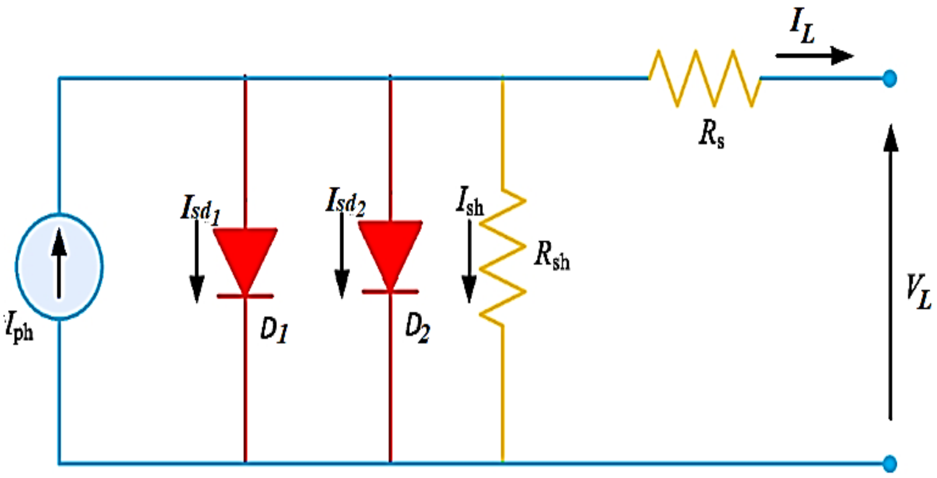

Fig. 3.3. (b): The equivalent circuits of double diode model.

There are also other models which can be derived from these two basic models, such as the three-diode model, which is rarely used due to its high computational complexity that does not simplify the reverse saturation current equation, among other derivatives.

C. The photovoltaic Module (PVM)

Taking into account N_p by N_s solar cells with varied parallel or series connections, the resulting output current, I, can be explained using equations (10) and (11) for both SDM and DDM. The **Fig. 3.3 (c)** depicts the equivalent circuits of PV module [80].

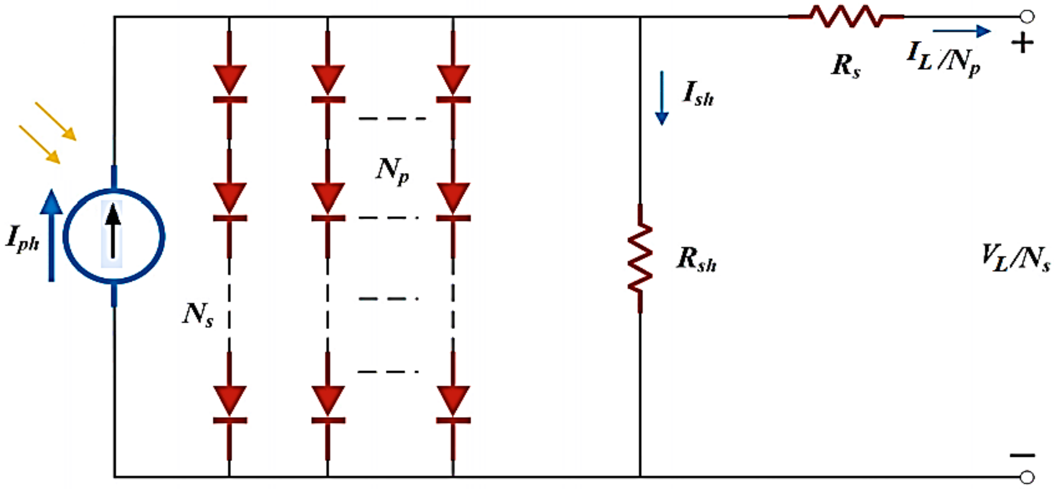

Fig. 3.3 (c): The equivalent circuits of PV cell model.

$$I = I_{ph}N_p - I_{sd}N_p\left(e^{\frac{v_L + R_S I_L\left(\frac{N_S}{N_p}\right)}{nV_t}} - 1\right) - \frac{V_L + R_S I_L\left(\frac{N_S}{N_p}\right)}{R_{sh}\left(\frac{N_S}{N_p}\right)} \tag{3.3}$$

$$I = I_{ph}N_p - I_{sd1}N_p\left(e^{\frac{V_L + R_S I_L\left(\frac{N_S}{N_p}\right)}{n_1 V_t}} - 1\right) - I_{sd2}N_p\left(e^{\frac{V_L + R_S I_L\left(\frac{N_S}{N_p}\right)}{n_2 V_t}} - 1\right) - \frac{V_L + R_S I_L\left(\frac{N_S}{N_p}\right)}{R_{sh}\left(\frac{N_S}{N_p}\right)} \tag{3.4}$$

3.3.1.4. Maximum Power Point Tracking (MPPT)

The MPPT techniques are used in PV systems to optimize the power output of solar panels by continuously tracking the MPP under different environmental conditions. This has led to extensive research and the development of various methods to address specific disadvantages. The **figure (3.4)** depicts the current and power under constant temperature and irradiance. The experimental method for building a solar model involves using key points on the I-V curve, such as the short circuit point (A), maximum power point (B), and open circuit point (C). For a four-parameter model, four equations are used to calculate the parameters (I_0, I_{pv}, α, R_s) by using a substitutable points A, B, C, and the zero value of the power derivative with respect to voltage (MPP D). For a five-parameter model, an additional point (E) is considered, which is the voltage midway between the open circuit voltage (V_{oc}) and the MPP voltage point (V_{mp}). The voltage value of this point can be determined by a specific equation (3.5) [87][88],

$$V_m = \frac{1}{2}(V_{mp} + V_{oc}) \tag{3.5}$$

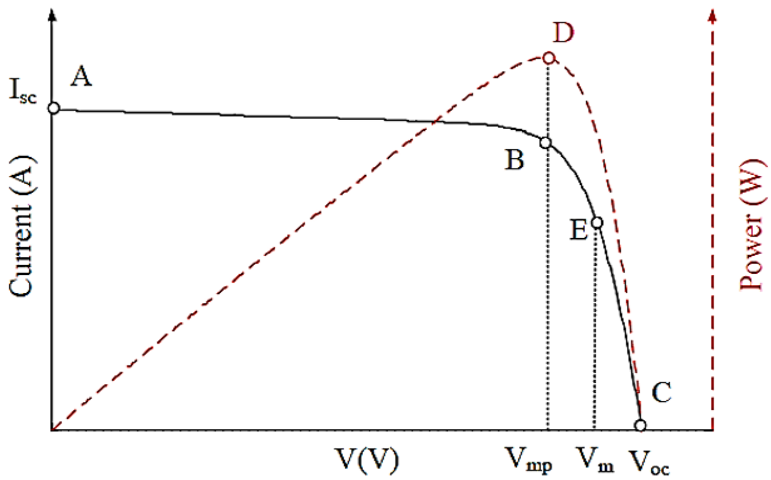

Fig. 3.4: The current and power under the condition of constant temperature and irradiance.

3.3.1.5. Electrical characteristics of a Photovoltaic (PV) cell

The electrical characteristics of a photovoltaic (PV) cell, including the current-voltage (I-V) and power-voltage (P-V) relationships, are essential for understanding its behavior and performance. These characteristics help determine the cell's efficiency, and its response to environmental changes such as varying sunlight intensity, temperature, and load.… etc. They illustrate how the current output changes with different voltage levels across the cell's terminals under various conditions [89].

- **Example:** The typical characteristics of the PV cell are illustrated by the current versus voltage (I-V) and the power versus voltage (P-V) curves, shown in **figure (3.5 and 3.6).**

The **Table 3.1** represents the electrical parameters for the PV module from Tata Power Solar Systems TP250MBZ.

Table. 3.1: PV module parameters of Tata Power Solar Systems TP250MBZ.

PV-parameters	Abbreviations	Values
Maximum-power	Pmax	249 W
Voltage at MPPT	Vmax	30 V
Current at MPPT	Imax	8.3 A
Short circuit current	Isc	8.83 A
Open circuit voltage	Voc	36.8 V
Temperature coeffecient Isc	Tsc	0.063805 (%/deg.C)
Temperature coeffecient Voc	Toc	-0.33 (%/deg.C)
Series-connected cells	No.cells	60 (Ncell)

- **The Influence of illumination**

The **figure (3.5)** demonstrates the Influence of illumination on I-V and P-V characteristics curves of PV module at various irradiance and constant temperature of 25°C.

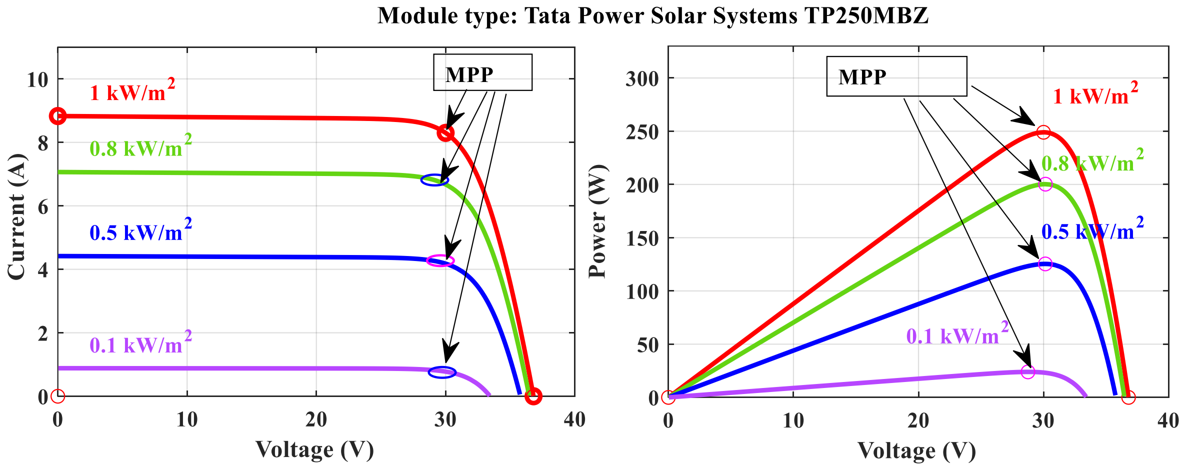

Fig. 3.5: The I-V and P-V curves of PV module at various irradiance and constant temperature of 25°C.

- **the Influence of temperature**

The figure (3.6) Demonstrates the Influence of temperature on I-V and P-V characteristics of PV module at various temperatures and constant irradiance of 1000 W/m2.

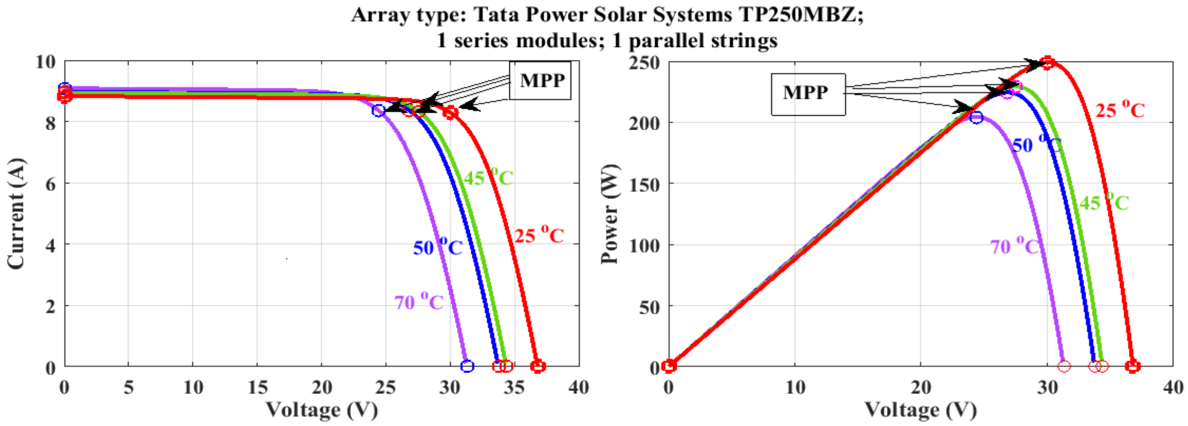

Fig. 3.6: The I-V and P-V curves of PV module at constant irradiance of 1000 W/m^2 and various temperatures.

Figure 3.6 shows that as the temperature decreases, the open-circuit voltage increases, while the short-circuit current decreases. The main factor contributing to the drop in current at lower temperatures is a reduction in saturation current. Since the decrease in current has a greater effect than the increase in open-circuit voltage, the overall maximum power output decreases.

3.3.1.6. Stochastic modeling of Solar power plant

Monte Carlo simulations are used to model the probability of different outcomes in processes influenced by random variables. For solar irradiance, this involve simulating various atmospheric conditions, like the sunlight angles, cloud coverage, and other that affect the solar energy received on a surface. The output depends on solar irradiance (G) which follows a lognormal probability density function (PDF), with mean μ and standard deviation σ is [8]:

$$f_G(G) = \frac{1}{G\sigma\sqrt{2\pi}} \exp\left\{\frac{-(\ln G-\mu)^2}{2\sigma^2}\right\} \text{ for } G > 0 \tag{3.6}$$

Mean of lognormal distribution is defined as:

$$M_{lgn} = \exp\left(\mu + \frac{\sigma^2}{2}\right) \tag{3.7}$$

3.3.1.7. Solar photovoltaic power Uncertainty Modeling

The solar irradiance (G) to energy conversion for solar PV is given by:

$$P_s(G) = \begin{cases} P_{sr}\left(\frac{G^2}{G_{std}R_c}\right) & \text{for } 0 < G < R_c \\ P_{sr}\left(\frac{G}{G_{std}}\right) & \text{for } G \geqslant R_c \end{cases} \tag{3.8}$$

where, G_{std} is the solar irradiance in standard environment. R_c is a certain irradiance point. P_{sr} is the rated output power of the solar PV unit.

- **Example 1:**

G_{std} is set as 800W/m^2. R_c is a set as 120W/m^2. P_{sr} is a set as 50 MW; $R_c = 120\text{W/m}^2$

nbins = 30; the number of bins for histogram,
Monte Carlo simulation size = 8000; the number of Monte Calro scenarios.

- **PDF parameters of solar PV power plants**

Table. 3.2: summarizes the selected parameters for lognormal PDF.

Solar PV plant	
Lognormal PDF parameters	**Lognormal mean, M_{lgn}**
$\mu = 6$ $\sigma = 0.6$	$G = 483\ \text{W/m}^2$

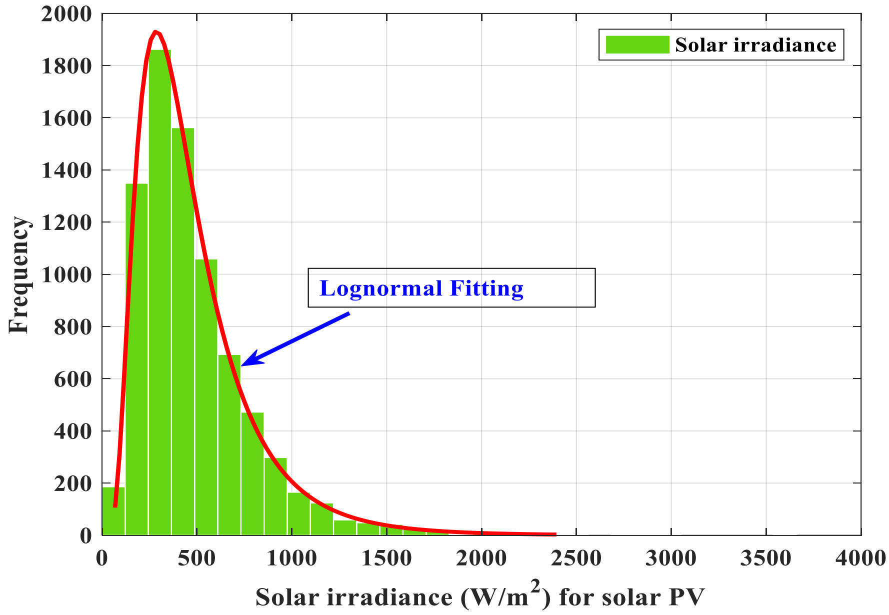

Fig. 3.7: Solar irradiance distribution for solar PV ($\mu = 6$ $\sigma = 0.6$) (example 1)

The **figure (3.7)** indicates frequency distribution and lognormal fitting of solar irradiance after running Monte Carlo simulation with a sample size of 8000.

The histogram in **figure (3.8)** illustrates the stochastic power output from a solar PV plant. The magenta dotted line represents the scheduled power that the solar PV plant is supposed to deliver to the grid. This scheduled power is a predetermined amount agreed upon between the Independent System Operator (ISO) and the solar PV firm owner.

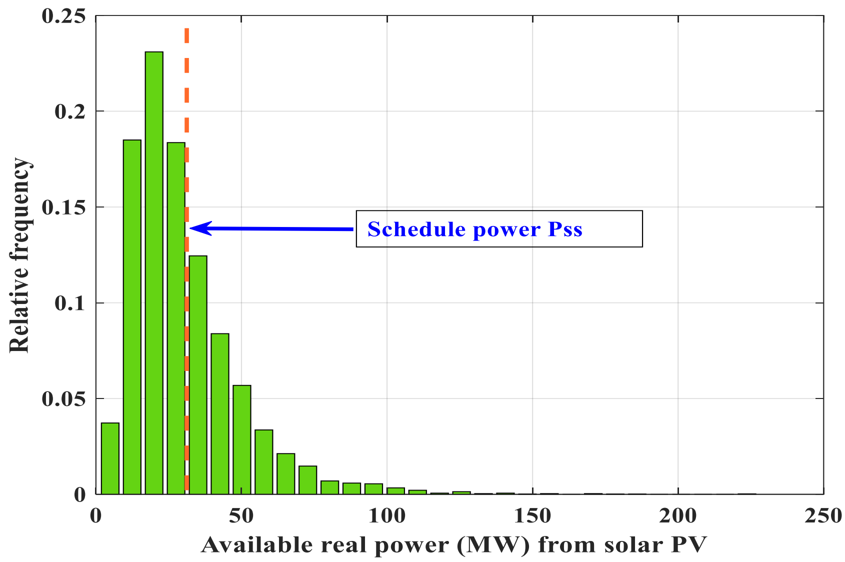

Fig. 3.8: Real power distribution (MW) of Solar PV (exemple 1).

3.3.2. Wind Turbine sources

Wind energy is a renewable energy that comes from the wind. It's made by using wind turbines generation, which are tall machines with big blades. When the wind blows, it turns the blades, creating a kinetic energy used to generate electricity. This form of energy is clean and environmentally friendly. However, its availability fluctuates due to weather conditions, requiring careful planning for integration into the electrical network, and additional power sources support wind energy to stabilize the electrical supply. Wind farms consist of multiple wind turbines, are set up to produce significant amounts of power and are connected to transmission and distribution networks [35].

3.3.2.1. State of Art about the wind turbine

Wind power has a long history, initially has been used for mechanical tasks such as pumping water and grinding grain. In the Middle Ages, windmills were used across the Mediterranean, but by the end of the 18th cycle, around 10,000 wind turbines were in service only in the Netherlands. The first electricity-generating wind turbine was built in 1887 created by Scottish engineer James Blyth. followed by wind turbine invented in 1888 in Cleveland with a capacity of generated about 12 kilowatts (kW) of power. Since then, wind turbines have become more advanced, with a shift in the late 20th century to large-scale wind farms for electricity generation. Technological advancements since the 1990s have led to the development of wind turbines exceeding 5 MW, with 12 MW turbines currently being developed. The largest turbine in the world is GE's Haliade-X, the industry's first 12 MW turbine. The average size of offshore turbines installed in 2019 was

7.8 MW, up from 6.8 MW in 2018 according to trade body Wind Europe. The first prototype was installed at the Port of Rotterdam in 2019 for testing, with commercialization expected in 2021. Government subsidies have enabled the development of offshore wind farms, which now produce alternating current for electricity grids, similar to thermal power plants. In recent decades, technological advancements have significantly increased the efficiency and capacity of wind turbines, making wind energy a crucial part of the global energy mix, providing clean renewable electricity [88].

3.3.2.2. Types of wind turbine

There are two major types of wind turbine basics of wind turbine technologies available depending on the turbine's axis of rotation [88][89] [90]:

A. Horizontal axis wind turbines (HAWTs)

In the HAWT (**figure (3.9))**, a prominent rotor shaft and electric generator are essential components. The gearbox increases the slow rotation of the blades rotation speed to improve electricity generation efficiency. The main rotor shaft is designed vertically, offering high efficiency and the ability to generate power from winds coming from multiple directions.

Fig. 3.9: Horizontal axis wind turbine.

B. Vertical axis wind turbines (VAWTs)

The VAWTs (**figure (3.10))**, can harness winds from various directions. However, Horizontal Axis Wind Turbines (HAWTs) generally perform better in wind power extraction, making them more common in commercial use. On the other hand, VAWTs are a wind turbine type that is much less used. However, recent advancements have led to important new trends in the use and benefits of VAWT technologies provided by researchers and manufacturers [88][91].

Fig. 3.10: Vertical axis wind turbine.

3.3.2.3. Operation and Components of Wind Turbines

The major components of a wind turbine system are shown in the following **figure (3.11)** [88][91].

1. Anemometer: Measures wind speed and transmits the data to the controller.

2. Blades: Captures the kinetic energy from the wind and converts it into rotational energy.

3. Brake: The brake is used to stop the shaft in case of emergency.

4. Controller: It is used for starting up, and controlling the turbine's speed and adjusts operation for optimal performance and safety.

5. Gear box: The main function of gear is to rise the speed from the high-speed shaft to another shaft. It is connected direct to the generator.

6. Generator: It is the most important part of the wind energy system. Converts the rotational energy from the rotor into electricity.

7. Shaft: It is used for changing the low speed to high speed by the rotor.

8. Nacelle: The rotor attaches to the nacelle that fixed at the top of the tower.

9. Pitch: It is used to stop blades or to increase the speed in case of high and low power generation.

10. Rotor: It consists of blades and hub.

11. Tower: The quality of power generation depends on the height of towers.

12. Wind Vane: It is a sensor to track the wind's flow and communicate with yaw to change the direction of the blades.

13.Yaw Drive: It is used to track the wind direction

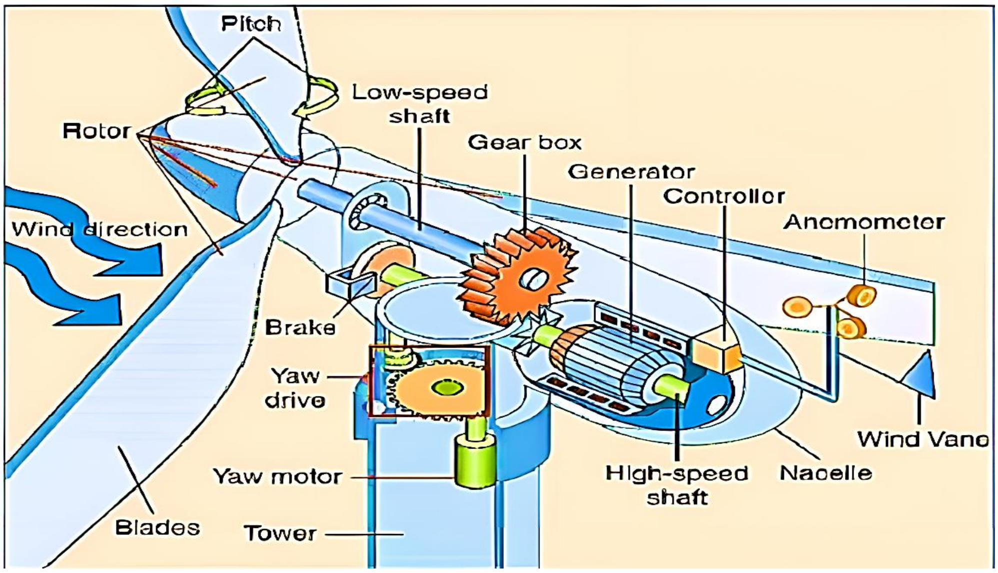

Fig. 3.11: Inside wind turbines showing mechanical, electrical, and control components.

3.3.2.4. Wind turbine electric generators technology

The major type of wind turbine generators can be represented in the following **figure (3.12)**:

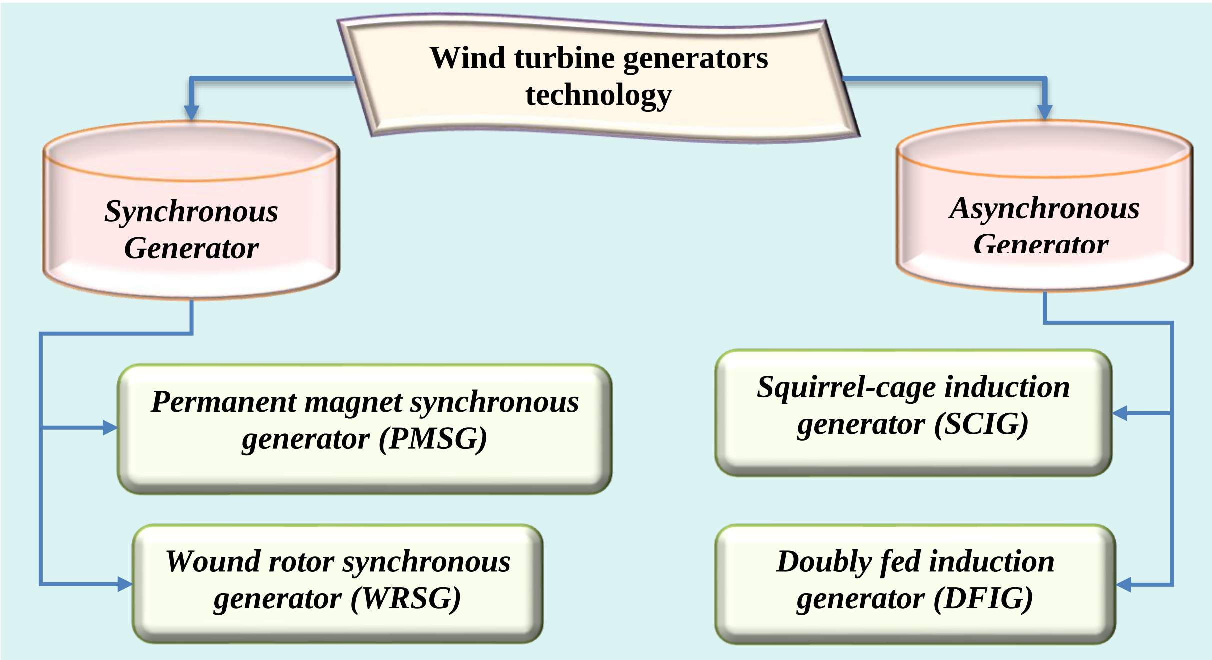

Fig. 3.12: Type of Wind turbine generators.

3.3.2.5. Wind energy conversion system (WECS)

The Wind Energy Conversion System (WECS) includes wind turbines, generators, control systems, and interconnection apparatus. The blades convert wind kinetic energy into mechanical energy, which is then transformed into electrical energy by a generator. Most generators require high speeds to generate electricity. The power output is transmitted to the grid via a transformer, with a controller in place to prevent disturbances and protect the electrical system. Wind farms can be located in various areas, such as offshore, onshore, and hilly regions, …. etc. the **figure (3.13)** illustrates the block diagram of the WECS [90].

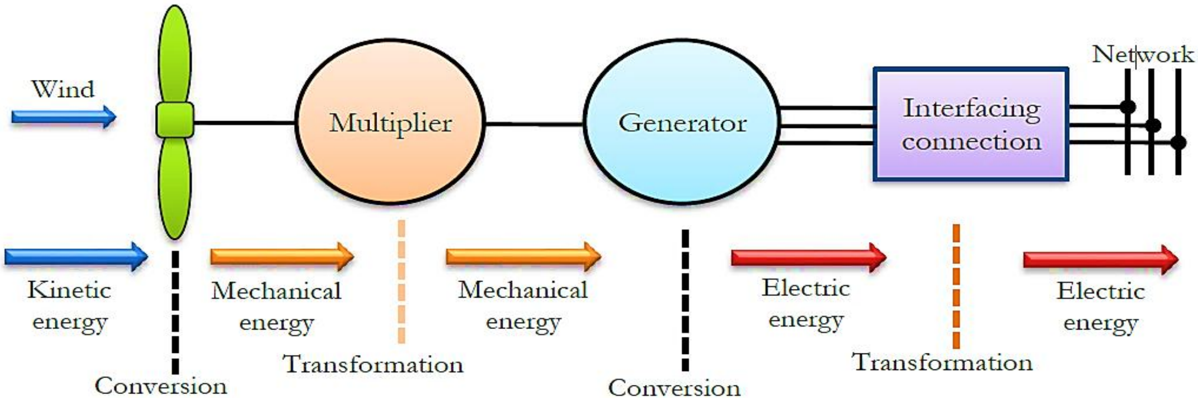

Fig. 3.13: The wind energy conversion system (WECS).

The kinetic energy (E_k) can be expressed as follows:

$$E_k = \frac{1}{3}\, m{v_{wind}}^2 = \frac{1}{2}(\rho A){v_{wind}}^2 \qquad (3.9)$$

Where:

$\boldsymbol{m}$	is the mass of air passing through a given area "$\boldsymbol{A}$"
$\boldsymbol{\rho}$	is the air density 1.225 (kg/m^3)
A	A= ΠR^2 is the surface area swept by the rotor (m^2)
$\boldsymbol{v_{wind}}$	is the wind speed at the center of the rotor (m/sec),
λ	Tip speed ratio of the rotor blade
β	Blade pitch angle (deg)

The mechanical output power of the wind turbine is given by the following equation:

$$\boldsymbol{P_m = C_p(\lambda, \beta)\frac{\rho A}{2} v_{wind}^3} \qquad (3.10)$$

$\boldsymbol{C_p}$	is the performance coefficient of the wind energy conversion
$\boldsymbol{P_m}$	Mechanical output power of the turbine (W)

With: $\lambda = \frac{\Omega_t R_t}{V}$

Where, R_t is the rotor blade radius in m, Ω_t is the low-speed shaft turbine speed in rad/sec [92].

3.3.2.6. Stochastic modeling of wind power plant

the Weibull probability density function (PDF) is used to model and characterize the variations in wind speed distributions. The PDF helps identify the frequency distribution of wind speeds over specific periods, which is crucial for the wind industry to differentiate between different speeds. The formula for the Weibull distribution PDF is provided in equation (3.11) [93]:

$$f_V(V) = \frac{\beta}{\alpha}\left(\frac{v}{\alpha}\right)^{\beta-1} e^{\left[\left(-\frac{v}{\alpha}\right)^{\beta}\right]} \tag{3.11}$$

Where; f_V is the PDF of wind speed, (β) and, (α) represent the shape factor and scale factor, respectively, v is the wind speed(m/s).

The mean of Weibull distribution is expressed as follow (3.12):

$$M_{wbl} = \alpha^m * \Gamma\left(1 + \frac{m}{\beta}\right), m = 1,2, \dots \dots n \tag{3.12}$$

Where; gamma function Γ is given by equation (3.13) as follow:

$$\Gamma(\mathrm{x}) = \int_0^{\infty} \exp^{-t}\ t^{x-1} dt \tag{3.13}$$

3.3.2.7. Wind speed distribution

The Weibull fitting and wind frequency distributions shown in **figure (3. 14)** are derived from 8000 Monte-Carlo scenarios. According to reference [68], the design requirements for wind turbines specify the highest turbulent class IA, certifying turbines to operate effectively at a maximum annual average wind speed of 10 m/s at hub height [9].

The windfarms' shape (β) and scale (α) parameters are carefully selected to maintain a maximum Weibull mean value, remains around besides.

- **Example 2: PDF parameters of wind power plants**

The table (3.3) represent the PDF parameters Values of selected Weibull shape (β) and scale (α). **The figure (3.14)** represents the Wind speed distribution for wind farm **(example 2).**

Table. 3.3: PDF parameters Values of selected Weibull shape (β) and scale (α).

Wind power generating plants		
Windfarm	Weibull PDF parameters	Weibull mean, M_{wbl}
	$\alpha = 10$ $\beta = 2$	$v = 8.862$ m/s

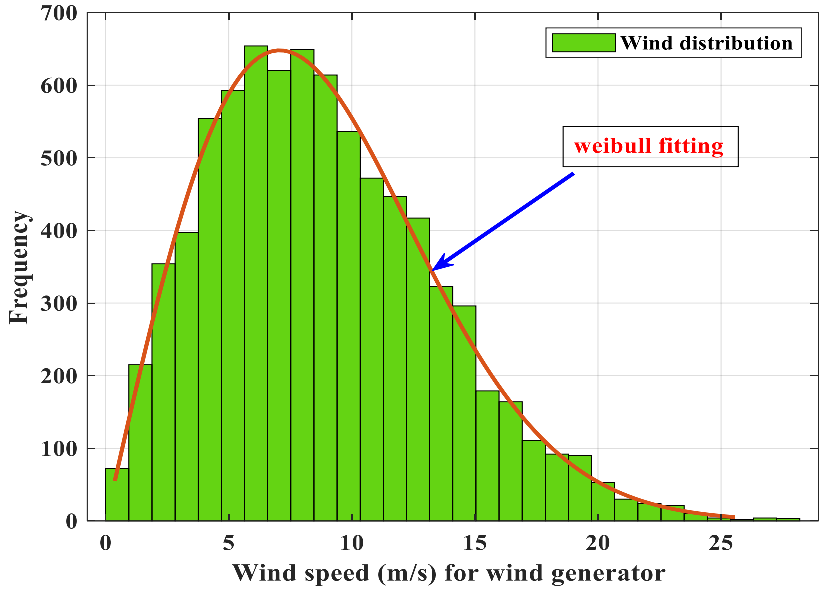

Fig. 3.14: Wind speed distribution for wind farm ($\alpha = 10, \beta = 2$) (example 2)

3.3.2.8. Modeling of Wind Power Uncertainty power

The Weibull distribution is widely used in statistical analysis, particularly in studies related to wind energy. Output power of a wind turbine, the PDFs for two different scale and shape factors, also the relationship between the power generated, and wind speed are represented in the following equations (3.14) [94]:

$$p_w(v) = \begin{cases} 0, & \text{for } v < v_{\text{in}} \text{ and } v > v_{\text{out}} \\ p_{wr}\left(\frac{v - v_{in}}{v_r - v_{in}}\right) & \text{for } v_{\text{in}} \leq v \leq v_r \\ p_{wr} & \text{for } v_r < v \leq v_{\text{out}} \end{cases} \tag{3.14}$$

Where, p_w denotes the sized output power of the windfarm (installed capacity), v_{in} indicates the cut-in wind speed, and v_{out} denotes the cut-out wind speed of the turbine, v_r represents the wind speed rated, the sized output of a particular wind turbine is indicated by p_{wr}.

3.3.2.9. Operating Region and control strategies of the Wind Turbine

Referring to equation (3.13), it may be observed that the variable wind power is discrete in a couple of regions of wind speeds. The power curve shows the theoretical relationship between wind speed and the wind turbine's output, which is divided into three speed control the v_{in} wind speed, the rated wind speed v_{r} , and the v_{out} wind speed [92][93]. Which represent by four discrete operating zones of the turbine, probabilities can be distinguished in the **figure (3.15)** [10]:

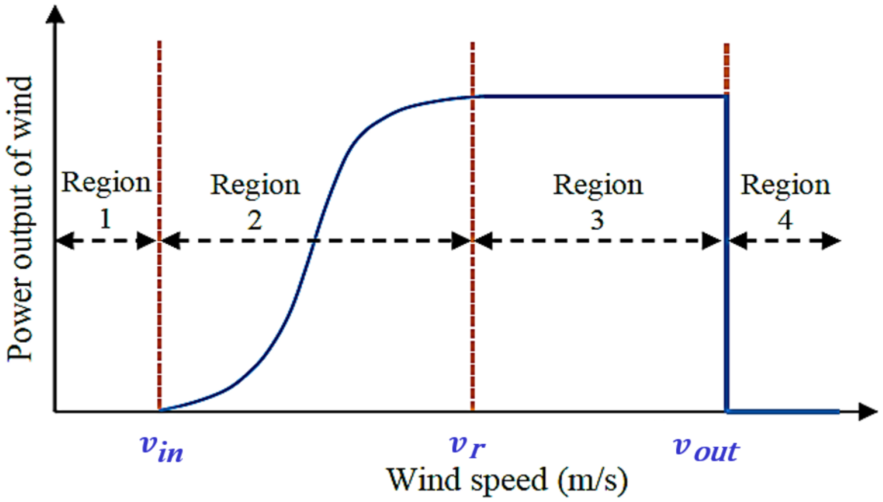

Fig. 3.15: The wind power output curve.

In the **first region**, when the wind speed (v) is below v_{in} speed, there is no power will be produced due to the very low speeds. In **the second region**, when the wind speed (v) is more than v_{in} speed and below the rated speed v_r; wind turbines are started to generate power when the wind speed exceeds v_{in}, and the power generated increases with the wind speed grows until the **rated power** of the turbine is reached at the rated speed v_r. In the **third region**, where wind speeds from v_r to v_{out}, the power generation remains constant until cut-off wind speed (v_{out} in the **figure 3.15**). In the **fourth region**, to avoid high mechanical damage, the wind turbine is stopped when wind speeds exceed the v_{out}wind speed limit.

3.3.2.10. Calculation of wind power probabilities

It can be noticed that the output power from a wind generator is non-continuous and is limited to specific wind speeds. [94]. From equation 3.15, it's evident that if the wind speed v is less than v_{in} and above v_{out}, Additionally, when the wind speed falls within the range $v_r \leq v \leq v_{\text{out}}$; the turbine produces power P_{wr}. Wind output power probabilities for each zone are calculated by as follows equation (3.16) [3]:

$$f_w(p_w)\{p_w = 0\} = 1 - \exp\left[-\left(\frac{v_{\text{in}}}{\alpha}\right)^{\beta}\right] + \exp\left[-\left(\frac{v_{\text{out}}}{\alpha}\right)^{\beta}\right] \tag{3.15}$$

$$f_w(p_w)\{p_w = p_{wr}\} = \exp\left[-\left(\frac{v_r}{\alpha}\right)^{\beta}\right] - \exp\left[-\left(\frac{v_{\text{out}}}{\alpha}\right)^{\beta}\right] \tag{3.16}$$

On the other hand, the chances of achieving the rated and output power of the wind turbine for the continuous portion is being between v_{in} and v_{r} and is mentioned as follows:

$$f_w(P_w) = \left(\frac{k(v_r - v_{in})}{\alpha P_{wr}}\right)\left(\frac{v_{in}P_{wr} + P_w(v_r - v_{in})}{\alpha P_{wr}}\right)^{(\beta-1)} \cdot \exp\left(-\left(\frac{v_{in}P_{wr} + P_w(v_r - v_{in})}{\alpha P_{wr}}\right)^{\beta}\right) \tag{3.17}$$

Where;

$\rho = P_W / P_{wr}$ is the ration of linear range wind speed to cut-in wind speed, $l = (v_r - v_{in}) / v_{out}$ is the ratio of wind power output to rated wind power.

3.4. Conclusion

This chapter offers a detailed exploration of renewable energy sources. It provides a systematic classification scheme and in-depth analysis of specific types, including solar photovoltaic and wind power. The next chapter focuses to the study of the optimal power flow (OPF). Highlighting their importance in identifying and addressing issues within electrical networks. It delves into the description of the optimal power flow problems in a hybrid network, taking into account the integration of renewable energy sources.

CHAPTER 4: Optimal power flow management.

4.1. Introduction

Power flow (PF) is one of the primary challenges faced by managers of an electrical energy production and transport system. It is a key element in enhancing, planning and the smooth operation of electrical networks. The problem of optimal power flow (OPF) has been a key research focus since it was introduced by Carpentier in 1962. OPF aims to minimize the total cost of power generation while reducing power losses and adhering to both equality and inequality constraints [17]. As well as to plan for future growth of the electrical power systems, the issue of OPF is considered an essential operator’s tool, that has emerged as one of the more complex problems that must be solved [35]. OPF plays a significant role in solving modern optimization problems in power systems management, planning, and operation [95], It provides real-time optimization to ensure efficiency and safety way when increasing load demand is an urgent challenge, aiming to find optimal operating conditions within physical, management, and engineering constraints of energy system operators in electrical grids [96]. The primary objective of OPF is to assess and ensure network safety by optimizing a specific objective while respecting constraints. This problem is typically complex, non-linear, large-scale, multi-dimensional, and involves non-convex constraints [97].

This chapter provides an overview of the Optimal Power Flow (OPF). It starts with a brief modeling of the electrical network elements, followed by a concise overview about the formulation of the OPF problem, including objective functions, and constraints, highlighting their key features.

4.2. Modeling of the electrical network elements

The analysis of power flow is generally conducted on a network whose electrical components and their models are known. When the network modeling is accurate, the results of the analysis reflect, quite reliably, the measurements taken in the field [98][99].

4.2.1. Generator model

Generators are the network elements capable of providing active power to the system. They can also produce or consume reactive power to maintain a certain level of voltage. The production limits of generators are defined by:

$$P_{G_i}^{min} \leq P_{G_i} \leq P_{G_i}^{max} \tag{4.1}$$

$$Q_{G_i}^{min} \leq Q_{G_i} \leq Q_{G_i}^{max} \tag{4.2}$$

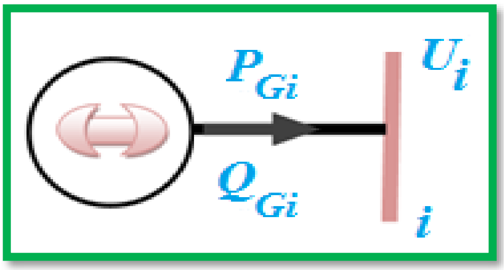

Fig. 4.1: Generator Model.

4.2.2. Load model

Loads represent the consumers connected to the network (industries, services, households, etc.). They are modeled by constant powers independent of nodal voltage:

$$S_{D_i} = P_{D_i} + jD_{D_i} \tag{4.3}$$

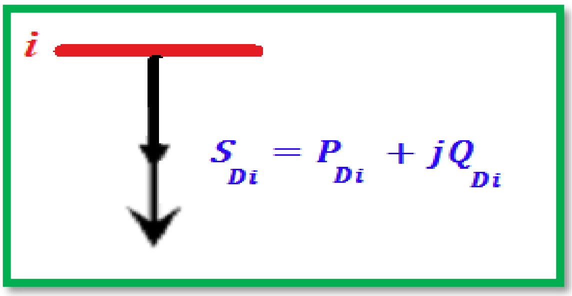

Fig. 4.2: load model.

Reactive power can be positive or negative depending on whether the load is inductive or capacitive in nature.

4.2.3. Transformers

An electrical energy transformer is represented by an asymmetric π quadrupole. The associated parameters are the transformation ratio a_{ij} and the leakage impedance. **(Figure 4.3).**

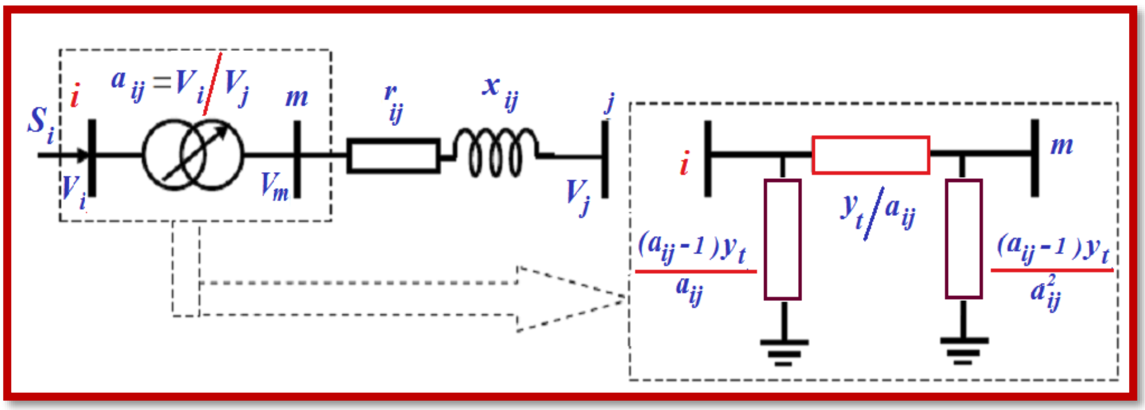

Fig. 4.3: transformer model.

4.2.4. Transmission lines

Transmission lines are typically modeled using their classic π equivalent circuit, where the transverse conductance is neglected (see **figure (4.4)**).

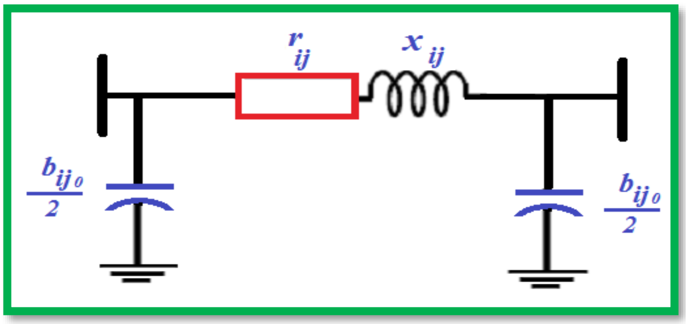

Fig. 4.4: Model of a π-form transmission line.

The nodal admittance matrix of a line connecting between the buses i and j is given by:

$$\underline{Y} = \begin{pmatrix} y_{ij} + \frac{y_{ij_0}}{2} & -y_{ij} \\ -y_{ij} & y_{ij} + \frac{y_{ij_0}}{2} \end{pmatrix} \quad (4.4)$$

Where the series admittance $\mathbf{y_{ij}}$ represent by:

$$\underline{y}_{ij} = \frac{1}{r_{ij}+jx_{ij}} = g_{ij} - jb_{ij} \quad (4.5)$$

$\mathbf{r_{ij}}$: series resistance of line; $\mathbf{x_{ij}}$: series reactance of line;

The transversal admittance corresponding to capacitive effects is written as:

$$\underline{y}_{ij_0} = jb_{ij_0} \quad (4.6)$$

$\mathbf{b_{ij_0}}$: The transverse susceptance.

4.2.5. Shunt elements

Shunt devices, typically used for reactive power compensation and voltage support, are modeled by admittances $y_i$of the form:

$$y_i = g_i + jb_ic \quad (4.7)$$

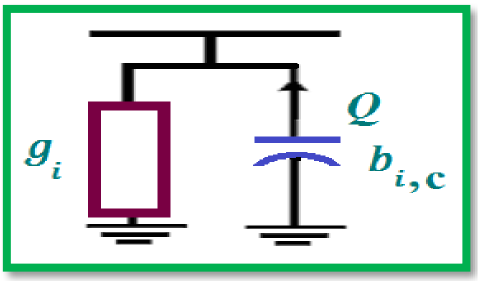

Fig. 4.5: Shunt Element Model.

4.3. Types of bus

Busbars (bus) in a system are generally classified into three types [99]:

4.3.1. Reference bus

This busbar serves as a reference point where the magnitude and phase angle of the voltage are specified. This busbar accounts for the difference between the predicted loads and the generated energy, which is caused by losses in the network.

4.3.2. Load bus

In these busbars, active and reactive powers are specified. The magnitude and phase angle of bus voltages are unknown. These busbars are referred to as P-Q buses.

4.3.3. Generation (Regulation, control) bus

Also known as voltage-controlled bars. In these nodes, active power and voltage magnitude are specified. The phase angle of the voltage and reactive power are to be determined. Limits on the reactive power value are also specified. These busbars are referred to as P-V buses.

Table. 4. 1: Bus Types.

Type of bus	Known Variables	Unknown Variables
PQ	Active and reactive powers (P,Q)	Voltage magnitude and phase angle (V,δ)
PV	Active power and voltage (P,V)	Voltage angle and reactive power (δ,Q)
Reference	Voltage magnitude and angle (V,δ)	Active and reactive powers (P,Q)

4.4. Description of the Power Flow

In electrical networks, power flows from plants to load centers. The calculation of power flow helps in identifying power system behavior, it is crucial for control and planning applications to ensure the network operates within limits. Solving a power flow problem involves determining and aims to collect detailed information under specified operating conditions about [12][97]:

- Voltage angles and magnitudes for each node.
- Power flows through transmission lines from one node to another.
- Power is injected at a node, active and reactive losses in the electrical network.

4.4.1. Methods for solving of Power Flow (PF)

Nonlinear equations defining the power flow (PF) problem require iterative algorithms for resolution. The study of power flow is essential for analyzing and understanding the behavior of electrical power system networks under various operating conditions. Several methods are used to address their issues, the most commonly used iterative algorithms include [12]:

- Gauss-Seidel Method.
- Newton-Raphson Method.
- Fast Decoupled Method

Each method has its advantages and limitations, and the choice of method depends on factors such as the size and complexity of the power system, the desired level of accuracy, and the computational resources available. The first numerical method used was the Gauss-Seidel iterative method. This method requires a large number of iterations for large networks and a very long convergence time. The most well-known method is the Newton-Raphson (N-R) method. The latter requires more time per iteration than the Gauss-Seidel method, but it only requires a few iterations to reach the solution, even for large networks [12].

4.5. Description and formulation of the OPF problems

Optimal Power Flow (OPF) focuses on determining the best operating conditions for a power system. As a crucial tool for energy management optimization, OPF aims to enhance a specific objective function while adhering certain constraints. The OPF challenge can typically be described in the following manner [100][101]:

- **Optimize:**
- $f(x, u)$ (is the modeled fitness function of OPF) (4.8)
- **Subjected to:**
- $G_i(x, u) = 0 \quad i = 1,2, \dots \dots \dots . m$ (is the equality **constraints**) (4.9)
- $H_j(x, u) \leq 0 \quad j = 1,2, \dots \dots \dots . p$ (is the inequality **constraints**) (4.10)

Here; u indicates the decision variables; x indicates the state variables.

the following equation (4.11) can be used to explain the vector of state variables [100]:

$$x = \left[P_{G_1}, V_{L1} \dots V_{L,NPQ}, Q_{G,1} \dots Q_{G,N_G}, S_{TL,1} \dots S_{TL,NTL}\right] \quad (4.11)$$

where, P_{G1} represents the power of the slack bus, V_L, denotes the voltage of the load bus. The generator's reactive power is represented by Q_G, S_{TL} represents the apparent power flow in the transmission lines.

The follow formula (4.12) can be explained the controlled variables (u) vector [100]:

$$u = [P_{G_2} \dots P_{G,NG}, V_{G,1} \dots V_{G,NG}, Q_{C,1} \dots Q_{C,n_C}, T_1 \dots T_{N_{Tr}}] \qquad (4.12)$$

Where, P_G denotes the generator's power, the injected shunt compensator's reactive power units and their number are indicated by Q_c, and n_C, respectively, the transformer's tap setting and their number are denoted by T, and N_{Tr}. The generator's bus voltage is represented by V_G.

4.5.1. Types of Optimal Power Flow

The **figure (4.6)** illustrated the main types of Optimal Power Flow.

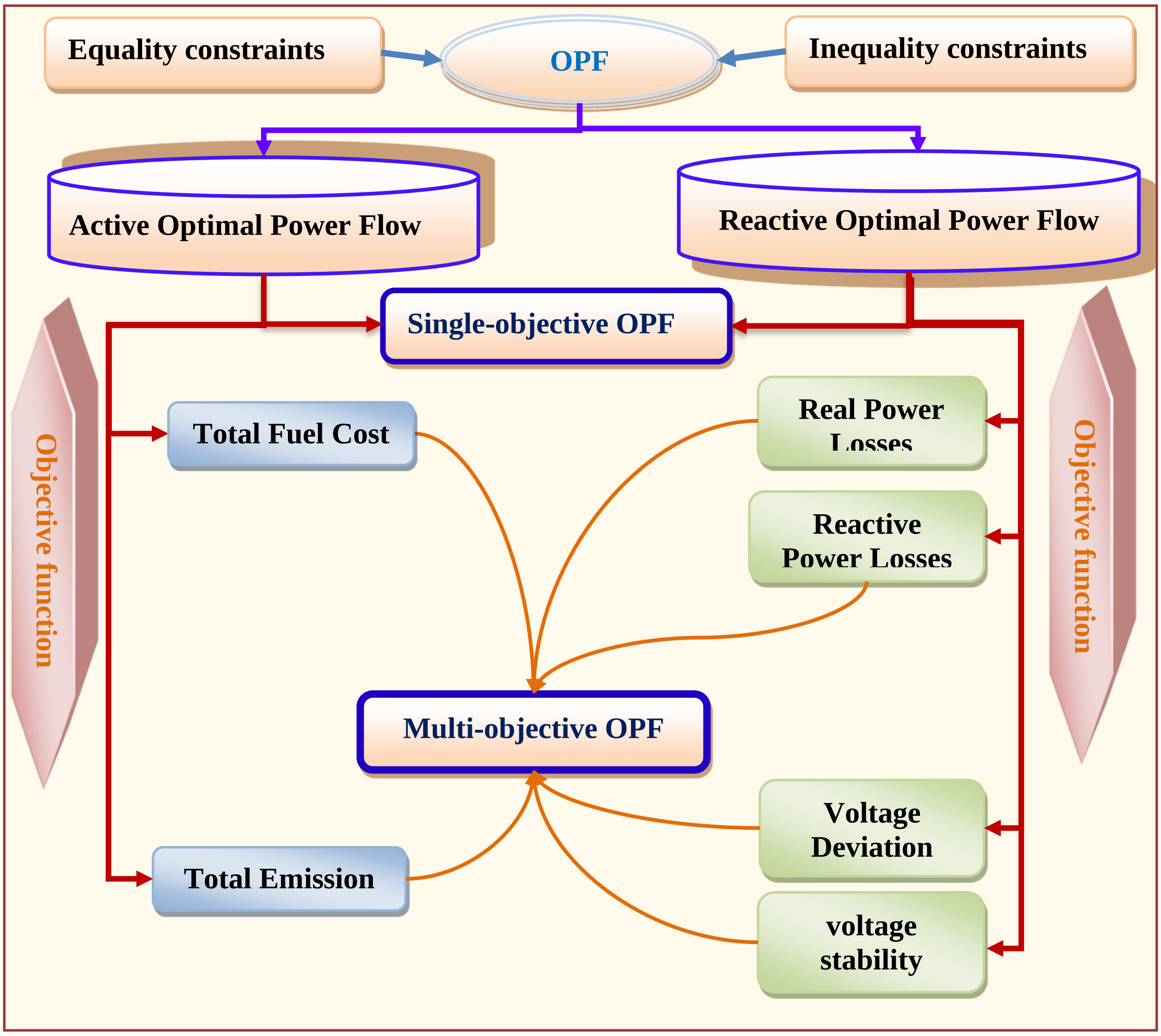

Fig. 4.6: Types of Optimal Power Flow.

4.5.2. Objective Functions

The main types of OPF can be categorized into various types, distinguished by objectives, constraints, solution methodologies, and reflecting the nature of power management they entail. Here Some well-known objectives can be identified as below [58]:

A) Minimizing the Total Cost of Thermal Power Generation Units (TFC):

The power generation cost is primarily dependent on operating costs, which consist of fuel costs for thermal generators being a significant component in the thermal power plants. The relationship between the generated power (MW) and the fuel cost ($/h) is typically represented through a quadratic equation using a single polynomial, as demonstrated in the following equation (4.13) [9][100].

$$F_1 = C_{TG}(P_{TG}) = \sum_{i=1}^{N_{TG}} (c_i P_{TG_i}^2 + b_i P_{TG_i} + a_i) \ (\$/\mathrm{h}) \tag{4.13}$$

Where: F_1 stands for the total thermal cost, N_{TG} denotes to the total number of thermal generators.

B. Emission gas (TEG)

During the process of power generation, conventional energy sources are known to emit harmful gases into the atmosphere. The fitness function Emission (ton/h) can be expressed through equation (4.14); [8][100][102].

$$F_2 = E = \sum_{i=1}^{N_{TG}} \left[(\alpha_i + \beta_i P_{TGi} + \gamma_i P_{TGi}^2) \times 0.01 + \omega_i e^{(\mu_i P_{TGi})}\right] \tag{4.14}$$

C. The cost of Power Generating Units incorporation valve-point effect

The cost function for fuel-based generation units is non-convexity containing multiple increases due to valve point stacking effects. This creates a ripple effect on the price curve. The cost function with incorporation valve-point effect, as outlined in the equation (4.15) [9][40][63][102]:

$$F_3 = C_{TG}(P_{TG}) = \sum_{i=1}^{N_{TG}} a_i + b_i P_{TGi} + c_i P_{TGi}^2 + \left| d_i \times \sin\left(e_i \times \left(P_{TGi}^{min} - P_{TGi}\right)\right)\right| \tag{4.15}$$

Where F_3 is the total fuel cost with the valve-point effect. P_{TGi}^{min} refers to the minimum real power limit of the i^{th} thermal generators.

D. The Price of Power Generating Units with presence of renewable energy

- ***Cost evaluation of uncertain wind power plants generators***

Since wind power is intermittent, the Monte Carlo simulations are employed to address the uncertainty and associated costs. The estimated cost of wind power intermittency is considered in three different manners: Direct, reserve, and penalty prices [40].

- **Direct Price of Stochastic wind Plant**

Wind power generators are stochastic power plants that are typically owned by private companies, often referred to as independent system operators (ISOs). These ISOs can sell fixed amounts of electricity to the network operator. When an ISO owns a wind farm, there is no direct price component unless the ISO chooses to recover some of the setup or maintenance costs. On the other hand, the ISO must pay a direct price based on a pre-agreed amount of power supply. The direct cost of the j^{th} wind plant is represented by the scheduled power $P_{ws,j}$, as shown in the following equation (4.16);

$$C_{w,j}\left(P_{ws,j}\right) = g_{wj}P_{ws,j}. \tag{4.16}$$

Here, the direct cost coefficient linked to j^{th} wind wind-farm is denoted g_{wj}[9][40].

- **Reserve wind power plants generators**

The inherent uncertainty in weather conditions can cause power generation to fall below scheduled levels. To mitigate this issue and ensure a stable power supply, a spinning reserve is crucial. This reserve maintains agreed-upon power levels despite wind farm output fluctuations and increased demand, acting as a safety net. The ISO network should maintain a rotating reserve to handle these uncertainties and ensure uninterrupted power to end-users. The reserve cost component for wind power plants is the cost of forcing a generator to meet overestimated power, as outlined in equation (4.17):

$$C_{Rwj}\left(P_{wsj} - P_{wavj}\right) = K_{Rwj}\left(P_{wsj} - P_{wavj}\right) = K_{Rwj}\int^{P_{wsj}}\left(P_{wsj} - p_w\right)f_{wj}(p_w)dp_w \tag{4.17}$$

where, the reserve cost coefficient for wind power plants is denoted by K_{Rwj}, while the current power available from the plant is P_{wavj}. $f_{wj}(p_w)$ indicate the PDF of the wind power generator.

The right-hand side for **the reserve price** can be expressed as follows equation (4.18).

$$K_{Rwj}\int_0^{P_{wsj}}\left\{\left(P_{wsj}-p_w\right)\frac{\beta(v_r-v_{in})}{\alpha^{\beta}*P_{wrj}}\left[v_{in}+\frac{p_w}{P_{wrj}}(v_r-v_{in})\right]^{\beta-1}\exp\left[-\left(\frac{v_{in}+\frac{p_w}{P_{wrj}}(v_r-v_{in})}{\alpha}\right)^{\beta}\right]\right\}dp_w \quad (4.18)$$
$$+K_{Rwj}\left(P_{wsj}-0\right)*f_{wj}\left(p_w\right)\left\{p_w=0\right\}$$

Here, P_{wrj} denotes the rated output power of the j^{th} wind power plant [9].

- **Penalty Price of Stochastic wind Plant**

Underestimated power occurs when a wind farm's current power provided more than what is the demand needed value, leading to excess power being wasted. If there is no control over thermal unit output power. If there is no way to control the output power from thermal units, the excess power will go to waste. In this case, ISO should be charged a penalty fee for the extra power. The penalty price for underestimating wind power can be calculated using equation (4.19).

$$C_{Pwj}\left(P_{wavj}-P_{wsj}\right)=K_{Pwj}\left(P_{wavj}-P_{wsj}\right)=K_{Pwj}\int_{P_{wsj}}^{P_{wrj}}\left(p_w-P_{wsj}\right)f_{wj}(p_w)dp_w \quad (4.19)$$

The penalty cost coefficient of a wind generating units is represented by K_{Pwj}, and the specified output power for the j^{th} wind is denoted by p_{wrj} [8][63].

To expand the right-hand side for the penalty cost, the following formula can be expressed the penalty price (4.20):

$$K_{Pwj}\int_{P_{wsj}}^{P_{wrj}}\left\{\left(p_w-P_{wsj}\right)\frac{\beta(v_r-v_{in})}{\alpha^{\beta}*P_{wrj}}\left[v_{in}+\frac{p_w}{P_{wrj}}(v_r-v_{in})\right]^{\beta-1}\exp\left[-\left(\frac{v_{in}+\frac{p_w}{P_{wrj}}(v_r-v_{in})}{\alpha}\right)^{\beta}\right]\right\}dp_w$$
$$+K_{Pwj}\left(P_{wrj}-P_{wsj}\right)*f_{wj}(p_w)\{p_w=p_{wr}\}$$
$$(4.20)$$

- ***Cost evaluation of uncertainties in solar photovoltaic power* [8][100]:**

The direct cost for the solar PV plant is given by:

$$C_s\left(P_{ss,k}\right)=h_sP_{ss,k} \quad (4.21)$$

Where, $P_{ss,k}$ is the scheduled power from the solar PV plant, h_s is the direct cost coefficient.

Similar to wind power plants, solar PV plants also experience intermittent and uncertain outputs due to natural fluctuations in solar radiation. Strategies for managing overestimation and underestimation of solar power should align with those for wind power. However, it's important to note that solar radiation is characterized by a lognormal probability distribution function (PDF). **The reserve cost** for the k^{th} solar PV plant is:

$$C_{Rs,k}\left(P_{ss,k} - P_{sav,k}\right) = K_{Rs,k}\left(P_{ss,k} - P_{sav,k}\right)$$
$$= K_{Rs,k} * f_s\left(P_{sav,k} < P_{ss,k}\right) * \left[P_{ss,k} - E\left(P_{sav,k} < P_{ss,k}\right)\right] \quad (4.22)$$

Where, $K_{Rs,k}$ is the reserve cost coefficient for the k^{-th} solar PV plant

Penalty cost for the underestimation of k $^{-th}$ solar PV plant is:

$$C_{Ps,k}\left(P_{sav,k} - P_{ss,k}\right) = K_{Ps,k}\left(P_{sav,k} - P_{ss,k}\right)$$
$$= K_{Ps,k} * f_s\left(P_{sav,k} > P_{ss,k}\right) * \left[E\left(P_{sav,k} > P_{ss,k}\right) - P_{ss,k}\right] \quad (4.23)$$

Where, $K_{Ps,k}$ is the penalty cost coefficient pertaining to kth solar PV plant.

$P_{sav,k}$ is the actual available power from the same plant. $f_s\left(P_{sav,k} < P_{ss,k}\right)$ is the probability of solar power shortage occurrence than the scheduled power ($P_{ss,k}$, $E(P_{sav,k} < P_{ss,k})$ is the expectation of solar PV power plant above $P_{ss,k}$.

- The objective of OPF is to minimize the generation cost. the objective function ($F_{3.1}$): Minimize the total cost including all thermal and wind energy price, where the emission cost is not included is given by the follow equation:

  $$F_{3.1} = C_T(P_{TG}) + \sum_{j=1}^{N_{WG}} \left[C_{w,j}\left(P_{ws,j}\right) + C_{Rw,j}\left(P_{ws,j} - P_{wav,j}\right) + C_{Pw,j}\left(P_{wav,j} - P_{ws,j}\right)\right] \quad (4.24)$$

- The objective function ($F_{3.2}$), including the total cost including all thermal and renewable energy price, where the emission cost is not included is given by the follow equation:

$$F_{3.2} = C_T(P_{TG}) + \sum_{j=1}^{N_{WG}} \left[C_{w,j}\left(P_{ws,j}\right) + C_{Rw,j}\left(P_{ws,j} - P_{wav,j}\right) + C_{Pw,j}\left(P_{wav,j} - P_{ws,j}\right)\right]$$
$$+ \sum_{k=1}^{N_{SG}} \left[C_{s,k}\left(P_{ss,k}\right) + C_{Rs,k}\left(P_{ss,k} - P_{sav,k}\right) + C_{Ps,k}\left(P_{sav,k} - P_{ss,k}\right)\right] \quad (4.25)$$

- To study the change in generation scheduling when emission gas is imposed, the objective function ($F_{3.3}$): is constructed to Minimize the total cost including all thermal and wind energy price, is given by the follow equation:

$$F_{3.3} = C_T(P_{TG}) + \sum_{j=1}^{N_{WG}} \left[C_{w,j}\left(P_{ws,j}\right) + C_{Rw,j}\left(P_{ws,j} - P_{wav,j}\right)\right.$$
$$\left. + C_{Pw,j}\left(P_{wav,j} - P_{ws,j}\right)\right] + \left|d_i \times \sin\left(e_i \times \left(P_{TGi}^{min} - P_{TGi}\right)\right)\right| \quad (4.26)$$

- The objective function ($F_{3.4}$), including the cost including all thermal and renewable energy price, where the emission gas cost is imposed is given by the follow equation:

$$F_{3.4} = C_T(P_{TG}) + \sum_{j=1}^{N_{WG}} \left[C_{w,j}\left(P_{ws,j}\right) + C_{Rw,j}\left(P_{ws,j} - P_{wav,j}\right) + C_{Pw,j}\left(P_{wav,j} - P_{ws,j}\right)\right] +$$
$$\sum_{k=1}^{N_{SG}} \left[C_{s,k}\left(P_{ss,k}\right) + C_{Rs,k}\left(P_{ss,k} - P_{sav,k}\right) + C_{Ps,k}\left(P_{sav,k} - P_{ss,k}\right)\right] + \left|d_i \times \sin\left(e_i \times \left(P_{TGi}^{min} - P_{TGi}\right)\right)\right|$$

(4.27)

where, N_{WG} and N_{SG} represent the number of wind generators and solar PV units in the network, respectively. All other cost components are determined using the specified equations (4.26, 4.27).

E. Real Power Losses (RPL)

Equation (4.28) describes the expression of fitness function associated to power loss minimization:

$$F_4 = P_{\text{loss}} = Min\left[\sum_{i=1}^{NTL} G_{ij}\left(V^2{}_i + V_j^2 - 2V_iV_j\cos\ \theta_{ij}\right)\right] \tag{4.28}$$

B. Enhancement of the Voltage Stability:

The voltage stability index problem is recognized as one of the challenges in modern energy systems, and its fitness function can be modeled using the following equations (4.29) and (4.30) [40]:

$$F_5 = L_j = \left|1 - \sum_{i=1}^{N_G} F_{ji}\frac{V_i}{V_j}\right| \qquad \text{where } j = 1,2,\dots,NPQ \tag{4.29}$$

$$F_{ji} = -[\boldsymbol{Y_L}]^{-1}[\boldsymbol{Y_{LG}}] \tag{4.30}$$

Where; the index value of the j[th] bus is represented BY L_j; $\boldsymbol{Y_L}$and $\boldsymbol{Y_{LG}}$ are determined from the electrical grid.

F. Total Voltage Deviation (TVD):

The Total Voltage Deviation (TVD) expressed using equation (4.31), refers to minimizing the fluctuations of voltage magnitudes across the power system from a reference value of 1 per unit (pu) [40][79] [102]:

$$F_6 = TVD = \left(\sum_{i=1}^{NPQ} \left|V_{L_i} - 1\right|\right) \tag{4.31}$$

G. the Total cost with renewable energy cost and loss cost (Gross cost):

The total cost of the network, considering wind energy, thermal power, and power loss, is given by equation (4.32) [53]:

$$F_7 = min\{F_{3.3} + P_{\text{loss}} * 10^3 * 0.1\}. \tag{4.32}$$

The total cost of the network, considering wind energy, solar sources, thermal units, and power loss, is given by equation (4.33) [53]:

$$F_{7,1} = min\{F_{3.4} + P_{\text{loss}} * 10^3 * 0.1\}. \tag{4.33}$$

5.5.3. Constraints system

To optimally achieve the above objectives, it is necessary to satisfy a collection of limitations that include both equality and inequality constraints must be fulfilled.

5.4.3.1. Equality constraints

The equality constraints reflect to the physical properties of an energy system. These constraint functions that control the system creating from the equilibrium between generated power, load power consumption, and losses, as well as both active and reactive power balance [40][54]. It is feasible to classify equality constraints according to equations (4.34, and 4.35):

$$P_{G_i} - P_{D_i} = V_i \sum_{\substack{i=1 \\ j=1}}^{N_b} V_j\left(G_{ij}\cos\left(\theta_{ij}\right) + B_{ij}\sin\left(\theta_{ij}\right)\right) \tag{4.34}$$

$$Q_{G_i} - Q_{D_i} = V_i \sum_{i=1}^{N_b} V_j\left(G_{ij}\sin\left(\theta_{ij}\right) - B_{ij}\cos\left(\theta_{ij}\right)\right) \tag{4.35}$$

5.4.3.2. Inequality Constraints Systems

The system's inequality constraints represent security and operational limitations, which are elaborated upon below [103]:

A. *Generation constraints:*

The constraints related to the both the active power and reactive power plants generating units, as well as constraints on voltage magnitudes are expressed as follows equations (4.36, 4.37 and 4.38) [79][100] [102]:

$$P_{G_i}^{min} \leq P_{G_i} \leq P_{G_i}^{max} \tag{4.36}$$

$$Q_{G_i}^{min} \leq Q_{G_i} \leq Q_{G_i}^{max} \tag{4.37}$$

$$V_{G_i}^{min} \leq V_{G_i} \leq V_{G_i}^{max}; \qquad i = 1,2,\dots,N_G \tag{4.38}$$

B. *Security constraints*

Security constraints involve limits on voltage magnitudes at load buses, power transmission line limits, and transformer tap settings [40][100].

- **Power transmission line limit**

The equation (4.39) explains the capacity constraint power transmission line [100]:

$$\left|S_{L,i}\right| \leq S_{L,i}^{max}; i = 1,2,\dots,N_{\mathrm{STL}} \tag{4.39}$$

- **Load bus: voltage magnitudes of load bus**

Equation (4.40) describes the boundaries voltage load buses [100][104][105]:

$$V_{L,i}^{min} \leq V_{L,i} \leq V_{L,i}^{max}; \quad i = 1,2, \dots, \text{NPQ} \tag{4.40}$$

Where; the i[th] load bus is represented by $V_{L,i}$.

- **Transformer: tap setting transformer** [100]

The equation (4.41) refers to constraints tap setting Transformer ranges:

$$T_{Tr,i}^{min} \leq T_{Tr,i} \leq T_{Tr,i}^{max}; \quad i = 1,2, \dots, N_{Tr} \tag{4.41}$$

C. Shunt capacitor:

The equation (4.42) refers to constraints of shunt capacitors [104].

$$Q_{C,i}^{min} \leq Q_{C,i} \leq Q_{C,i}^{max}; \quad i = 1,2, \dots, n_C \tag{4.42}$$

D. FACTS Devices Constraints:

TCSC: $$\tau_{TCSCm}^{min} \leq \tau_{TCSCm} \leq \tau_{TCSCm}^{max} \forall m \in N_{TCSC} \tag{4.43}$$

TCPS: $$\Phi_{TCPSn}^{min} \leq \Phi_{TCPSn} \leq \Phi_{TCPSn}^{max} \forall n \in N_{TCPS} \tag{4.44}$$

SVC: $$Q_{SVCj}^{min} \leq Q_{SVCj} \leq Q_{SVCj}^{max} \forall j \in N_{SVC} \tag{4.45}$$

The equations (4.43, 4.44, and 4.45), respectively, refer to the boundaries on FACTS controllers – TCSC, TCPS, and SVC [102][56][64] [102].

4.6. Conclusion

This chapter aimed to provide a comprehensive overview of the fundamental concepts related to Optimal Power Flow (OPF). It began with the modeling of electrical network elements, followed by a summary of power flow calculations and the iterative methods used to solve it. Next, it presented the formulation of the OPF problem, including the mathematical framework necessary for its analysis and solution. The chapter also explored various types of objective functions within the OPF framework, such as minimizing of generation costs, the total emission gas, … etc, were defined, tailored to specific operational goals. Additionally, it discussed the inherent constraints, ensuring that solutions are optimal, feasible, and safe within the operational limits of the power system. The next chapter presents the global optimization methods used for solving the Optimal Power Flow (OPF) problem, followed by a detailed discussion of those methods applied in our thesis.

CHAPTER 5: Global optimization methods

5.1. Overview about the optimization

Optimization offers significant advantages in the practical field of engineering. In electrical network, it plays a crucial role in ensuring that electrical power systems operate efficiently, economically, and securely. The OPF problem involves in finding the optimal settings for variables like generator outputs and voltage levels while adhering to constraints such as power balance and transmission limits. Given the complexity, non-linearity, and high dimensionality of power systems[106][107], it requires the use of optimization methods to solve it. The chapter focuses on the global optimization techniques, it starts by introducing fundamental definitions of optimization problems, including the notions of local optimum and global optimum. Then, it provides an overview about the optimization in the context of electrical network. Specific attention is given to the methods used to address particular issues on electrical power system, such as optimal power flow (OPF).

5.2 Notion of Optimization

Optimization is defined by the search of the most effective solution to a problem, by identifying the combination of control variables that aimed to either minimizing or maximizing an objective function within a defined search space while adhering to specific constraints. Solving an optimization problem, requires firstly accurately modeling the system and selecting efficiency measures to quantitatively define it [12]. The formulation of any optimization problem can be considered as follows (figure 5.1):

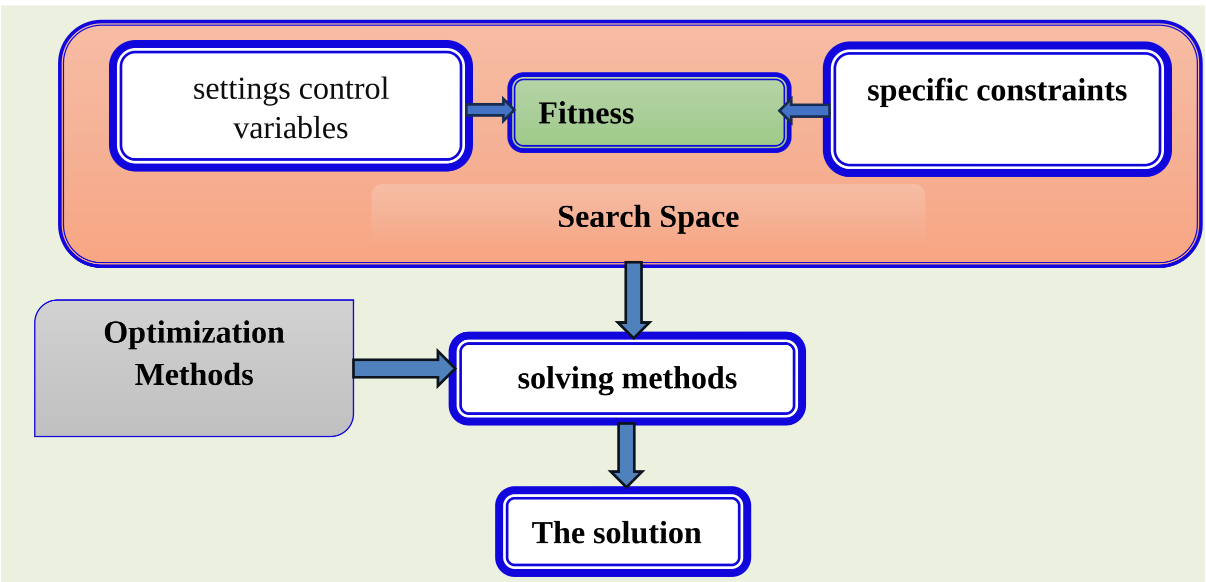

Fig. 5.1: The basic steps of solving an optimization problem.

5.3 Types of Optimizations

An optimization problem is defined as, "Finding the best solution from a set of solutions where every solution in the set satisfies problem constraints." Generally, optimization can be categorized into two types: (i) Single-Objective optimization (ii) multi-objective optimization [108]:

5.3.1. Single-objective Optimization problem

A model that addresses only a single objective at once and provides a solution concerning that single objective is known as Single-objective optimization [108]. The mathematical formulation of this problem with consideration of constraints, is given as follows:

- **Optimize** $f(x, u)$ (5.1)
- **Subjected to**
- $G_i(x, u) = 0 \quad i = 1,2, \dots \dots \dots . m$ (is the equality **constraints**) (5.2)
- $H_j(x, u) \leq 0 \quad j = 1,2, \dots \dots \dots . p$ (is the inequality **constraints**) (5.3)

5.3.2. Multi-objective Optimization problem

A multi-objective optimization (MOO) problem involves optimizing several objective functions simultaneously. The aim is to find the best trade-offs between conflicting objectives while adhering to certain equality and inequality constraints, leading to an infinite number of potential solutions. These solutions are known as Pareto fronts or Pareto optimal solutions [17][109]. The MOO problem can be mathematically modeled as the given equation:

- **Optimize** $\{ f_1(x, u), f_2(x, u), \dots \ f_k(x, u)\}$ (5.4)

Subject to

- $G_i(x, u) = 0 \quad i = 1,2, \dots \dots \dots . m$ (is the equality **constraints**) (5.5)
- $H_j(x, u) \leq 0 \quad j = 1,2, \dots \dots \dots . p$ (is the inequality **constraints**) (5.6)

Here; f denotes the modeled fitness function; u represents the decision variables; x indicates the state variables, k is the number of objective functions.

Solving a multi-objective optimization problem involves finding solutions that best align with the decision maker's preferences among a range of viable compromise solutions. Instead of a single optimal solution, the solution is a set of solutions known as the Pareto-optimal solution set. This process, called Pareto Optimization, uses the concepts of dominance and Pareto optimality to simultaneously address all objectives. The Pareto concept, introduced by the Italian economist and sociologist Vilfredo Pareto in 1986, states that a solution x is Pareto-optimal if no other solution in the feasible space X dominates it. These solutions are termed non-dominated or non-inferior solutions [17]. To better understand Pareto optimality, it is important to first define Pareto dominance and the Pareto frontier.

- **Definition (Pareto Domination):**

Let two decision vectors $u = [u_1, \dots, u_n]$ and and $v = [v_1, \dots, v_n]$ be in the objective function space where a minimization problem is considered. Denoted that vector u dominates vectors v ($u \le v$), if and only if: all components of u are less than or equal to their corresponding ones in v, and at least one component of u is strictly less than its corresponding one in v, i.e.:

$$\forall\, i \in \{1,2, \dots k\},\ F_i(u) \le F_i(v), \exists\, i \in \{1,2, \dots n\},\ F_i(u) < F_i(v) \quad (5.7)$$

- **Definition (Pareto Frontier):**

the Pareto Front also known as Trade-off Surface, is the collection of all Pareto-optimal points in the objective function space (Fig. 2.21). These points represent solutions where no other solution in the feasible space dominates them according to the Pareto dominance criterion. Specifically, a solution x dominates another solution x' if, for all criteria f_i (with i ranging from 1 to m), $f_i(x) \le f_i(x')$, with at least one strict inequality. A Pareto-optimal solution is non-dominated, meaning no other solution in the feasible space dominates it according to this criterion. This leads to a set of solutions forming an optimality frontier, known as the Pareto front or trade-off surface. The **figure (5.2)** illustrates the Pareto Frontier for minimizing F_1, and F_2.

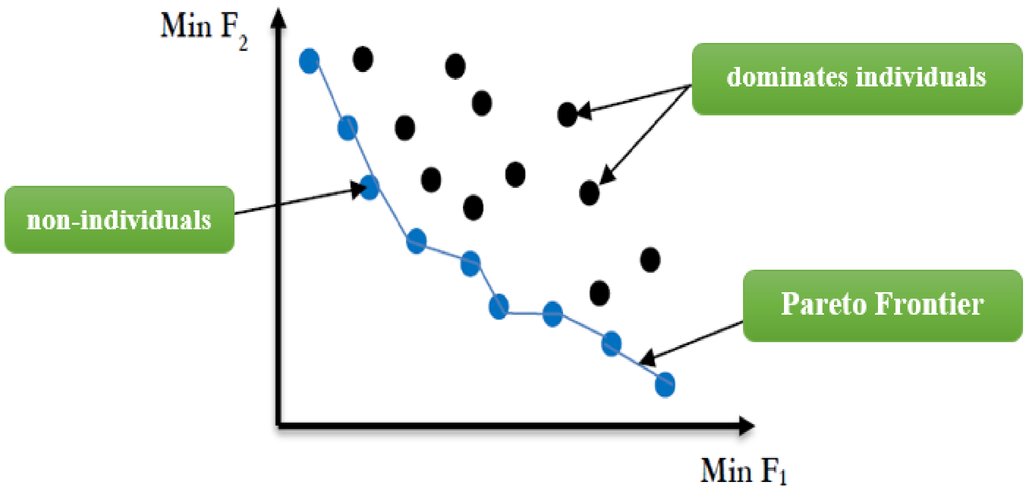

Fig. 5.2: Pareto Frontier of minimum (F1, F2).

The solutions positioned on the Pareto front cannot be compared, as none is systematically better than the others across all objectives. It is up to the decision-maker to choose which solution to retain.

5.4. Methods for solving optimization problems

Optimization techniques are primarily categorized into two groups: deterministic methods and Approaches methods [110]. Additionally, there's a pseudo-class known as the hybrid method, which emerges from combining different methods. This classification is illustrated in **figure (5.3)** [111].

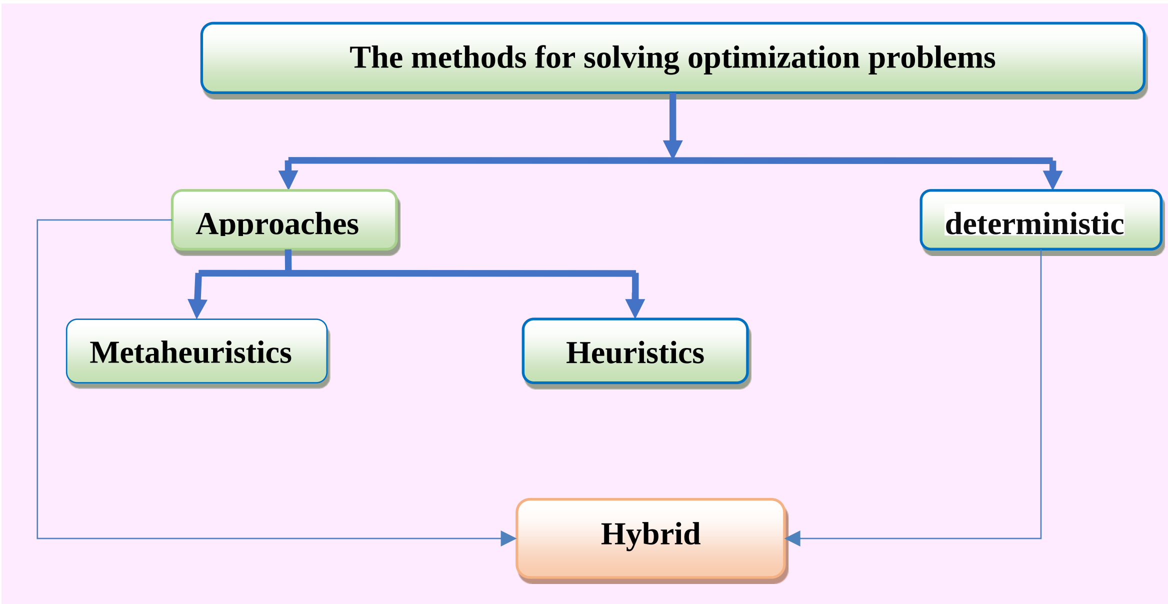

Fig. 5.3: Classification of optimization methods.

5.4.1. determinist methods:

These methods are referred to as deterministic because they always lead, from a specific starting point, to the same final result. However, their limitation lies in possibly converging to a local optimum in cases where the objective function has multiple optima. They include techniques such as Branch & Bound, mathematical methods, … etc [110][111].

5.4.2. Non-deterministic (approaches) methods:

These methods are use probabilistic and random transitions process to explore the search space and converge to the global optimum. This category includes heuristic and metaheuristic methods[110][112].

5.4.2.1. Heuristic methods:

Among these methods are the Monte Carlo method, simulated annealing, …. and others. These methods start with an initial solution and attempt to improve it within the problem's constraints. Progress toward an optimal solution is achieved by successively testing a neighboring solution to the current one. **The figure (5.4)** illustrates a simple representation of a traversal-based (heuristic) optimization method [100] [112].

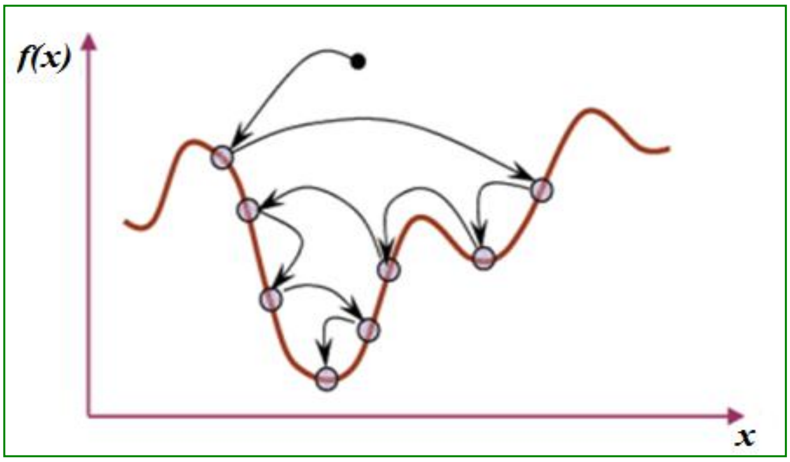

Fig. 5.4: Simplified heuristic approach.

5.4.2.2. Metaheuristic methods:

Metaheuristic algorithms, are often inspired by natural phenomena, and have become part of the most widely used stochastic optimization algorithms. Their simplicity and robustness have led to successful applications in various optimization fields. As global optimization methods, they avoid being trapped in local optima, overcoming the limitations of classical and heuristic methods. A schematic representation of metaheuristics is provided in **figure (5.5)** [110][112][113].

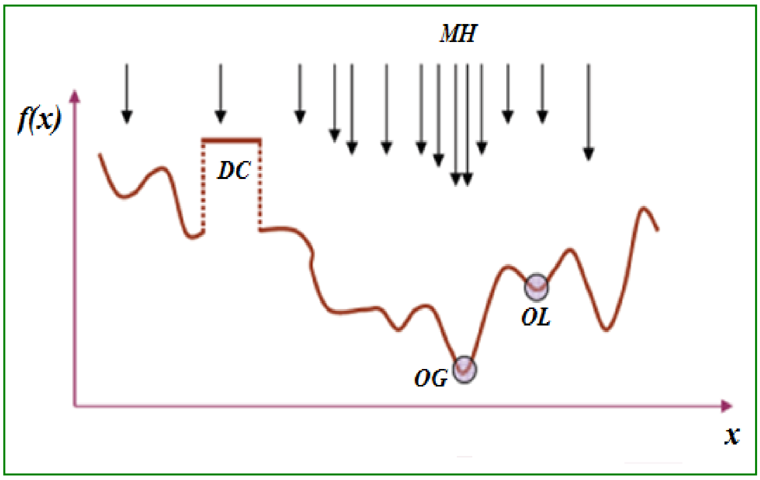

Fig. 5.5: Simplified Metaheuristic Approach.

In this representation, metaheuristics (MH) aim to find the global optimum (OG) of a complex optimization problem (f(x)), that may encompass elements such as discontinuities (DC), while avoiding entrapment in local optima (OL) [110].

5.5. Overviews of the Optimization in Electrical Networks

Research interest in optimizing electrical networks field began in 1919, focusing on enhancing the efficiency of power systems. In 1943, Steinberg and Smith published a classic book titled "Economy Loading of Power Plants and Electric Systems" deals notable contributions include on incremental methods and loss modeling, and the research have been continued, where the classic economic equations were discovered by Kirchmayer and Stagg in 1951. Kirchmayer's 1958 work on economic operation of power systems, laying the groundwork for modern economic operations in power distribution. In 1958, Kirchmayer published a book entitled "Economic Operation of Power Systems," where the author presented the formulation of the conventional economic dispatch problem. These efforts culminated in the development of the first algorithms for power flow analysis and the pursuit of optimal power flow, highlighted by Squires' and Carpentier's research in the early 1960s. This period marked the beginning of systematic optimization in electrical networks, with a focus on real-time operational studies to achieve demand satisfaction efficiently and cost-effectively. Recently, several optimization problems require considering time scales from planning to operation. Network operators must conduct several real-time studies (minutes, hours, days, year) to meet demand optimally at minimal cost [17].

5.6. Resolution of optimal power flow (OPF) by optimization methods

The resolution of Optimal Power Flow (OPF) problems is a critical area in power system engineering. OPF seeks the most cost-effective generation dispatch that satisfies demand while adhering to system constraints such as generator limits, network capacity, and operational security. Algorithmic optimization methods have been employed for several years in the planning, operation, and control of electrical networks due to the complexity of large-scale electrical network solutions [81][114]. These techniques can be classified into two categories: conventional methods and Intelligence optimization methods are depicted in **figure (5.6)** [115].

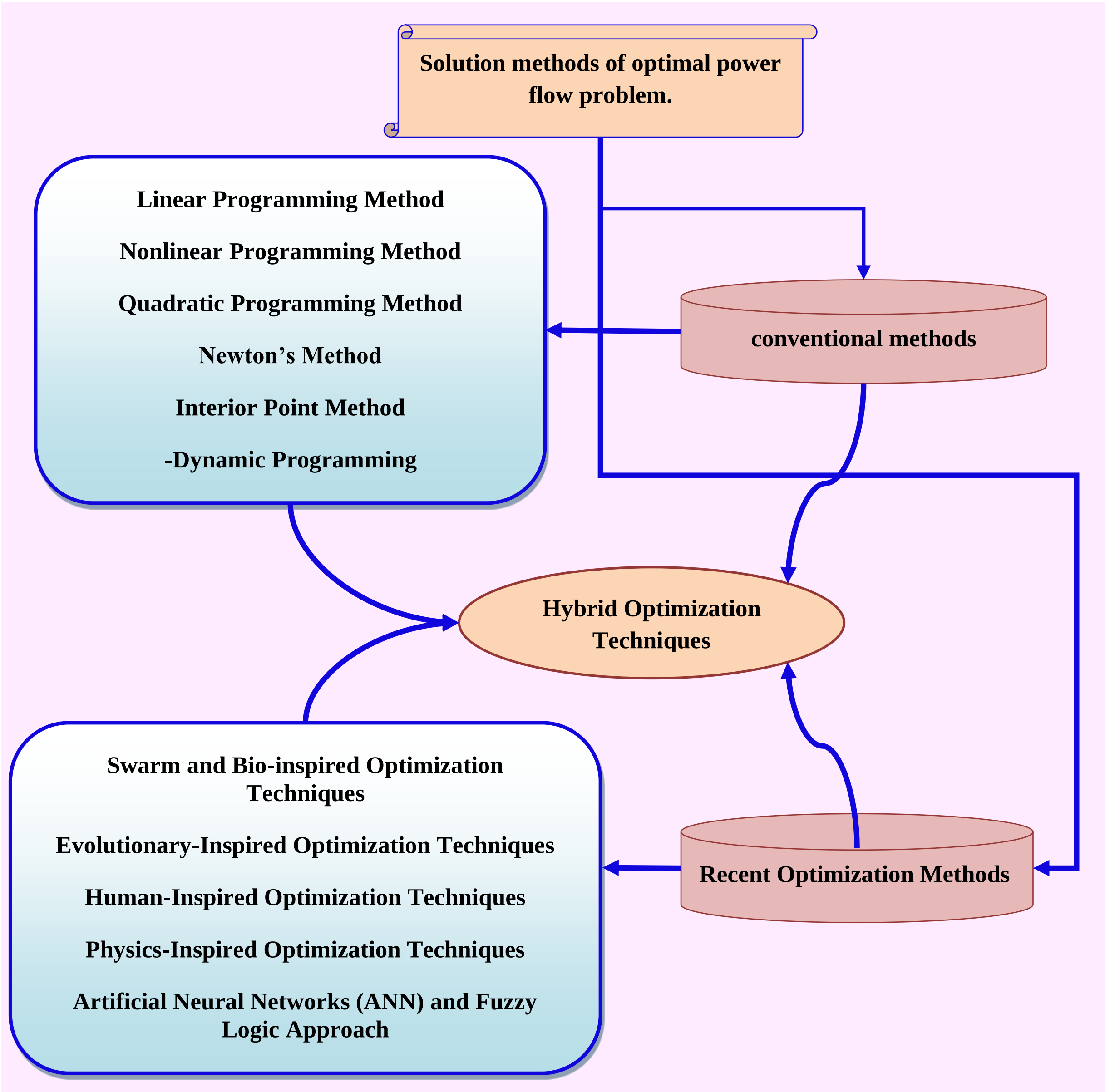

Fig. 5.6: Solution methods of optimal power flow problem.

5.6.1. Conventional optimization methods for OPF Problem

The majority of traditional optimization methods rely on sensitivity analysis and gradient-based methodologies. In 1968, Dommel and Tinney introduced the first solution approach for the OPF problem, since then, several conventional methods have been developed and applied to solve the OPF problems, such as mixed-integer programming (MIP), linear programming (LP), nonlinear programming (NLP), … etc.

these optimization methods have significant limitations and challenges, including prolonged convergence times, complex algorithms, and difficulty in generating optimal solutions. These methods often struggle with the high nonlinearity and multimodal nature of large and complex

OPF problems, leading to potential entrapment in local minima. Additionally, the precision of these methods can be compromised by rounding errors in digital computation. Therefore, there is a crucial need for developing optimization techniques that can address these drawbacks, ensuring faster, more reliable solutions for real-time power system operations [90][115].

5.6.2. Recent optimization methods for optimal power flow

The recent intelligence methods based on evolutionary or metaheuristic optimization techniques have been proposed to solve the non-linear or non-convex complex optimization problems in small and large-scale systems [115]. Recently, several of them were developed and implemented in the electrical power system for solving the OPF problems [99][116]. Such as:

Evolutionary-based methods, Among these methods: like the Genetic Algorithm (GA), Differential Evolutionary (DE), enhanced genetic algorithms (EGA),…. etc.

Swarm and Bio-inspired Optimization Techniques, like Particle Swarm Optimisation (PSO), such as bat algorithms (Bat), Artificial Bee Colony algorithm (ABC) [117], enhanced Equilibrium Optimizer (EEO) [118], Peafowl Optimization Algorithm [119], …etc.

Physics-Inspired Optimization Techniques (PIOA), Among these methods: Improved colliding bodies optimization algorithm (ICBO) [120], and Galaxy-based Search Algorithm (GbSA) [121], a physics-guided graph convolution neural network (GCNN) [122]. Thermal Exchange Optimization (TEO) [123], …etc.

Human-Inspired Optimization Techniques, are inspired by human behaviors, especially when it comes to thinking or making decisions. Some of the most popular human-inspired techniques are Group Search Optimizer (GSO)[124], The Teaching Learning Based Optimization (TLbO) [125], etc…

Various hybrid metaheuristic algorithms have been developed and continue to be developed every day. Some of these have been applied for solving the OPF problem like; the hybrid PSO and GSA [126] [126], hybrid DE with harmony search algorithm (DE-HSA) [127]. The hybrid Harrison Hawk Optimization based on Differential Evolution (HHODE)algorithm [128], …etc. and others **v**arious hybrid metaheuristic algorithms was developed and applied for solving the single and mult-objective OPF.

5.7. Details of some methods applied in this thesis theses

5.7.1. The Genetic Algorithm (GA)

GA is relied on the genetics and natural selection laws, t provides the best solutions by explore the search space, in a parallel manner to get the optimal solution from population of points. Therefore, GA can avoid the local optimal solution problem. Real-Coded GA consists of four essential phases which are initial population, evaluation function, selection, and genetic operators (mutation and crossover). GA algorithm guides the population into convergence to obtain the global optimal solution. Primarily, the initial population or chromosome population is created. Depending on genetic operators, new chromosomes are created which in turn create a new population with improved fitness of the objective function. This procedure is repeated till the improvement is stopped. It can be accomplished after a certain number of iterations [129][130]. The flowchart of the GA as shown in the **figure (5.7).**

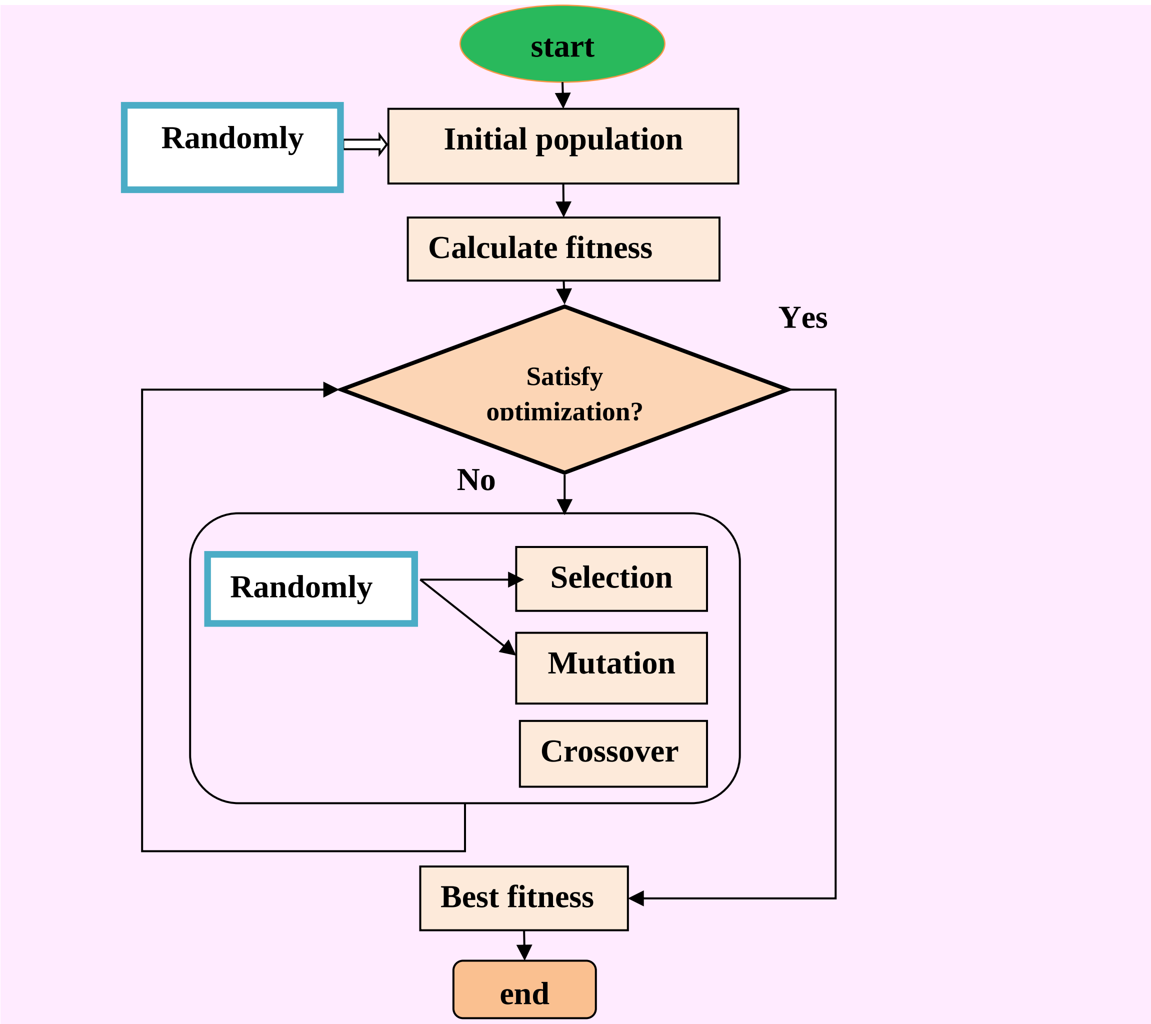

Fig. 5.7: Flowchart of the GA.

5.7.2. Particle Swarm Optimization (PSO) algorithm

The PSO algorithm is inspired from the social behavior of birds, to find the best optimum value of the function/problem [43], it is initialized with a group of random particles, each representing a potential solution to the problem, and then searches for optima by updating generations. In every iteration, each particle is updated by two" best" values. The first one is the best solution (fitness) it has achieved so far, the best position of particle. The other best value that is tracked by the particle swarm optimizer is the best value obtained so far by any particle in the population (the global best position) [131]. The best-known local position for the particle affects the movement of each particle. The position and velocity of N particles change until they attain the target. Equation (5.8) is used to update the particle's position and equation (5.9) is used to update the velocity of the particle. $v_i(t)$ is the particle's velocity at t time step, $x_i(t)$ denotes the position of particle (i), r_1 and r_2 have range 0 to 1 and they represent random values, c_1 and c_2 represents the positive acceleration coefficients. By adding a velocity $v_i(t)$ to the present position, the particle's position changes [132][133]:

$$x_i(t+1) = x_i(t) + v_i(t+1) \tag{5.8}$$

$$v_i(t) = v_i(t-1) + c_1 r_1[lb(t) - x_i(t-1)] + c_2 r_2[gb(t) - x_i(t-1)] \tag{5.9}$$

The flowchart of PSO as shown in the figure 5.8

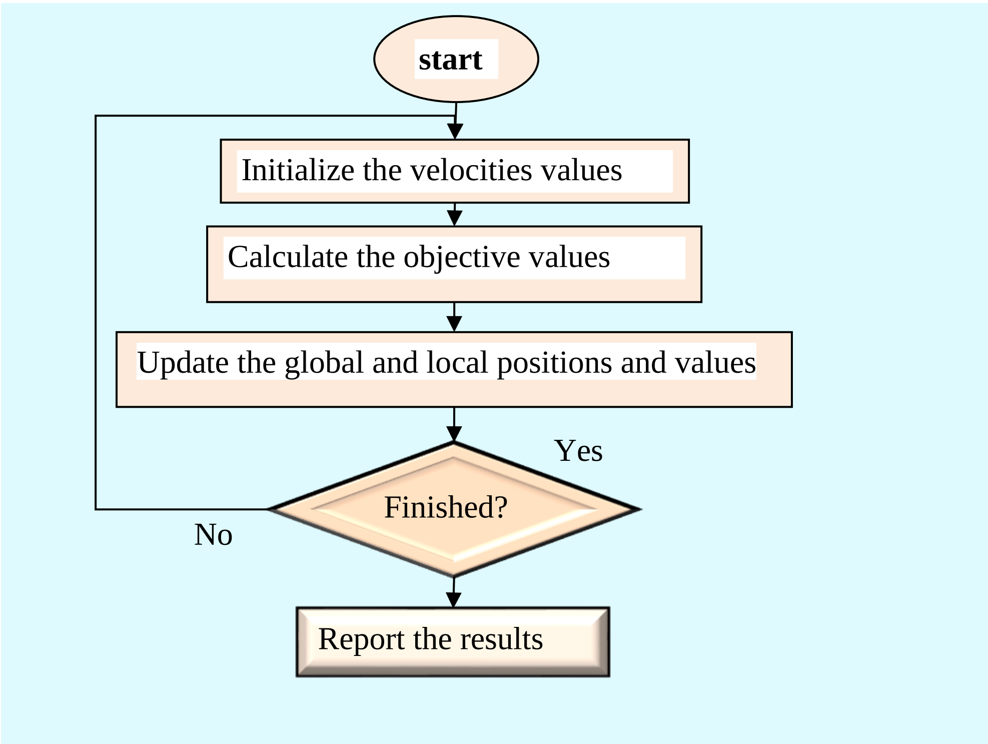

Fig. 5.8: Flowchart of the PSO algorithm.

5.7.3. Dandelion Optimizer algorithm

Firstly, this part discusses the basic concept of the suggested algorithm which is the dandelion optimizer (DO), their biological mechanism, and motivation. The flowchart of the DO algorithm is provided in the **figure (5.9)**, then, the mathematical model represents as follow:

a. Inspiration

in 2022, Shijie Zhao introduced a new algorithm which is known as the dandelion optimizer (DO), scientifically recognized as Herba taraxaci is a perennial herb in the family Asteraceae. It may attain a length over 20 centimeters. The head of dandelions is formed like florets. Typically, the seeds consist of hundreds of crest-like hairs, a beak, and an achene [134].

b. Mathematical model

This part is primarily dedicated to the mathematical formulation of DO, it provides the mathematical representation of the two types of meteorological conditions and analyzes their landing steps [134].

Step 1: Initialization [134][135]

DO algorithm performs iterative optimization based on the initial population. Each dandelion seed is supposed to be a candidate solution, and its population is expressed as follows:

$$\text{Population} = \begin{bmatrix} x_1^1 & \dots & x_1^{\dim} \\ \vdots & \ddots & \vdots \\ x_{\text{Pop}}^1 & \dots & x_{\text{Pop}}^{\dim} \end{bmatrix} \tag{5.10}$$

Where; Pop refers to the population size, dim denotes the variable's scale. Each candidate solution is randomly created between in interval limits by upper bound (Ub) and lower bound (Lb), and the expression of the i^{th} individual Xi is:

$$X_i = \text{ rand } \times (Ub - Lb) + Lb \tag{5.11}$$

where i refers to a random integer between 1 and Pop, and $rand$ is a random number in the range 0 and 1. the upper and the lower boundaries are expressed as follow (5.12) [134][135]:

$$\begin{aligned} Lb &= [lb_1, \dots, lb_{\dim}] \\ Ub &= [ub_1, \dots, ub_{\dim}] \end{aligned} \tag{5.12}$$

During startup, DO considers the individual has a highest fitness value to be the first elite, it is roughly equivalent to the optimal site of dandelions to flower. Taking the minimum value as an illustration, the initial elite is X_{Elite} [134] can be expressed as follow (5.13):

$$f_{\text{best}} = Min\big(f(X_i)\big)$$
$$X_{\text{Elite}} = X\Big(\text{ find }\big(f_{\text{best}} == f(X_i)\big)\Big) \tag{5.13}$$

where $find$ () denote two indices with equal value.

Step 2: Rising step

In the buoyant step, dandelion seeds must attain a particular height before they are able to separate from their parent plant. Depending on factors such as whether conditions like humidity, wind speed, etc. dandelion seeds will grow to varying heights. Here, the weather is divided into the two situations described below [134].

- **Situation-1** [134][135][135]

On bright days, wind speed can be represented by the lognormal distribution ln $Y \sim N$ (μ, σ2). The wind velocity determines how high a dandelion seed will grow. If the wind is stronger, the dandelion will fly higher and its seeds will disperse further. In this instance, the relevant mathematical expression is:

$$X_{t+1} = X_t + \alpha * v_x * v_y * \ln\ Y * (X_s - X_t) \tag{5.14}$$

where Xs denotes the randomly position of the dandelion seed at iteration t. Xt denotes the chosen location in the search space at iteration t. An expression that returns a randomly generated position as shows as follow equation (5.15):

$$X_s = \text{rand}\ (1, \text{Dim}) * (UB - LB) + LB \tag{5.15}$$

ln Y represents the random vector distribution subject to $\mu = 0$; $\sigma^2 = 1$, and its mathematical expression as follows equation (5.16):

$$\ln\ Y = \begin{cases} \frac{1}{y\sqrt{2\pi}} \exp\left[-\frac{1}{2\sigma^2}(\ln\ y)^2\right] & y \geq 0 \\ 0 & y < 0 \end{cases} \tag{5.16}$$

In eq. 16, y refers to the standard normal distribution (0 and 1).

α is a variable utilized to control the length of each search step, can be expressed by the follow

$$\alpha = \text{rand}() * \left(\frac{1}{T^2}t^2 - \frac{2}{T}t + 1\right) \tag{5.17}$$

α is a random disturbance in the interval [0,1] in the process of nonlinear decay approach 0.

v_x and v_y represent the coefficients of the dandelion's lift component due to separate eddy currents. The equation (5.18) is used to determinate the force in the variable dimension.

$$r = \frac{1}{e^{\theta}}$$
$$v_x = r\cos\ \theta \quad (5.18)$$
$$v_y = r\sin\ \theta$$

where θ fluctuates at random in the interval $[-\pi, \pi]$.

- **Situation-2:**

On a damp day, dandelion seeds struggle to rise effectively with the breeze due to air resistance and humidity.

$$X_{t+1} = X_t \times k$$
$$k = 1 - \text{rand}() * q \quad (5.19)$$

A dandelion utilized k to adjust its position search space. The domain (q) can be provided by the equation (5.20):

$$q = \frac{1}{T^2 - 2T + 1} t^2 - \frac{1}{T^2 - 2T + 1} t + 1 + \frac{1}{T^2 - 2T + 1} \quad (5.20)$$

Finally, the mathematical formula for the rising stage of a dandelion seed is:

$$X_{t+1} = \begin{cases} X_{t+1} = X_t + \alpha \times v_x \times v_y \times \ln\ Y \times (X_s - X_t) & \text{randn } < 1.5 \\ X_{t+1} = X_t \times k & \text{else} \end{cases} \quad (5.21)$$

The function randn () creates random numbers with a normal distribution.

Step 3: Descending step

The DO employs Brownian motion to recreate the trajectory of a moving dandelion (5.22).

$$X_{t+1} = X_t - \alpha \times \beta_t \times (X_{\text{mean } t} - \alpha \times \beta_t \times X_t) \quad (5.22)$$

β_t symbolizes the Brownian motion.

$$X_{\text{mean\_t}} = \frac{1}{\text{pop}} \sum_{i=1}^{pop} X_i \quad (5.23)$$

Step 4: Landing step

The landing step of the dandelion seed decided by random chance based on the improvements results of the first two steps. As the number of iterations increases, the algorithm ought to converge to the best optimal solution [134][135]. The evolution of the population to the final leads global optimum solution which is mathematically expressed by the following (5.24):

$$X_{t+1} = X_{\text{elite}} + \text{lev } y(\lambda) \times \alpha \times (X_{\text{elite}} - X_t \times \delta) \quad (5.24)$$

X_{elite} represents the seed's optimal location.

$$\text{levy}(\lambda) = s \times \frac{w \times \sigma}{|t|^{\frac{1}{\beta}}} \quad (5.25)$$

The constant value for s is 0.01, b represents a randomly integer from the range 0 to 2. w and t; are arbitrary numbers fluctuate in the interval [0, 1], mathematically stated by the follow (5.26):

$$\sigma = \left(\frac{\Gamma(1+\beta)\times\sin\left(\frac{\pi\beta}{2}\right)}{\Gamma\left(\frac{1+\beta}{2}\right)\times\sin\left(\frac{\beta-1}{2}\right)}\right) \tag{5.26}$$

The value of β is 1.5, and d can be calculated by the equation (5.27):

$$\delta = \frac{2t}{T} \tag{5.27}$$

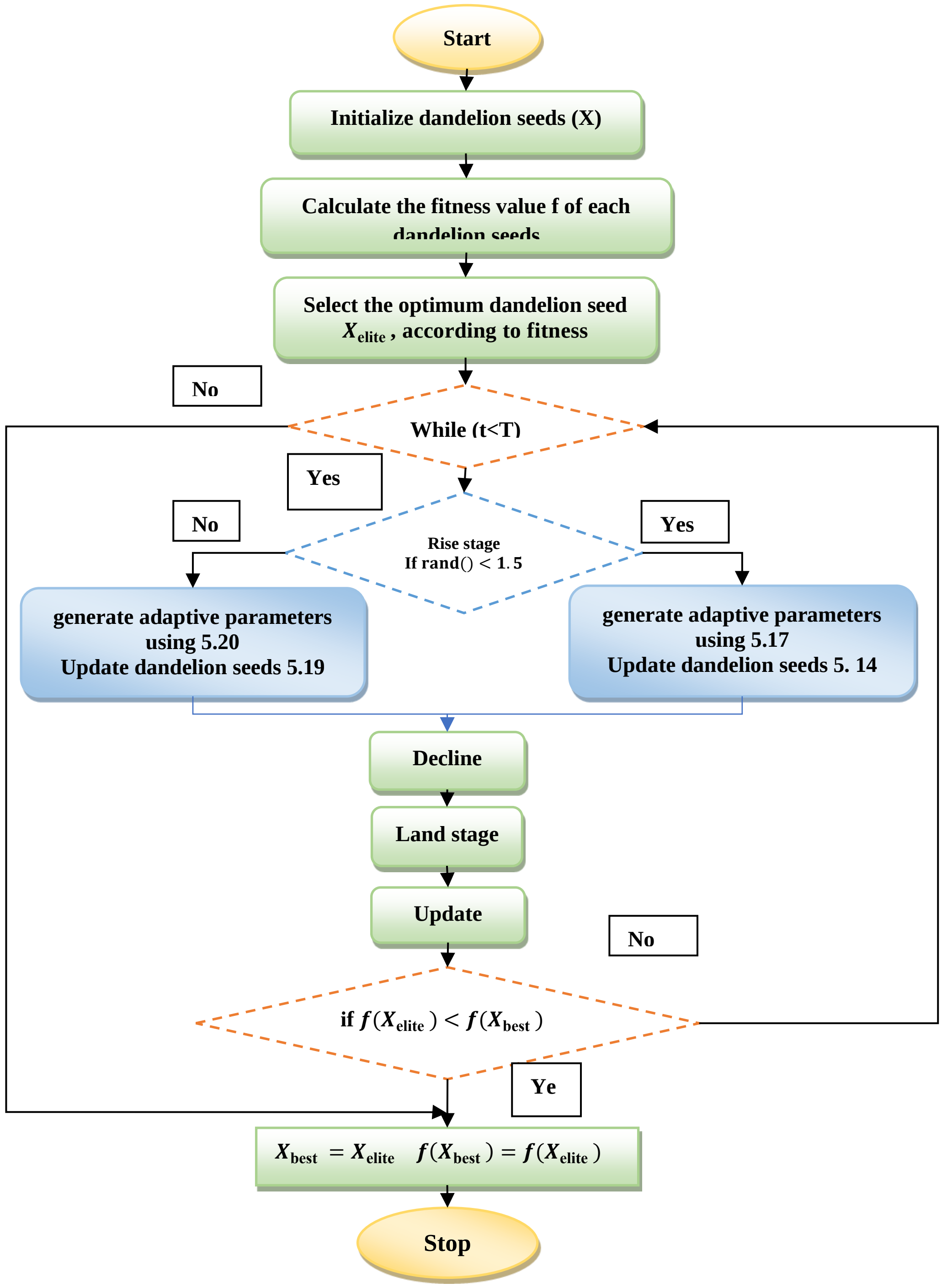

Fig. 5.9: The flowchart of the proposed DO.

5.7.3. Salp Swarm Algorithm

Salp swarm algorithm (SSA) is a swarm-based algorithm, Salps are one of the marine organisms from the Salpidae family, with a similar appearance to jellyfish. In the procedure for foraging the food, the algorithm starts by randomly selecting an initial population of salps based on their fitness function values, archiving solutions using a roulette wheel, and updating the positions of leading and follower salps to ensure the best solution until an end condition is met. Modern optimization techniques are commonly used to solve OPF problems and have proven high performance in various optimization problems [136].

For an optimization problem with n variables, the Salpi position is represented by a vector of n elements: $x_i = [x_j^1 , x_j^2, \dots, x_j^n]$

The position of the leader in the salp chain is updated by the following equation (5.28):

$$x_j^1 = \begin{cases} F_j \left| c_1 \left(\left(ub_j lb_j \right) \right) c_2 \right| lb_j, c_3 > 0.5 \\ F_j - c_1 \left(\left(ub_j - lb_j \right) \right) c_2 + lb_j, c_3 \leq 0.5 \end{cases} \tag{5.28}$$

Where; x_j^1, F_j denotes the location of the first salp (leader) and the food source in the j th dimension, respectively.

ub_j , lb_j symbolize the boundaries of j^{th} dimension, c_1 , c_2, and c_3 are random numbers uniformly created between 0 and 1. In fact, they determine whether the next location in j th dimension should be positive or negative infinity as well as the step size.

The coefficient c_1 is the most crucial parameter in SSA because it strikes the balance between exploration and exploitation. It expressed by the following equation (5.30):

$$c_1 = 2e^{-\left(\frac{4l}{L}\right)^2} \tag{5.30}$$

Where; l symbolizes the current iteration; L represents the maximum number of iterations.
To update the location of the followers, the bellow equations are used (Newton's law of motion) equation (5.31):

$$x_j^i = \frac{1}{2} a t^2 + v_0 t \tag{5.31}$$

Where; $i \geq 2$, x_j^i represents the location of ith follower salp in jth dimension, t is time, v_0 is the initial speed, and $a = \frac{V_{final}}{V_0}$ where $v = v - x_0 t$.

The location of the leader is updated; the location of the followers will change according to the following equation (5.32):

$$x_j^i = \frac{1}{2}\left(x_j^i + x_j^{i-1}\right) \tag{5.32}$$

Where x_j^i refers to the location of agent i, in the jth dimension with $2 \leq i \leq n$. The swarm behavior of salp chains is simulated based on the above-described mathematical formula. SSA solution process for optimize single objective problems are shown in the flowchart **(figure (5.10))**

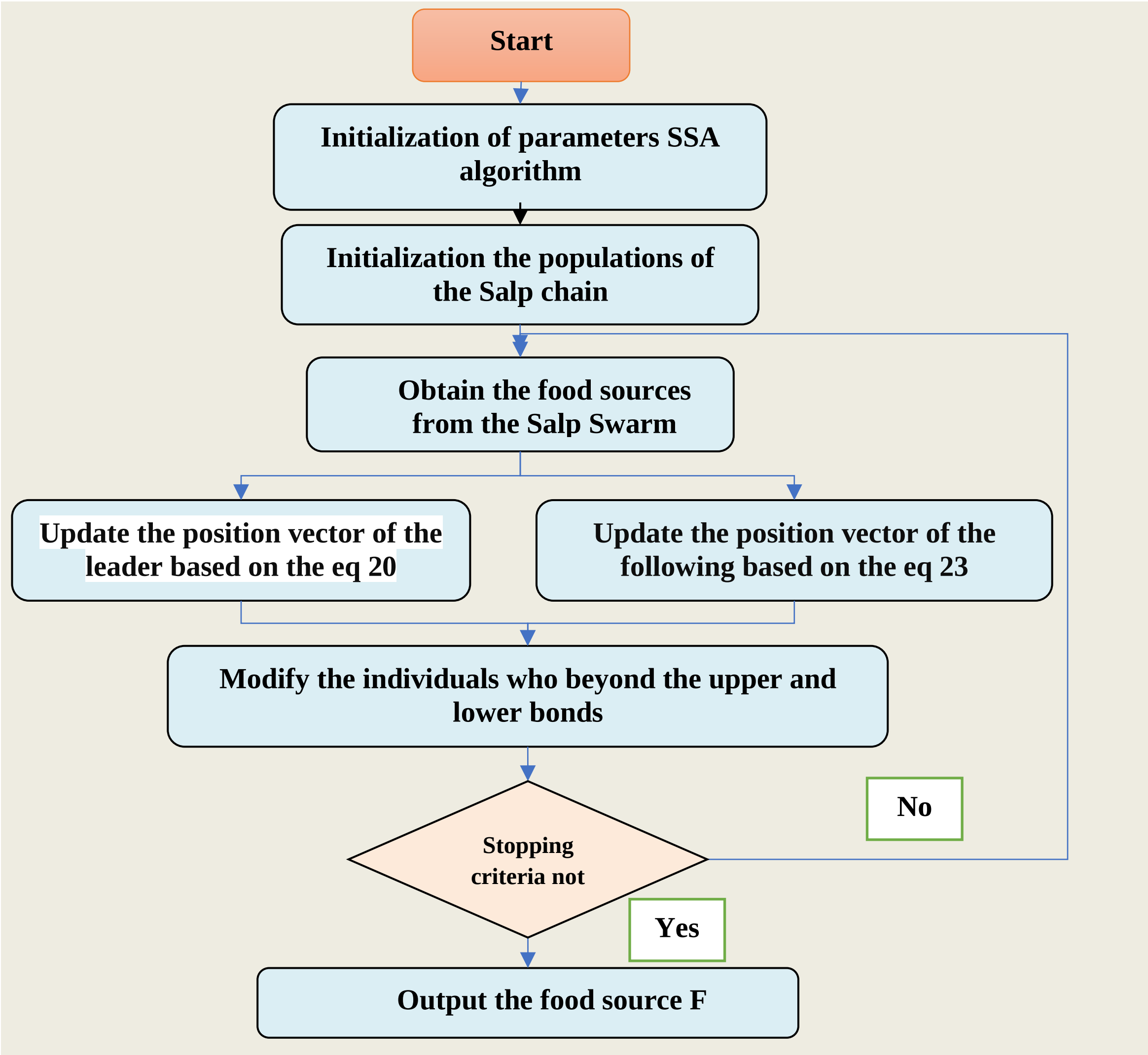

Fig. 5.10: flowchart of SSA algorithm.

The muti-objective SSA flowchart is shown in the **(figure 5.11)** [136]:

Best compromise solution

The best compromise solution from the calculated non-dominated solutions is found out by utilizing a fuzzy-based approach. A membership value is calculated in fuzzy-based method using the objective function values obtained from non-dominated solutions. The membership value (μ_m) for mth solution in a pareto optimal set is given by:

$$\mu_m = \begin{Bmatrix} 1 & J_m \le J_m^{\min} \\ \frac{J_m^{\max} - J_m}{J_m^{\max} - J_m^{\min}} & J_m^{\min} < j_m < J_m^{\max} \\ 0 & J_m \ge J_m^{\max} \end{Bmatrix} \quad (5.33)$$

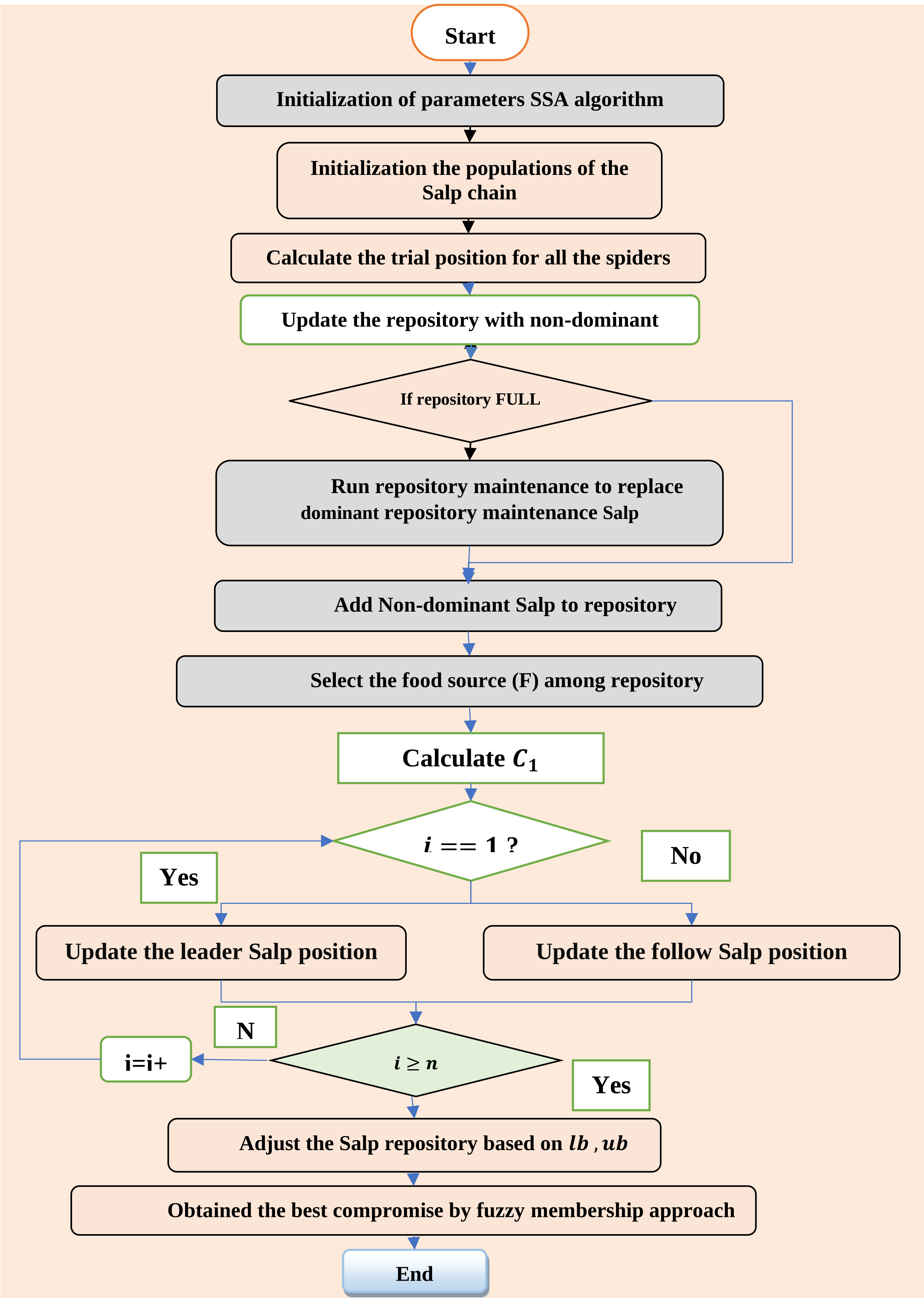

Fig. 5.11: flowchart of the MSSA algorithm.

5.7.4. Thermal exchange optimization (TEO)

The Thermal Exchange Optimization (TEO) method, introduced by Kaveh and Dadras in 2017, is inspired by physical phenomena to address optimization problems. This algorithm leverages the Newtonian law of cooling to determine the optimal solution. It operates based on the temperature-induced behavior of objects, with positions changing as they switch between warm and cold states to reveal updated positions. In the TEO optimizer, search agents are divided into two groups: candidate search agents (cooling objects with temperatures representing optimizing variables) and remaining agents (representing the environment). The method involves a process that mirrors these behaviors to find the optimal solution [137][138]. The steps of the original TEO algorithm are outlined in a flowchart depicted in **figure (5.12)**.

The algorithm begins by initializing the temperatures for all search agents or objects, as described in equation (5.34) [137].

$$\boldsymbol{T}_k^0 = \boldsymbol{T}_{Min} + \mathrm{rand}_k \cdot (\boldsymbol{T}_{Max} - \boldsymbol{T}_{Min}) \qquad k=1,\ldots\ldots\ldots, N \tag{5.34}$$

Where; $\boldsymbol{T}_k^0$ represents the initial solution vector for the kth object, $\boldsymbol{T}_{Max}$ and $\boldsymbol{T}_{Min}$ are the upper and lower boundaries for the solution vector, rand_k is a vector of random numbers generated independently for the kth object, with each component ranging between 0 and 1, $\boldsymbol{N}$ denotes the number of objects or search agents [137].

The process involves evaluating the temperatures of all objects and arranging them in descending order based on their cost function values. This ensures that the first $\mathrm{N_{Pop}}$ number of objects are maintained, equal to the number of presumed objects. The best historically obtained solution must be saved in thermal memory (TM) to enhance efficiency and reduce complexity. TM is updated with new solutions at each iteration [137].

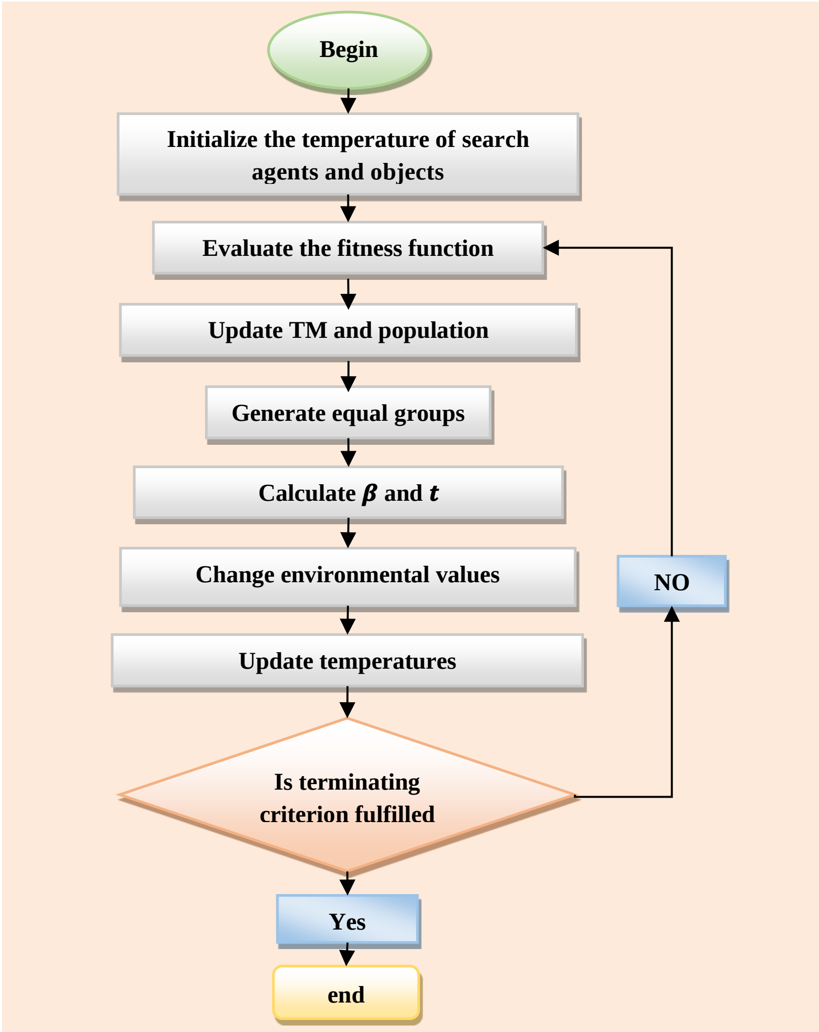

Fig. 5.12: Flowchart of the TEO algorithm.

As shown in **figure (5.13)**, the objects are separated into two equal sections. The first section, extending from T_1 to $T_{\frac{n}{2}+1}$, serves as the environment object, and the latter section is designated as the cooling object.

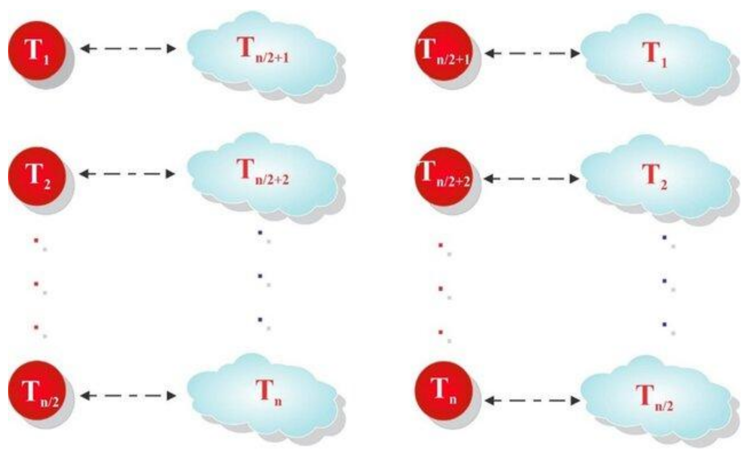

Fig. 5.13: Pairing cooling objects and environmental solutions.

The Newtonian law of cooling states that the rate of heat loss from an object is directly proportional to the temperature difference between the object and its environment. This relationship is expressed in equation (5.35).

$$\frac{Te(t)-Te_{\text{Env}}}{Te_0-Te_{\text{Env}}}=exp(-\beta t) \tag{5.35}$$

Where: $Te(t)$ refers to the new temperature at time t after thermal exchange between an object at initial temperature Te_0 and the environment at temperature Te_{Env}. The constant β is related on parameters such as heat capacity and the object's specific density. It can be noted that when β is higher, the object's temperature changes less.

β is defined to reduce the solution's cost and variance. Its value is given as follows (5.36):

$$\beta=\frac{f_i}{f_{max}} \tag{5.36}$$

Where f_i indicates the current object's cost and f_i is the highest cost among the worst objects in the population. t corresponds to the iteration number, as shown in the follow (5.37).

$$t=\frac{\text{Iter}}{\text{Max-Iter}} \tag{5.37}$$

where, Iter is the current iteration and, $Max-$ Iter is the maximum number of iterations.

The first of the dual mechanisms for escaping local optima involves randomizing environmental solutions before updating the temperature using the follow equation (5.38) [137].

$$\boldsymbol{T}_i^{Env}=(1-(C_1+C_2\times(1-t))\times\text{ Rand })\times\boldsymbol{T}_i^{''\text{Env}} \tag{5.38}$$

Where, $\boldsymbol{T}_i^{''\text{Env}}$ and $\boldsymbol{T}_i^{Env}$ denote the object's temperature before and after modification, respectively; C_1 and C_2 are internal control parameters; Rand is a random vector within the interval [0, 1]. The equation (5.39) was designed to reduce randomness as the algorithm approaches its final iterations, thus balancing exploitation [138].

$$T_i^{\text{New}}=T_i^{\text{Env}}+\left(T_i^{\text{Env}}-T_i^{\text{Old}}\right)\times\exp(-\beta\times t) \tag{5.39}$$

Where; T_i^{Old} and T_i^{New} denotes the prior and current temperatures of the i^{th} object, β and t being the parameters previously mentioned.

The second mechanism for escaping local optima aims for a global optimum by introducing the parameter Pro within the range (0,1). This parameter determines whether a component of each cooling object needs replacement. For each agent, if a randomly generated number Ran(i), uniformly distributed between 0 and 1, and Ran(i)<*Pro*, a dimension of that agent is randomly regenerated according to Equation (5.40) [137]:

$$T_i^{j} = T_j^{\min} + \text{random} \cdot \left(T_j^{\max} - T_j^{\min}\right) \tag{5.40}$$

Stopping criteria of the algorithm: The algorithm manages the maximum number of iterations. Upon reaching this limit, it reports the best solution found. If the limit is not reached, the algorithm continues and re-evaluates the temperature. The process ends after several iterations [138].

Multi-objective thermal exchange optimization

Because of the structural similarity to a single-objective TEO, only essential differences are mentioned briefly. The essential distinctions between the introduced MOTEO and its basic single-objective version primarily revolve around two aspects: the arrangement of objects and the measurement of parameter β, which is reformulated according to Equation (5.41) [138].

$$\beta = \frac{r_i}{\boldsymbol{N}_{Pop}} \tag{5.41}$$

Here, r_i represents the final ranking of the solution, while $\boldsymbol{N}_{Pop}$ is the number of populations.

In TEO, a higher β parameter corresponds to an increased cost value of the solution (Eq. (5.36)). In MOTEO, each solution requires multiple cost values, unlike TEO where each solution has a single cost value. Consequently, a new formulation (Eq. (5.41) is proposed, which functions similarly. Solutions that belong to a higher rank on the Pareto front have a higher β parameter.

The Flowchart of the **figure (5.14)** explain the basic of MOTEO.

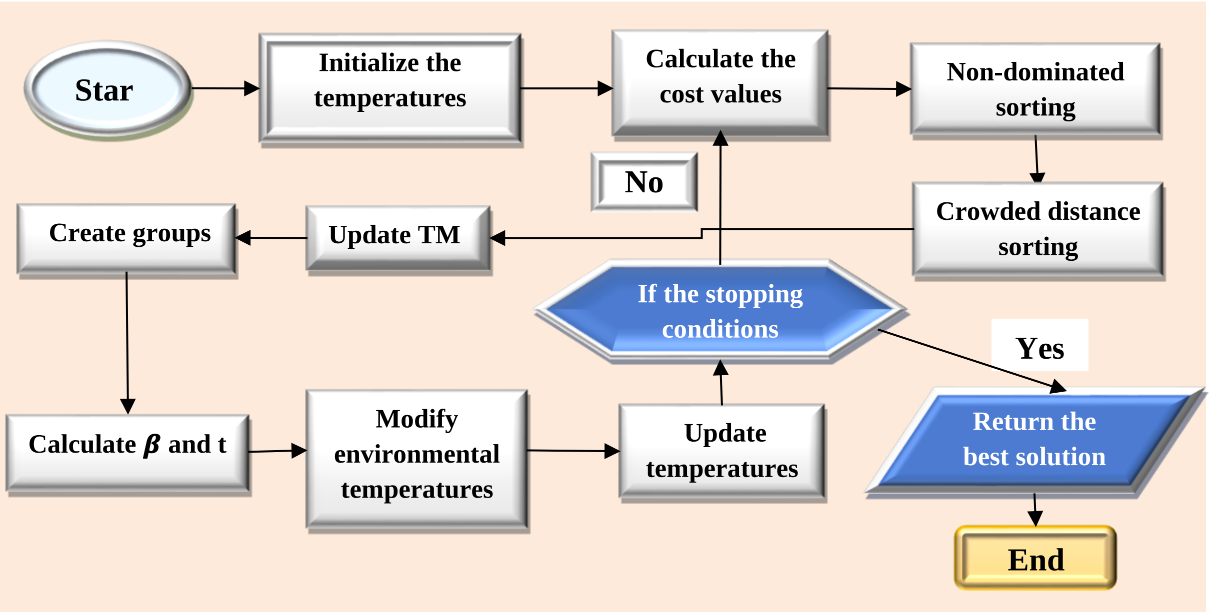

Fig. 5.14: Flowchart of the proposed MOTEO algorithm.

The remaining steps are similar to those in TEO, Further details about MOTEO can be retrieved from the reference [137].

5.7.5. Fitness Distance Balance based Artificial Ecosystem Optimization Algorithm: FBD-AEO

5.7.5.1. AEO algorithm

The AEO algorithm is inspired by the natural ecosystem of Earth, mimicking the behaviors of living organisms to achieve ecological balance. The production, consumption, and decomposition are utilized as mechanisms to model the flow of energy through an ecosystem. The candidate solutions are depicted as producers, consumers, and decomposers, each having fitness values reflecting their energy levels [139]. The **figure (5.15)** depicted the AEO ecosystem:

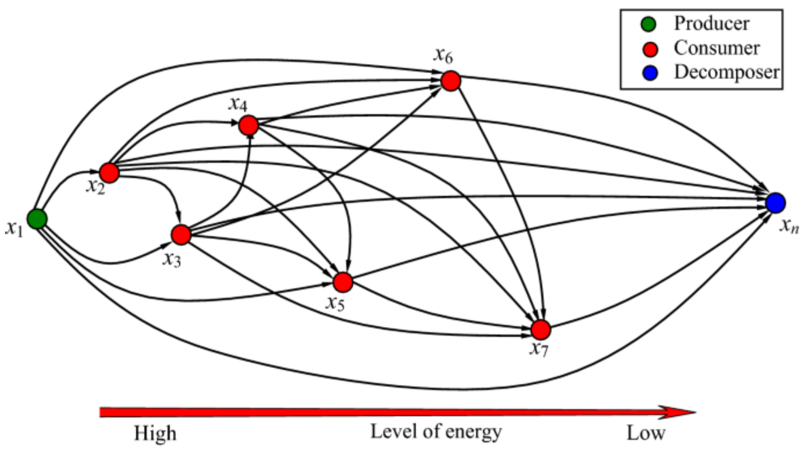

Fig. 5.15: An AEO ecosystem.

the producer as the pool candidate solution with the highest energy level (x_1). Conversely, candidates with the lowest energy levels, x_3 and x_n, represent the best individuals and labeled as decomposers. The remaining candidates, x_2 to x_7 are classified as consumers and are evenly distributed among herbivores (x_2 and x_5), carnivores (x_4 and x_6), and omnivores (x_3 and x_7). The solutions are arranged in order by energy levels, with arrows indicating energy exchange among them.

The next section elaborates the algorithm's operators and search process [139].

1. Production operator

The objective of the operation is to lead other individuals in the population to explore various areas in the search space associated with the updated individual, represented as follows:

$$x_1(t+1) = (1-\gamma)x_n(t) + \gamma x_{rnd}(t) \quad (5.42)$$

Here, the population dimension is indicated by n, t is denoted the number of iterations. γ is a coefficient used in the linear movement. x_{rnd} is the position of an individual in the search space.

2. Operator of Consumption

The AEO algorithm involves consumers sustaining energy flow by feeding lower-level producers. Positions of individuals are updated based on the worst, a randomly chosen, or a combination of both, using the equations (5.43) and (5.43):

$$C = \frac{1}{2}\frac{v_1}{|v_2|} \quad (5.43)$$

$$v_1 \sim N(\mu, \sigma), v_2 \sim N(\mu, \sigma) \quad (5.43)$$

Where, distribution $N(\mu, \sigma)$ refers to a normal distribution with a mean ($\mu = 0$), and a standard deviation ($\sigma = 1$).

In the AEO ecosystem, different consumer types have distinct consumption patterns, which are considered when updating their positions. such as herbivores who exclusively feed on specific producers like x_i, as explained by the following equation (5.44) [139]:

$$x_i(t+1) = x_i(t) + C.(x_i(t) - x_1(t)), i \in [2, n] \quad (5.44)$$

When the i^{th} consumer is a carnivore, it selects another organism with a higher energy level, chosen randomly from the range of x_2 to x_{i-1}. The consumption process is described by equation (5.45):

$$x_i(t+1) = x_i(t) + C.\left(x_i(t) - x_j(t)\right), i \in [3, n], \quad j = \text{rand}\ [2, i-1] \quad (5.45)$$

If the i^th consumer is an omnivore, it consumes both the producer $x_1$and another consumer with higher energy selected from the interval from x_2 to x_{i-1}. as represented by the following equation (5.46):

$$x_i(t+1) = x_i(t) + C \cdot \left(R_2 \cdot \left(x_i(t) - x_1(t)\right)\right) + (1 - R_2) \cdot \left(x_i(t) - x_j(t)\right), i \in [3, n], j = \text{rand}\ [2, i-1] \quad (5.46)$$

Here, 'R_2' represents a random number that falls within the range of 0 to 1.

3. Operator for Decomposition

The AEO algorithm simulates the decomposition phase, where decomposers like bacteria or fungi break down dead organisms' remains. It introduces parameters like e and h (weight coefficients) and D (decomposition factor). it updates the position of the i[th] individual based on decomposer's position, denoted x_n (the best individual). This determines their next position in the ecosystem. This process is defined mathematically as the process of decomposition:

$$x_i(t+1) = x_n(t) + D \cdot (e \cdot x_n(t) - h \cdot x_i(t)), i = 1, \dots, n \tag{5.47}$$

$$D = 3u, u \sim N(\mu, \sigma), \mu = 1 \text{ and } \sigma = 1 \tag{5.48}$$

$$e = R_3 \cdot \text{randi}([1,2]) - 1 \tag{5.49}$$

$$h = 2 \cdot R_3 - 1 \tag{5.50}$$

The steps of the AEO algorithm's pseudo code represented in reference [139]:

5.7.5.2. FDB selection method

The AEO algorithm was improved by incorporating the FDB selection approach. The FDB selection technique is a method that calculates score values based on the impact of candidates on finding a solution, considering fitness values (X_{best}) and the distance of the population from the most successful solution, known as (P_{best}). This approach enhances the exploration capability of a Metaheuristic Algorithm (MHA) during the search process. The stages of calculating score values using the FDB selection technique are as follows [139]:

Stage 1**:** The Euclidian metric is used to determine the distance of the i[th] solution candidate from P_i to p_{best} in an optimization problem of size 'm' and 'n', as follows:

$$\forall P_i, D_{P_i} = \sqrt{\left(p_{i[1]} - p_{\text{best }[1]}\right)^2 + \left(p_{i[2]} - p_{\text{best }[2]}\right)^2 + \dots + \left(p_{i[m]} - p_{\text{best }[m]}\right)^2}, i=1 \dots\dots n \tag{5.51}$$

Stage 2**:** The distance of each individual in the ecosystem area can be explained using the vector D_p as outlined below:

$$D_P \equiv \begin{bmatrix} d_1 \\ \cdot \\ \cdot \\ d_n \end{bmatrix}_{n\times 1} \tag{5.52}$$

Stage 3: The FDB score is calculated by considering each individual's fitness value within the ecosystem and incorporating the distance vector in equation (5.52). Parameters are adjusted to fit within the [0, 1] interval, with normalized fitness and distance values represented by norm_F and norm_{Dp}, in the following manner (5.53) [139]:

$$\,^{n}_{i=1}\forall P_i, S_{P_{[i]}} = w * \text{norm}_{F_{[i]}} + (1 - w) * \text{norm}_{Dp_{[i]}} \tag{5.53}$$

Stage 4: The FDB method employs a random or probabilistic approach to select individuals from the S_p vector, prioritizing the superior FDB score value over the other methods. The FDB score of each individual can be explained by using by the vector S_p as outlined in the equation (5.54):

$$s_p \equiv \begin{bmatrix} s_1 \\ \cdot \\ \cdot \\ \cdot \\ s_n \end{bmatrix}_{n\times 1} \tag{5.54}$$

5.7.5.3. FDB-AEO method

The FDB-AEO algorithm aims to improve the representation of natural energy flows by involving organisms with higher energy levels in the decomposition process. This is achieved by updating the positions of individuals using both organisms. A novel individual, x_{FDB}, was selected to enhance the search process within the conventional AEO algorithm through decomposition. The equation (5.47) was modified and tested with different variations distinct cases, as detailed in **Table 5**.1. The changes made were highlighted in Algorithm 2 marking the implementation of the new approach referred to as FDB-AEO [139].

Table. 5. 1: Mathematical representation of the FDB-AEO.

	Description and Mathematical representation of FDB_AEO
Case 1	The FDB method is introduced to modify Equation (5.47) from the original AEO algorithm, with 90% of the initial solution candidate using Equation (24). $x_l(t+1) = x_{FDB}(t) + D \cdot \left(e \cdot x_n(t) - h \cdot x_l(t)\right), i = 1, \ldots, n$ (5.55)
Case 2	The AEO algorithm has been modified with a new approach using the FDB method, replacing the second solution candidate $x_n(t)$ with the chosen candidate, and operating Equation (5.55) at 100% throughout the search process. $x_l(t+1) = x_n(t) + D \cdot (e \cdot x_{FDB}(t) - h \cdot x_l(t)) i = 1, \ldots, n$ (5.56)
Case 3	Equation (5.49) developed in Case-1 was executed continuously at a 100% rate throughout the entire search process life cycle.
Case 4	Equation (5.56) was applied at a of 10% rate, while Equation (5.47) developed in Case-2 was executed at a rate of 90% during the entire search process life cycle.

The pseudo code of introduced method can be explanted as follow [139]:

Algorithm 2. FDB-AEO algorithm's pseudo code is as follows:
Begin
Initialize the ecosystem: by randomly creating a set of $X_i$solutions
for $i = 1$: n
Compute the fitness values (fit_i) and determine the best solution (X_{best})
end for
while (the termination condition is not met, continue the process for a maximum fitness evaluation (MaxFEs) is reached.)
the position of X_1 is updated by applying the Eq (5.42) **during the Production stage**.
for $i = 2$: n **do during** ***Consumption stage***
If(rand $< 1/3$) the location of $X_i$is updated by applying the Eq (5.44; Herbivore)
Else If ($1/3 < rand < 2/3$ the location of $X_i$is updated by applying the Eq (5.45); Carnivore)
Else the position of X_i is updated by applying the Eq (5.46; omnivore)
End Else If
End If
end for
For $i = 1$: n **do**
Compute the fit_i and determine X_{best}
end for
for $i = 2$: n **do** ***During Decomposition Stage***
the distance of each individual is determined by applying Eq (5.51)
the FDB score for each individual is determined by applying Eq (5.54)
end for;
Generate D_p and $S_p$vectors by applying Eq (5.52) and Eq (5.54)
For $i = 1$: n **do**
the location of X_i is updated by applying eq (5.55) for case-1 and eq (5.56) for case-2
determine the fitness fit_i
end for
the X_{best} is updated
end while
Return the best solution X_{best}

5.7.6. Fitness Distance Balance based Archimedes Optimization Algorithm: FBD-AOA

5.7.6.1. Archimedes Optimization Algorithm (AOA)

The AOA is one of the most promising methods among the various Physics-Inspired Optimization Algorithms (PIOA). It is inspired by the forces acting on objects submerged in a fluid and their positions within the fluid. This algorithm is developed based on Archimedes' principle, which states that when an object is fully or partially submerged in a fluid, it experiences an upward force equal to the weight of the fluid displaced by the object [139].

- **Algorithmic stages**

The various stages of the AOA algorithm can be mathematically detailed as bellow.

Stage 1— initialization stage: Initialize the locations of each object applying (5.57):

$$O_i = lb_i + \text{ rand } \times (ub_i - lb_i); \quad i = 1,2,\dots,N \tag{5.57}$$

where O_i denotes the i^{th} object in a population of N objects. The boundaries of the search-area are symbolized by lb_i and ub_i, respectively.

Initialization of the density (*den*) and volume (*vol*) for each i^{th} object applying (5.58, 5.59):

$$\text{den}_i = \text{ rand} \tag{5.58}$$

$$\text{vol}_i = \text{ rand} \tag{5.59}$$

Here, " rand " refers to the dimensional vector 'D' containing random numbers within the [0, 1] interval.

The initialization of the acceleration acc_i of i^{th} object applying the equation (5.60):

$$acc_i = lb_i + rand \times (ub_i - lb_i) \tag{5.60}$$

During this stage, the focus is on obtaining the initial population and identifying the best object with the highest fitness value.

Stage 2—Update volumes, and densities [140]

The volume and density of i^{th} object are updated for the next iteration $(t + 1)$ using the following formula**:** (5.61, 5.62):

$$\text{vol}_i^{t+1} = \text{ vol}_i^t + \text{ rand } \times \left(\text{vol}_{\text{best}} - \text{ vol}_i^t \right) \tag{5.61}$$

$$\text{den}_i^{t+1} = \text{ den}_i^t + \text{rand} \times \left(\text{den}_{\text{best}} - \text{ den}_i^t \right) \tag{5.62}$$

Here; vol_{best} , and den_{best} represent the volume and density of the best object discovered so far, respectively, while "rand" denotes a random number that is uniformly distributed.

Stage 3— Density factor and Transfer operator;

The initial phase involves the collision of objects striving to reach a state of equilibrium. This process is supported by a transfer operator, denoted as TF, which facilitates transitions in the search space, aiming to maintain a balance between exploration and exploitation. It is defined as follows (5.63, 5.64):

$$TF = \exp\left(\frac{t-t_{max}}{t_{max}}\right) \tag{5.63}$$

$$d^{t+1} = \exp\left(\frac{t_{max}-t}{t_{max}}\right) - \left(\frac{t}{t_{max}}\right) \tag{5.64}$$

Where; d^{t+1} exhibits a decreasing trend over time indicates convergence within the identified promising region.

Stage 4.1—Exploration phase (collision between objects occurs) [140]

If $TF \leq 0.5$, The collision involves the selection of material (mr), and updating their acceleration for the next iteration (t+1) using the equation (5.65).

$$acc_i^{t+1} = \frac{\mathrm{dent}_{mr} + \mathrm{vol}_{mr} \times acc_{mr}}{\mathrm{den}_i^{t+1} \times \mathrm{vol}_i^{t+1}} \tag{5.65}$$

Here, the acceleration, density, and volume of a random material of i[th] object are represented by acc_{mr}, dent_{mr} and vol_{mr}.

Exploration is guaranteed in one-third of iterations, and using a value other than 0.5 can alter the equilibrium between exploratory and exploitative phases.

Step 4.2—Exploitation phase (no collision between objects)

If $TF > 0.5$, there is no collision between objects, and updating its acceleration for the next iteration (t+1) using the equation (5.66):

$$acc_i^{t+1} = \frac{\mathrm{den}_{\mathrm{best}} + \mathrm{vol}_{\mathrm{best}} \times acc_{\mathrm{best}}}{\mathrm{den}_i^{t+1} \times \mathrm{vol}_i^{t+1}} \tag{5.66}$$

where acc_{best} is the acceleration of the best object.

Step 4.3— normalization the acceleration

To determine the percentage of change, it is necessary to standardize the acceleration applying equation (5.67).

$$acc_{i-\mathrm{norm}}^{t+1} = u \times \frac{acc_i^{t+1} - min(acc)}{max(acc) - min(acc)} + l \tag{5.67}$$

In this context, the normalization range is defined by the upper (u) and lower (l) limits set to 0.9 and 0.1 respectively.

The percentage of step that each agent will change is determined by $\mathrm{acc}_{\mathrm{i-norm}}^{\mathrm{t+1}}$. A high acceleration value indicates that the i^{th} object is far from the global optimum, and in the exploration phase. Otherwise, the object is in the exploitation stage.

Stage: 5- Updating the position

If $TF \leq 0.5$ **(during the exploratory stage)**, the next locations of the i^{th} object at iteration $t+1$ applying the equation follow (5.68):

$$X_i^{t+1} = X_{fab} + C_1 * \text{ rand } * \text{acc}_{\text{norm }i} .* (X_{\text{rand}} - X_i^t) \tag{5.68}$$

where C_1 denotes a constant equal to 2, the current normalized acceleration value is represented by the parameter $\text{acc}_{\text{norm }i}$

However, if $TF > 0.5$ (**during the exploitative stage**), the positions of the objects are updated by applying the equations (5.69, 5.70).

$$X_i^{t+1} = X_{\text{best}}^t + F \times C_2 * \text{ rand } * acc_{i-\text{ norm}}^{t+1} * d.* (C_3 * TF * X_{\text{best}}^t - X_i^t) \tag{5.69}$$

or

$$X_i^{t+1} = X_{\text{best}}^t - F \times C_2 * \text{ rand } * acc_{i-\text{ norm}}^{t+1} * d.* (C_3 * TF * X_{\text{best}}^t - X_i^t) \tag{5.70}$$

Where, X_i^t is referred to the location of the object at the t[th] iteration that has the i[th] solution; while the object which has the best placement is represented by X_{best}^t.

The optimal values for AOA are achieved through three parameters: C_1, C_2, and C_3. AOA uses the transfer operator TF to transition from the exploration to the exploitation stage [140].

F denotes the flag that can be used to alter the direction of motion applying the equation (5.71):

$$F = \begin{cases} +1 \text{ if } P \leq 0.5 \\ -1 \text{ if } P > 0.5 \end{cases} \tag{5.71}$$

where $P = 2 \times rand - C_4$

Step 6—Evaluation

The objects must be evaluated based on the fitness function f, and the best solution found so far must be recorded. should be assigned accordingly by X_{best}^t, den_{best}, vol_{best}, and acc_{best}.

5.7.6.2. FBD-AOA: Fitness Distance Balance based AOA

The exploitation task in AOA is achieved through equations (69, 70), refers to the optimal material from the set of objects, focusing on intensification around X_{best}^t without collisions between objects. Equation (68) uses a vector X_{rand}, selected randomly from available materials, to enhance diversity process. The search performance of AOA is influenced by the locations of the guide objects in the equations (68,69 and 70). Analysis of these equations reveals that three distinct objects X_i^t, X_{best}^t and X_{rand} lead the search proceed in AOA [141].

In AOA, the denoted as the first of these three leaders, which is the object chosen from among the population members in a sequential manner:

X_i^t, is chosen sequentially from the population.

the X_{rand} , is chosen randomly.

X_{best}^t has the optimal fitness value.

The Fitness-Distance Balance (FDB) technique is used to effectively select vectors that guide the search process in population-based metaheuristic algorithms. This allows for redesigning convergence equations for neighborhood search and diversity tasks in AOA, using the FDB-based guidance process. Equations (5.69, 5.70) crucial for AOA's convergence have been modified to include this mechanism. The vector chosen by the FDB selection mechanism replaces some of the X_i^t, X_{rand} and X_{best} guides in these equations to improve exploitation and exploration phases.

Table. 5. 2: Mathematical explanations of variations of FDB-AOA

	Explanation	Convergence equations revamped by utilizing the FDB-based leader selection method
Case-1	$X_i^t \leftarrow X_{fbd}^t$	$X_i^{t+1} = X_{fbd}^t + C1 *$ rand $* acc_{i-norm}^{t+1} * d.* \left(X_{\mathrm{rand}} - X_i^t\right)$
	$X_{\mathrm{best}}^t \leftarrow X_{fbd}^t$	$X_i^{t+1} = X_{fbd}^t + F \times C_2 * rand * acc_{i-norm}^{t+1} * d.* \left(C_3 * TF * X_{\mathrm{best}}^t - X_i^t\right)$
	$X_i \leftarrow X_{fbd}^t$	$X_i^{t+1} = X_{fbd}^t - F \times C_2 * rand * acc_{i-norm}^{t+1} * d.* \left(C_3 * TF * X_{\mathrm{best}}^t - X_i^t\right)$
Case-2	$X_i^t \leftarrow X_{fbd}^t$	$X_i^{t+1} = X_{fbd}^t + C1 *$ rand $* acc_{i-norm}^{t+1} * d.* \left(X_{\mathrm{rand}} - X_i^t\right)$
	$X_{\mathrm{best}}^t \leftarrow X_{fbd}^t$	$X_i^{t+1} = X_{fbd}^t + F * C2 *$ rand $* acc_{i-norm}^{t+1} * d \cdot* \left(C_3 * TF * X_{\mathrm{best}}^t - X_i^t\right)$
Case-3	$X_i^t \leftarrow X_{fbd}^t$	$X_i^{t+1} = X_{fab} + C1 *$ rand $* acc_{i-norm}^{t+1} * d \cdot* \left(X_{\mathrm{rand}} - X_i^t\right)$
	$X_{\mathrm{best}}^t \leftarrow X_{fbd}^t$	$X_i^{t+1} = X_{fdb} + F * C2 *$ rand $* acc_{i-norm}^{t+1} * d \cdot* \left(C_3 * TF * X_{\mathrm{best}}^t - X_i^t\right)$
	$X_{best}^t \leftarrow X_{fbd}^t$	$X_i^{t+1} = X_{fbd}^t - F * C2 *$ rand $* acc_{i-norm}^{t+1} * d \cdot* \left(C_3 * TF * X_{\mathrm{best}}^t - X_i\right)$

Upon examining Table 5.2, it becomes clear that three distinct variations of FDB-AOA were generated and labeled as the cases (1 to 3). To achieve this, these variations were utilized to assign certain guide locations in equations (5.68, 5.69 and 5.70) utilizing the FDB method [141].

- **The framework of the pseudo code of the proposed FBD-AOA method**

Input: The size of the population: N, the maximum number of iterations Max_Iter, C_1, C_2, C_3 and C_4
Output: Optimal solution;
Initialize: create a population of objects by randomly assigning their positions, densities, and volumes, respectively;
Acceleration (acc) of each object is created randomly on D-dimensional search space
Calculate the fitness value for each object;

Find the best solution X_i^t, X_{best}^t and X_{rand} by using the equation of Case1, Case 2, and Case 3;
Evaluate The starting population will be analyzed and the individual with the highest fitness value will be selected.;
Set iteration counter t = 1
while Iter ≤ Max_Iter & FEs ≤ MaxFEs do
for each object i **do**
Density and volume of each object can be updated using the following equations: (61,62);
Updating the transfer and density reducing factors TF and d; applying (63,64);
if Iter ≤ T F ≤ 0.5 **then**
Exploration stage;
Updating and normalize acceleration by utilizing equation (65) to ensure accurate results;
Updating the locations; by using the equation of Case1, Case 2, and Case 3;
else
Exploitation stage;
Updating and normalize acceleration to ensure accurate results by utilizing equation (65,66);
Updating the direction flag F (71);
Updating the location by using the equation of Case1, Case 2, and Case 3;
End
end
Evaluate Assuming a fitness function is in place, assess each item and choose the one with the highest fitness value;
Set FEs = FEs + 1 ;
Set t = t + 1 ;
end
Return the global optimum solution X_{best}

5.8. Other's multi-objective method for solving OPF

Some multi-objective algorithms have been suggested for solving the OPF problem comprising two or more fitness functions like the non-dominated sorting genetic algorithm (NSGA-III) [142], multi-objective particle swarm optimization (MOPSO) [143]. In [144], a powerful and stable method called the Multi-Objective Adaptive Guided Differential Evolution (MOAGDE), was used for solving the MOOPF, and can find the best Pareto optimum solutions. In [145] a recent multi-objective version named Improved Multi-Objective Manta-Ray Foraging Optimization (IMOMRFO), this method has the ability to achieve the best compromise solution with high efficiency, and precision... etc. These modern optimization techniques can mostly be used to solve the OPF problem and have proven their high performance in several power-engineering optimization problems. In our work, highly effective optimization methods are required. Some new and efficient metaheuristic techniques have been proposed with the aim is solving the classical OPF problem, also OPF considers stochastic renewable energies and FACTS technology. These algorithms namely;

5.9. Conclusion

This chapter represent optimization methods are essential tools for identifying the best solutions to complex problems across various domains. Partially an overview about the global optimization method, not to mention the classification of optimization methods. In the present work, we are interested in simple and hybrid metaheuristic methods for solving the optimal power flow problem we detail some of them, which will be used for solving the optimal power in the electrical transmission network. In the following chapter, we will present the application of recent optimization algorithms for solving some problem in electrical fields, like the optimization the electrical parameters of PV models, also for solving the optimal power flow problem.

CHAPTER 6: Applications and Results

6.1. Introduction

Metaheuristics are considered a powerful tool to assist in solving difficult optimization problems. This chapter focuses on the practical application of optimization algorithms to address various problems in the electrical field. The chapter is organized into three phases: The first application involves estimating the electrical parameters of PV panel models. The second application addresses the OPF for both single and multi-objective scenarios in two systems: the IEEE 30-bus system and the Algerian electrical transmission network DZA-114 bus. The third application solves the OPF with the integration of renewable energies and FACTS devices in both electrical networks mentioned previously. All conducted results within a uniform computational condition, utilizing an HP PC with an Intel(R) Core (TM) i5-1035 G1 CPU, 8 GB of RAM, running on the Windows 10 64-bit operating system, and employing MATLAB 2021a. The system also included a 256 GB hard drive.

6.2. Application 1: Estimation of the PV panels parameters

The accurate and reliable identification of photovoltaic (PV) parameters is essential for the effective utilization of PV panel energy. This part proposes a novel optimization approach named Dandelion Optimizer (DO) Algorithm, that operates in conjunction with the Newton-Raphson method, creating a robust approach for extracting PV parameters panels. Nevertheless, the task of identifying PV parameters is commonly recognized as multimodal, presenting a complex optimization challenge. metaheuristic algorithm capable of efficiently addressing and mitigating the limitations associated with solar cell parameters, the results have been validated in the reference [146].

6.2.1. Problem statement of estimation of Parameter for PV Solar cell Models

The process of determining the PV parameters has become an optimization problem, that aims to reduce the disparity (error) between the k^{th} point measured and simulated current values. The Root Mean Square Error (RMSE) is frequently employed as a fitness function; it can be expressed by the following equation (6.1) [147]:

$$minh(x) = RMSE(X) = \sqrt{\frac{1}{N}\sum_{k=1}^{N} \left(I_K^{meas} - I_K^{sim}\right)^2} \tag{6.1}$$

Where N indicates the number of measured data I-V data, $I_K^{sim}$is the simulated current value, and $I_K^{meas}$is the measured current value.

Consequently, for the PV solar cell models, the error function values $f(V_L \cdot I_L \cdot \boldsymbol{X})$ can be expressed as following equations (6.2) and (6.3) [147]:

- **For SDM**

$$\begin{cases} f(V_L \cdot I_L \cdot \boldsymbol{X}) = I_{ph} - I_{sd}\left(\exp\left(\frac{V_L + R_S I_L N_S}{n N_S \frac{kT}{q}}\right) - 1\right) - \frac{V_L + R_S I_L N_S}{R_{sh} N_S} - I_L \\ X = \{I_{ph} \cdot I_{sd} \cdot R_S \cdot R_{sh} \cdot n\} \end{cases} \quad (6.2)$$

- **For DDM**

$$\begin{cases} f(V_L \cdot I_L \cdot X) = I_{ph} - I_{sd1}\left(\exp\left(\frac{V_L + R_S I_L}{n_1 \frac{kT}{q}}\right) - 1\right) \times I_{sd2}\left(\exp\left(\frac{V_L + R_S I_L}{n_2 \frac{kT}{q}}\right) - 1\right) - \frac{V_L + R_S I_L}{R_{sh}} - I_L \\ , \\ X = \{I_{ph} \cdot I_{sd1} \cdot I_{sd2} \cdot R_S \cdot R_{sh} \cdot n_1 \cdot n_2\} \end{cases} \quad (6.3)$$

The function involves quantifying the overall error between the observed and simulated current using the root mean square error (RMSE). can be also formulated as follow (6.4) [146]

$$RMSE(\boldsymbol{X}) = \sqrt{\frac{1}{N}\sum_{k=1}^{N} f(V_L \cdot I_L \cdot \boldsymbol{X})^2} \quad (6.4)$$

X indicates a vector that summarizes the unknown parameters to be determined.

6.2.2. Experimental results for the PV solar cell parameter

The Dandelion Optimizer (DO) Algorithm is investigated to identify the parameters for solar PV models in limited benchmark case studies of optimization, including the RTC France silicon solar cell with both types SDM and DDM. The effectiveness of the current leading method (DO) algorithm, is evaluated by comparing it against two other well-established and powerful metaheuristic techniques to assess the performance, such as the genetic algorithm (GA), Particle Swarm optimizer (PSO) algorithm. The simulation results demonstrate the superiority and reliability of the proposed method to other reported comparative approaches. Consequently, it is evident that (DO) stands out as a highly effective approach for precisely extracting the parameters of PV solar cells/panels models.

6.2.2.1. Optimization process of Metaheuristic Algorithm

To determine the parameters of solar PV cells, the DO technique is applied to minimize the fitness function (RMSE) described in equation (6.1). During optimization and fitness function computation, the Newton-Raphson technique utilizes DO to acquire the solar PV cell parameters. Subsequently, the Newton-Raphson method addresses the equation described in equations (6.2), (6.3) at a specific voltage, resulting in a substantially reduced absolute error in the output current. The optimization process represents in the **figure (6.1)**:

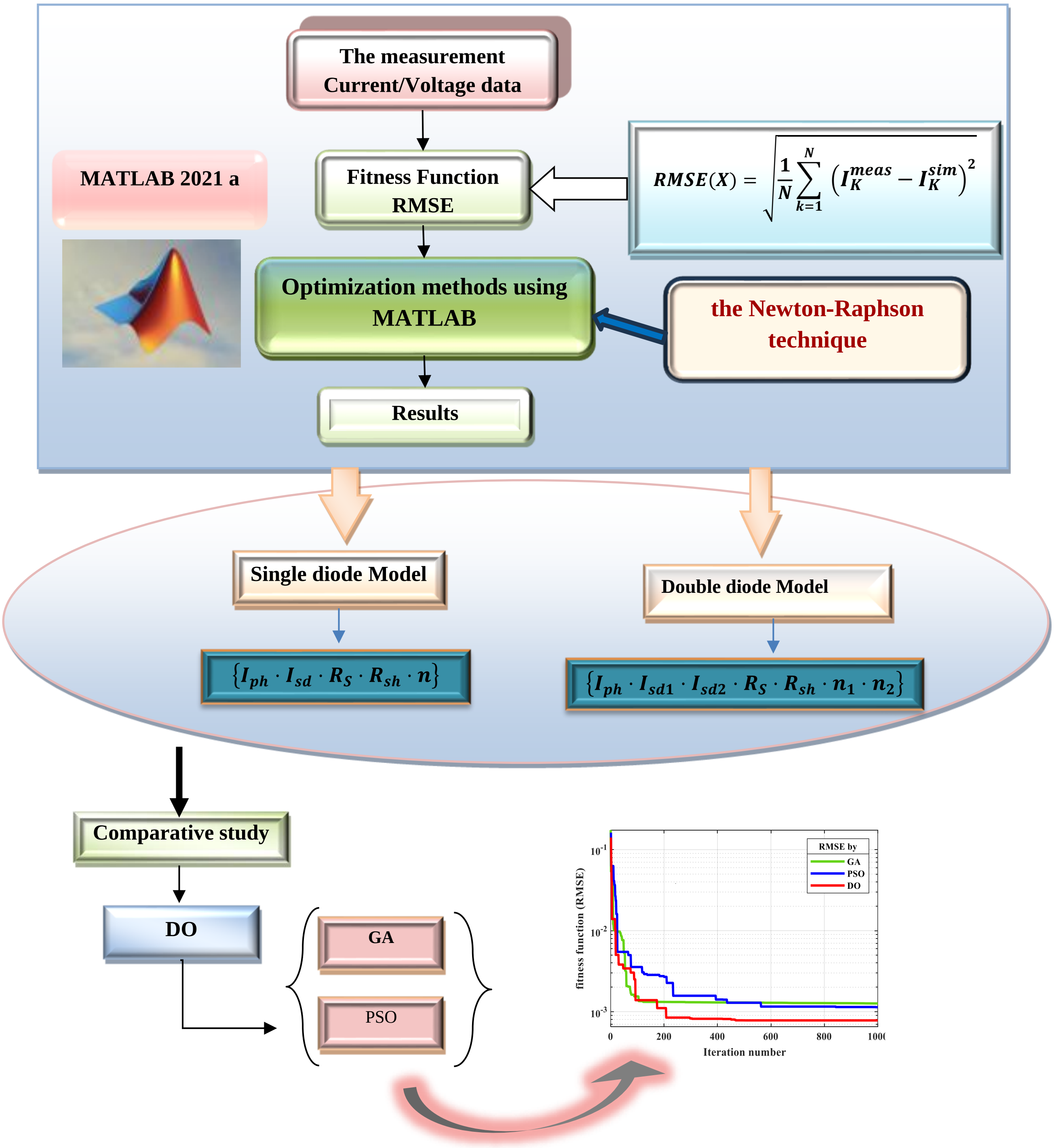

Fig. 6.1: Optimization process for extracting the parameters of solar PV cells.

The corresponding **table (6.1)** represent the Parameters boundaries of the standard R.T.C France solar cell for both types of PV cell models: single-diode and double-diode. The dataset comprised 26 pairs of experimental data points, representing current and voltage under conditions of 33 °C temperature and 1000 W/m² irradiance [147].

Table. 6.1: the Parameters boundaries of SDM and DDM PV model's Parameters boundaries.

Parameters	Single Diode		Parameters	Double Diode	
	Lower-Bound	Upper-Bound		Lower-Bound	Upper-Bound
$I_{ph}(A)$	0	1	$I_{ph}(A)$	0	1
$I_{sd}(\mu A)$	0	1	$I_{sd1}/I_{sd2}(\mu A)$	0	1
$R_S(\Omega)$	0	0.5	$R_S(\Omega)$	0	0.5
$R_{Sh}(\Omega)$	0	200	$R_{Sh}(\Omega)$	0	200
n	1	2	n_1/n_2	1	2

To demonstrate the performance of the presented algorithm (DO), in extraction the PV parameters of solar cell model the optimized results have been compared with 2 well-known algorithms, such as GA and PSO. To obtain a logical comparison, the results of the three approaches were compared under a similar condition as illustrates in **the table (6.2)**.

Table. 6.2: Parameter Settings of The Proposed Algorithms.

Algorithm	Parameters	Value
All algorithms	Population size	50
	Maximum iterations	1000
DO	α	[0, 1]
	k	[0, 1]
PSO	Local Weight (c1)	1.2
	Local Weight (c2)	1.4
	Inertia Weight (w1)	0.5
	Inertia Weight (w2)	0.9
GA	Selection type	roulette
	mutation	0.8
	Crossover	0.6

6.2.2.2. Optimization Results of PV parameters

A. Case 1: Results of the Single Diode model (SDM)

The table (6.3) displays the simulation results, presenting the best values of the five extracted parameters $\{I_{ph},\ I_{sd}, R_s,\ R_{sh}, n\}$ that must be calculated. Since no information regarding the parameter values is provided, the RMSE value serves as an indicator to assess the accuracy of the extracted parameters. According to the results, the proposed method (DO) technique achieved the best RMSE value of **7.78921e-04**, were followed by PSO and GA.

The **figure (6.2)** describes a comparison between the convergence graphs of the fitness function (RMSE) obtained by each optimization algorithms for a single diode model.

Table. 6.3: Comparison results among three methods on SDM.

Algorithm	GA	PSO	DO
$I_{ph}(A)$	0.7596	0.7609	0.760745
$I_{sd}(\mu A)$	0.2241	0.2104	0.330135
$R_S(\Omega)$	0.0384	0.0383	0.0362889
$R_{Sh}(\Omega)$	68.3404	46.2915	54.5641
m	1.4449	1.4392	1.48338
RMSE	1.3682e-3	9.7962e-04	7.78921e-04

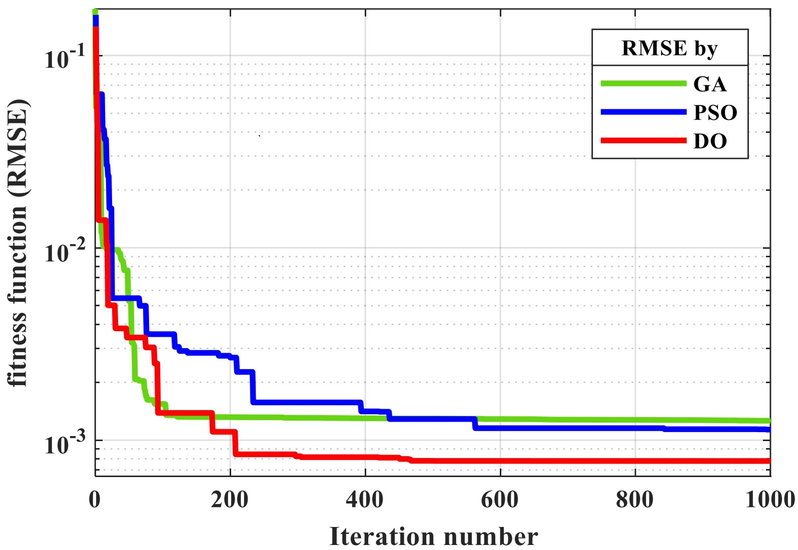

Fig. 6.2: Convergence curves of the RMSE for SDM.

This **figure (6.2)** distinctly demonstrates that the DO algorithm converges to the best solutions, showcasing its superior accuracy compared to other algorithms. This firmly establishes that parameter extraction using the presented method achieves higher accuracy compared to other methods. It can be seen that the best optimal solution obtained by dandelion optimizer algorithm. The comparison between the others algorithm show that DO converges quicker than the other metaheuristic techniques and continues to exploit the global optimum value to achieve better convergence with an accuracy. it can successfully converge to the optimal value of RMSE in the case of a SDM and the composition of convergence demonstrates the efficiency of reported method to a certain extent. In addition, the extracted parameters can be used to Improve modeling real solar power plants. The best PV parameters obtained from FDB-AEO are utilized to plot I-V and P-V graphs.

The **figures (6.3 (a)) and (6.3 (b))** depict the comparison of simulated and measured current-voltage (I-V) and power-voltage (P-V) curves, respectively, obtained with the single-diode model.

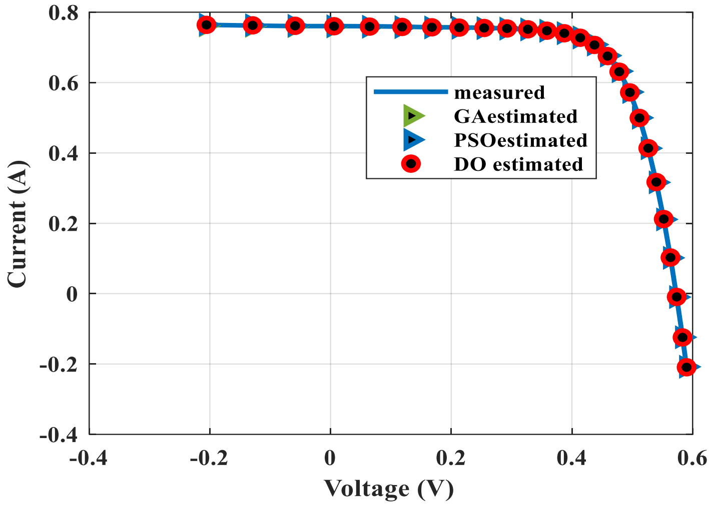

Fig. 6.3 (a): I-V curves with the measured and estimated data for SDM.

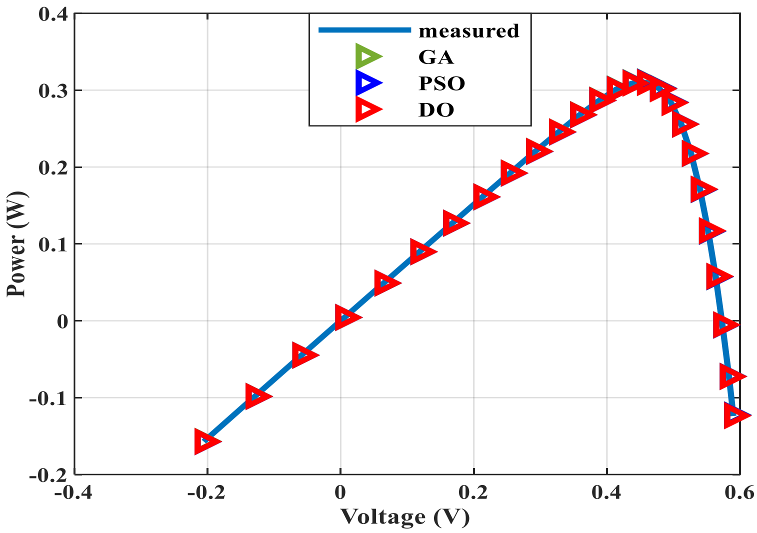

Fig. 6.3 (b): P-V curve with the measured and estimated data for SDM.

These figures demonstrate that the simulated results values achieved by DO are showcasing highly consistent I-V and P-V curves. This reveals that the parameters of the SDM predicted by DO are more accurate than the two others metaheuristic methods. It's unnecessary to mention after these results, as the optimized parameters achieved clearly demonstrate that the simulated data generated by DO were extremely close to the experimental dataset. Which confirm that best extract PV parameters of the SDM among the two others optimization approaches.

B. Case 1: Results of the Single Diode model (SDM)

In this case, The DDM, in contrast to the SDM, requires the identification of seven parameters that must be extracted. The simulation results for the DDM displays in the **table (6.4)**, which including the seven extracted parameters $\{I_{ph}, I_{sd1}, I_{sd2}, R_S, R_{Sh}, n1, n2\}$, and the RMSE values of the comparing techniques on the DDM. It can be observed that the proposed DO obtained the lowest value of fitness function (RMSE) as a value (**9.8666e-04**) among the other methods.

Table. 6.4: Comparison Results Among Different Algorithms on DD Model.

Algorithms	**GA**	**PSO**	**DO**
$I_{ph}(A)$	0.7615	0.7608	0.76077
$I_{sd1}(\mu A)$	0.8020	-0.0829	0.0891729
$I_{sd2}(\mu A)$	0.2953	0.3466	0.302307
$R_S(\Omega)$	0.0355	0.0363	0.0365362
$R_{Sh}(\Omega)$	51.6081	53.6593	54.548
N1	1.9987	1.4869	1.41558
N2	1.4780	1.8459	1.55766
RMSE	1.26159e-3	9.8680e-04	9.8666e-04

the convergence graphs of the best fitness function (RMSE) obtained by the presented algorithm compared for each three tested methods is illustrated in the **figure (6.4).**

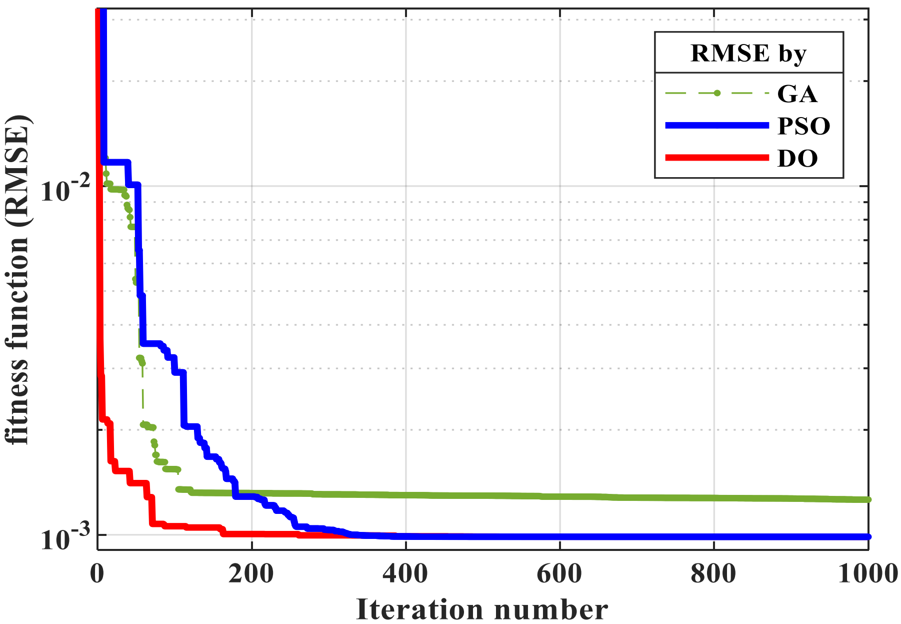

Fig. 6.4: Convergence curves of the RMSE for DDM

from this figure it can be noticed that the best solutions have been achieved by using the DO, these results reveal that Only DO algorithm can find better solutions at a faster rate than the comparison of the two other methods (GA, PSO), demonstrating DO's great capacity to achieve the best optima. Through using the best model that extract by DO. Furthermore, the best parameter extract with the presented method is better than the others method, which used for plotting I-V and P-V curves.

The DDM's I-V and P-V characteristic graphs can be illustrate in **figures (6.5 (a), 6.5 (b))**. Besides. These figures demonstrate that the measured and simulated data produce highly consistent I-V and P-V curves, revealing the best PV parameters of the DDM model predicted by DO more accurate.

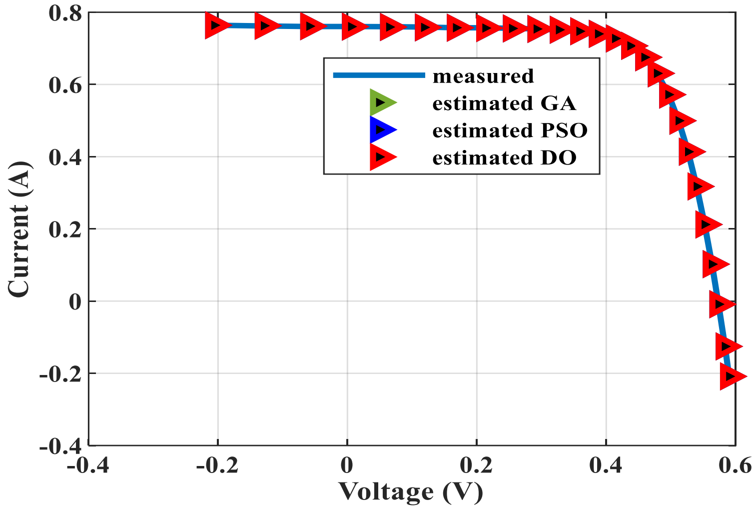

Fig. 6.5 (a). I-V curves with the measured and estimated data for DDM

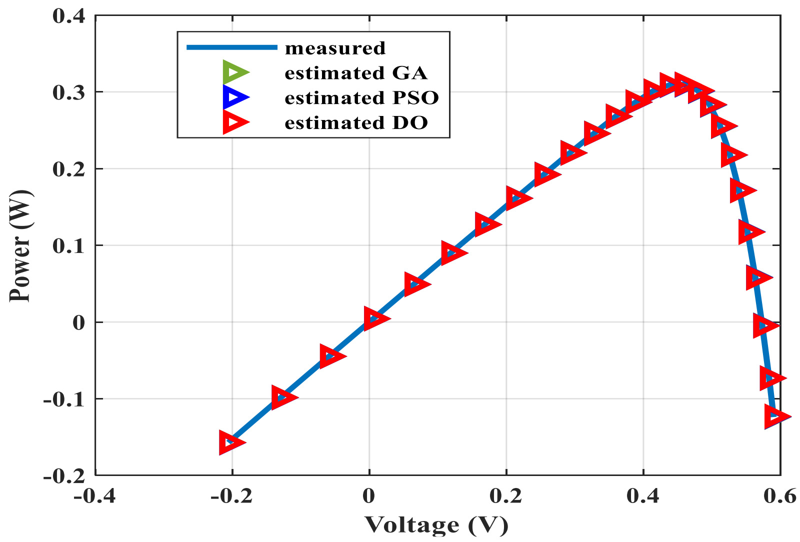

Fig. 6.5 (b) P-V curve with the measured and estimated data for DDM

This part presents the application of a new metaheuristic technique, namely Dandelion Optimizer (DO) Algorithm for extracting PV module parameters through optimization methods. The suggested DO technique can provide efficient results compared to other techniques, extracting the parameters of each PV model with high accuracy, precision, and rapidity. Furthermore, the collection of photovoltaic model parameters aims to enhance the control of real solar power plants. However, the extracted parameters can be applied for Improving the modulization of real solar power plants.

6.3. Application 2: optimal power flow (OPF)

The problem of optimal power flow (OPF) is classified into two categories: single-objective problem (OPF) and multi-objective problem (MOOPF). The treated objective functions include fuel cost, gas emissions, power losses, and voltage deviations. the first section aims to enhance the performance of the IEEE 30-bus network and the Algerian network using global optimization methods.

6.3.1. Application 2.1: electrical transmission network IEEE 30-bus test system

The first section aims to examine the performance of the proposed thermal exchange optimization (TEO) algorithm in solving the OPF problems with both types, the IEEE 30-bus electrical transmission network is taken as a tested network. For the **single-OPF problems**, five other powerful optimization methods used to compare the obtained results by the proposed TEO, like fitness distance balance-based Archimedes optimization algorithm (FDB-AOA) FDB-based artificial ecosystem optimization (FDB-AEO); salp swarm algorithm (SSA); Particle Swarm Optimization (PSO); and Genetic Algorithms (GA). For the **MOOPF**, the recent multi-objective version of thermal exchange optimization (MOTEO) algorithm, are used for solving the multi-objective OPF compared with, improved multi-objective manta-ray foraging optimization (IMOMRFO); Dynamic Switched Crowding Mult objective- Adaptive Guided Differential Evolution Algorithm (DSC-MOAGDE); multi-objective salp swarm algorithm (MSSA); multi-objective particle swarm optimization (MOPSO); and multi-objective genetic algorithm (MOGA), those results validated in the article with reference[123].

Overview of The IEEE 30-bus Test System:

The specific data for this test system are provided in **table (6.5),** the **table (6.6)** present the cost and emission generator coefficients, along with the boundary limits for output generation power boundary limits. The **figure (6.6)** shows the topology of the IEEE 30-bus test system [148].

Table. 6.5: Detailed Information on the IEEE 30-bus test system

Element		**Quantity**	**Details**
Buses-number		30	-
Branches-number		41	-
generators-number		6	**Slack-Bus is 1/** 2/ 5/ 8/ 11 and 13
capacitors-number		9	buses: 10 and 24
Transformer with tap changer		4	branches: 11/ 12/ 15 and 36
Total power demand	Active-power	-	283,4 MW
	Reactive-power	-	126,2 MVAR
Load-buses		24	-

Table. 6.6: Cost and Emission Coefficients of Generating Units in the IEEE 30-bus System

Bus	c_i	b_i	a_i	$\gamma\ .\ 10^{-2}$	$\beta.\ 10^{-4}$	$\alpha.\ 10^{-6}$	$\xi.\ 10^{-4}$	$\lambda.\ 10^{-2}$	$P_{G_i}^{min}$	$P_{G_i}^{max}$
1	0.00375	2	0	4.091	-5.554	6.49	2.0	2.857	50	200
2	0.0175	1,75	0	2.543	-6.047	5.638	5.0	3.333	20	80
5	0.0625	1	0	4.258	-5.094	4.586	0.01	8.0	15	50
8	0.00834	3.25	0	5.326	-3.55	3.38	20.0	2.0	10	35
11	0.025	3	0	4.258	-5.094	4.586	0.01	8.0	10	30
13	0.025	3	0	6.131	-5.555	5.151	10.00	6.667	12	40

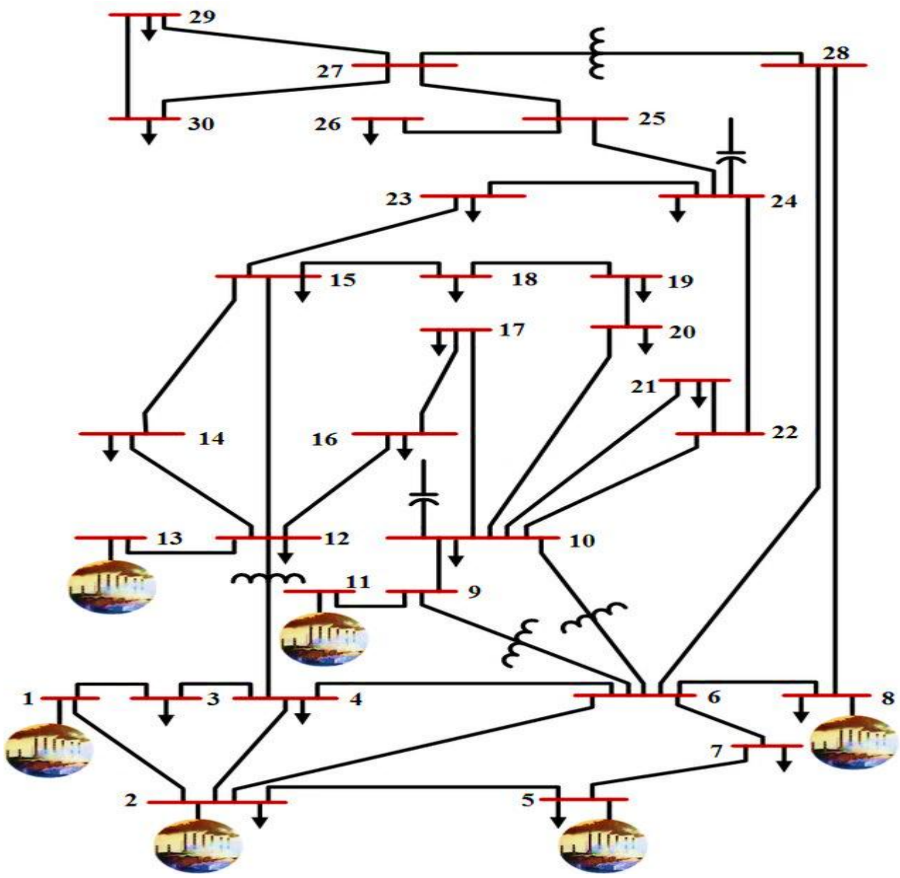

Fig. 6.6: Schema of IEEE 30-bus test-system.

- **Numerical Results and Discussions**

To ensure a rational comparison, all simulation cases and algorithms were compared under identical conditions. The parameter settings for the algorithms are detailed in the **table (6.7)**.

Table. 6.7: Internal parameters settings of the algorithms.

	The name of Algorithm	Parameters	Value
	All algorithms	Population size	20
		Maximum iterations	200
Single objective	**TEO**	C1	1.2
		C2	2.2
	FDB_AOA	The default parameters settings of the algorithm	
	FDB_AEO	The default parameters settings of the algorithm	
	SSA	C1	[0, 1]
		C2	Rand ()
		C3	Rand ()
	PSO	Inertia-Weight (w1)	0.5
		Inertia-Weight (w2)	0.9
		Local-weight (C1)	1.2
		Local-weight (C2)	1.4
	GA	Selection type	roulette
		Crossover	0.8
		mutation	0.14

multi-objective	**MOTEO**	C1	1.2
		C2	2.2
		Percentage of Crossover	0.7
		Percentage of Mutation	0.4
		Mutation	0.02
	IMOMRFO	The default parameters settings of the algorithm	
	DSC-MOAGDE	The default parameters settings of the algorithm	
	MSSA	The default parameters settings of the algorithm	
	MOPSO	c1	1.2
		c2	1.4
		Beta	0.1
		Lambda	0.9
		w	1
		wdamp	0.95
	MOGA	The default parameters settings of the algorithm	

For each case, the optimized-results include the optimal settings of the control variables, total fuel cost (TFC), total emission gas (TEG), active power losses (APL), and voltage deviation (VD). **Table (6.8)** represents the all cases addressed in this part of research.

Table. 6.8: cases addressed in this research.

case n°	fitness Functions
case 1	Total Fuel Cost (TFC)
case 2	Total Emission Gas (TEG)
case 3	Active Power losses (APL)
case 4	Voltage Deviation (VD)
case 5	TFC and TEG simultaneously
case 6	TFC and APL simultaneously
case 7	APL and VD simultaneously
case 8	TFC, TEG, and APL simultaneously

6.2.1.1. Single-Objective OPF problem: IEEE 30-bus

The effectiveness of the proposed TEO was initially assessed by applying it to single-objective OPF problems. The summary of the simulated-results for each test case is provided in **table (6.9).**

Table. 6.9: The summary of the simulated-results of the TEO on for addressing single-objective OPF.

P_{Gi} (MW)	case 4	case 3	case 2	case 1
P_{G1}	173.1889	51.9111	70.1690	176.4878
P_{G2}	71.4215	79.9957	71.4234	48.8374
P_{G5}	15.0800	49.9983	49.1068	21.4310
P_{G8}	11.4022	34.9973	34.6021	21.9482
P_{G11}	10.7081	29.9984	28.2083	12.1969
P_{G13}	12.0000	39.9968	33.8037	12.0000
Total fuel cost ($/h)	815.1328	968.5297	929.7806	**802.3607**

Emission gas (ton/h)	0.3673	0.2216	**0.21929**	0.3665
Active power losses (MW)	10.4008	**3.4976**	3.9134	9.5012
ΔV (p.u)	**0.67514**	0.7237	0.7219	0.6829
CPU-time (sec)	**17.0174**	**17.2302**	**17.28617**	**16.9921**

To showcase the superiority of the TEO algorithm, its simulated-results were compared with other algorithms, such as the FDB-AOA, FDB-AEO, SSA, PSO, and the GA. These comparisons have proven the effectiveness of TEO in solving single-objective OPF problems on the IEEE 30-bus electrical network. In this section, these cases are discussed:

- **Case 1: Minimization of the Total fuel cost (TFC (MW)):**

In the initial case, the TFC was chosen as the fitness function. The simulation results, as shown in **table (6.10)**, compare the presented technique (TEO) with other methods. The values for the best TFC were nearly the same across all methods. Notably, the value of TFC obtained by TEO is **802.3607 $/h** while requiring less execution time. The convergence characteristics for TFC fitness function using TEO and other algorithms are depicted in **figure (6.7)**.

Table. 6.10: The optimized-results of the proposed TEO method and others: Case 1.

P_{Gi} (MW)	**TEO**	**FDB-AOA**	**FDB-AEO**	**SSA**	**PSO**	**GA**
P_{G1}	176.4878	176.9304	176.6824	176.8127	178.2879	172.7648
P_{G2}	48.8374	49.5669	48.8565	48.7627	48.5015	52.0187
P_{G5}	21.4310	21.3281	21.5157	21.5116	21.4564	22.9486
P_{G8}	21.9482	20.5942	21.6382	21.7192	20.2835	20.9285
P_{G11}	12.1969	12.5504	12.2217	12.1158	11.9820	10.8531
P_{G13}	12.0000	12.0000	12.0013	12.0000	12.5260	13.2136
Total fuel cost ($/h)	**802.3607**	**802.3883**	**802.3604**	**802.3603**	**802.4219**	**802.8716**
Total Emission gas (ton /h)	0.3665	0.3678	0.3671	0.3674	0.3715	0.3544
Total Active power losses (MW)	9.5012	9.5700	9.5157	9.5220	9.6373	9.3273
ΔV (p.u)	0.6829	0.6829	0.6828	0.6827	0.6823	0.6817
CPU-time (sec)	**16.9921**	18.5131	17.3033	17.5517	18.2526	22.7751

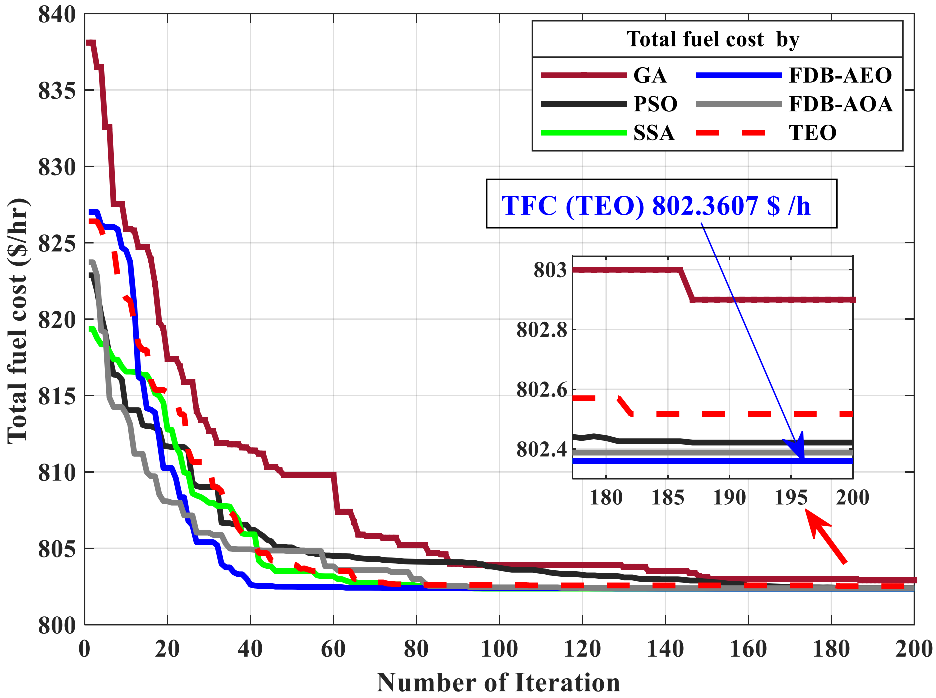

Fig. 6.7: Convergence behaviors for minimization of TFC: Case 1: IEEE 30-bus.

- **Case 2: Minimization of total emission gas (TEG):**

The second case was chosen the total emission gas (**TEG**) as a fitness function. The simulation results obtained through the presented technique (TEO), compared with other methods are shown in **table 6.11**. It was observed that TEO achieved the highest reduction in **TEG**, with a value of **0.2137 ton/h**, compared with to other techniques, while requiring less execution time. The convergence characteristics for minimizing TEG using the presented algorithm and the others' compared algorithms are illustrated in **figure (6.8).**

Table. 6.11: The simulated-results of the proposed TEO method and others: Case 2.

P_{Gi} (MW)	**TEO**	**FDB-AOA**	**FDB_AEO**	**SSA**	**PSO**	**GA**
P_{G1}	70.5539	68.3633	68.2291	68.1098	68.8179	70.1690
P_{G2}	68.2759	72.2541	71.3491	71.2237	70.9642	71.4234
P_{G5}	50.0000	49.9968	49.9992	50.0000	50.0000	49.1068
P_{G8}	35.0000	34.9782	34.9990	35.0000	35.0000	34.6021
P_{G11}	30.0000	29.9980	29.9988	30.0000	30.0000	28.2083
P_{G13}	33.4010	31.6380	32.6383	32.8757	32.4405	33.8037
Total fuel cost ($/h)	931.5967	934.5488	935.0626	935.3462	934.0096	929.7806
Total Emission gas (ton /h)	**0.2137**	**0.2176**	**0.2176**	**0.21756**	**0.21756**	**0.21929**
Total Active power losses (MW)	3.8308	3.8285	3.8136	3.8092	3.8225	3.9134
ΔV (p.u)	0.7238	0.7235	0.7237	0.7237	0.7236	0.7219
CPU-time (sec)	**17.2861**	17.9821	18.1378	17.2877	18.47389	20.55941

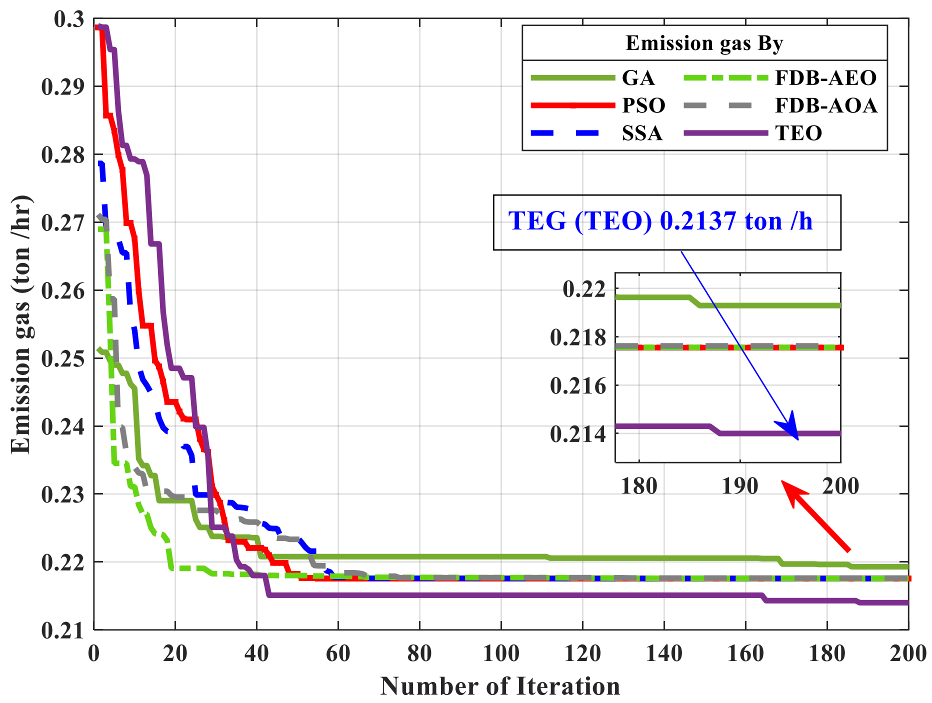

Fig. 6.8: Convergence behaviors for minimization TEG: Case 2: IEEE 30-bus.

Case 3: minimizing the total active power losses (APL):

The third fitness function focused on minimizing the total active power losses (APL). **Table (6.12)** summarizes the optimal results obtained using the proposed TEO method and other techniques. Remarkably, the TEO method achieved the best solution with a value of **3.4976 MW.** The **figure (6.9)** depicts the convergence behaviors for minimizing total real power loss (**APL**) using the proposed method compared to other methods.

Table. 6.12: The simulated-results of the proposed TEO method and others: Case 3.

P_{Gi} (MW)	**TEO**	**FDB_AOA**	**FDB_AEO**	**SSA**	**PSO**	**GA**
P_{G1}	51.9111	52.3605	52.4025	51.9292	53.2708	55.74086
P_{G2}	79.9957	79.7951	79.7951	79.9865	79.4866	78.40561
P_{G5}	49.9983	49.9887	49.9487	49.9955	49.6869	49.90884
P_{G8}	34.9973	34.9931	34.9731	34.9982	34.9979	34.30025
P_{G11}	29.9984	29.9124	29.9224	29.9940	29.8611	28.80385
P_{G13}	39.9968	39.8547	39.8647	39.9946	39.6225	39.81672
Total fuel cost ($/h)	968.5297	967.5097	967.3385	968.4830	964.7394	960.9912
Total Emission gas (ton /h)	0.216	0.3662	0.3663	0.2216	0.2213	0.2216
Total Active power losses (MW)	**3.4976**	**3.5045**	**3.5065**	**3.4979**	**3.5259**	**3.5761**
ΔV (p.u)	0.7237	0.7236	0.7236	0.7237	0.7236	0.7225
CPU-time (sec)	**17.2302**	17.5368	17.3758	17.3293	18.7029	21.7652

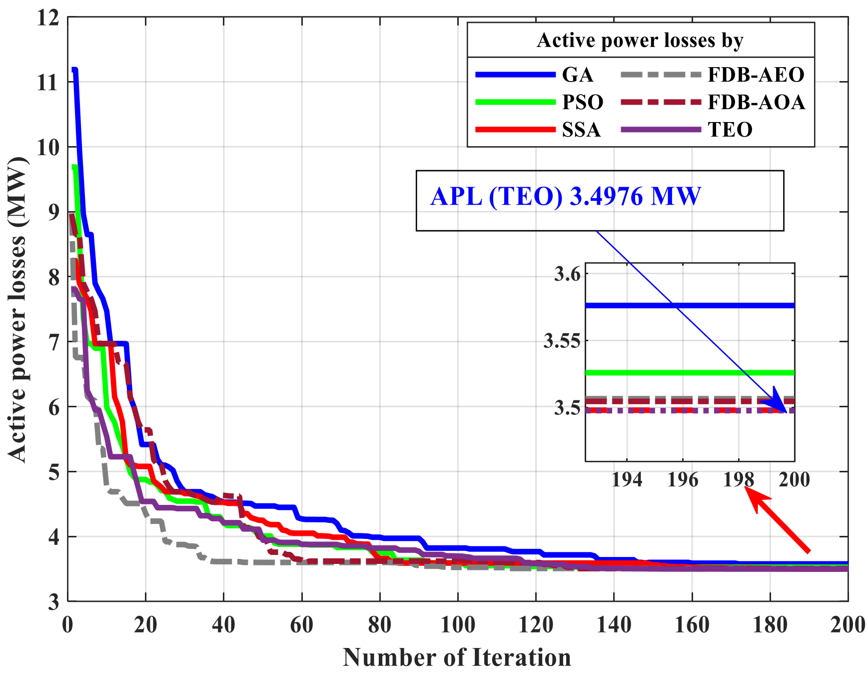

Fig. 6.9: Convergence behaviors for minimization APL: Case 3: IEEE 30-bus.

- **Case 4: Total Voltage Deviation minimization (TVD):**

the voltage deviation was selected as the fitness function in this case. **Table 6.13** presents the optimized results using the presented method (TEO) along with results from other algorithms. It is evident that the TEO method achieves the optimal solution with a value of **0.67514 p.u**, despite the fact that the values obtained by all methods are nearly identical. The **figure (6.10)** displays the convergence behaviors for TVD minimization comparing the proposed TEO method with other techniques.

Table. 6.14: The simulated-results of the proposed TEO method and others: Case 4.

P_{Gi} (MW)	**TEO**	**FDB-AOA**	**FDB-AEO**	**SSA**	**PSO**	**GA**
P_{G1}	173.1889	168.2957	189.3845	169.6567	159.4153	194.0816
P_{G2}	71.4215	72.8975	50.8421	74.3248	80.0000	25.2490
P_{G5}	15.0800	15.7564	20.5075	15.2995	15.0000	35.0760
P_{G8}	11.4022	13.3754	10.3819	10.4383	13.5643	15.5173
P_{G11}	10.7081	10.5875	10.6836	10.0772	11.4546	10.8967
P_{G13}	12.0000	12.5457	12.2959	13.8788	13.5325	12.3078
Total fuel cost ($/h)	815.1328	815.7353	804.4774	817.9730	823.6236	825.5293
Total Emission gas (ton /h)	0.3673	0.3553	0.4069	0.3598	0.3290	0.4204
Total Active power losses (MW)	10.4008	10.0582	10.6954	10.2753	9.5667	9.7284
ΔV (p.u)	**0.6751**	**0.6765**	**0.6754**	**0.6754**	**0.6789**	**0.6806**
CPU-time (sec)	**17.0174**	18.4908	17.654262	17.4028	18.5927	22.6669

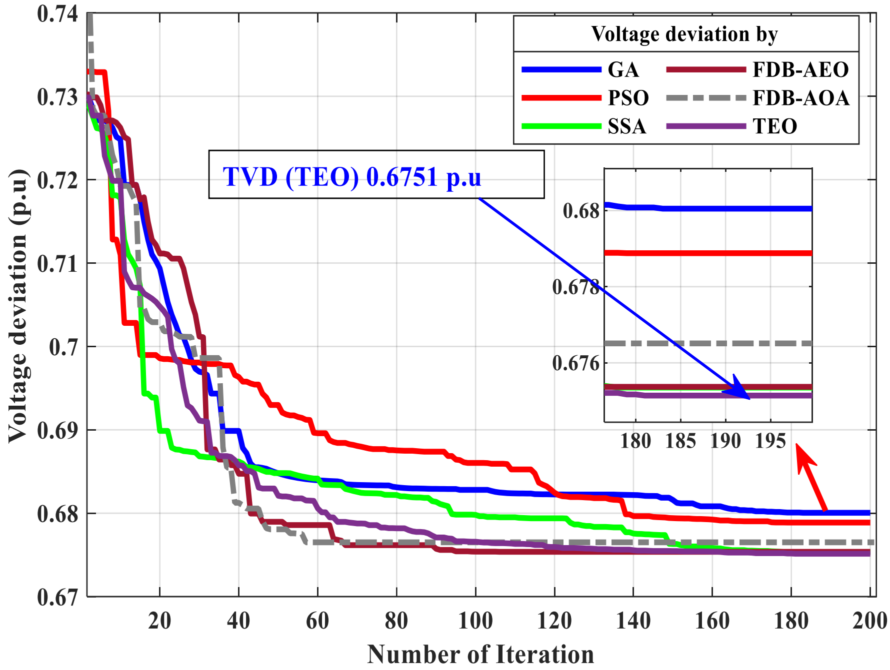

Fig. 6.10: Convergence characteristics for minimization of TVD: Case 4: IEEE 30-bus.

Table (6.15) provides a comparison of the simulated results achieved by the proposed TEO and other investigated techniques for a single OPF problem on the IEEE 30-bus test system.

Table. 6.15: Comparison summary of the optimized-results between TEO and the others for all cases.

Algorithms	***VD (p.u)***	***APL (MW)***	***TEG (ton/h)***	***TFC ($/h)***
Initial	0.6380	17.528	0.8983	875.1688
Case	**4**	**3**	**2**	**1**
TEO	0.6751	3.4976	0.2193	802.3607
FDB-AOA	0.6765	3.5045	0.2176	802.3883
FDB-AEO	0.6754	3.5065	0.2176	802.3604
SSA	0.6754	3.4979	0.2176	802.3603
PSO	0.6789	3.5259	0.2176	802.4219
GA	0.6801	3.5761	0.2137	802.8716

- **Discussion of The Results of The Single Objective OPF: IEEE 30-bus**

The optimized results clearly highlighted the effectiveness of the proposed TEO method over other prominent metaheuristic algorithms. It accurately addresses different single-objective OPF problem instances and frequently yields lower values for most cases studied. Furthermore, TEO provides optimal solutions within competitive computational execution time compared to other algorithms. In the majority of cases, TEO method delivered optimal solutions among other methods. These results demonstrate that the TEO algorithm exhibits superior performance in terms of convergence speed, solution quality, and execution time. Consequently, TEO can be a highly powerful and robust competitive tool for addressing various OPF problems.

- **Statistical Analysis and Robustness of the Proposed Method (TEO)**

To evaluate the robustness and efficiency of each method, particularly the TEO, in solving optimal power management problems, a detailed statistical analysis was conducted. Five key-indices were computed: the mean, the minimum (Best), the median, the maximum and the standard deviation (SD) across 50 independent runs. The **table (6.16)** demonstrates that the proposed TEO method yielded the most optimal solution, exhibiting a lower SD of **0.03361** in comparison to other methods. **Figure (6.11)** illustrates the evolution simulation of TFC across trials for the TEO method and the other techniques. The **figure (6.12)** provides a comparative analysis of the optimized TFC against trials for TEO in contrast with FDB-AOA, FDB-AEO, SSA, PSO, and GA. The results confirm that the TEO method consistently achieved the best solution with the lowest SD, demonstrating its accuracy and stability in solving various OPF problems.

Table. 6.16: Comparative Statistical Analysis of TEO and Various Algorithms.

	TEO	FDB-AOA	FDB-AEO	SSA	PSO	GA
Mean	802.4007	802.8336	802.5861	802.4023	802.9784	803.5740
Best	802.3607	802.3883	802.3604	802.3603	802.4219	802.8716
Median	802.3937	802.7317	802.4575	802.3956	802.9017	803.5873
Max	802.5286	803.8324	803.5488	802.5243	803.8347	804.5768
SD	0.03361	0.3745	0.2905	0.035402	0.382200	0.385200

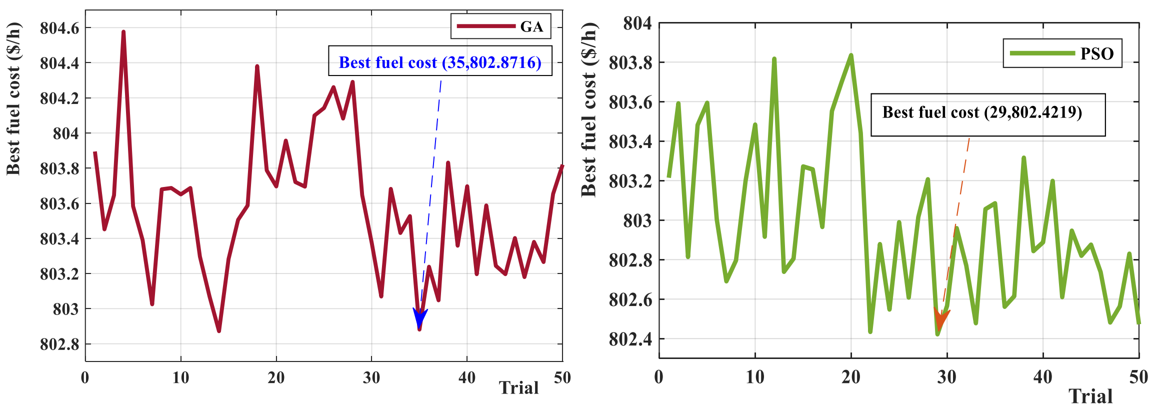

(a) (b)

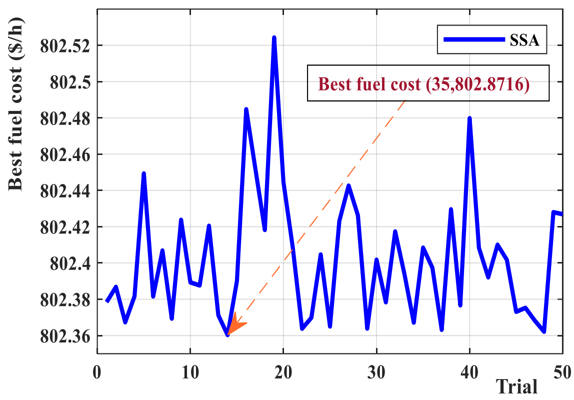

(c)

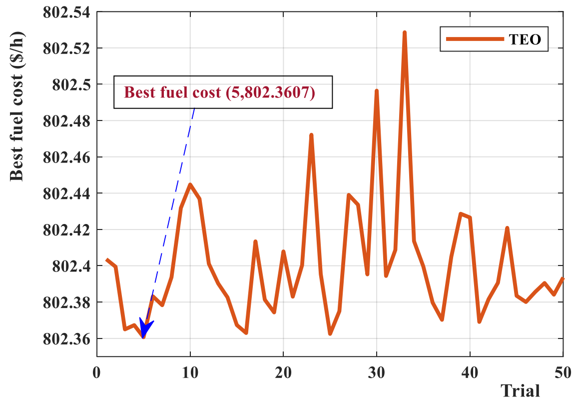

(d)

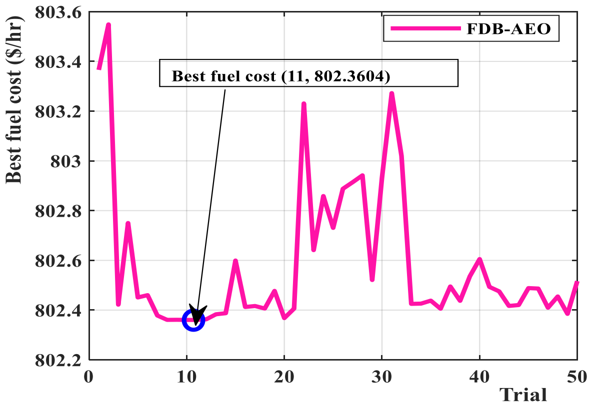

(e)

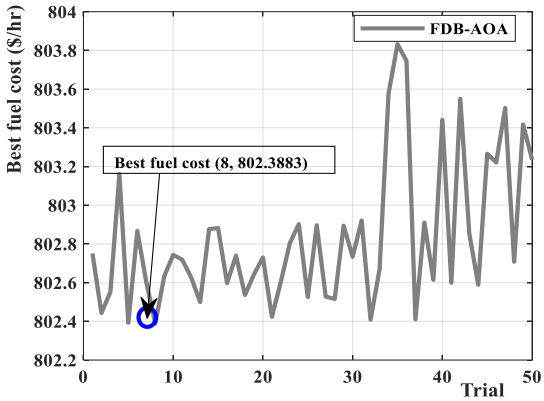

(f)

Fig. 6.11: Evolution of simulated TFC against trials for: (a) GA, (b) PSO, (c) SSA, (d) TEO, (e) FDB-AEO, (f) FDB-AOA.

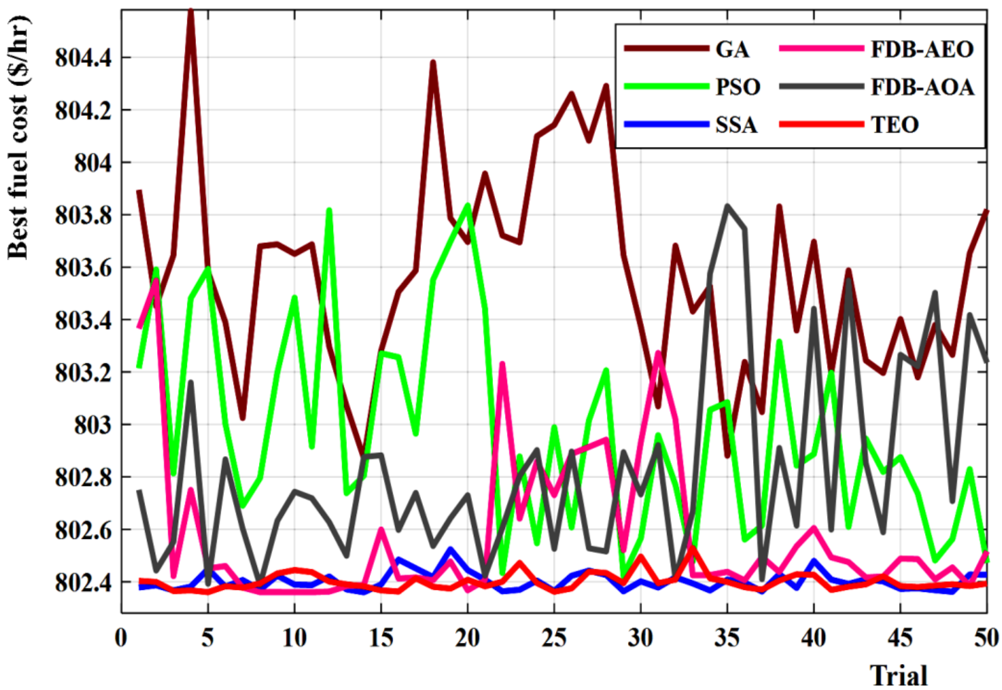

Fig. 6.12: The optimized TFC against trials for TEO, compared with FDB-AOA, FDB-AEO, SSA, PSO, and GA

- **Discussion of results using statistical analysis: cases 1 to 4: IEEE 30-bus**

To evaluate the robustness of the proposed algorithm (TEO), a statistical analysis of cases 1 to 4 were conducted, where all cases executed with 10 independent runs for each case/ algorithm. A boxplot graph was utilized to display the distribution of the solutions based on five-statistical indices. **The table (6.17)** displays the statistical results, while **(figure 6.13)** shows the box plot of the fitness values for the TEO method and other algorithms. The analysis of the findings indicates that the proposed algorithm is statistically superior with a lower standard deviation (SD) compared to other techniques and exhibits consistent search performance across nearly all cases for the single OPF problems. The minimum and maximum values were also favorable, highlighting the method's ability to achieve optimal solutions efficiently, where it can be concluded that the TEO algorithm is highly effective for solving various OPF problems.

Table. 6.17: Comparative of the statistical analysis for all cases (1 to 4) of TEO method and other.

Case		TEO	FDB_AOA	FDB_AEO	SSA	PSO	GA
1	**Mean**	802.4074	802.8073	802.5184	802.4258	803.1650	803.5104
	Best	802.3607	802.3883	802.3604	802.3603	802.4219	802.8716
	Median	802.3966	802.6757	802.3782	802.4325	803.1084	803.5851
	Max	802.5286	803.8324	803.5488	802.5243	803.8347	804.5768
	SD	0.0511	0.4171	0.3884	0.0550	0.4502	0.5152
2	**Mean**	0.2165	0.2179	0.2178	0.2176	0.2177	0.2201
	Best	0.2137	0.2176	0.2176	0.2176	0.2175	0.2193
	Median	0.2172	0.2176	0.2177	0.2176	0.2177	0.2199
	Max	0.2183	0.2192	0.2188	0.2178	0.2179	0.2209
	SD	0.0018	6.2058e-04	3.5997e-04	8.3593e-05	1.0529e-04	5.3991e-04
3	**Mean**	3.5036	3.5159	3.5291	3.5133	3.5495	3.5882
	Best	3.4976	3.5045	3.5053	3.4979	3.5259	3.5761
	Median	3.5009	3.5175	3.5185	3.5115	3.5370	3.5818
	Max	3.5183	3.5321	3.6423	3.5464	3.6507	3.6308
	SD	0.0074	0.0085	0.0406	0.0160	0.0375	0.0171
4	**Mean**	0.6756	0.6774	0.6762	0.6773	0.6798	0.6817
	Best	0.6751	0.6765	0.6754	0.6754	0.6789	0.6806
	Median	0.6754	0.6771	0.6763	0.6777	0.6797	0.6816
	Max	0.6763	0.6799	0.6772	0.6797	0.6813	0.6856
	SD	4.7044e-04	0.0012	6.6073e-04	0.0014	7.7405e-04	0.0014

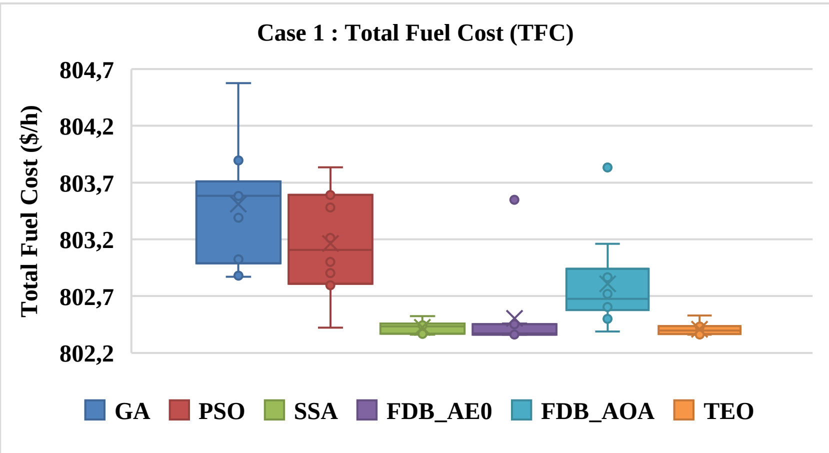

(b) case 1

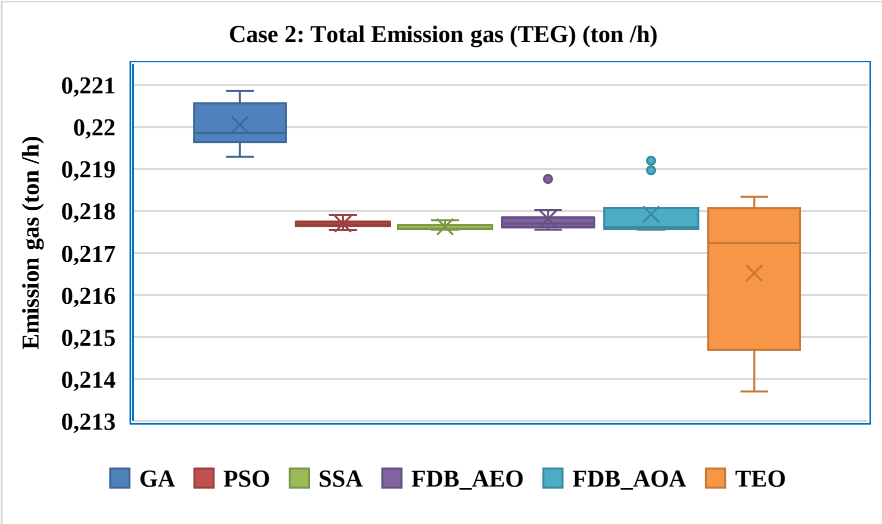

(c) case 2

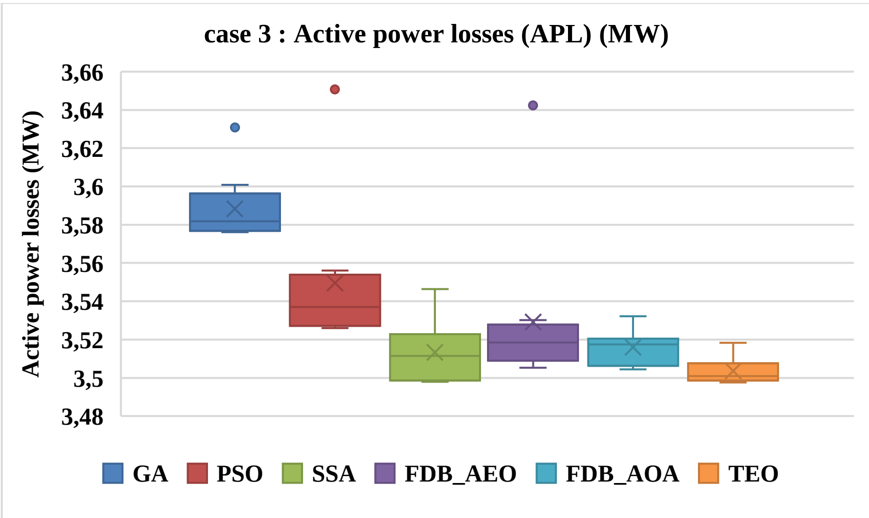

(d) case 3

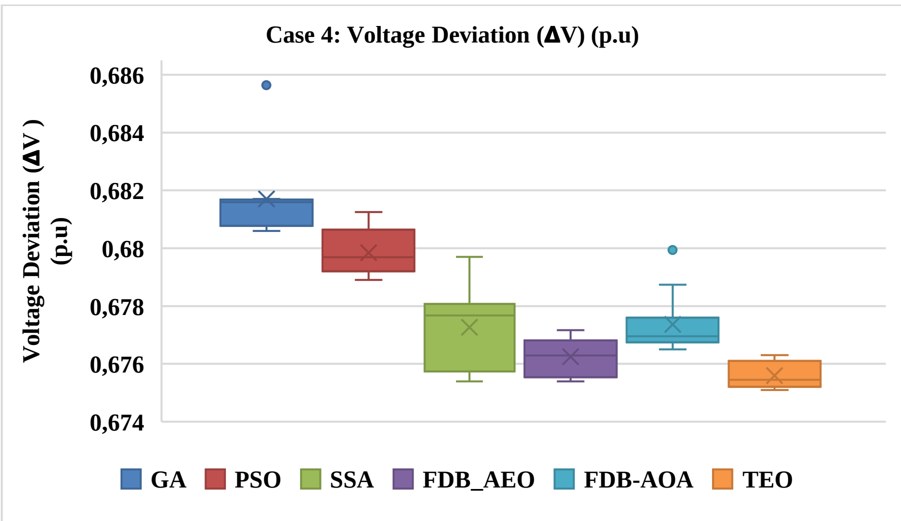

(e) case 4

Fig. 6.13: Boxplot of various fitness values for all algorithms and cases: Cases 1-4.

6.2.1.2. Multi-objective OPF problems (MOOPF)

In this section, we applied multi-objective metaheuristic methods for multi-objective OPF (MOOPF). The MOOPF has been employed to enhance the performance of practical power systems in terms of energy quality and operational security. A recent version of MOTEO has been applied to address various combined conflicting bi-objective functions. The performance of the proposed MOTEO has been verified and examined using the standard **IEEE 30-bus test system**. The results will be presented, analyzed, and discussed in the following

- **Results and discussions of dual-fitness function**

To evaluate the efficiency of the MOTEO method, its ability and particularity, a comparative study was conducted. The bi-dimensional Pareto fronts produced by MOTEO were compared with those generated by other algorithms, including IMOMRFO, DSC-MOAGDE, MSSA, MOPSO, and MOGA.

- **Case 5: Optimizing TFC and TEG simultaneously:**

The goal of this case is to optimize two fitness functions simultaneously: the TFC ($/h) and the TEG (ton /h), simultaneously. **Table (6.18)** compares the optimized-results obtained using MOTEO with those from other algorithms. The findings indicate that MOTEO delivers the most-effective total cost at **970.82189** $/h, outperforming other methods. The **figure (6.14)** shows the Pareto fronts generated by the proposed MOTEO method and other techniques.

Table. 6.18: Comparative of simulated dual-fitness function (TFC-TEG): Case 5: IEEE 30-bus.

P_{Gi} (MW)	**MOTEO**	**IMOMRFO**	**DSC-MOAGDE**	**MSSA**	**MSSA**	**MOPSO**	**MOGA**
P_{G1}	129.0920	123.6978	124.3816	129.7038	129.7038	119.5862	11h8.9466
P_{G2}	61.2001	73.7514	51.6604	56.7952	56.7952	65.9017	60.1173
P_{G5}	26.4864	19.9763	34.9932	30.7532	30.7532	28.2659	33.5915
P_{G8}	31.3122	27.5029	33.1353	30.2075	30.2075	33.1777	27.1607
P_{G11}	25.5441	22.2963	18.3483	21.9756	21.9756	25.5318	23.4719
P_{G13}	16.4142	23.0856	26.9306	20.4509	20.4509	17.1631	26.1024
Total cost ($/h)	**970.8219**	**979.5550**	**978.6653**	**971.84984**	**971.84984**	**973.0574**	**977.9700**
Emission gas (ton/h)	**0.26939**	**0.26886**	**0.26162**	**0.26894**	**0.26894**	**0.2579**	**0.2552**
Total fuel cost ($/h)	822.4796	831.5045	834.6016	823.7553	823.7553	831.0422	837.4416
Active power losses (MW)	6.6490	6.9104	6.0494	6.4862	6.4862	6.2264	5.9904
ΔV (p.u)	0.7091	0.6687	0.6691	0.7075	0.7075	0.7105	0.7112
CPU-time (sec)	30.7970	34.3546	32.7852	19.4735	19.4735	32.4147	29.9906

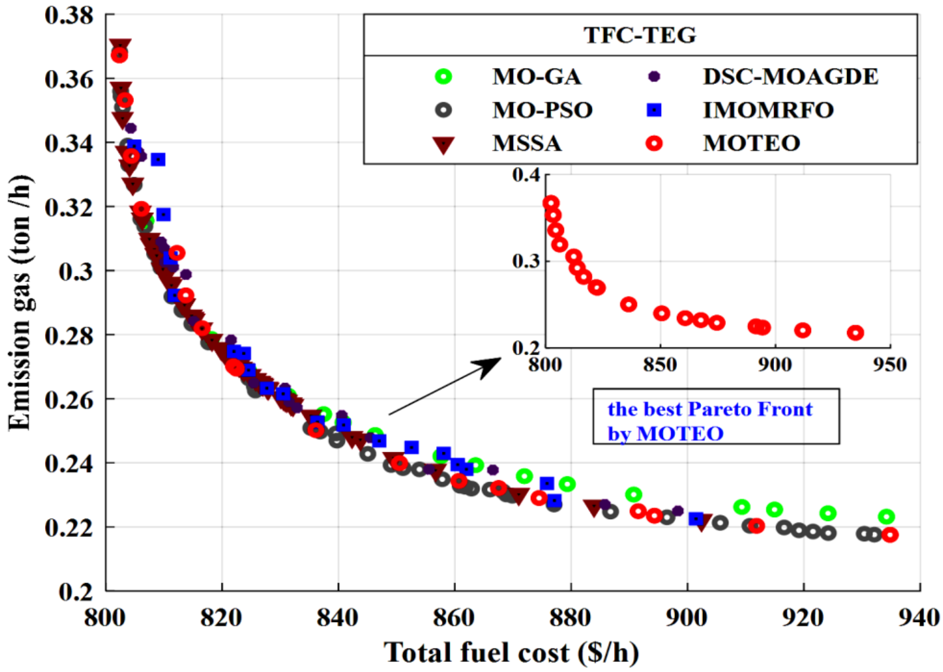

Fig. 6.14: The dual-dimensional Pareto front solutions for Case 5: IEEE 30-bus.

- **Case 6: Optimizing the TFC ($/h) and APL (MW) simultaneously: IEEE 30-bus**

This case study deals on optimizing of dual-fitness function the TFC ($/h) and APL (MW) simultaneously. The **figure (6.15)** illustrates the optimal solutions for the dual-dimensional Pareto fronts, which were generated by the MOTEO method as well as other comparative methods. The **table (6.19)** provides the simulated trade-off values for control variables, as achieved by the proposed MOTEO algorithm and other compared techniques.

Table. 6.19: Comparative of optimized dual-fitness function (TFC- APL): Case 6: IEEE 30-bus.

P_{Gi} (MW)	**MOTEO**	**IMOMRFO**	**DSC-MOAGDE**	**MSSA**	**MOPSO**	**MOGA**
P_{G1}	127.1674	122.3850	133.9546	117.4630	122.3352	132.7925
P_{G2}	47.6816	62.8179	49.4046	58.7366	58.4186	54.0488
P_{G5}	30.8446	28.4283	33.5581	34.9059	38.1387	32.7928
P_{G8}	35.0000	30.1119	22.4309	31.1443	34.4243	29.4633
P_{G11}	26.5488	22.8256	23.8560	21.8392	18.6077	17.3037
P_{G13}	22.2764	23.2041	26.7483	25.1411	17.4201	23.5788
Total fuel cost ($/h)	**828.9341**	**828.8290**	**829.317**	**838.8245**	**837.8367**	**824.4156**
Total emission gas (ton /h)	0.2631	0.2608	0.2740	0.2531	0.2595	0.2739
Active power losses (MW)	**6.1188**	**6.3728**	**6.5526**	**5.8302**	**5.9444**	**6.5799**
ΔV (p.u)	0.6770	0.6715	0.6720	0.7104	0.7038	0.7030
CPU-time (sec)	31.4976	32.1245	34.8751	18.6996	31.7991	31.7540

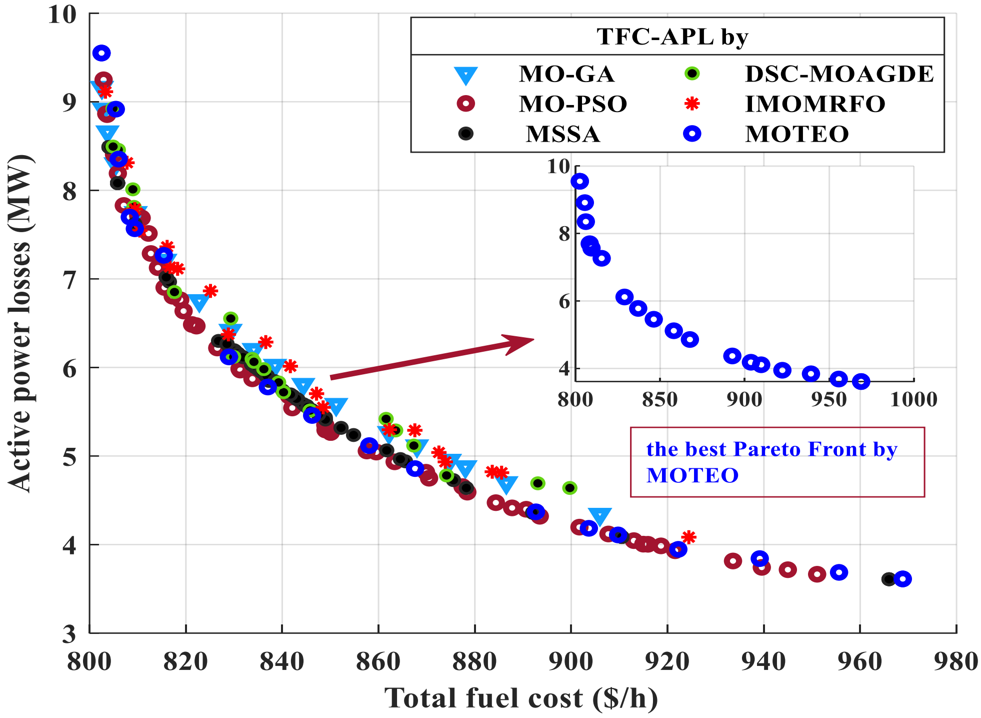

Fig. 6.15: The Dual-Dimensional Pareto front solutions for Case 6: IEEE 30-bus.

- **Case-7: optimizing the APL (MW) and the VD (p.u) simultaneously:**

This case focuses on examining the conflict tradeoff between Active Power Loss (MW) and Voltage Deviation (VD) (p.u). The statistical simulation results for this case are shown in the **table (6.19)**. The **figure (6.16)** displays the dual-Dimensional Pareto fronts created by the Thermal Emission Optimization (TEO) algorithm compared with other algorithms, where highlights a comparative analysis of the MOTEO against other metaheuristic algorithms.

Table. 6.20: Comparative of optimized dual-fitness function (APL and VD): Case 7

P_{Gi} (MW)	**MOTEO**	**IMOMRFO**	**DSC-MOAGDE**	**MOSSA**	**MOPSO**	**MOGA**
P_{G1}	57.1299	100.3876	108.5225	99.6784	74.0321	76.4181
P_{G2}	80.0000	63.2410	51.2789	73.6429	78.0799	75.9677
P_{G5}	50.0000	45.0850	49.6713	42.8278	49.1559	49.9982
P_{G8}	33.7980	26.5437	25.4817	26.6675	35.0000	34.4495
P_{G11}	26.2274	26.3753	22.7374	16.0669	11.5237	25.5862
P_{G13}	40.0000	26.5988	30.5887	29.8292	39.9856	25.1417
Total fuel cost ($/h)	959.9527	877.4701	885.3373	876.8233	933.8563	921.0733
Total emission gas (ton /h)	0.2235	0.2349	0.2421	0.2418	0.2331	0.2226
Active power losses (MW)	**3.7553**	**4.937**	**4.9856**	**5.3127**	**4.3772**	**4.1614**
ΔV (p.u)	**0.7198**	**0.7158**	**0.7129**	**0.7041**	**0.7022**	**0.7173**
CPU-time (sec)	30.7970	31.8754	32.8756	22.9968	32.8041	30.8146

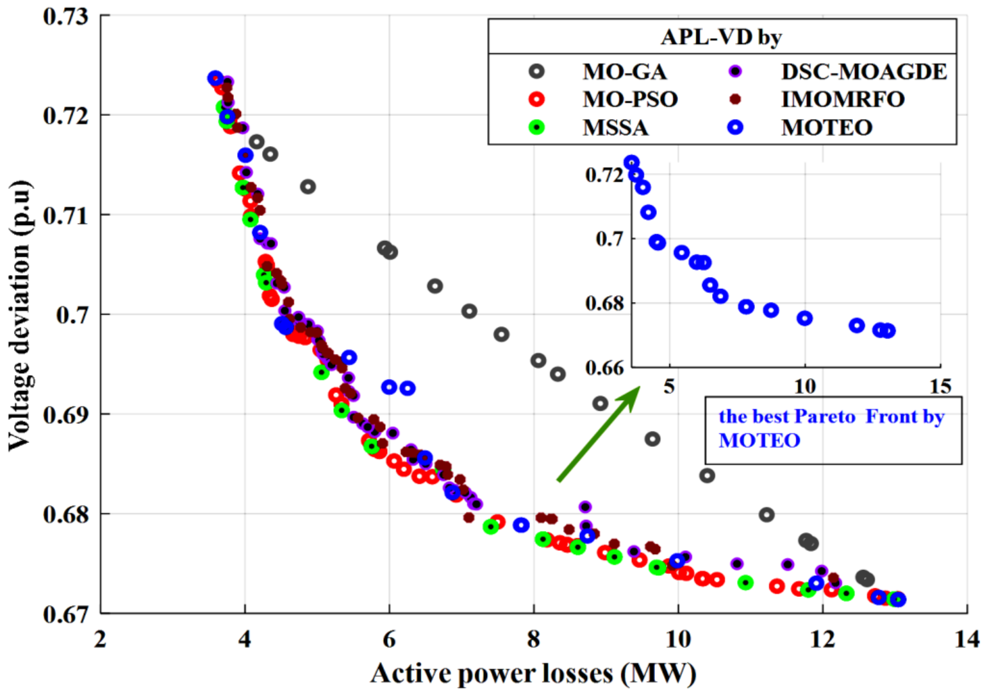

Fig. 6.16: The Dual-Dimensional Pareto front solutions for Case 7: IEEE 30-bus.

Table 6.20 provides a comparison of the optimized results achieved by the MOTEO method with those obtained from other techniques.

Table. 6.21: A comparative study between MOTEO with other metaheuristics algorithms.

Cases		MOTEO	IMOMRFO	DSC-MOAGDE	MSSA	MOPSO	MOGA
5	**TFC (\$/h)**	822.4796	831.5045	834.6016	823.7553	831.0422	837.4416
	TEG (ton/h)	0.26939	0.26886	0.26162	0.26894	0.25790	0.2552
	TFC (\$/h)	970.8219	979.5550	978.6653	971.8498	973.0574	977.9700
6	**TFC (\$/h)**	828.9341	828.8290	829.317	838.8245	837.8367	824.4156
	APL (MW)	6.1188	6.3728	6.5526	5.8302	5.9444	6.5799
7	**APL (MW)**	3.7553	4.937	4.9856	5.3127	4.3772	4.1614
	VD (p.u)	0.7198	0.7158	0.7129	0.7041	0.7022	0.7173

- **Discussion of results**

The simulation results focused on resolving the Multi-Objective Optimal Power Flow (MOOPF) problems, three cases were examined to simultaneously address two conflicting objective functions.

the **case 5 (IEEE 30-bus).**, investigate the Dual-fitness function concentrated on addressing to simultaneously the Total Fuel Cost (TFC) and Total Emissions Gas (TEG). As indicated in the **table 6.17**, the MOTEO algorithm achieved an optimal compromise solution with a TFC of **822.4796 \$/h** and a TEG of **0.26939 ton/h**. This resulted in a significantly reduced total fuel cost of **970.8218974 \$/h** compared to other algorithms. The **figure 6.14** illustrates the trade-off curve between total fuel cost and emissions gas produced by the MOTEO and other methods. It is evident that MOTEO provides the best Pareto optimal front with a highly uniform distribution.

the case 6 (IEEE 30-bus)., investigate the Dual-fitness function aimed to optimize the trade-off between the TFC and APL. According to the **table 6.18**, the optimal compromise solution achieved using the proposed MOTEO method is **828.9341 $/h** for TFC and **6.1188** MW for APL. The **figure (6.15)** illustrates the optimal Pareto front generated by MOTEO in comparison to other techniques. These solutions obtained cover a broader range of the entire Pareto front and exhibit a uniform distribution.

The **case 7 (IEEE 30-bus)**., investigate the Dual-fitness function focused to optimize the trade-off between Active Power Loss (APL) and Voltage Deviation (VD). **The table 6.19** displays the optimal compromise solution achieved by the TEO algorithm compared to other powerful optimize algorithms. The best results from MOTEO are **3.7553** MW for APL and **0.71982** p.u for VD. The **figure (6.16)** illustrates the dual-dimensional Pareto front distribution for this case, showing that MOTEO provides a more uniformly distributed Pareto optimal front than other algorithms.

These results indicate that the present MOTEO algorithm clearly highlight its superiority over other methods, including the MSSA. MOTEO consistently achieved the best compromise solutions for all cases, providing the highest and most uniformly distributed Pareto front. It also covered a wider range of fitness functions studied.

- **Case-8: optimizing three fitness functions: Total fuel cost, Total emission gas, and active power losses (IEEE 30-bus)**.

This case aims to validate the effectiveness of the presented method by optimizing three fitness functions simultaneously: Total Fuel Cost (TFC), total emission gas (TEG), and total power losses (APL). The **table (6.22)** provides a summary of the optimized results for the best compromise solutions. The **figure (6.17)** illustrates the three-dimensional Pareto fronts achieved by the MOTEO.

Table. 6.22: The best compromise solutions based Three-Dimensional Pareto fronts generated by the MOTEO.

P_{Gi} (MW)	**Best Total Fuel Cost**	**Best Active Power Losses**	**Best Emission Gas**	**best compromise solution**
P_{G1}	176.4878	51.9111	70.1690	113.8162
P_{G2}	48.8374	79.9957	71.4234	69.9688
P_{G5}	21.4310	49.9983	49.1068	35.1111
P_{G8}	21.9482	34.9973	34.6021	33.5876
P_{G11}	12.1969	29.9984	28.2083	24.7972
P_{G13}	12.0000	39.9968	33.8037	12.0000
Total fuel cost ($/h)	802.3607	968.5297	929.7806	**844.3766**
Emission gas (ton /h)	0.3665	0.2216	0.21929	**0.25262**
Active power losses (MW)	9.5012	3.4976	3.9134	**5.8808**
ΔV (p.u)	0.6829	0.7237	0.7219	0.6690
CPU-time (sec)	16.9921	17.2302	17.2861	37.1027

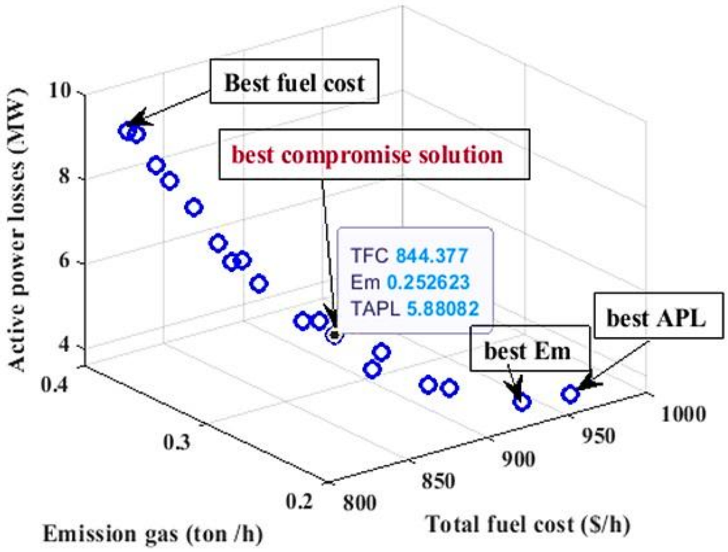

Fig. 6.17: The Three-Dimensional Pareto fronts based MOTEO: Case 8.

In this section, the Thermal Exchange Optimization (TEO) algorithm has been successfully adapted and applied to enhance solutions for both single and multi-objective OPF problems. it was implemented and validated on the standard IEEE 30-bus test system to optimize various fitness functions. Simulation results demonstrated that TEO can consistently produce the best solutions for all objective functions, with high accuracy and faster execution time than competitive algorithms. Additionally, the multi-objective version of TEO (MOTEO) was investigated for combined objective function OPF problems.

These results showed that the method could find near-global solutions by optimizing control variables related to the IEEE 30-bus test system. Overall, TEO proved to be highly effective in solving various single and multi-objective OPF problems.

6.3.2. Application 2.2: electrical Algerian DZA-114 bus transmission network

- **Overview of Algeria's Electrical Network:**

Algeria's electricity network comprises three main networks: the interconnected national network (RIN), PIAT, and isolated southern networks (RIS). These networks rely on electric energy production from gases, including diesel, steam, combined cycle, and hydropower stations.

The Algerian National Electricity Production Company (**SPE**) ensures the production of these networks. The Algerian Electricity Production Company (**SKTM**) was established in 2013 to build and operate these stations. RIN has 40 stations and covers the north of Algeria with electricity. PIAT has 28 gas turbine-interconnected power plants, covering large areas in the southwest. RIS is a group of isolated stations spread across 26 sites in the middle and far south of the Sahara, covering remote areas. The Algerian Electricity and Gas Company's 2020 report summarizes these networks. The **figure (6.18)** represents the Electrical network Algeria

Electricity in Algeria is generated from a mix of energy sources. The country relies on natural gas for the majority of its electricity generation, taking advantage of its vast natural gas reserves. Besides, Algeria has been increasingly investing in renewable energy sources, particularly solar and wind power, given its abundant solar potential across the vast Saharan area and wind potential in certain regions [149].

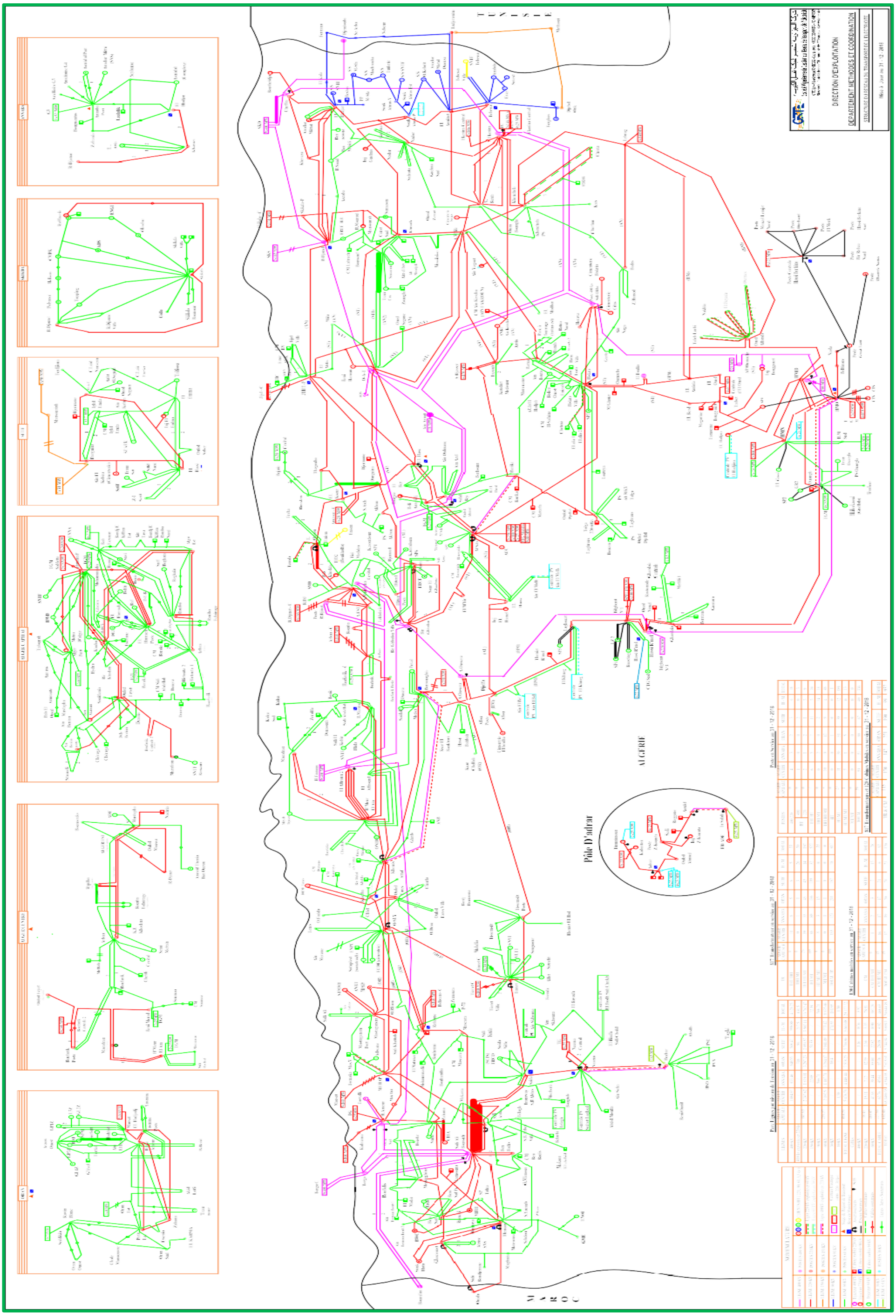

Fig. 6.18: Topology of the Algerian Network.

The **table (6.23)** represents the conventional power plants that make up the national electric power production park, with the various types of turbines and the installed capacities.

Table. 6. 23: Conventional National Electricity Generation Plants.

Region	Locality	Type	Installed Capacity (MW)
Alger	ALGER PORT	TG fixed	2x36 MW
	HAMMA2	TG fixed	2x209 MW
	BAB EZZOUAR	TG fixed	2x27 MW
	HAMMA	TG Mobile	2x24 MW
	SEBLLETE	TG Mobile	2x25 MW
	BARAKI	TG Mobile	3x24 MW
Blida	LARBAA	TG fixed	4x140 MW
	BOUFARIK1	TG fixed	4x24 MW
	BOUFARIK2	TG fixed	3x235 MW
	BOUFARIK3	TG Mobile	2x24 MW
	BENI MERED	TG Mobile	2x24 MW
Tipaza	AHMER EL AIN	TG Mobile	3x24MW
Boumerdes	RAS DJINET	TV	4x168 MW
Bejaia	AMIZOUR	TG Mobile	8x23 MW
	IGHIL EMDA	TH	2x12 MW
	DARGUINAH	TH	2x32,5+5,2 MW
Oran	MARSAT TV	TV	5x168 MW
	RAVIN BLANC	TV	1x73 MW
	ORAN EST	TG fixed	2x40 MW
	MARSET	TG fixed	8x23 MW
Rilizane	RILIZANE	TG fixed	3x155 MW
Tiaret	TIART1	TG fixed	4x30 MW
	TIART2	TG fixed	3x100 MW
Naama	NAAMA	TG fixed	8x23 MW
Jijel	JIJEL	TV	3x196 MW
	ERRAGUENE	TH	1x14,4 MW
	MANSOURIAH	TH	2x50 MW
Annaba	ANNABA	TG Fixed	2x36 MW
Skikda	SKIKDA	TV	2x131MW
Oum El Bougui	F'KRINA 1	TG Mobile	4x25 MW
	F'KIRINA2	TG Fixed	2x146 MW
Batna	AIN DJASSER 1	TG Fixed	2x126 MW
	AIN DJASSER 2	TG Fixed	2x132 MW
	AIN DJASSER 3	TG Fixed	277,5 MW
Khenchela	LABRAG	TG Fixed	3x140 MW
M'sila	M'SILA 1	TG Fixed	2x23 MW
	M'SILA 2	TG Fixed	3x100 MW

	M'SILA 3	TG Fixed	2x215 MW
	M'SILA 4	TG Mobile	12x24 MW
El Oued	EL OUED	TG Mobile	8x23 MW
Laghouat	TILGHEMT 1	TG Fixed	2x100 MW
	TILGHEMT 1	TG Fixed	3x197 MW
Hassi R'Mel	H.R. NORD	TG Fixed	4x22 MW
Ghardaïa	GHARDAÏA	TG Fixed	2x8,5 MW
Béchar	BECHAR	TG Fixed	4x6 MW
Adrar	ADRAR	TG Mobile	3x15MW+2x20MW+4x25MW
	ADRAR	TG Mobile	2x23 MW
	KABERTENE	TG Mobile	2x23 MW
	TIMIMOUN	TG Mobile	2x23MW+2x25MW
Ouargla	H.M.NORD 1	TG Fixed	5x24 MW
	H.M.NORD 2	TG Fixed	2x100 MW
	H.M.NORD 3	TG Fixed	3x220 MW
	H.M.S	TG Fixed	2x16+2x20 MW
	H.M.OUEST	TG Fixed	4x123 MW
	H.M.OUEST	TG Mobile	4x23 MW
	OUARGLA	TG Mobile	4x24 MW
Tamanrasset	IN SALEH ANCIENNE CENTRALE	TG Fixed	2x3,5 MW
	IN SALEH NOUVELLE CENTRALE	TG Fixed	
Biskra	OUMECHE2	TG Fixed	457 MW
Total	12019 MW		

- **Renewable Energies in Algeria:**

Algeria is committing to the path of renewable energies to provide comprehensive and sustainable solutions to environmental challenges and issues related to the conservation of fossil fuel energy resources. This commitment is demonstrated through the launch of an ambitious program for the development of renewable energies, which was adopted by the Government in February 2011, revised in May 2015, and designated a national priority in February 2016.

In this section of the program, the decision was made to install renewable energy capacity of approximately 22 MW by 2030 for the national market. Algeria positions itself as a major player in the production of electricity from photovoltaic and wind sources, incorporating biomass, cogeneration, geothermal, and beyond 2021, solar thermal energy. These sectors will be the drivers of sustainable economic development capable of stimulating a new model of economic growth. By 2030, 37% of the installed capacity and 27% of the electricity produced for national consumption will be of renewable origin. The **table (6.24)** represents the Development Plan for Renewable Energies (RE) in Algeria. The graph in **figure (6.19)** shows the percentage of renewable energy participation in Algeria [149] .

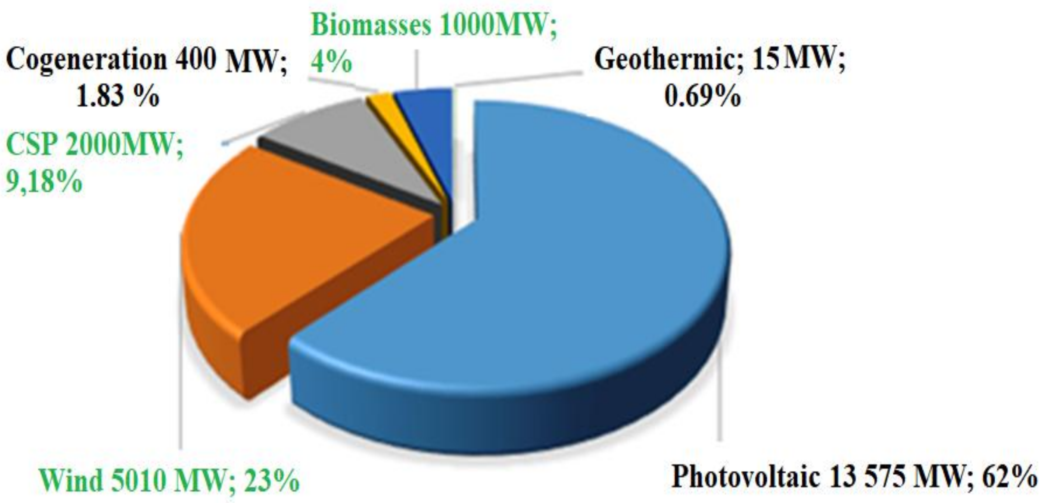

Fig. 6.19: Percentage of Renewable Energy Contribution in Algeria.

Table. 6. 24: The Development Plan for Renewable Energies (RE) in Algeria.

Sector	1st Phase 2015-2020	2nd Phase 2021-2030	TOTAL (MW)
Photovoltaic (MW)	3 000	10 575	13 575
Wind (MW)	1 010	4 000	5 010
CSP (MW)	–	2 000	2 000
Cogeneration (MW)	150	250	400
Biomasses (MW)	360	640	1 000
Geothermic (MW)	05	10	15
TOTAL	4 525	17 475	22 000

- **Electricity Transportation**

The overall length of the electricity transmission network to be constructed over the period 2021-2030 is about 20,296 km, adding to this a continuity of 12,744 km registered in the project. Therefore, by 2030, the total length of the electricity transmission network will reach 64,204 km, including 15,628 km at 400 kV, 25,516 km at 220 kV, and 22,442 km at 60 kV for a power of 98,540 MVA. The State of the Algerian Electricity Transmission Network can be seen in the **annex (B)**

- **Brief Description of Algerian Network DZA-114 bus:**

This section represents the study of the DZA-114 bus Algerian network very high and high voltage network (220 kV, 90 kV, and 60 kV), with a base power of 100 MVA and a frequency of 50 Hz. The system comprises 114 bus, 175 branches between it 160 lines, and 15 transformers, 15 generators bus (Refer to the **table (6.24)**). The bus N° 4 (MERSAT EL HADJADJ 1)) represents the reference bus. The requested active and reactive powers are 3727 MW and 2070 MVAR, respectively [150].

The others data of the test system including the cost and emission generator coefficients, and output generation power boundary limits are indicated in the **table (6.25)**. The detailed of the remaining network parameters can be found in **Annex C**.

Table. 6.25. The cost and emission coefficients of generator of DZA-114 bus.

bus n°	a ($/h)	b ($/MWh)	c ($/MWh)	γ .10^{-2}	β.10^{-4}	α.10^{-6}	ξ.10^{-4}	λ.10^{-2}	$P_{Gi}min$ (MW)	$P_{Gi}max$ (MW)
4	0	1,5000	0,0085	4.091	-5.554	6.49	2.0	2.857	135	1350
5	0	1,5000	0,0085	2.543	-6.047	5.638	5.0	3.333	135	1350
11	0	2,5000	0,0170	4.258	-5.094	4.586	0.01	8.0	10	100
15	0	2,5000	0,0170	5.326	-3.55	3.38	20.0	2.0	30	300
17	0	1,5000	0,0085	4.258	-5.094	4.586	0.01	8.0	135	1350
19	0	2,5000	0,0170	6.131	-5.555	5.151	10.00	6.667	34.5	3450
22	0	2,5000	0,0170	4.091	-5.554	6.49	2.0	2.857	34.5	3450
52	0	2,5000	0,0170	2.543	-6.047	5.638	5.0	3.333	34.5	3450
80	0	2,5000	0,0170	4.258	-5.094	4.586	0.01	8.0	34.5	3450
83	0	2,5000	0,0170	5.326	-3.55	3.38	20.0	2.0	30	300
98	0	2,5000	0,0170	4.258	-5.094	4.586	0.01	8.0	30	300
100	0	2,0000	0,0030	6.131	-5.555	5.151	10.00	6.667	60	600
101	0	2,0000	0,0030	2.543	-6.047	5.638	5.0	3.333	20	200
109	0	2,5000	0,0170	5.326	-3.55	3.38	20.0	2.0	10	100
111	0	2,5000	0,0170	6.131	-5.555	5.151	10.00	6.667	10	200

- **Results and discussion of the Algerian DZA-114 bus system**

To ensure a rational comparison, for all algorithms and all test cases are evaluated under the same conditions. The parameter settings for the investigated algorithms are provided in the **table (6.26)**. the results have been validated in article [151].

Table. 6.26: Internal parameters settings of the algorithms.

	Algorithm name	Parameters	Value
Single Objective	All algorithms	Population size	20
		Maximum iterations	200
	SSA	C1	[0, 1]
		C2	Rand ()
		C3	Rand ()

	FDB-AOA	The standard parameters of the algorithm	
	FDB-AGDE	The standard parameters of the algorithm	
	PSO	Local-weight (C1)	1.2
		Local-weight (C2)	1.4
		Inertia-Weight (w1)	0.5
		Inertia-Weight (w2)	0.9
	GA	Selection type	roulette
		Crossover	0.8
		mutation	0.14
Multi-Objective	All algorithms	Population size	30
		Maximum iterations	200
	MSSA	The same parameters of single-objective	
	IMOMRFO	The standard parameters of the algorithm	
	MOAGDE	The standard parameters of the algorithm	
	MOPSO	c1	1.2
		c2	1.4
		Beta	0.1
		Lambda	0.9
		w	1
		wdamp	0.95
	MOGA	The same parameters of single-objective	

For all cases, the simulation results including optimized control variables, total fuel cost, emission gas, active power losses, and voltage deviation for each case studied. The efficacy of the presented method is firstly evaluated by testing it on solving single-objective OPF problems, where considered as the fitness function as cases defined 1 to 4, respectively, outlined in the **table (6.27)**.

Table. 6.27: cases addressed in this research.

case n°	**fitness Functions**
case 1	Total Fuel Cost (TFC)
case 2	Total Emission Gas (TEG)
case 3	Active Power losses (APL)
case 4	Voltage Deviation (VD)
case 5	TFC and TEG simultaneously
case 6	TFC and APL simultaneously
case 7	APL and VD simultaneously

6.3.2.1. Results for single objective OPF: DZA-114 bus

The optimization results for single objective optimal power flow of the Algerian electrical transmission network have been displayed in in the **table (6.28).**

Table. 6.28: The optimized-results of the SSA on solving single objective OPF: DZA-114 bus.

Case n°	Basic case	**Case-1**	**Case-2**	**Case-3**	**Case-4**
P_{Gi} **(MW)**	**PF Results**	best total fuel cost	Best emission	best real power losses	best Voltage
P_{G4}	**685.7288**	439.85	276.3885	635.7388	456.9045
P_{G5}	**300.0000**	437.78	306.8064	322.6835	488.0436
P_{G9}	**160.0000**	89.744	99.5333	79.9867	82.5101
P_{G11}	**60.0000**	199.26	300.0000	98.3909	59.8197
P_{G15}	**640.0000**	419.81	362.1059	920.4699	966.6086
P_{G19}	**100.0000**	193	324.4990	225.2328	147.7499
P_{G22}	**60.0000**	189.24	223.3329	83.2238	74.7200
P_{G52}	**80.0000**	182.12	307.6514	60.7177	70.9815
P_{G80}	**100.0000**	188.82	333.5935	230.2072	200.8062
P_{G83}	**230.0000**	200.99	299.7223	136.1116	177.0300
P_{G98}	**100.0000**	190.14	278.8932	258.0908	256.3906
P_{G99}	**550.0000**	600	315.7833	395.4260	568.3707
P_{G101}	**360.0000**	200	198.5963	131.3668	158.3078
P_{G109}	**180.0000**	98.282	99.1130	61.8733	96.2336
P_{G111}	**200.0000**	188.61	113.2864	156.9999	15.3149
Total fuel cost($/h)	**20279.8971**	**19112.3865**	22449.1353	23540.5993	23285.2335
Emission gas (ton /h)	**7.2270492**	5.3525	**4.0842**	7.8162	8.2961
Active power losses (MW)	**78.7290**	90.6414	112.3054	**69.5197**	92.7918
ΔV (pu)	**5.9640**	5.5046	4.9024	4.8740	**4.6443**

Comparisons between others metaheuristic Algorithm for Single objective OPF (DZA-114 bus)

- **Case-1: Minimization of the total fuel cost (TFC):**

The first test-case selected the TFC as a fitness function. The **table (6.29)** displays the simulation results the presented technique compared with other techniques. The best value of best total fuel cost (TFC) is **19112.3865** $/h by SSA**.** It is confirmed that the proposed method achieved a best TFC compared to other techniques. The convergence behaviors for TFC minimization using the SSA, and using other methods are illustrated in the **figure (6.20).**

Table. 6.29: The optimized results of the presented method (SSA) with other methods: Case-1 (TFC).

P_{Gi} (MW)	**GA**	**PSO**	**FDB-AEO**	**FDB-AGDE**	**SSA**
P_{G4}	441.3542	444.7957	445.9433	450.9130	439.85
P_{G5}	98.6748	443.7174	448.1945	444.8310	437.78
P_{G9}	186.5285	99.1171	100.0000	100.0000	89.744
P_{G11}	442.5086	193.1787	185.8029	204.3595	199.26
P_{G15}	186.8243	428.6254	433.1015	431.2601	419.81

P_{G19}	192.4012	185.2617	178.8697	190.0207	193
P_{G22}	221.6163	184.9244	186.6244	180.6828	189.24
P_{G52}	177.5782	222.9960	219.4415	219.3801	182.12
P_{G80}	182.7515	178.0932	190.8652	174.7080	188.82
P_{G83}	184.9586	177.6919	185.7325	173.3296	200.99
P_{G98}	596.4143	179.4278	163.7683	172.5920	190.14
P_{G99}	197.9487	598.6572	600.0000	600.0000	600
P_{G101}	99.6190	199.9662	200.0000	199.9982	200
P_{G109}	181.0059	99.8857	99.9969	99.9874	98.282
P_{G111}	441.3542	183.2407	181.5148	176.6913	188.61
Total fuel cost ($/h)	**19143.79731**	**19119.7233**	**19117.9132**	**19114.6005**	**19112.3865**
Emission gas (ton /h)	5.3820	5.4199	6.3017	6.3027	5.3525
Active power losses (MW)	93.4329	92.5791	92.8554	91.7538	90.6414
ΔD (pu)	5.0269	5.0335	5.0327	5.0395	5.5046

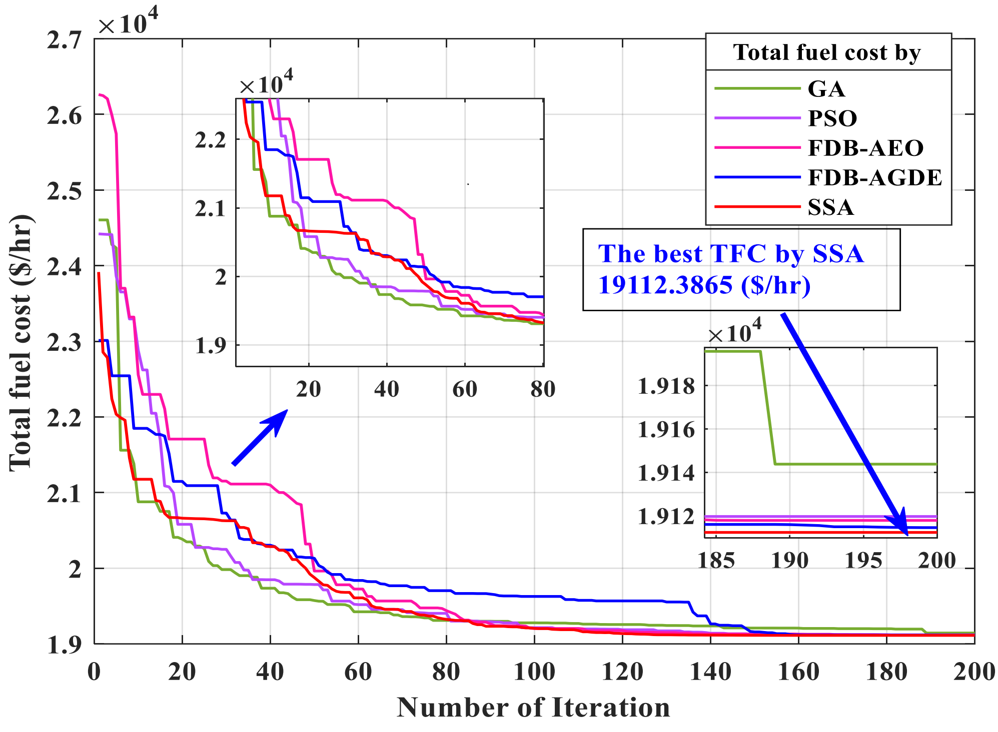

Fig. 6.20: Convergence behaviors Case-1 (TFC): DZA-114 bus.

- **Case-2: Minimization of total emission gas (TEG): DZA-114 bus**

For the second case, the fitness function selected is the **TEG**. The optimized results provided by the presented technique (SSA) compared with others are depicted in the **table (6.30)**. It is found that the proposed technique achieves also the best emission gas reduction with **4.0842** ton/h compared to other techniques. The convergence behaviors for TEG minimization using the proposed method and others methods are illustrated in the **figure (6.21).**

Table. 6.30: The optimized results of the presented method (SSA) with other methods: Case-2 (TEG).

P_{Gi} (MW)	GA	PSO	FDB-AEO	FDB-AGDE	SSA
P_{G4}	292.9974	248.2788	258.9893	251.3234	276.3885
P_{G5}	423.3632	428.5374	362.7838	355.2241	306.8064
P_{G9}	85.0514	91.7722	94.4987	81.2784	99.5333
P_{G11}	252.3854	276.4781	286.6390	291.9606	300.0000
P_{G15}	304.7992	365.8312	441.2171	472.2324	362.1059
P_{G19}	314.0827	310.9162	288.5013	293.0996	324.4990
P_{G22}	304.9745	231.7692	297.5242	228.3690	223.3329
P_{G52}	288.9326	295.6254	245.9000	260.7893	307.6514
P_{G80}	251.6559	301.2011	263.8524	283.4866	333.5935
P_{G83}	298.1651	269.7798	259.6053	277.1591	299.7223
P_{G98}	280.1524	261.8819	240.5429	270.4210	278.8932
P_{G99}	339.2441	354.3412	368.1259	315.3478	315.7833
P_{G101}	158.2305	170.1631	168.8416	179.6355	198.5963
P_{G109}	76.0399	83.0979	80.8053	94.4346	99.1130
P_{G111}	164.9440	146.1378	178.9827	184.1532	113.2864
Total fuel cost ($/h)	22147.14142	21881.50129	21560.9441	21879.11546	22449.13532
Emission gas (ton /h)	**4.3483**	**4.2880**	**4.2794**	**4.1860**	**4.0842**
Active power losses (MW)	108.0184	108.8114	109.8096	111.9143	112.3054
ΔV (pu)	5.0582	5.0403	5.0232	5.0148	4.9024

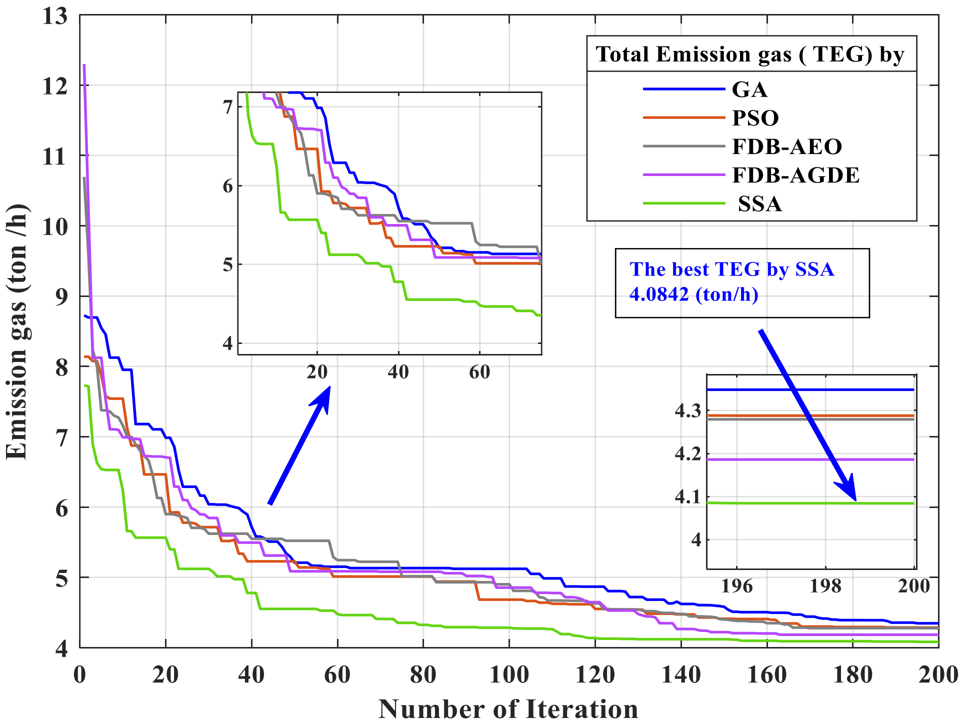

Fig. 6.21: Convergence behaviors Case-2 (TEG): DZA-114 bus.

- **Case-3: Total active power losses minimization (APL): DZA-114 bus**

The third fitness function investigated to reduce the total active power losses. The optimal simulation results provided using the proposed SSA and other techniques are shown in the **table (6.31).** It should be mentioned that the best optimal solution has been obtained by the presented method (SSA) with a value of **69.5197** MW. The **figure (6.22)** shows the convergence characteristics for total real power loss minimization using PSO, and GA methods.

Table. 6.31: The optimized results of the presented method (SSA) with other methods: Case-3 (APL).

P_{Gi} **(MW)**	GA	PSO	FDB-AEO	FDB-AGDE	SSA
P_{G4}	439.9458	365.7657	518.9781	452.1984	635.7388
P_{G5}	513.3839	599.6127	444.6349	361.8633	322.6835
P_{G9}	91.6856	80.5851	61.1502	18.8524	79.9867
P_{G11}	114.0715	88.1017	140.1536	184.1320	98.3909
P_{G15}	944.2857	943.3121	940.0917	747.0010	920.4699
P_{G19}	131.2056	185.9844	159.9486	337.7885	225.2328
P_{G22}	150.4902	133.8323	153.6974	166.3049	83.2238
P_{G52}	122.9086	73.6524	72.3336	236.2942	60.7177
P_{G80}	273.7247	211.2281	280.4907	262.8132	230.2072
P_{G83}	174.8377	163.7556	38.2410	208.1574	136.1116
P_{G98}	83.7452	151.9281	198.4820	174.9177	258.0908
P_{G99}	391.5079	460.5948	430.9463	237.1952	395.4260
P_{G101}	173.8566	110.7522	136.3748	188.1373	131.3668
P_{G109}	88.7510	74.3375	77.8514	21.7169	61.8733
P_{G111}	105.3903	153.5694	144.8830	200.0000	156.9999
Total fuel cost ($/h)	22868.33815	23056.962852	23218.00166	22649.36893	23540.5993
Emission gas (ton /h)	7.4308	7.7259	7.7117	6.6203	7.8162
Active power losses (MW)	**72.7904**	**70.0121**	**71.2574**	**70.3724**	**69.5197**
ΔV (pu)	4.8882	4.8860	4.8874	4.6924	4.8740

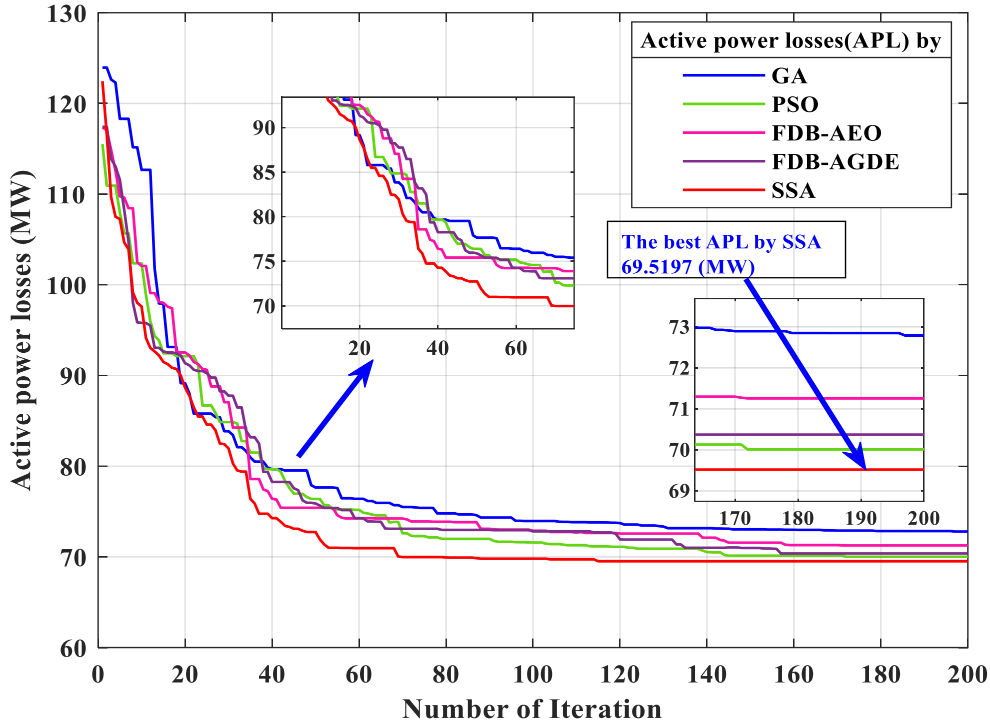

Fig. 6.22: Convergence behaviors Case-3 (APL): DZA-114 bus.

- **Case -4: Voltage deviation reduction (VD)**

The voltage deviation was selected as the fitness function in this case. The **table (6.32)** represents the details of comparison between the simulation results provided by the proposed SSA and other techniques. It can be noticed that the SSA method achieves the best optimum with a value of **4.6443 p.u**. Noting that the values obtained by all method are almost the same. The **figure (6.23)** illustrates the convergence characteristics for TVD minimization.

Table. 6.32: The optimized results of the presented method (SSA) with other methods: Case-4 (VD).

P_{Gi} (MW)	GA	PSO	FDB-AEO	FDB-AGDE	SSA
P_{G4}	458.3476	398.2230	329.3276	458.8286	456.9045
P_{G5}	457.7954	508.6369	595.9885	446.0468	488.0436
P_{G9}	83.9645	84.6882	82.3079	85.8415	82.5101
P_{G11}	61.4709	87.2995	72.4909	86.1745	59.8197
P_{G15}	992.5692	980.2919	972.6804	967.2426	966.6086
P_{G19}	150.7192	145.8350	147.7946	166.1033	147.7499
P_{G22}	104.7027	107.4142	126.5004	88.6974	74.7200
P_{G52}	80.9465	64.8533	66.8551	67.1451	70.9815
P_{G80}	220.4691	245.0874	251.2492	277.2997	200.8062
P_{G83}	147.4238	202.6802	163.4654	178.6827	177.0300
P_{G98}	290.5340	227.9015	285.8397	261.5302	256.3906
P_{G99}	526.2594	507.2536	475.5052	481.8673	568.3707

P_{G101}	118.9333	157.7361	160.6566	150.2857	158.3078
P_{G109}	87.4529	89.1487	79.4917	86.0436	96.2336
P_{G111}	36.8854	13.6114	11.7098	18.2385	15.3149
Total fuel cost ($/h)	23781.3285	23515.22777	24027.32688	23634.25748	23285.2335
Emission gas (ton /h)	8.2190	7.9801	8.0795	7.8533	8.2961
Active power losses (MW)	91.4739	93.6610	94.8630	93.0275	92.7918
ΔV (pu)	**4.6828**	**4.6497**	**4.6506**	**4.6577**	**4.6443**

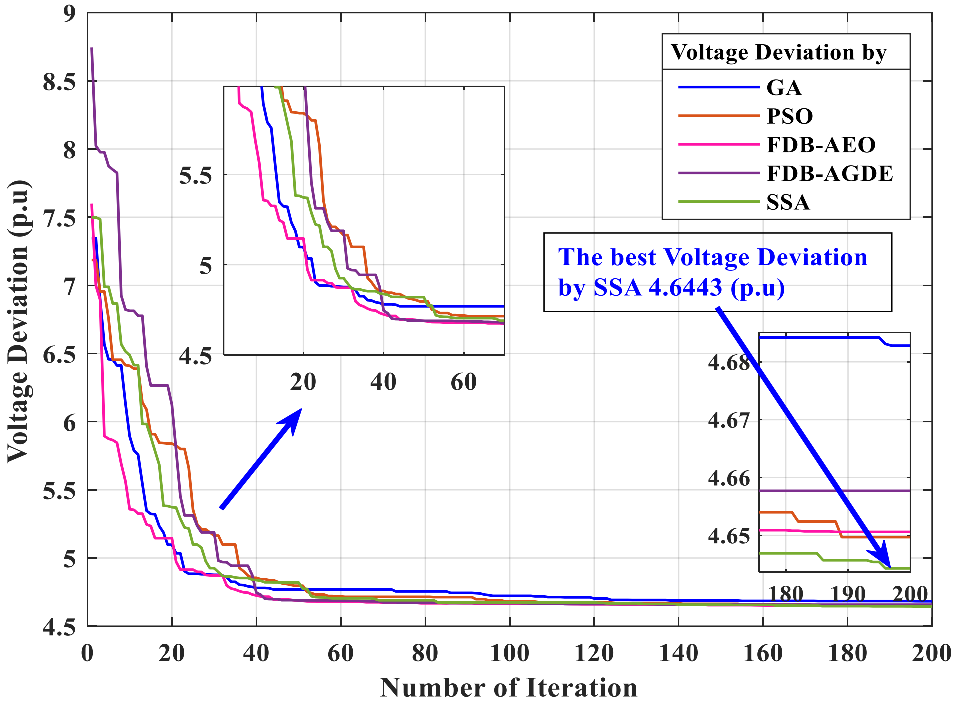

Fig. 6.23: Convergence behaviors Case-4 (VD): DZA-114 bus.

6.3.2.2. The multi-objective OPF problems for the Algerian electrical network

The multi objective version of MSSA has investigated to solve the multi-objective OPF problems. Three cases have been examined defined as cases (5–7), respectively, discussed in the **table (6.27)**, the optimization results of the two-dimensional Pareto fronts generated by the proposed algorithm obtained for all cases are presented in the **table (6.33)**.

Table. 6.33: The optimized-results of the MSSA on solving MOOPF problem: DZA-114 bus.

Case no	Basic case	**Case-5**	**Case-6**	**Case-7**
P_{Gi} **(MW)**	**PF Results**	best compromise solution	best compromise solution	best compromise solution
P_{G4}	**685.7288**	376.3970	536.2660	586.2689
P_{G5}	**300.0000**	400.0589	428.3914	304.4923
P_{G9}	**160.0000**	98.9196	95.9281	76.3598
P_{G11}	**60.0000**	207.8086	153.9687	142.2449

$\boldsymbol{P_{G15}}$	**640.0000**	391.3443	563.8197	904.1013
$\boldsymbol{P_{G19}}$	**100.0000**	219.9714	207.6193	146.9017
$\boldsymbol{P_{G22}}$	**60.0000**	200.4412	139.5627	101.9878
$\boldsymbol{P_{G52}}$	**80.0000**	211.0548	148.6944	82.0539
$\boldsymbol{P_{G80}}$	**100.0000**	214.4151	215.7726	224.0819
$\boldsymbol{P_{G83}}$	**230.0000**	248.3181	114.9111	135.5072
$\boldsymbol{P_{G98}}$	**100.0000**	261.1013	146.7918	217.3892
$\boldsymbol{P_{G99}}$	**550.0000**	514.7108	564.6631	566.5597
$\boldsymbol{P_{G101}}$	**360.0000**	197.6637	199.4248	179.7805
$\boldsymbol{P_{G109}}$	**180.0000**	98.0316	92.3123	81.1403
$\boldsymbol{P_{G111}}$	**200.0000**	179.0964	196.2229	72.3805
Total fuel cost ($/h)	**20279.8971**	**19663.4951**	**19563.5713**	22373.9327
Emission gas (ton /h)	**7.2270492**	**4.6691**	6.0573	7.8787
Active power losses (MW)	**78.7290**	92.3329	**75.5289**	**91.0956**
ΔV (pu)	**5.9640**	376.3970	4.8383	**4.7301**

- **Comparison between others metaheuristic Algorithm for MOOPF**

- **Case-5: Optimize TFC and TEG simultaneously: DZA-114 bus**

The objective of this case is to simultaneously optimize two fitness functions: the Total fuel cost (TFC) in $/h and the Total Emissions Generation (TEG) in tons/h. The **table (6.34)** displays the optimized results obtained by the MSSA compared with other algorithms. It is observed that the MSSA provides the best compromise solution, achieving **19663.4951 $/h** for TFC and **4.6691 tons/h** for TEG. The generated Pareto fronts are illustrated in **figure (6.24)**

Table. 6.34: Comparison of optimized bi-objective solution (TFC-TEG): Case-5: DZA-114 bus.

$\boldsymbol{P_{Gi}}$ (MW)	**MO-GA**	**MOPSO**	**IMOMRFO**	**MOAGDE**	**MSSA**
$\boldsymbol{P_{G4}}$	341.1615	352.8853	351.1319	350.5236	376.3970
$\boldsymbol{P_{G5}}$	363.6492	398.0214	412.0015	378.3374	400.0589
$\boldsymbol{P_{G9}}$	96.2389	89.2873	99.6348	92.7290	98.9196
$\boldsymbol{P_{G11}}$	252.0871	225.7332	240.2114	263.7530	207.8086
$\boldsymbol{P_{G15}}$	417.1490	385.6989	409.0640	398.1910	391.3443
$\boldsymbol{P_{G19}}$	234.1866	233.5706	236.8004	195.7241	219.9714
$\boldsymbol{P_{G22}}$	235.6544	263.6436	186.2104	246.5597	200.4412
$\boldsymbol{P_{G52}}$	236.6033	176.1026	223.5301	220.1493	211.0548
$\boldsymbol{P_{G80}}$	222.8752	259.8355	193.5673	240.7137	214.4151
$\boldsymbol{P_{G83}}$	238.2909	261.3794	265.3354	241.8408	248.3181
$\boldsymbol{P_{G98}}$	222.5384	228.7170	253.3185	209.2535	261.1013
$\boldsymbol{P_{G99}}$	507.5017	491.1026	514.6986	527.5233	514.7108
$\boldsymbol{P_{G101}}$	197.3107	198.1990	197.0012	198.7246	197.6637

P_{G109}	84.6380	95.2583	57.8604	94.5191	98.0316
P_{G111}	171.3355	162.2119	178.9214	161.5865	179.0964
Total fuel cost ($/h)	**19898.9615**	**20021.9075**	**19912.1748**	**19779.084**	**19663.4951**
Emission gas (ton /h)	**4.565**	**4.5943**	**4.7031**	**4.6428**	**4.6691**
Active power losses (MW)	91.0495	94.6467	92.2873	93.1287	92.3329
ΔV (pu)	4.8533	4.8659	4.8708	4.8710	4.8612

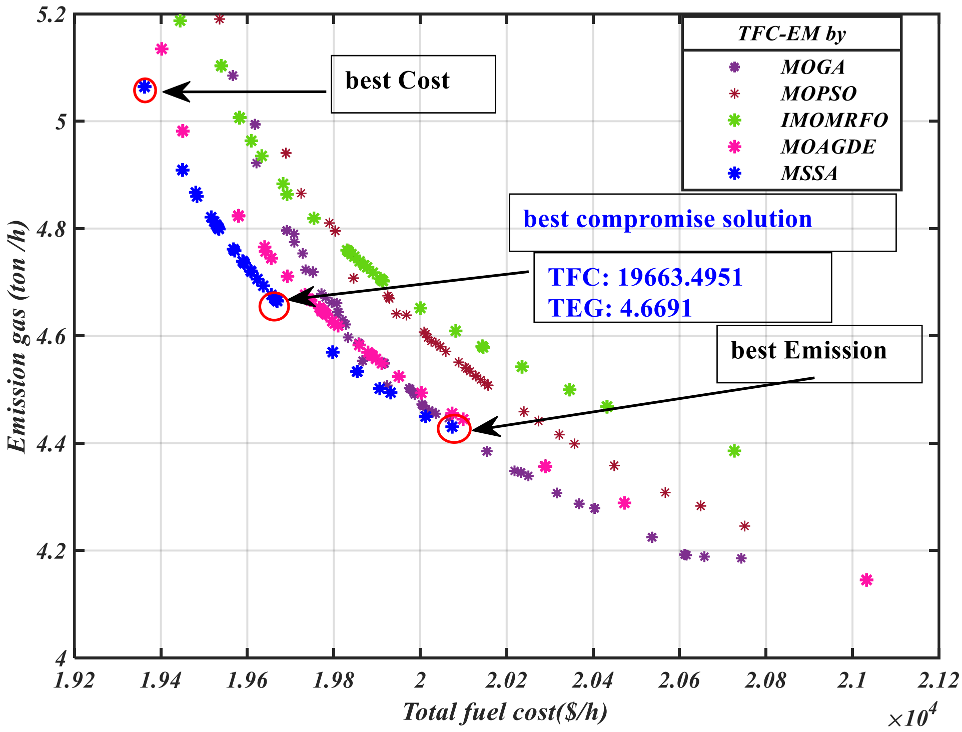

Fig. 6.24: Two-dimensional Pareto fronts Case-5 (TFC-TEG): DZA-114 bus.

- **Case-6: Optimize the TFC and APL simultaneously: DZA-114 bus**

In this case, the Total fuel cost (TFC) in $/h and the total active power loss (APL) in MW are optimized simultaneously. The optimal solutions for the two-dimensional Pareto fronts achieved by the presented algorithm and other algorithms are illustrated in the **figure (6.25).** The **table (6.35)** provides the optimized tradeoff values between TFC and total APL. It is observed that the MSSA provides the best compromise solution, achieving **19393.7583 $/h** for TFC and **76.1906 MW** for APL.

Table. 6.35: Comparison of optimized bi-objective solution (TFC-APL): Case-6: DZA-114 bus.

P_{Gi} **(MW)**	MOGA	MOPSO	IMOMRFO	MOAGDE	MSSA
P_{G4}	514.9751	487.37	517.0511	529.8159	529.2270
P_{G5}	430.7278	463.4	431.7238	415.9318	402.0877
P_{G9}	98.9073	89.597	99.6688	99.9163	95.3466

P_{G11}	194.2799	163.27	163.1303	156.1016	185.3201
P_{G15}	523.9212	506.5	556.3174	558.4663	525.4788
P_{G19}	221.3493	203.52	210.3420	211.2837	233.0956
P_{G22}	162.5432	187.42	160.6531	159.8023	170.7419
P_{G52}	124.4027	144.79	144.4622	141.5681	142.7965
P_{G80}	221.5734	190.65	221.1123	224.9465	183.9432
P_{G83}	125.9382	185.21	173.9254	146.5160	152.2240
P_{G98}	145.0677	164.89	123.2111	146.9919	141.8667
P_{G99}	544.2664	534.07	526.0238	521.0945	565.6298
P_{G101}	199.6169	199.55	199.9467	199.9153	199.8454
P_{G109}	99.4002	99.328	89.6315	99.2346	93.5034
P_{G111}	197.0861	186.03	187.0202	192.3325	183.9015
Total fuel cost ($/h)	**19484.5737**	**19356.5942**	**19581.4465**	**19593.5207**	**19393.7583**
Emission gas (ton /h)	5.7324	5.5919	5.7723	5.7777	5.8041
Active power losses (MW)	**77.0554**	**76.6318**	**77.2214**	**76.7720**	**76.1906**
ΔV (pu)	4.8363	4.8449	4.8444	4.8379	4.8475

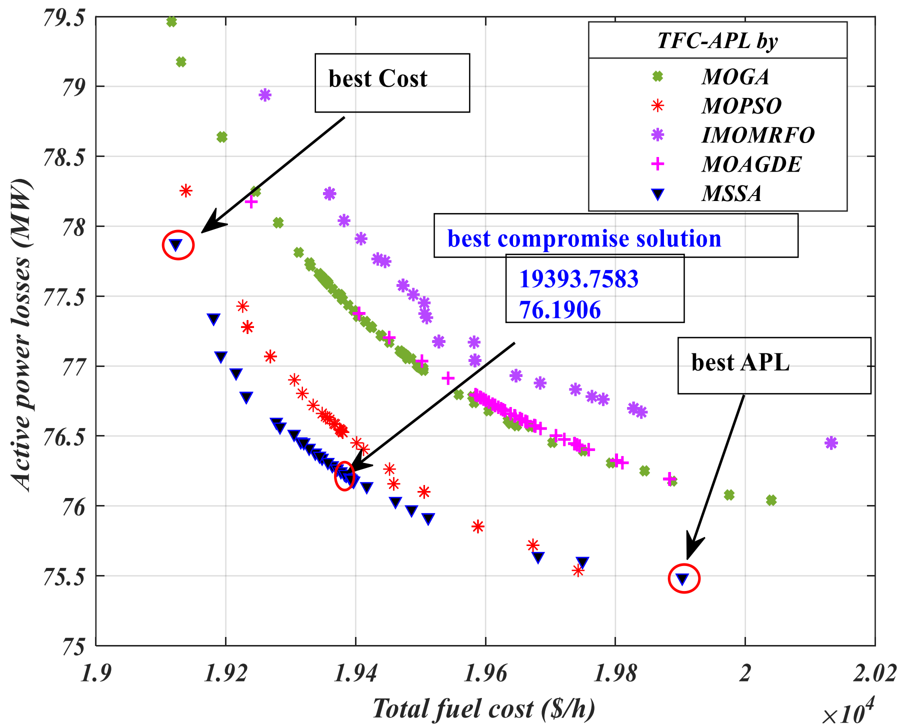

Fig. 6.25: Two-dimensional Pareto fronts Case-6 (TFC-APL): DZA-114 bus.

- **Case-7: Optimize the APL and the VD simultaneously: DZA-114 bus**

This case focuses on analyzing the conflict between Active Power Loss (APL) in MW and Voltage Deviation (VD) in p.u. The **table (6.36)** represents depicted a comparative between simulation results obtained by MSSA with other metaheuristics algorithms for this case. The **figure (6.26)** illustrates the dual-dimensional Pareto fronts generated by the presented algorithm compared to those produced by other algorithms.

Table. 6.36: Comparison of optimized bi-objective solution (APL- VD): Case-7: DZA-114 bus.

P_{Gi} (MW)	MOGA	MOPSO	IMOMRFO	MOAGDE	MOSSA
P_{G4}	652.6786	380.5321	207.7658	195.5304	586.2689
P_{G5}	384.5313	556.9589	675.7647	655.5226	304.4923
P_{G9}	73.5760	93.6420	78.6656	95.2020	76.3598
P_{G11}	67.1284	128.8260	201.8909	151.5610	142.2449
P_{G15}	886.5833	941.2603	900.4413	873.1600	904.1013
P_{G19}	178.5829	144.6802	139.1205	147.5389	146.9017
P_{G22}	95.5154	71.8696	126.6836	147.9902	101.9878
P_{G52}	74.9736	79.2930	69.0152	89.4171	82.0539
P_{G80}	334.3914	228.6215	260.2248	287.7941	224.0819
P_{G83}	100.6441	110.1968	126.6351	104.1777	135.5072
P_{G98}	244.9363	213.6323	205.3452	179.1073	217.3892
P_{G99}	426.8000	561.6052	493.4477	555.8767	566.5597
P_{G101}	156.1477	156.5885	170.2023	175.8986	179.7805
P_{G109}	87.1449	66.1375	86.4081	77.6831	81.1403
P_{G111}	86.1810	85.7691	78.5160	84.8655	72.3805
Total fuel cost ($/h)	23897.7036	22781.2813	2324.49867	22726.789393	22373.9327
Emission gas (ton /h)	8.0973	7.9829	7.6693	7.6220	7.8787
Active power losses (MW)	**95.9462**	**92.3661**	**93.2611**	**92.5576**	**91.0956**
ΔV (pu)	**4.9133**	**4.6779**	**4.7412**	**4.7464**	**4.7301**

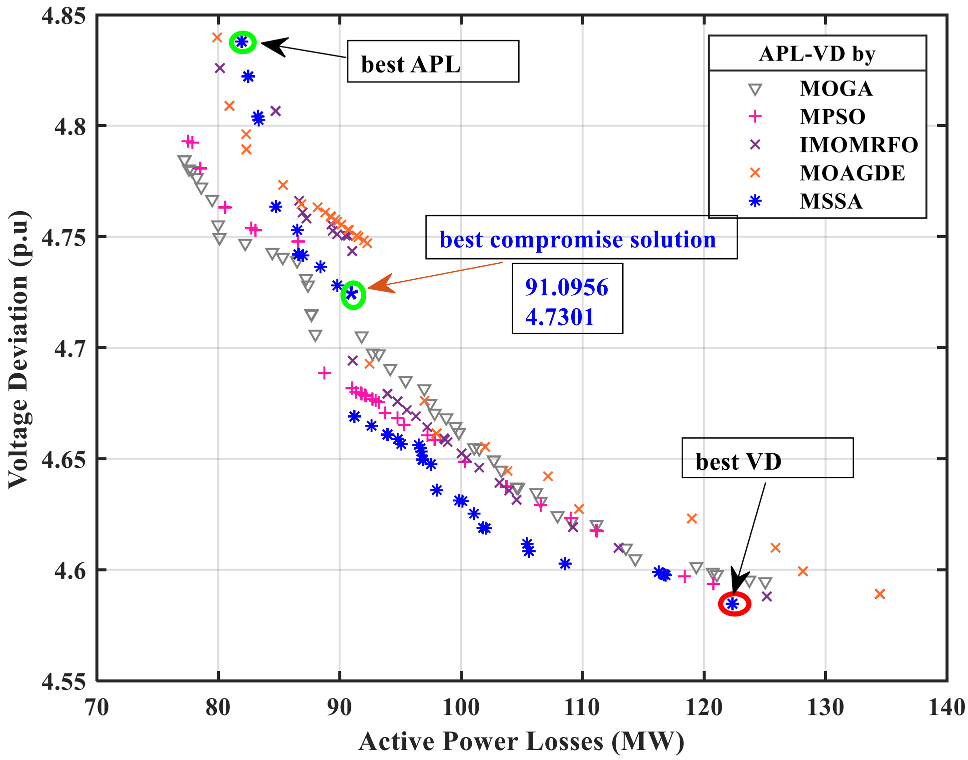

Fig. 6.26: Two-dimensional Pareto fronts Case-7 (APL-VD): DZA-114 bus.

Discussion of The Results of the DZA-114 bus

From improvement results of the optimization, which are mentioned in the **table (6.26)** (Case-1 to 4), it is found that the proposed proved with efficiently the ability for solving the single-objective OPF problem, can provided considerably to an optimum value when compared the optimized-values with the basic value for majority cases studied (without optimization).

Case-1: As can be seen from the **table (6.27)**, the proposed SSA is used to optimize fitness function contains a single goal which is the reduction of total fuel cost, the optimization results are presented in the **table (6.29) Case-1**, it can be observed that the proposed can be reduce the cost with a value **19112.3865 $/h** compared with the other optimization methods. The convergence behaviors are mentioned in the **figure (6.19)**, it can be seen that the SSA can be converge to the best solution.

Case-2: The proposed SSA is used to optimize fitness function minimization of total Emission Gas (**TEG**), the optimization results are presented in the **table (6.30) Case-2**, it can be observed that the proposed can reduce the TEG with a value **4.0842** ton/h compared with their value with the other optimization methods. The convergence behaviors are mentioned in the **figure (6.20**), where it can be seen that the SSA can converge to the best optimal solution**.**

Case-3: The reported method (SSA) is used to optimize the single fitness function OPF which contains the minimization of APL, the optimization results are presented in the from the **table (6.31) Case-3**, it can be observed that the proposed method can be reduced the APL with a value **69.5197 MW** compared with others algorithms. The convergence behaviors are mentioned in the **figure (6.21)**, it can be observed that the SSA algorithm converge to the best optimal solution**.**

Case-4: This case investigated to optimize of total Active power losses, the optimization results are presented in the from the **table (6.32) Case-4**, it can be observed that the proposed can be reduced the Voltage Deviation with a value **4.6443 p.u** compared with others algorithms. The convergence behaviors are mentioned in the **figure (6.22)**, it can be seen that the SSA can be converge to the optimal solution**.**

Case-5: As can be seen from the **table (6.34)**, MSSA is used to optimize a two-dimensional Pareto front, which incorporates both total fuel cost (TFC) and total emission gas (TEG) pairs. Noting the simultaneous optimization of this pair noticed, the best compromise solution with **TFC** value **19663.4951** $/h and **TEG** value **4.6691** ton/h, compared to the others methods, the

figure (6.23) shows the trade-off graphs of relationship between total fuel cost and emissions gas. It can be observed that the proposed algorithm is achieved the best optimal Pareto optimal front with a very uniform distribution compared then others algorithms.

Case-6, the bi-objective function focused to solve are two-dimensional Pareto fronts of the total fuel cost associated with the real power losses, the best compromise solution of this pair provided by the proposed are **19393.7583 $/h** of TFC value and **76.1906** MW of APL value, respectively, As can be seen from **the table (6.35)**. The **figure (6.24)** shows the optimal Pareto frontiers, which obviously the relationships between this pair. These solutions evenly cover the whole Pareto optimal front with a highest uniformity distribution compared then others algorithms. Where, it can be noticed that the two functions have contradictory objectives.

Case-7, the Pareto fronts of the bi-objectives function of real power losses with Voltage deviation. The **table (6.36)** displays the optimized-results for the best compromise solution with an APL value **91.0956** MW and VD value **4.7301** p.u. The **figure (6.24)** depicts the relationship between the two-dimensional Pareto Front solutions of this pair, it can be noticed that has a higher uniform distribution Pareto front, compared then others algorithms.

In this part, the so-named **Salp Swarm Algorithm** has been presented, and its performance has been demonstrated for solving the OPF problems with both types single and multi-objective in large scale (DZA-114 bus), which can be clearly observed the highest quality and precision from the improvement.

6.4. Application 3: Integration of Renewable energy and FACTS Devices

The integration of renewable energy sources (RES) into power grids, addresses challenges such as voltage fluctuations and power system security. supported by FACTS devices. This part presents **the contributes of this thesis,** it deals with FACTS devices compensation with the presence of renewable energies. Where taken a recent stochastic optimization algorithm called Fitness-distance balance-based (FDB-AOA) Archimedes Optimization Algorithm in solving the Optimal Power Flow (OPF) problems within a recently adopted state of the electrical transmission grid, which is the **modified IEEE 30-bus** test system, validated by an article **Erreur ! Source du renvoi introuvable.**[152]; and the modified Algeria electrical network **DZA-114 bus**, validated by an article [153];

It is worth noting that the satisfaction of power balance equations is crucial in ensuring the power flow convergence, in other words, it must be ensured the satisfaction of the equality constraints. The MATPOWER program is employed to calculate the dependent variables based on the Newton–Raphson method for power flow by taking the control variables as input. During the optimization process by MATLAB, The FDB-AOA algorithm used in this article has successfully achieved to the best results, as indicated by the comparison results obtained through other metaheuristics algorithms. Among the various inequality constraints, real power generators (excluding swing generator), taps transformer, generator bus voltages, and boundaries limits of each compensator's devices are the control variables. The optimization approach selects a viable value that falls within the boundaries for each of these variables. Active power of the swing generator, line capacities, load bus voltages, and reactive power generators are the states and controls variables [9].

6.4.1. Application 3.1: Application on the modified IEEE 30-bus test system

A new hybrid stochastic optimization algorithm called Fitness-distance balance-based (FDB-AOA) Archimedes Optimization Algorithm in solving the Optimal Power Flow (OPF) problems within a recently adopted state of the electrical transmission grid, which is the modified IEEE 30-bus test system.

The system includes the integration of both conventional thermal-based generating plant units incorporating uncertain and intermittent renewable energy sources, particularly wind energy generators, along with the addition of multi-type of Flexible AC Transmission System (FACTS) devices into the electrical grid escalates and evens the complexity of the (OPF) problem, mainly due to the irregularity of their performance. Several tests/cases are performed, A stochastic wind energy has been modeled utilizing appropriate suitable probability density functions. The optimization goal takes into account the cost of thermal generation, the direct cost of scheduled wind power, and the penalty cost for underestimating wind power. Additionally, the locations and sizing of the FACTS devices are optimized to reduce the generation cost, real power losses, and gross cost of the adopted test system.

- **Brief Description of the adopted IEEE 30-bus test system**

This part provides an overview of the essential data related to the modified IEEE 30-bus electrical transmission grid, where the two thermal generators located on buses 5 and 11 have been substituted with wind power plant generators. Additionally, FACTS devices like thyristor-controlled series compensators (TCSC), thyristor-controlled phase shifters transformer (TCPST), and static VAR compensators (SVC) – (two of each type) are optimally placed in the most suitable locations, and parameter setting of the device are obtained using metaheuristic optimization algorithms. Those are identified and represented with dotted lines in the diagram displayed of the topology the test system uses in this study in the **figure (6.27).** The **table (6.37)** represents a detailed data of this test system [8].

Table. 6.37: An overview characteristic of the adopted network: modified IEEE 30-bus test-system.

Element		quantity	Details
Buses-number		30	-
Branches-number		41	-
Thermal generators-number		6	**Slack-Bus is 1/** 2/ 8 and 13
capacitors-number		9	Buses number: 10 and 24
Wind generators -number		2	Buses number: 5 and 11
Transformer with tap changer		4	Branches number: 11- 12- 15, and 36
TCSC		2	Branches and sizing are optimized
TCPS		2	
SVC		2	Buses and sizing are optimized
Total power demand	**Active-power**	-	283,4 MW
	Reactive-power	-	126,2 MVAR
Load-buses		24	-
The voltage range of generators bus		6	[0,90–1,10] (p.u)
The voltage range of the load bus		24	[0,95–1,1] (p.u)

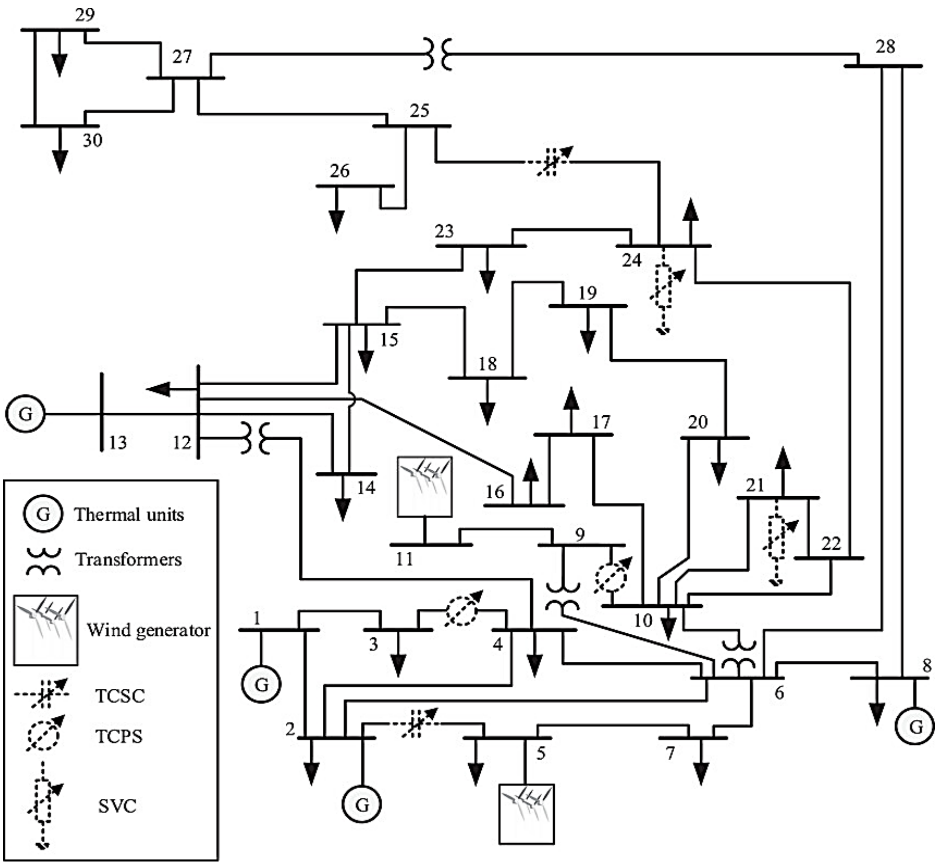

Fig. 6.27: Schema of the modified IEEE 30-Bus System.

6.4.1.1. Impact of Schedule Power and PDF Parameters on Wind Generation Costs

The **table (6.38)** displays the chosen Weibull shape (β), and scale (α) parameters for these newly implemented generators. Additionally, the total rated power value is provided for each wind power plant, also their cost coefficients [9].

Table. 6. 38: cost coefficients and PDF parameters for stochastic models of wind generators.

Windfarm Number of buses	**Number of turbines**	**Total Rated power, P_{wr}(MW)**	**PDF-parameters**		**Price coefficients ($/MWh)**		
			α	β	Direct,g_{wj}	Reserve,K_{Rwj}	Penalty, K_{Pwj}
WG_5 *(5)*	25	75	9	2	1,60	3,0	1,50
WG_{11} *(11)*	20	60	10	2	1,75	3,0	1,50

Wind frequency and Weibull fitting distributions shown in figures (6.28 (a), and 6.28 (b)) are acquired after 8000 Monte-Carlo scenarios run. This norm defines the design criteria for wind turbines and establishes the highest turbulent class IA that a turbine under which a turbine can be approved for operation, with a maximum yearly average wind speed at hub height of 10 m/s.

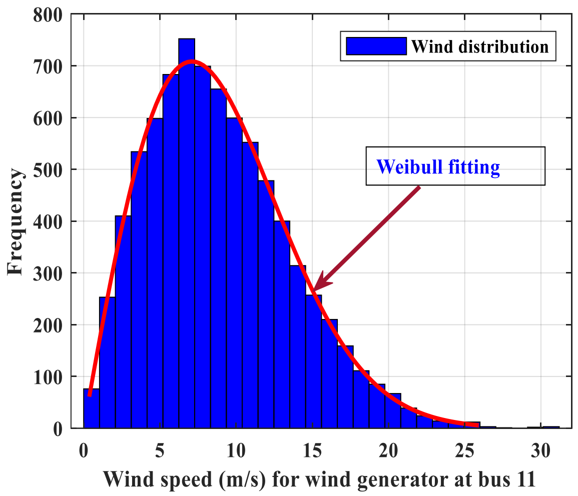

Fig. 6.28 (a): Wind speed distribution for wind farm1 at bus 5 (α = 9, β = 2).

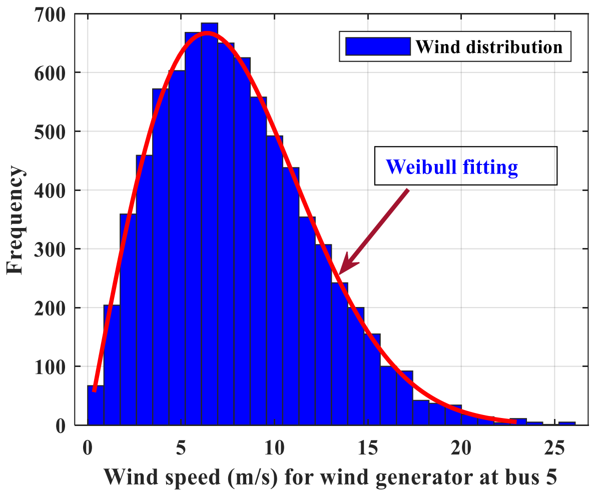

Fig. 6.28 (b): Wind speed distribution for wind farm 2 at bus 11 (α = 10, β= 2).

In order to investigate the fluctuation in generation costs of wind power, the first two study scenarios aim to analyze and test how the cost of generating wind power changes when the schedule power and PDF parameters are modified.

- **Scenario: 1 Scheduled power vs cost: modified IEEE 30-bus**

The Weibull probability density function (PDF) parameters utilized in this test align with those presented in **table (6.37)**. As well as the cost coefficients for wind power. It should be noted that the direct cost of wind is lower than the average cost of thermal power. Additionally, the penalty cost is lower than the direct cost. The scheduled power ranges from [0 to the rated power] of the wind farm, and the variations of reserve, direct, penalty, and total costs are plotted in the **figures (6.29 (a) and (b))** for the both wind farms. The total price is the summation of those costs associated with the scheduled power. The direct cost shows a linear relationship with the scheduled power. With an augmentation in the scheduled power, there is an accompanying elevation in the requisite spinning reserve, resulting in an upsurge in the reserve cost, and consequently, an escalation in the total generation cost. The penalty cost was appropriately reduced, but at a slower rate, with the amplification in the scheduled power.

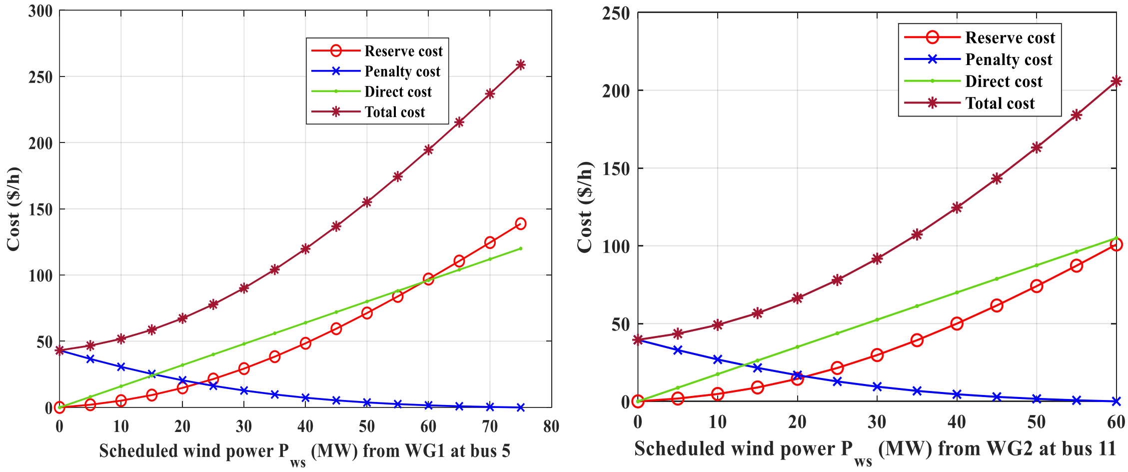

(a) WG1(bus 5) **(b)** WG2(bus 11)

Fig. 6.29: Variation of wind power cost vs scheduled power for wind generator (a) WG1, (b) WG2.

- **Scenario 2: Probability density function parameter vs cost: modified IEEE 30-bus**

Here, the scale (α) of Weibull distribution is varied while the shape parameters is constant ($\beta = 2$). The main goal was to see how it affects any changes in costs to the costs of wind power generator for a predetermined arbitrarily chosen schedule power. A scheduled power with value of 25 MW is fixed on the WG1 (5), while for the WG2 (11) was a 20 MW, which is about one-third of its installed capacity. The cost coefficients are the same as in **Scenario 1**. The **figures (6.30 (a)** and **(b))** illustrate the cost-to-scale factor curves for wind farm 1 and 2. The overall minimum cost is around the middle range of scale parameters. With a rising in the scale parameter, the wind speeds probability also increases at their higher value. If scheduled power is maintained, the penalty costs increase, resulting in an increase in the overall power cost. After a certain value of scale parameter, the reserve cost won't go down as much is not significant.

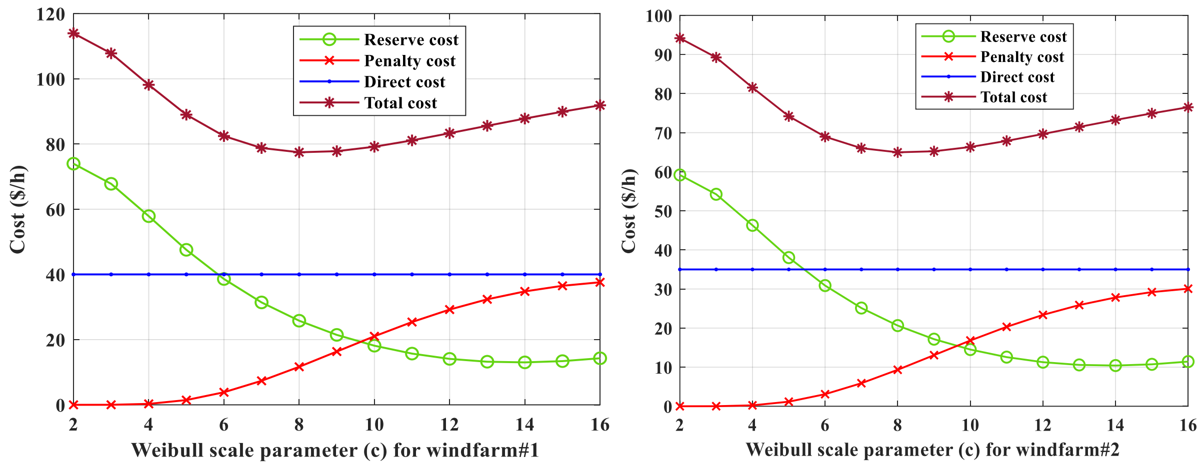

(a) windfarm#1 (bus 5) **(b)** windfarm#2 (bus 11)

Fig. 6.30: Variation of wind power cost (a) windfarm#1, (b) windfarm#2: modified IEEE 30-bus.

Case studies, Numerical Simulation results, discussion, and comparisons

Several case studies have been conducted on the electrical network, summarized in the **table (6.39)**. Each optimization case study includes a maximum of 500 iterations in a single run of the algorithm and is repeated 20 times.

Table. 6.39: Summary of all the cases addressed in this study: modified IEEE 30-bus.

Case number	Case explanation	Equation number
Case 1	Minimize generation cost ($\boldsymbol{C}_{\mathbf{gen}}$ **($/h)**)	Eq (4.26)
Case 2	Minimize real power loss ($\boldsymbol{P}_{\mathbf{Loss}}$ **(MW)**)	Eq (4.28)
Case 3	Minimize gross cost ($\boldsymbol{C}_{\mathbf{gross}}$ **($/h)**)	Eq (4.32)

This section is divided into two subsections. The **first subsection** of study cases aims to assess the effectiveness of the proposed algorithm (FDB-AOA) for determining the optimal placement and size of FACTS devices in the modified IEEE 30-bus system. The **second subsection** involves a comparative study, where the proposed algorithm is compared with other methods mentioned in the references [9], like SHADE, MSA, ABC to demonstrate the superiority of this algorithm and their effectiveness for solving the OPF problems.

It is worth noting that the optimization problem involves 27 state and control variables, including the current settings of FACTS devices (SVC, TCSC, and TCPS). Each FACTS device has two control variables: one for location and one for device rating. During the optimization process, the allocation variable indicates either the bus or branch number depending on the FACTS device type, with the nearest integer value used for power flow studies. The parameter values were determined through extensive trials, with careful selection of population sizes and iterations. Each algorithm was run independently 60 times for each case study to record the optimal outcomes and corresponding parameters. The **table (6.40)** presents the cost and emission coefficients of the thermal generators in the modified IEEE 30-bus system.

Table. 6.40: Price and emission coefficients of the modified IEEE 30-bus.

Generator	Bus	a	b	c	d($/h)	e(rad/MW)	α	β	γ	w	μ
T_{G1}	1	0	2	0.00375	18	0.037	4.091	-5.554	6.49	0.0002	2.857
T_{G2}	2	0	1.75	0.0175	16	0.038	2.543	-6.047	5.638	0.0005	3.333
T_{G8}	8	0	3.25	0.00834	12	0.045	5.326	-3.55	3.38	0.002	2
T_{G13}	13	0	3	0.025	13.5	0.041	6.131	-5.555	5.151	0.0001	6.667

6.4.1.2. Optimization Results of Modified IEEE 30-bus Power System

This section details the simulation results achieved by applying the proposed FDB-AOA algorithm on the modified IEEE 30-bus system. It is organized into two detailed subsections:

A. Subsection One: Study results of FBD-AOA algorithm: modified IEEE 30-bus

This part is dedicated to confirming and evaluating the efficiency of the reported approach, FDB-AOA in solving OPF problems on the modified IEEE 30-bus system. The optimization results of all cases studied are tabulated, explanted, discussed and analyzed in this subsection.

For all test cases, the simulation results include the optimal settings of control variables, total fuel cost, total emission gas, active power losses, gross cost, voltage deviation, and the positions and ratings of FACTS devices. The **table (6.41)** details the parameters that led to the optimization of the network for each objective function across all trial runs. This includes the optimized control variables, locations, and sizing of FACTS devices, as well as the bus and branch numbers where connections are specified. Specifically, it lists the buses connected to SVCs and the branch numbers designated for TCSC and TCPS. FACTS devices are frequently utilized in power systems to enhance their loading capacity, particularly in those that are operating at or close to their maximum capabilities.

In Case 1, wherein the aim is to minimize the fitness function generation cost **(C_{gen} ($/h)** in Eq (4.26), the reported algorithm can be successful favorable results with a cost value of **806.9817 $/h.** Wind power plant generators are scheduled more frequently than thermal units due to their lower costs. However, scheduling wind generators at their maximum capacity is impractical as it increases reserve costs due to insufficient wind power to maintain scheduled output over long periods. The large inductive load means SVCs often operate at or near maximum capacity. Bus 21 and bus 24 identified as the optimal locations for the SVCs. The optimal branches for TCSC and

TCPS are 2, 35, 9, and 14, respectively. FACTS devices are often installed in networks to enhance loading capability.

In Case 2, the goal is to minimize real power loss ($\boldsymbol{P}_{\mathbf{loss}}$ **(MW)** as defined **in Eq (2.28)).** The FACTS devices' allocation and rating is optimized to enhance the capacity of network to its maximum. Due to that, the proposed algorithm attained a favorable result with a real power loss of **1.7619 MW**. The scheduling outcomes of wind generators are commonly more than those of thermal units due to their lower costs. In this scenario, the optimal locations for the two SVCs are at buses 24 and 21. Additionally, the most suitable branches for connecting the TCSC and TCPS are identified as branches 14, 25, 35, and 13, respectively.

In **Case 3**, where the primary objective is to minimize the gross cost ($\boldsymbol{C}_{\mathbf{gross}}$ **(\$/h) (Eq (2.32))**). This objective highlights the crucial importance of combining both cost and loss considerations into a single objective function. One of a simple way to achieve this is the creating a cost model that incorporates the converted energy cost equivalent of the loss. Cost converted of power losses considered in this work is which is 0.10 dollars per kilowatt-hour (**0.10 \$/kWh**). The fitness function of $\boldsymbol{C}_{\mathbf{gross}}$ can be explanted by the following expression:

$$C_{\text{gross}} = C_{\text{gen}} + P_{\text{loss}} \times 10^3 \times 0.10,$$

Here, P_{loss} is in MW and C_{gen} is determined as the given in equations. (9 and 5).

The optimal gross cost achieved by the proposed method is **1104.6652 \$/h**. In case 3, the combined optimal generation cost and loss cost depend on the price coefficients for both wind and thermal power generators, as well as the unit price of energy. Considering both objectives together results in a reduced gross cost. The scheduling outcomes show wind power generators are used more than thermal units. The optimal locations for the two SVCs are buses 21 and 24. The best branches for connecting the TCSC and TCPS are numbers 25, 34, 35, and 1.

Table. 6.41: the optimized results utilizing FBD-AOA: modified IEEE 30-bus.

Control variables	Min	Max	Case 1	Case 2	Case 3	Parameters	Min	Max	Case 1	Case 2	Case 3
P_{TG2}(MW)	20	80	40.4124	24.8067	39.5208	$\mathbf{P_{TG1}}$ **(MW)**	50	200	134.90801	50.35643	50.0
P_{WG5}(MW)	0	75	49.6771	75.0000	75.0000	$\mathbf{Q_{TG1}}$ **(MVAr)**	- 20	150	2.45649	-3.78806	-1.71349
P_{TG8}(MW)	10	35	10.0000	35.0000	35.0000	$\mathbf{Q_{TG2}}$ **(MVAr)**	- 20	60	16.89724	8.14154	10.90263
P_{WG11}(MW)	0	60	41.9307	60.0000	60.0000	$\mathbf{Q_{WG}}$ **(MVAr)**	- 30	35	24.67725	21.81749	22.43517
P_{TG13}(MW)	12	40	12.0000	40.0000	25.7542	$\mathbf{Q_{TG8}}$ **(MVAr)**	- 15	48.7	31.10329	30.50151	34.46611
V_1(p.u)	0.95	1.10	1.0741	1.0555	1.0599	$\boldsymbol{Q}_{\mathbf{WG11}}$**(MVAr)**	- 25	30	22.82884	22.63942	21.58632
V_2(p.u)	0.95	1.10	1.0592	1.0497	1.0547	$\mathbf{Q_{TG13}}$ **(MVAr)**	- 15	44.7	18.95830	26.11189	17.47834
V_5(p.u)	0.95	1.10	1.0374	1.0399	1.0438	$\boldsymbol{C}_{\mathbf{gen}}$ **(\$/h)**			806.9817	939.2806	917.1625
V_8(p.u)	0.95	1.10	1.0370	1.0451	1.0477	$\boldsymbol{P}_{\mathbf{Loss}}$ **(MW)**			5.5280	1.7631	1.8750

V_{11}(p.u)	0.95	1.10	1.0905	1.0870	1.0851	**C_{gross} ($/h)**	1359.7817	1115.5871	1104.6652
V_{13}(p.u)	0.95	1.10	1.0746	1.0825	1.0723	**V-D (p.u)**	0.89944	0.90793	0.92337
T_{11}(p.u)	0.90	1.10	1.0285	1.0232	1.0186	**Emission (ton/h)**	0.21356	0.14176	0.14188
T_{12}(p.u)	0.90	1.10	0.9465	0.9422	0.9405	**stability index**	0.139333	0.135576	0.1383147
T_{15}(p.u)	0.90	1.10	0.9945	1.0134	1.0060				
T_{36}(p.u)	0.90	1.10	0.9644	0.9890	0.9785				
FACTS rating						**FACTS placement**	**Case 1**	**Case 2**	**Case 3**
$\tau_{TCSC\ 1}$(%)	0	50%	25.71	50	15.43	**TCSC-1 branch, (con. buses):**	2, (1-3)	14, (9–10)	25, (2–5)
$\tau_{TCSC\ 2}$(%)	0	50%	49.81	20.94	50	**TCSC-2 branch, (con. buses):**	35,(25–27)	25, (10–20)	34, (25–26)
Φ_{TCPS1} (deg)	- 5°	5°	1.2688	4.2024	2.7135	**TCPS-1 branch, (con. buses):**	9, (6–7)	35, (25–27)	35, (25–27)
Φ_{TCPS2} (deg)	- 5°	5°	2.3059	1.3130	0.6170	**TCPS-2 branch, (con. buses):**	14, (9–10)	13, (9–11)	14, (9–10)
Q_{SVC1} (MVAr)	- 10	10	7.5888	9.6699	10.0000	**SVC-1 bus no:**	21	24	21
Q_{SVC2} (MVAr)	- 10	10	9.9955	9.9999	9.8752	**SVC-2 bus no:**	24	21	24

The bar chart graph illustrated in the **figure (6.31)**, represents the active power of the generators, excluding the slack generator, for each Case (1 to 3). Additionally, bar chart graph illustrates in the **figure (6.32)** represents the generator bus voltages and taps transformer (in p.u) for each case, also depicts the permissible intervals of control variables and their corresponding values for achieving optimal solutions for each objective function.

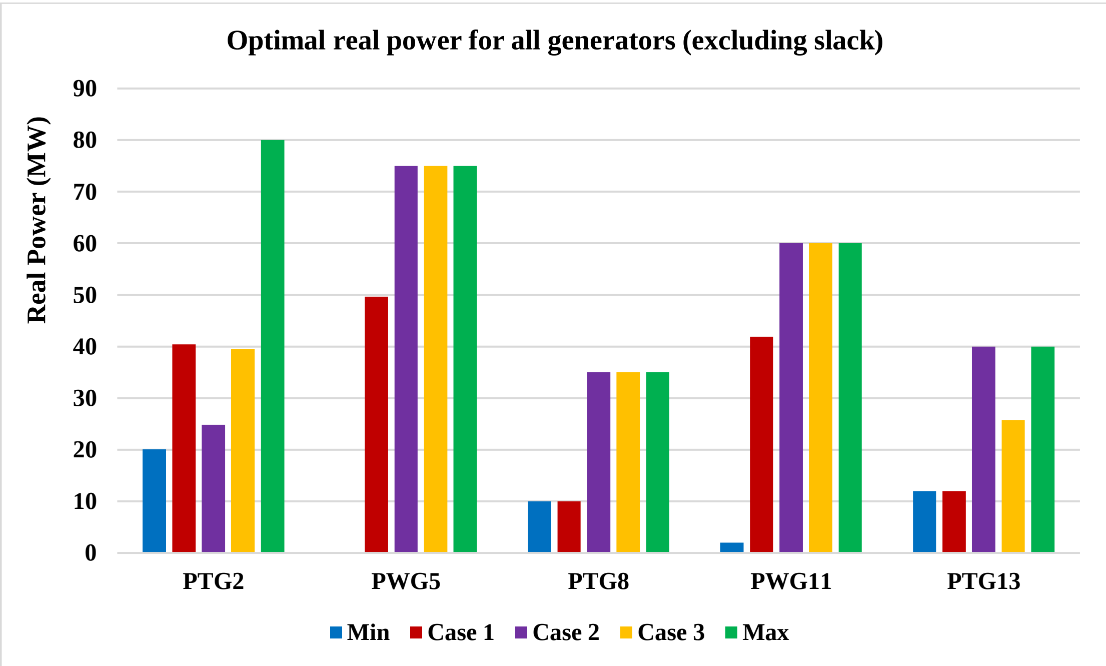

Fig. 6.31: Optimal real power for all generators (excluding slack): modified IEEE 30-bus.

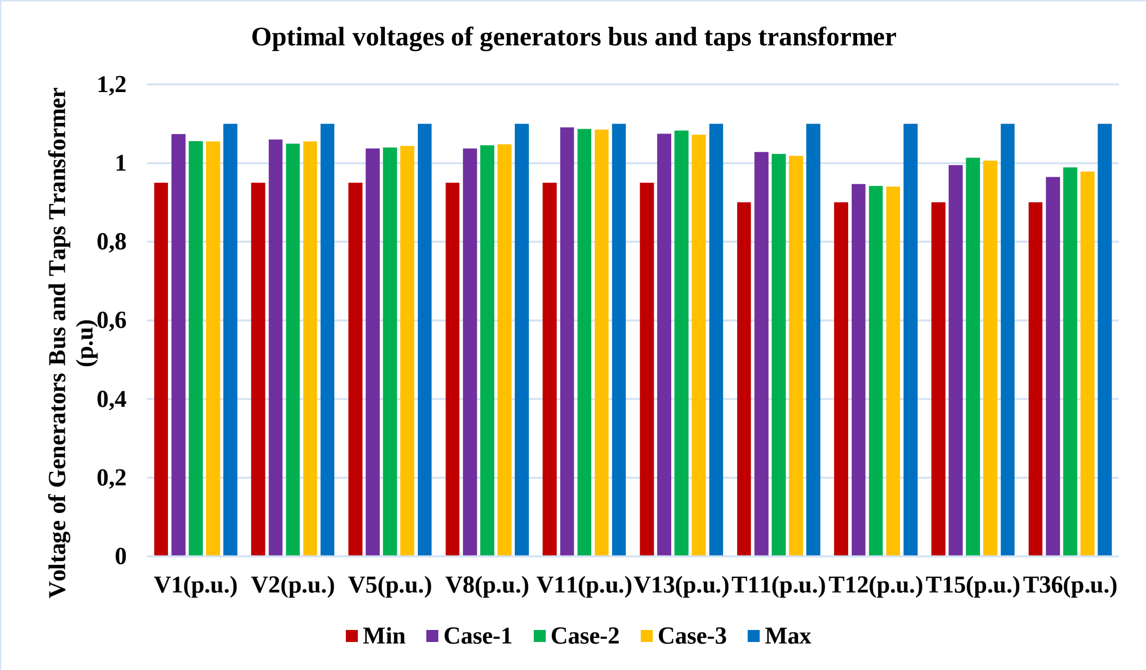

Fig. 6.32: Voltage of generators bus and taps transformer: Cases 1 to 3.

- **Breakdown of several prices for all cases (1 to 3): modified IEEE 30-bus**

The bar-chart graph presented in the **figure (6.33)** displays the breakdown of different costs. It should be noted that the penalty price for failing to utilize available wind energy is negligible, as the penalty price coefficient is the lowest. To reduce losses and optimize the gross cost in Cases 2 and 3, respectively, the generators associated with buses 5, 8, and 11 operate near their maximum capacities due to high power demand in these areas. The increased scheduled power from the wind power plants generators leads to higher reserve costs for overestimating power in Cases 2 and 3. Direct costs, linked to the scheduled output from wind generators, also rise with increased scheduled power. Total wind power costs include direct, penalty, and reserve costs. In Cases 2 and 3, thermal generator costs are lower than in Case 1 due to lower scheduled power, as illustrated in the **table (6.42)**. The cost of losses is based on the unit price of energy and is lower when optimized effectively.

Table. 6.42: Breakdown of several prices for each case: modified IEEE 30-bus.

Cost	Case 1	Case 2	Case 3
Direct cost	152.87914	224.99997	224.99999
Reserve cost	124.91548	239.62954	239.62908
Thermal cost	510.2714	448.3690	423.6801
Valve cost	11.1989	26.2821	28.8537
Gross cost	1359.7817	1115.5871	1104.6652
Penalty cost	7.716742	1.97377e-06	3.68918e-09
Wind power cost	285.5114	464.6295	464.6296
Loss cost	552.79912	176.3060	187.50273

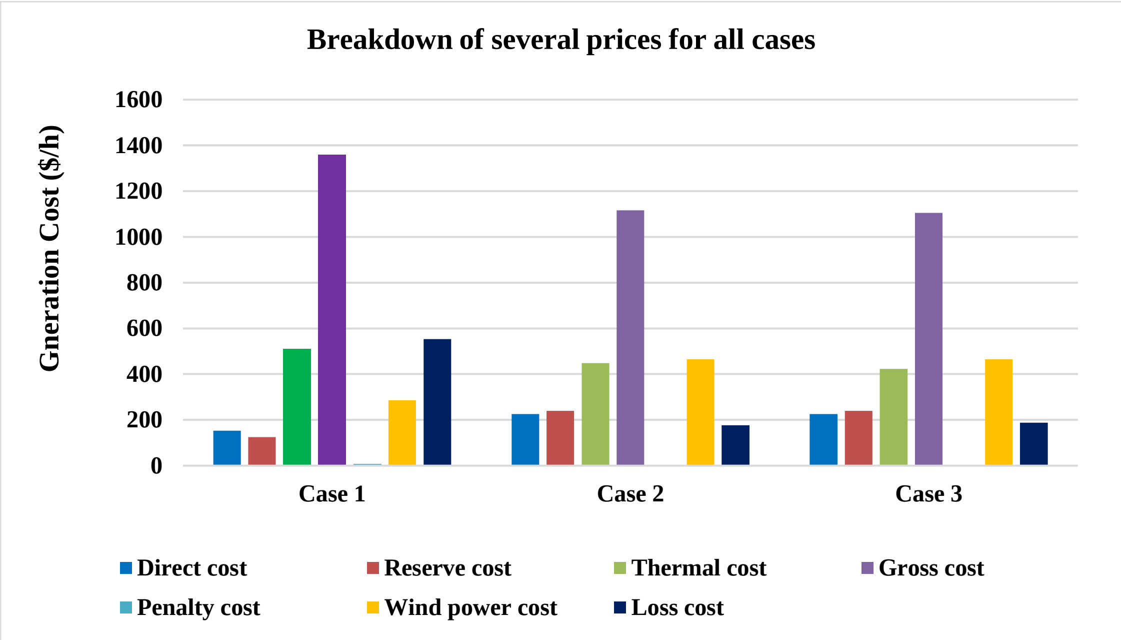

Fig. 6.33: Breakdown of several prices for all Cases (1 to 3): modified IEEE 30-bus.

The voltage profiles of all the case studies conducted on the modified system are illustrated in **figure (6.34).** The purpose of showcasing the profiles is to demonstrate that the algorithm has successfully adhered to the boundaries to critical constraints. Additionally, it is noteworthy that the generator's active and reactive power limitations have been met in all cases.

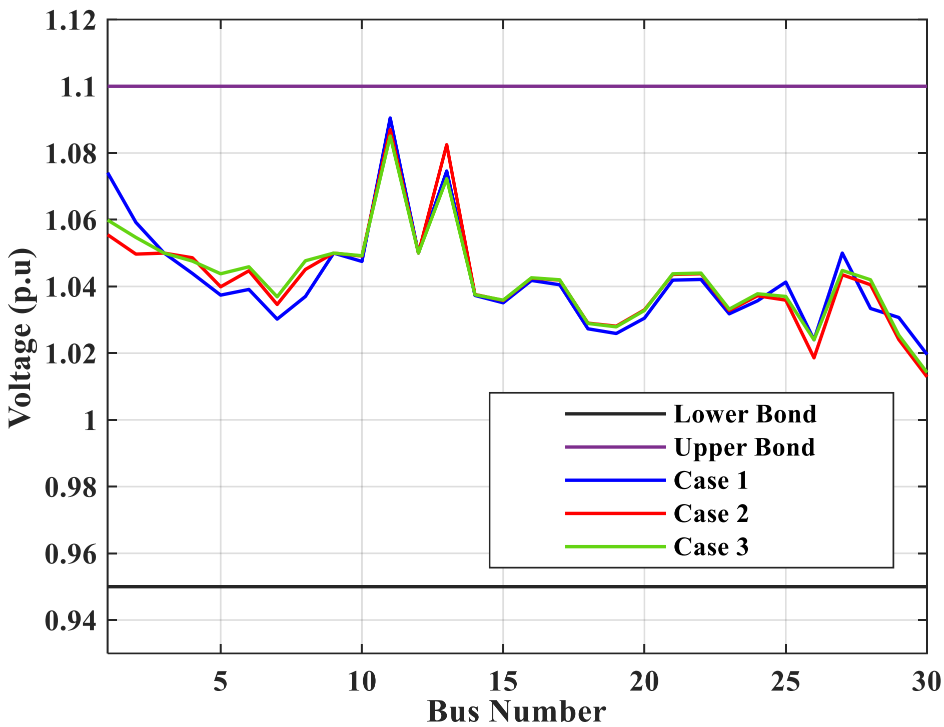

Fig. 6.34: Voltage profiles buses for the all Cases (1 to 3) by FBD-AOA: IEEE 30-bus.

B. Subsection Two: A Comparative studied between the FDB-AOA and others methods: the modified IEEE 30-bus

This subsection conducted a comprehensive experimental study to test to evaluate the performance and ensure the effectiveness of the presented method on suppose a comparison study between the reported metaheuristic algorithm FDB-AOA with several other optimization algorithms such as SHADE (Success history based adaptive differential evolution), MSA (moth swarm algorithm), and ABC (artificial bee colony), Each of these methods is incorporated with SF constraint handling method. To achieve a rational comparison, the fourth algorithms are compared under the same parameters, 500 iterations, 60 population size through 20 independent runs. The rest internal parameters considered for these algorithms are mentioned in the t**able (6.43)**.

Table. 6.43: Internal parameters settings of the algorithms.

Algorithm name	Parameters	Value
All algorithms	Population size	60
	Maximum iterations	200
	problem dimension, *D*	27
FBD-AOA	C1	2
	C2	6
	C3	2
SHADE-SF	The parameters standard of algorithms	
MSA-SF	Number of pathfinders	0.6
ABC-SF	Number of onlooker bees	6

Case 1: Generation Cost (C_{gen} ($/h)): modified IEEE 30-bus

The first case selected the **Generation Cost (C_{gen} ($/h))** as a fitness function. The **table (6.44)** displays the simulation results of the presented technique compared with other techniques**.** It is confirmed that the FDB-AOA achieved the best C_{gen} (**806.9817 $/h**) compared to other techniques. The convergence behaviors comparison of FDB-AOA with others methods are illustrated in the **figure (6.35)**.

Table. 6.44: The optimized results of the FDB-AOA and other methods: Case 1.

Control variables	Min	Max	ABC-SF	MSA-SF	SHADE-SF	FDB-AOA	Parameters	Min	Max	ABC-SF	MSA-SF	SHADE-SF	FDB-AOA
P_{TG2}(MW)	20	80	38.4875	37.2759	40.5121	40.4124	P_{TG1} (MW)	50	200	134.92549	134.90792	134.90792	134.90801
P_{WG5}(MW)	0	75	48.7195	48.3873	49.7500	49.6771	Q_{TG1} (MVAr)	- 20	150	1.14695	2.57931	0.72628	2.45649
P_{TG8}(MW)	10	35	12.7807	13.0321	10.0000	10.0000	Q_{TG2} (MVAr)	- 20	60	16.57761	18.78577	14.96911	16.89724
P_{WG11}(MW)	0	60	41.0930	41.1086	41.8414	41.9307	Q_{WG} (MVAr)	- 30	35	20.87681	24.70503	24.53619	24.67725
P_{TG13}(MW)	12	40	12.9148	14.1537	12.0000	12.0000	Q_{TG8} (MVAr)	- 15	48.7	32.36165	33.21619	34.20749	31.10329
V_1(p.u)	0.95	1.10	1.0737	1.0742	1.0715	1.0741	Q_{WG11}(MVAr)	- 25	30	25.85017	23.56955	28.00216	22.82884

V_2(p.u)	0.95	1.10	1.0590	1.0591	1.0567	1.0592	Q_{TG13} (MVAr)	- 15	44.7	19.28431	17.70916	35.24207	18.95830
V_5(p.u)	0.95	1.10	1.0383	1.0366	1.0349	1.0374	C_{gen} (\$/h)			808.3748	809.0827	807.2819	806.9817
V_8(p.u)	0.95	1.10	1.0392	1.0374	1.0350	1.0370	P_{loss} (MW)			5.5203	5.4658	5.6109	5.5280
V_{11}(p.u)	0.95	1.10	1.0962	1.0919	1.1000	1.0905	C_{gross} (\$/h)			1360.4048	1355.6432	1368.3719	1359.7817
V_{13}(p.u)	0.95	1.10	1.0735	1.0722	1.0905	1.0746	VD (p.u)			0.79408	0.90787	0.82634	0.89944
T_{11}(p.u)	0.90	1.10	1.0278	1.0172	0.9949	1.0285	Emission ton/h			0.21276	0.21230	0.21355	0.21356
T_{12}(p.u)	0.90	1.10	0.9296	0.9168	0.9297	0.9465	stability index			0.141635	0.137062	0.1376	0.139333
T_{15}(p.u)	0.90	1.10	0.9909	1.0090	1.0401	0.9945							
T_{36}(p.u)	0.90	1.10	0.9764	0.9695	0.9645	0.9644							
FACTS rating							FACTS location			ABC-SF	MSA-SF	SHADE-SF	FDB-AOA
$\tau_{TCSC\,1}$(%)	0	50%	03.31	49.98	49.95	25.71	TCSC-1 branch, (con. buses):			38,(27-30)	34,(25-26)	34, (25-26)	2(6-10)
$\tau_{TCSC\,2}$(%)	0	50%	49.74	25.22	26.00	49.81	TCSC-2 branch, (con. buses):			35, (25-27)	2, (1-3)	5, (2–5)	35(25–27)
Φ_{TCPS1} (deg)	- 5°	5°	1.0756	1.1331	1.4454	1.2688	TCPS-1 branch, (con. buses):			9, (6-7)	35, ((25-27)	35, (25–27)	9, (6–7)
Φ_{TCPS2} (deg)	- 5°	5°	2.5393	-1.3048	-1.3036	2.3059	TCPS-2 branch, (con. buses):			14, (9-10)	5, (2-5)	4, (3–4)	14, (9–10)
Q_{SVC1} (MVAr)	- 10	10	10.0000	5.6768	-9.1516	7.5888	SVC1 bus no:			24	19	9	21
Q_{SVC2} (MVAr)	- 10	10	9.9976	8.5451	9.9998	9.9955	SVC2 bus no:			7	24	24	24

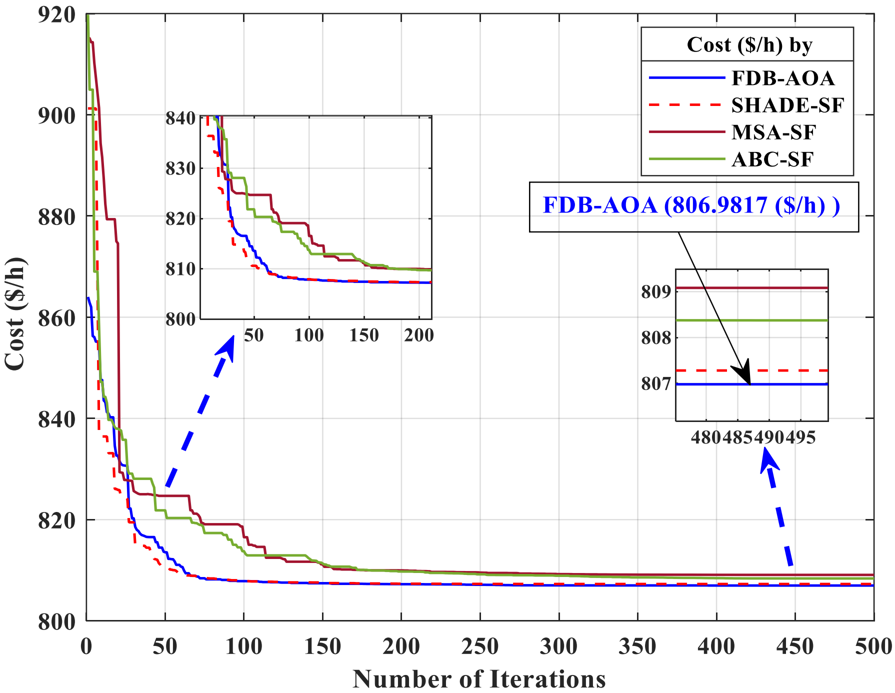

Fig. 6.35: Comparison of convergence behaviors of FDB-AOA and other methods Case 1.

Case 2: Real power losses (P_{loss} (MW)): modified IEEE 30-bus

The fitness function selected in this case is the **Real power losses (P_{loss} (MW))**. The **table (6.45)** shows the simulation results of the presented technique compared with other techniques**.** It is confirmed that the FDB-AOA attained the most favorable P_{loss} value, reaching (1.7631 **MW**), surpassing the performance of other techniques. The convergence behaviors comparison providing by FDB-AOA with others methods are illustrated in the **figure (6.36)**.

Table. 6.45: The optimized results of the FDB-AOA and other methods: Case 2: IEEE 30-bus.

Control variables	Min	Max	ABC-SF	MSA-SF	SHADE-SF	FDB-AOA	Parameters	Min	Max	ABC-SF	MSA-SF	SHADE-SF	FDB-AOA
P_{TG2}(MW)	20	80	38.7639	21.4021	31.1183	24.8067	P_{TG1}(MW)	50	200	52.21472	57.5785	50.00004	50.35643
P_{WG5}(MW)	0	75	75.0	73.3244	74.7902	75.0000	Q_{TG1} (MVAr)	- 20	150	-3.82946	-1.97128	-1.72849	-3.78806
P_{TG8}(MW)	10	35	35.0	34.6582	34.2543	35.0000	Q_{TG2} (MVAr)	- 20	60	8.35354	11.71275	9.92001	8.14154
P_{WG11}(MW)	0	60	60.0	58.4578	57.8523	60.0000	Q_{WG} (MVAr)	- 30	35	22.02555	22.07329	18.06980	21.81749
P_{TG13}(MW)	12	40	26.4970	39.9120	37.2154	40.0000	Q_{TG8} (MVAr)	- 15	48.7	30.14643	36.42547	30.97210	30.50151
V_1(p.u)	0.95	1.10	1.0595	1.0586	1.0495	1.0555	$\boldsymbol{Q}_{WG11}$(MVAr)	- 25	30	21.89586	19.31959	28.13659	22.63942
V_2(p.u)	0.95	1.10	1.0542	1.0516	1.0436	1.0497	Q_{TG13} (MVAr)	- 15	44.7	25.92275	20.41334	22.60228	26.11189
V_5(p.u)	0.95	1.10	1.0437	1.0400	1.0330	1.0399	$\boldsymbol{C_{gen}}$ **($/h)**			927.5848	934.6311	931.2582	939.2806
V_8(p.u)	0.95	1.10	1.0473	1.0459	1.0362	1.0451	$\boldsymbol{P_{loss}}$ **(MW)**			1.9089	1.9331	1.8304	1.7631
V_{11}(p.u)	0.95	1.10	1.0895	1.0811	1.0976	1.0870	$\boldsymbol{C_{gross}}$ **($/h)**			1104.0771	1127.9411	1114.2994	1115.5871
V_{13}(p.u)	0.95	1.10	1.0725	1.0702	1.0782	1.0825	VD (p.u)			0.89971	0.79076	0.87055	0.90793
T_{11}(p.u)	0.90	1.10	1.04	0.9700	1.0194	1.0232	Emission ton/h			0.14033	0.14408	0.14061	0.14176
T_{12}(p.u)	0.90	1.10	0.92	0.9904	0.9063	0.9422	stability index			0.13543415	0.1366307	0.13846	0.135576
T_{15}(p.u)	0.90	1.10	1.00	1.0296	0.9943	1.0134							
T_{36}(p.u)	0.90	1.10	0.98	0.9724	0.9644	0.9890							
FACTS rating							FACTS placement			ABC-SF	MSA-SF	SHADE-SF	FDB-AOA
$\boldsymbol{\tau_{TCSC\,1}}$(%)	0	50%	20.872	50	49.49	50	TCSC1 branch, (con.buses):			16, (12-13)	14, (9-10)	14, (9-10)	25, (2–5)
$\boldsymbol{\tau_{TCSC\,2}}$(%)	0	50%	17.183	25.71	5.14	20.94	TCSC2 branch, (con.buses):			14, (9-10)	25, (10-20)	25, (10-20)	34, (25–26)
$\boldsymbol{\Phi_{TCPS1}}$ **(deg)**	- 5°	5°	2.5650	0.0205	-1.9365	4.2024	TCPS1 branch, (con.buses):			33, (24-25)	32, (23-24)	35, (25–27)	35, (25–27)
$\boldsymbol{\Phi_{TCPS2}}$ **(deg)**	- 5°	5°	2.7192	4.1362	3.7699	1.3130	TCPS2 branch, (con.buses):			5, (2-5)	33	13, (9–11)	14, (9–10)
$\boldsymbol{Q_{SVC1}}$ **(MVAr)**	- 10	10	9.9362	9.9931	9.9992	9.6699	SVC1 bus no:			24	24	24	21
$\boldsymbol{Q_{SVC2}}$ **(MVAr)**	- 10	10	9.5065	6.6365	9.8919	9.9999	SVC2 bus no:			21	15	21	24

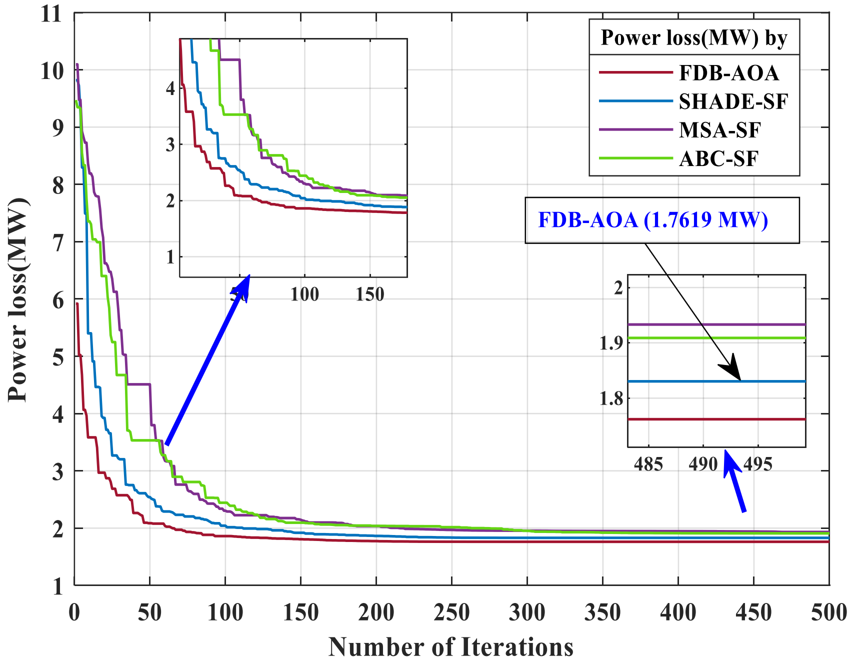

Fig. 6.36: Comparison of convergence behaviors of FDB-AOA with others methods Case 2.

Case 3: Gross cost ($\boldsymbol{C_{gross}}$ ($/h)): modified IEEE 30-bus

The third case selected the **Gross cost ($\boldsymbol{C_{gross}}$ ($/h))** as a fitness function. The **table (6.46)** displays the optimized results of the presented method in comparison to other techniques**.** The results confirm that the FDB-AOA achieved the best C_{gross} (**1104.6652$/h**) compared to other techniques. The convergence behaviors comparison of FDB-AOA with others methods are depicted in **figure (6. 37).**

Table. 6.46: The optimized results of the FDB-AOA and other methods: Case 3: IEEE 30-bus.

Control variables	Min	Max	ABC-SF	MSA-SF	SHADE-SF	FDB-AOA	Parameters	Min	Max	ABC-SF	MSA-SF	SHADE-SF	FDB-AOA
P_{TG2}(MW)	20	80	41.8884	44.4112	38.3339	39.5208	P_{TG1}(MW)	50	200	50.00007	50.00005	50.01043	50.0
P_{WG5}(MW)	0	75	72.9342	69.7845	74.9821	75.0000	Q_{TG1} (MVAr)	- 20	150	-1.20432	-4.27402	-2.49604	-1.71349
P_{TG8}(MW)	10	35	33.6876	32.4757	34.9999	35.0000	Q_{TG2} (MVAr)	- 20	60	11.28142	8.65557	10.31751	10.90263
P_{WG11}(MW)	0	60	58.7901	60.0000	59.9799	60.0000	Q_{WG} (MVAr)	- 30	35	18.83008	22.34026	22.90149	22.43517
P_{TG13}(MW)	12	40	28.0524	28.7138	27.0090	25.7542	Q_{TG8} (MVAr)	- 15	48.7	34.86774	30.71682	36.92161	34.46611
V_1(p.u)	0.95	1.10	1.0521	1.0571	1.0583	1.0599	Q_{WG11}(MVAr)	- 25	30	19.87786	22.63105	23.36909	21.58632
V_2(p.u)	0.95	1.10	1.0467	1.0522	1.0530	1.0547	Q_{TG13} (MVAr)	- 15	44.7	22.40255	26.28634	15.00205	17.47834
V_5(p.u)	0.95	1.10	1.0353	1.0403	1.0423	1.0438	C_{gen} **($/h)**			916.96218	916.04113	918.7899	917.1625
V_8(p.u)	0.95	1.10	1.0381	1.0448	1.0463	1.0477	P_{loss} **(MW)**			1.9528	1.9853	1.9158	1.8750
V_{11}(p.u)	0.95	1.10	1.0821	1.0870	1.0842	1.0851	C_{gross} **($/h)**			1112.2435	1114.5673	1109.2887	1104.6652
V_{13}(p.u)	0.95	1.10	1.0776	1.0832	1.0644	1.0723	VD (p.u)			0.85247	0.90566	0.78558	0.92337
T_{11}(p.u)	0.90	1.10	0.9921	1.0294	1.0232	1.0186	Emission ton/h			0.14112	0.14089	0.14166	0.14188
T_{12}(p.u)	0.90	1.10	0.9261	0.9447	0.9300	0.9405	stability index			0.135434	0.138385	13.77242	0.1383147
T_{15}(p.u)	0.90	1.10	1.0042	1.0269	1.0201	1.0060							
T_{36}(p.u)	0.90	1.10	0.9694	0.9728	0.9882	0.9785							
FACTS rating							FACTS placement			ABC-SF	MSA-SF	SHADE-SF	FDB-AOA
$\tau_{TCSC\,1}$(%)	0	50%	49.98%	49.83%	22.36%	0.1543	TCSC1 branch, (con.buses):			24,(19-20)	34,(25-26)	14, (9–11)	25, (2–5)
$\tau_{TCSC\,2}$(%)	0	50%	26.17%	26.90%	36.28%	0.5000	TCSC2 branch, (con.buses):			7, (4-6)	2,(1-3)	30, (15–23)	34, (25–26)
Φ_{TCPS1} **(deg)**	- 5°	5°	-0.6518	3.0878	0.7708	2.7135	TCPS1 branch, (con.buses):			34,(25-26)	35,(25-27)	13, (9–11)	35, (25–27)
Φ_{TCPS2} **(deg)**	- 5°	5°	2.8515	-0.7177	3.1159	0.6170	TCPS2 branch, (con.buses):			2, (1-3)	5,(2-5)	33, (24–25)	14, (9–10)
Q_{SVC1} **(MVAr)**	- 10	10	10.0000	9.8422	9.8557	10.0000	SVC1 bus no:			5	24	12	21
Q_{SVC2} **(MVAr)**	- 10	10	9.9993	10.0000	9.9951	9.8752	SVC2 bus no:			33	21	24	24

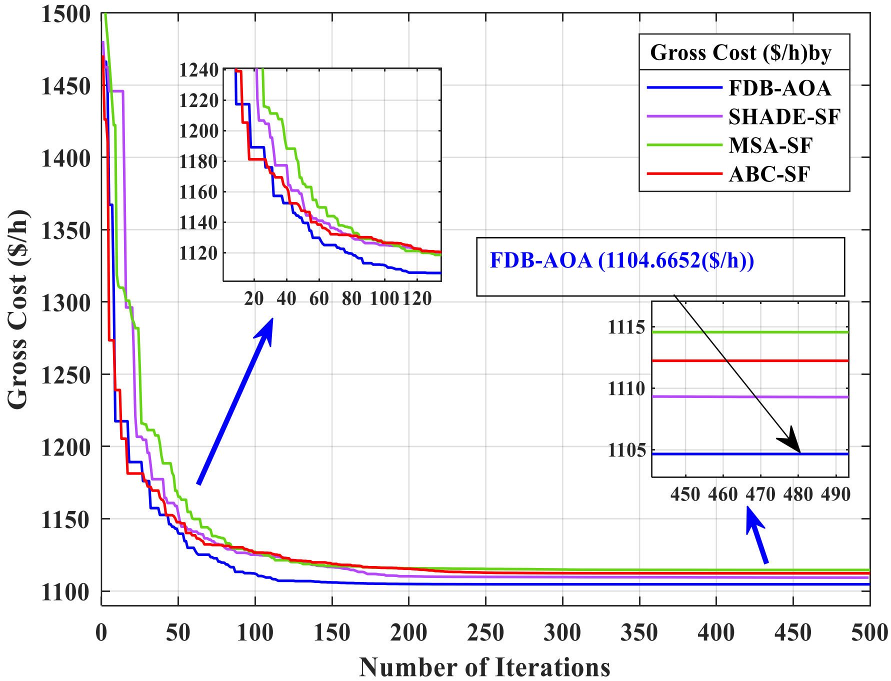

Fig. 6.37: Comparison of the convergence behaviors of FDB-AOA with other methods Case 3.

- **Discussion of The Results: modified IEEE 30-bus**

The tables (6.44, 6.45, 6.46), show the findings of the study conducted on the adopted test system IEEE 30-bus for various Cases achieved by the proposed FDB-AOA, and other techniques (SHADE-SF, MSA-SF; ABC-SF. According to the optimization results mentioned in those tables, it can be observed that the FDB-AOA algorithm has achieved the most satisfactory results while complying with all constraints. However, it is important to note that comparing the apparent numerical results of a constrained optimization problem is not a reliable method. Hence, it is crucial to verify the feasibility of the solutions.

The simulation results clearly demonstrate the superiority of the FBD-AOA method compared to three other population metaheuristic algorithms. It can be observed that this technique could solve the **single-objective OPF problem** involving wind power generators and various FACTS devices with high efficiency. It consistently provides lower values for most test cases and competitive computational times compared to other algorithms. It should be mentioned that the best results have been achieved by FBD-AOA. excelling in terms of optimal solution, convergence, efficiency, and minimal execution time.

The **figures (Figs. 6.35, 6.36, 6.37**), illustrate the convergence behaviors of the FBD-AOA method in comparison to other metaheuristic algorithms for cases 1 to 3, respectively. These diagrams indicate that the FBD-AOA algorithm exhibits faster convergence, following a uniform and systematic pattern. The SHADE-SF algorithm also converges rapidly and is a strong competitor in finding optimal solutions with precision similar to FBD-AOA. It performs consistently better in all cases compared to other algorithms. In contrast, MSA-SF and ABC-SF show irregular and erratic convergence, taking the longest time to reach the best solutions and often stagnating at various stages. For cases 2 and 3, the scheduling outcomes favor wind power plants over thermal units for all algorithms. The best locations and ratings for FACTS devices are detailed in the corresponding tables for each case.

- **Statical analyses and Robustness of the proposed Algorithm (FBD-AOA)**

For further evaluating the effectiveness of each method, particularly the proposed algorithm **(FBD-AOA)** in solving the stochastic OPF problems considering the location and rating of the FATCS devices. A statistical analysis was conducted to solve various problems related to optimal power management. This analysis measures the robustness and efficiency across multiple methods. It is important to mention that the values of all variables were determined after being executed 20 times independently for all methods and all cases. The statistical outcomes result for each case/ algorithm are displayed in **table (6.47).** These results are the best findings result achieved from running simulations, including the minimum, the maximum, the median and the and standard deviation (**SD. dev**) values. The results show that FBD-AOA consistently outperforms other techniques, achieving the best optimum values for most cases. In Case 1, the ABC-SF method performed better regarding **standard deviation**. Despite this, FBD-AOA generally delivered superior performance in other metrics like minimum, maximum, mean, and median values. Overall, the SHADE, MSA, and ABC methods also demonstrated competitive performance, outperforming most other algorithms across all cases. The **figures (6.38 (a), (b), and (c))** illustrates a comparison between the optimized results of the three cases versus trials for all algorithms. It is confirmed that the results of the reported technique (FBD-AOA) clearly prove its accuracy and stability in solving such single-objective functions.

Table. 6.47: The statistical results for all cases, and all methods: modified IEEE 30-bus.

Algorithm		Case 1	Case 2	Case 3
FDB-AOA	minimum	806.9817	1.7631	1104.6652
	maximum	807.3215	1.8141	1109.5872
	Mean	807.1166	1.7812	1106.81722
	median	807.1089	1.7759	1106.7065
	SD. dev.	0.0996	0.0169	1.2142
SHADE-SF	minimum	807.2819	1.8304	1110.3699
	maximum	807.6278	1.9194	1116.0245
	Mean	807.4189	1.8546	1112.7605
	median	807.3969	1.8464	1112.4692
	SD. dev.	0.0983	0.0221	1.313725
MSA-SF	minimum	809.0827	1.9331	1114.5673
	maximum	812.6054	1.9981	1119.8187
	Mean	810.3785	1.9605	1116.4827
	median	810.0616	1.9531	1115.0533
	SD. dev.	0.9738	0.02315	2.024056
ABC-SF	minimum	808.3748	1.9089	1112.2434
	maximum	811.3024	1.9687	1116.2784
	Mean	809.2804	1.932265	1114.1049
	median	809.0374	1.9261	1113.8023
	SD. dev.	0.8339	0.02248	1.3983186

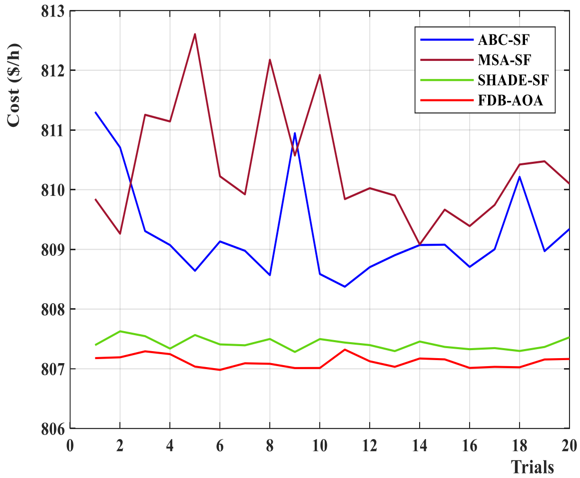

(a) Case 1

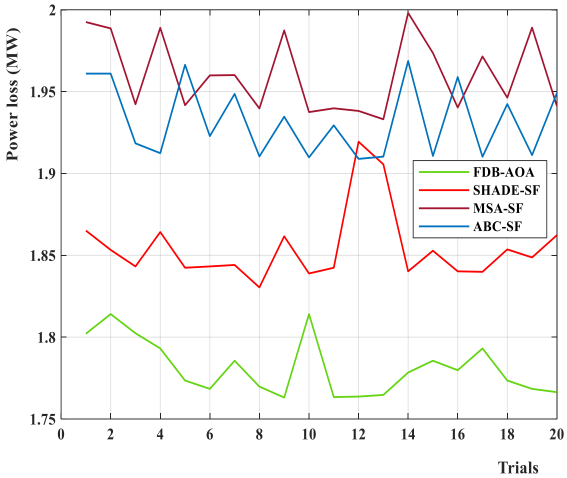

(b) Case 2

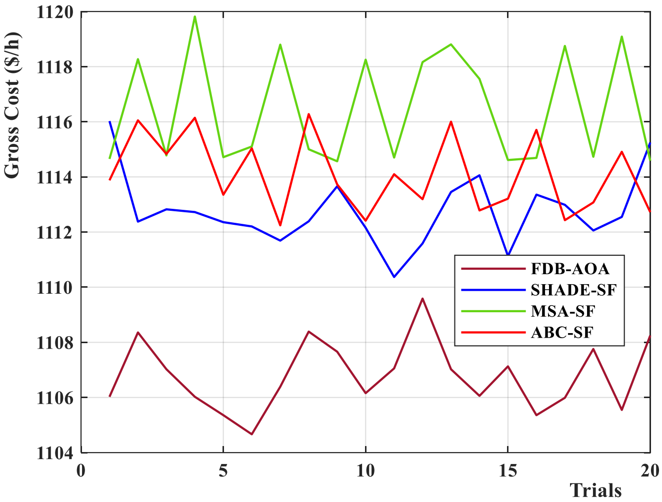

(c) Case 3

Fig. 6.38: comparison between the optimized of the three cases versus trials for all proposed algorithms

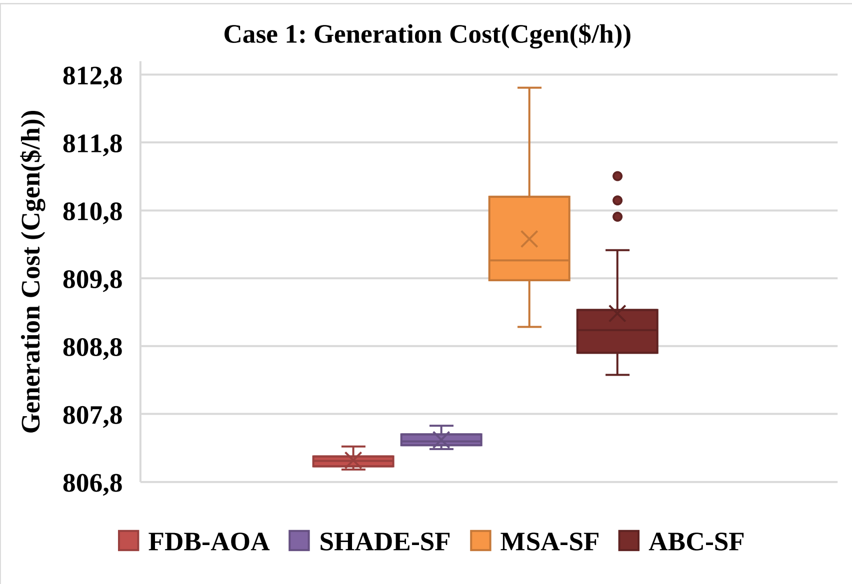

(a) case 1

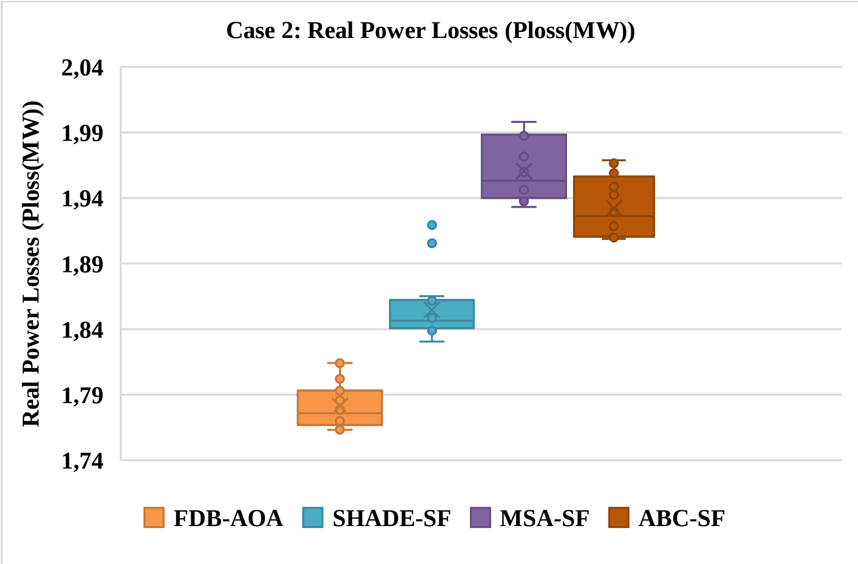

(b) case

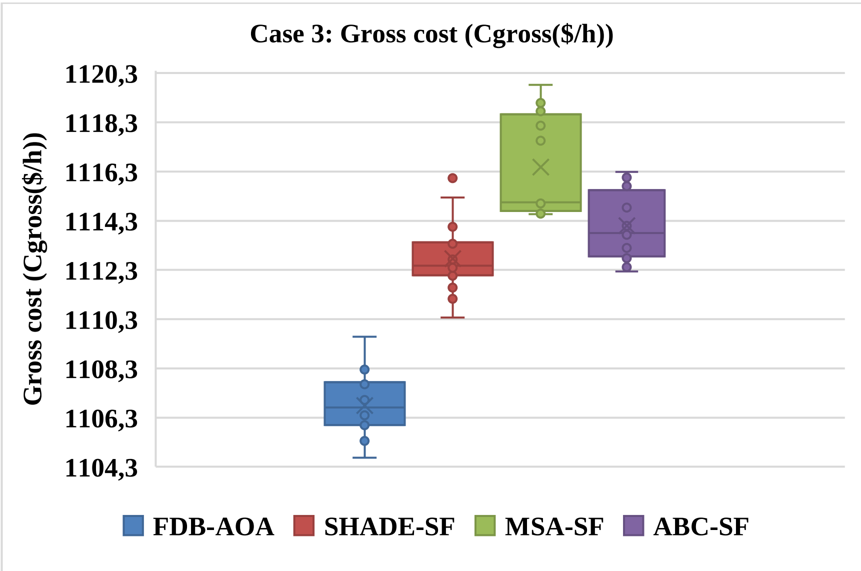

(c) case 3

Fig. 6.39: Boxplots of all algorithms for the benchmark functions cases 1-3: modified IEEE 30-bus.

The **table (6.48)** represent a comparison between the results obtained by the proposed method with the results of the SHADE-SF method [9].

Table. 6.48: Comparison between the results obtained by the FDB-AOA with those of the SHADE-SF method.

	Case 1	Case 2	Case 3
FDB-AOA (500 Iterations)	806.9817 **($/h)**	1. 7631 **(MW)**	1104.6652 **($/h)**
SHADE-SF (FES 30 000)	807.0166 **($/h)**	1.7467 **(MW)**	1104.0771 **($/h)**

- **Discussion of results using statistical analysis: test cases 1 to 3: modified IEEE 30-bus**

In order to evaluate the obtained outcomes, in this subsection, boxplots corresponding to each of the 3 benchmark cases (cases 1-3), and each candidate algorithm. For that, the Boxplots are an efficient way to depict and evaluate the robustness of the presented algorithm namely FBD-AOA compared to other algorithms in terms of dispersion of the solutions.

The **figures (6.39 (a), (b), and (c))** illustrates the boxplot of the benchmark fitness values for the FBD-AOA and other algorithms such as: SHADE-SF, MSA-SF, ABC-SF. it can be concluded that the proposed FBD-AOA is statistically superior compared to other techniques, and exhibited relatively a stable search performance in all test cases for single objective functions. It is confirmed that the reported technique (FBD-AOA) allows achieving the best solution at a reduced SD in the majority of cases compared to other methods.

This clearly proves the accuracy and stability of this algorithm. According to these preliminary results, it can be concluded that the proposed FBD-AOA algorithm can been saucerful used to solve various OPF problems. The boxplots presented in the figures indicate that, for the majority of cases, the boxplots of the reported method are among the narrowest and have the lowest values, providing further evidence of its superior performance.

This part presents a study conducted by the OPF on the modified IEEE 30-bus transmission electrical network, which incorporates wind power plants generators and multi-FACTS equipment. The total generation cost is calculated, including direct, reserve, and penalty prices of wind power. The study optimizes the location and sizing of different types of FACTS controllers in several case studies. The outcomes of each case study validate the rationale for the combined goal with superiority over other algorithms. The significance of optimizing the placement and rating of FACTS devices is highlighted through a described/explained the examination of a real-life scenario study. The results clearly demonstrate the superiority of the reported algorithm over other algorithms.

After having validated the proposed method on the modified electrical transmission network IEEE 30-bus test system, the next subsection deals the application of this proposed method (FDB-AOA) on large scale test system which is the modified of reel Algerian electricity network **DZA-114 bus**, with presence of renewable energy, also FACTS devices.

6.4.2. Application 3.2: The modified DZA-114 bus Algerian electric transmission network

This part of the chapter focuses on application of the proposed algorithms for solving the single OPF problems. The original DZA-114-bus Algerian Electric transmission network test system is modified by replacing three conventional thermal power plants with renewable energy, stochastic wind and solar power plants. our study focuses on the implementation of two wind farms, with power capacities of 345 and 300 MW, and solar photovoltaic with power 100 MW. These two wind farms are installed in busbar set 52 and busbar set 83, and solar in busbar 109, respectively. Additionally, FACTS devices SVC, TCSC, and TCPS – (two of each type) are optimally placed in the most suitable locations.
The system's data optimization targets include 57 variables to be optimized, including 15 active power values of generators, 15 voltage magnitudes of generators, and 16 tap-changer adjustments. The minimum and maximum operating limits of the control variables are given in the tables of results. The adopted objective functions are optimized using optimization algorithms such as ABC, MSA, SHADE, and the proposed FDB-AOA. The **table (6.49)** provides an overview characteristics of the adopted network DZA-114 bus.

Table. 6.49: An overview characteristic of the adopted network: the modified DZA-114 bus.

Element		quantity	Details
Buses-number		114	-
Branches-number		159	-
Thermal generators-number		15	**Slack-Bus is 4/** 5/ 9/11/15/17/19/22/98/100/101/111
Wind generators -number		2	Buses number: 52 and 83
Solar generators -number		1	Buses number: 109
Transformer with tap changer		16	Branches number: from 160 to 175
TCSC		2	Branches and sizing are optimized
TCPS		2	
SVC		2	Buses and sizing are optimized
Total power demand	**Active-power**	-	3727 MW
	Reactive-power	-	2070 MVAR
Load-buses			-
The voltage range of generators bus		15	[0,90–1,10] (p.u)
The voltage range of the load bus		99	[0,90–1,1] (p.u)

- **Case studies, Numerical Simulation results, discussion, and comparisons**

Several case studies have been conducted on the Algerian electrical network summarized in the **table (6.50)**. In each optimization test, the algorithm runs a complete cycle with a maximum of iterations (400). The variable settings are carefully recorded for each case.

Table. 6.50: Summary of all the cases addressed in this study: the modified DZA-114 bus.

Case number	Case explanation	Equation number
Case 1	Minimize generation cost (C_{gen} ($/h))	Eq (4.27)
Case 2	Minimize real power loss (P_{Loss} (MW))	Eq (4.28)
Case 3	Minimize gross cost (C_{gross} ($/h))	Eq (4.33)

This section is divided into two subsections. The first set of study cases aims to assess the effectiveness of the proposed algorithm (FDB-AOA) for determining the optimal placement and size of FACTS devices in a large scale the modified **DZA-114 bus** Algerian electrical transmission network system. The second section involves a comparative study, where the proposed algorithm is compared with other methods mentioned in the references [10], like SHADE, MSA, ABC to demonstrate the superiority of this algorithm and their effectiveness for solving the OPF problems. Each optimization case study includes a maximum of 400 iterations conducted in a single complete run of the algorithm. Each case is repeated 20 times, and the best value of the objective function, as well as the corresponding control variable settings, are recorded. The **figure (6.40)** represents the Solution methodology.

- **Solution methodology**

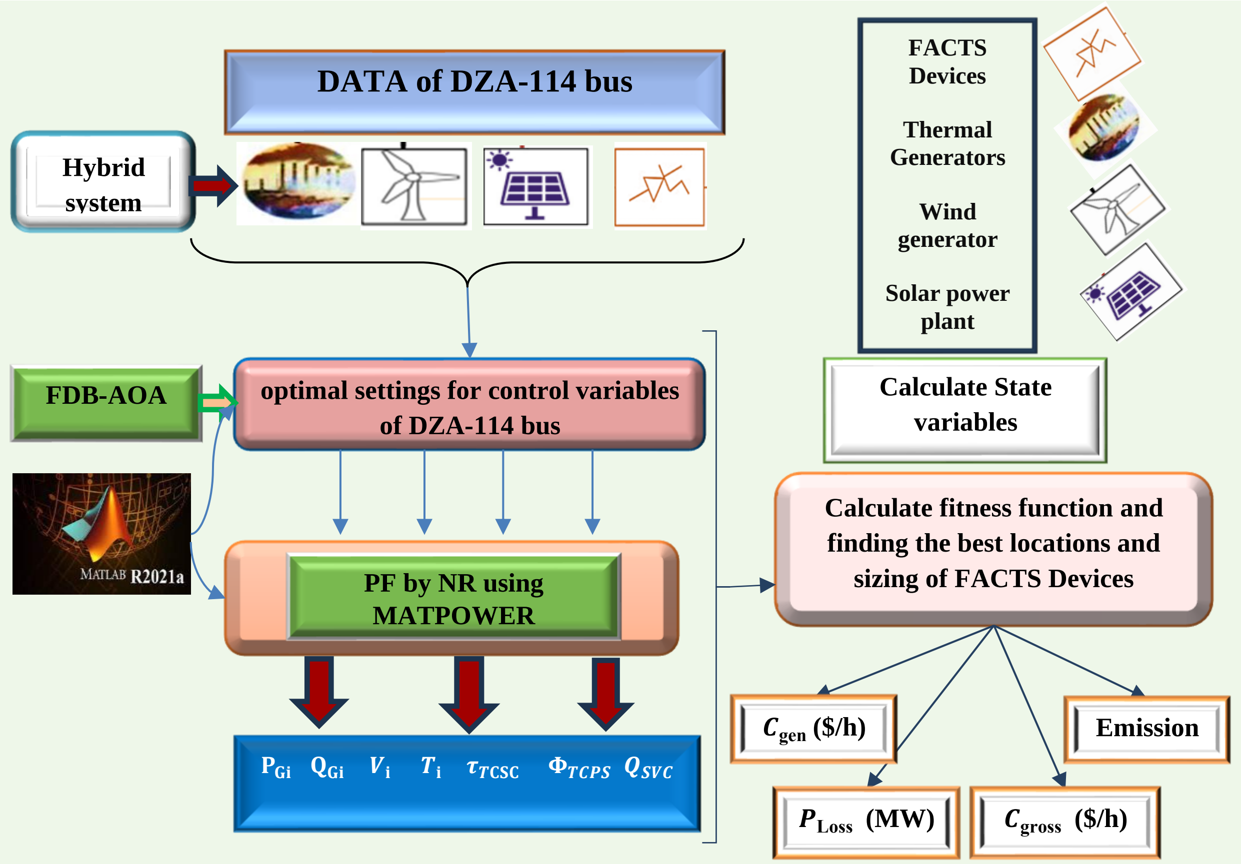

Fig. 6.40: Solution methodology.

6.4.2.1. Impact of Schedule Power and PDF Parameters on Wind Generation Costs

The table (6.51) displays the chosen Weibull shape (β), and scale (α) parameters for these newly implemented generators like solar and wind energy sources. Additionally, the total rated power value is provided for each wind power plant, also their cost coefficients.

Table. 6.51: cost coefficients and PDF parameters for stochastic models of wind generators: the modified DZA-114 bus.

Wind power generating plants					Solar PV plant		
Windfarm#	No. of turbines	Rated power, P_{wr}(MW)	Weibull PDF parameters	Weibull mean, M_{wbl}	Rated power, P_{sr}(MW)	Lognormal PDF parameters	Lognormal mean, M_{lgn}
1 (bus 52)	115	345	$\alpha = 9$ $\beta = 2$	$v = 7.976$ m/s	100 (bus 109)	$\mu = 6$ $\sigma = 0.6$	$G = 483$ W/m^2
2 (bus 83)	100	300	$\alpha = 10$ $\beta = 2$	$v = 8.862$ m/s			
Price coefficients ($/MWh)					**Price coefficients ($/MWh)**		
Direct, g_{wj}		Reserve, K_{Rwj}	Penalty, K_{Pwj}		Direct, h_s	Reserve, $K_{Rs,k}$	Penalty, $K_{PS,k}$
1,60		3,0	1,50		1.60	3	1.5
1,75		3,0	1,50				

Wind frequency and Weibull fitting distributions shown in **figures 6.41 (a)** and **(b)** are acquired after 8000 Monte-Carlo scenarios run. This norm defines the design criteria for wind turbines and establishes the highest turbulent class IA that a turbine under which a turbine can be approved for operation, with a maximum yearly average wind speed.

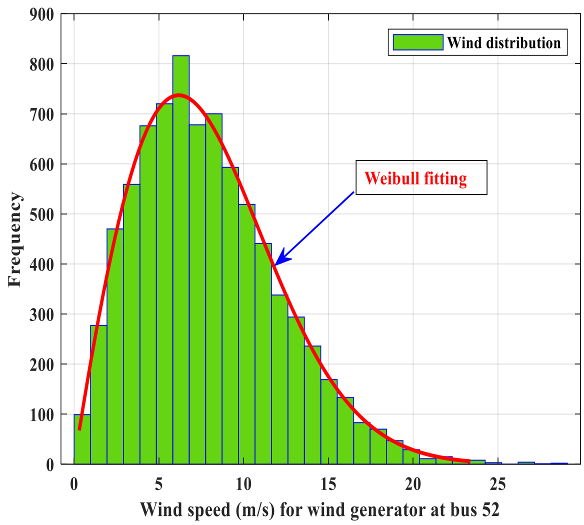

Fig. 6.41 (a): Wind speed distribution for wind farm1 at bus 52 ($\alpha = 9$, $\beta = 2$).

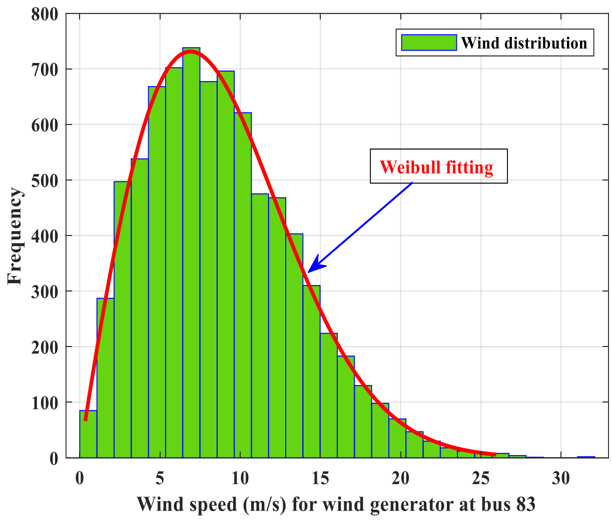

Fig. 6.41 (b): Wind speed distribution for wind farm 2 at bus 83 (α= 10, β=2).

The distribution of solar irradiance or solar PV generator is illustrated by **figure (6.42)**. The stochastic power-output of solar photovoltaic unit is illustrated by **figures (6.43)**

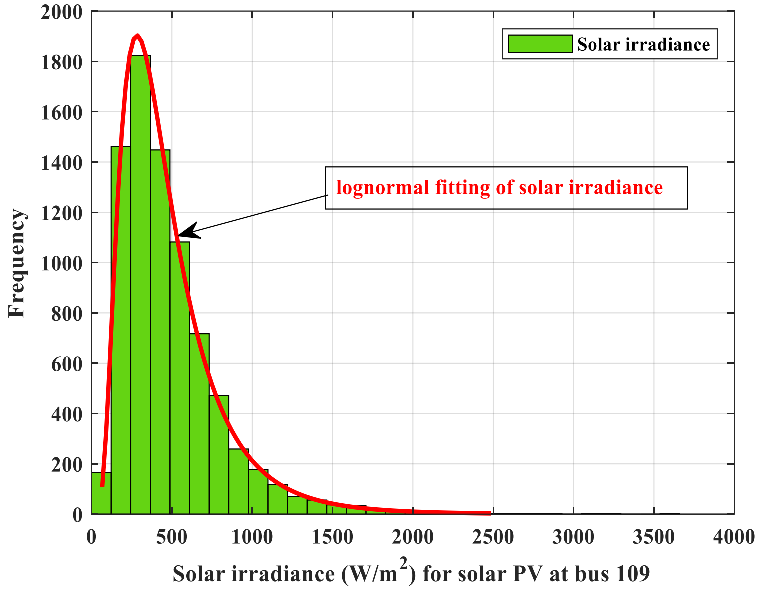

Fig. 6.42: Distribution of solar irradiance or solar PV generator at bus #109 ($\mu = 6, \sigma = 0.6$).

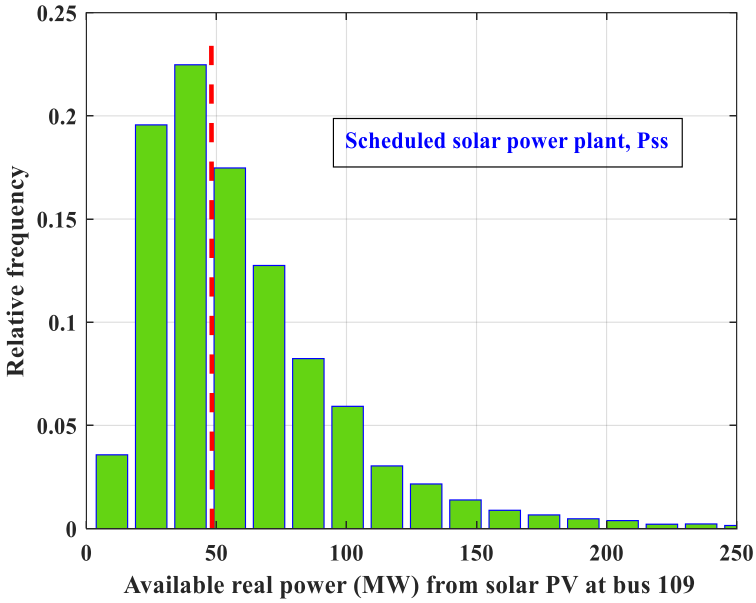

Fig. 6.43: Real power distribution (MW) of solar PV at bus 109.

A. VARIATION OF GENERATION COST OF RESs

The scheduled power of wind and solar is varied from zero to the rated power and variation in direct, penalty, reserve and total cost is shown in **figures (6.53, and 6.54)**. Moreover, with the increase of scheduled power, reserve cost is escalating due to large spinning reserve requirement. In addition, the direct cost increases linearly with the scheduled power. Whereas, the penalty cost decreases monotonically with the increase of scheduled power.

A.1. Scenario: 1 Scheduled power vs cost: modified DZA-114 bus

Notably, the Weibull probability density function (PDF) parameters utilized in this test align with those presented in the **table (6.50)**. It should be noted that the direct cost of wind is lower than the average cost of thermal power. Additionally, the penalty cost is lower than the direct cost. The scheduled power ranges from [0 to the rated power] of the wind farm, and the variations of reserve, direct, penalty, and total costs are plotted in **figures (6.44 (a) and (b)),** and for the both wind farms. The total price is the summation of those costs associated with the scheduled power. The direct cost shows a linear relationship with the scheduled power. With an augmentation in the scheduled power, there is an accompanying elevation in the requisite spinning reserve, resulting in an upsurge in the reserve cost, and consequently, an escalation in the total generation cost. The penalty cost was appropriately reduced, but at a slower rate, with the amplification in the scheduled power.

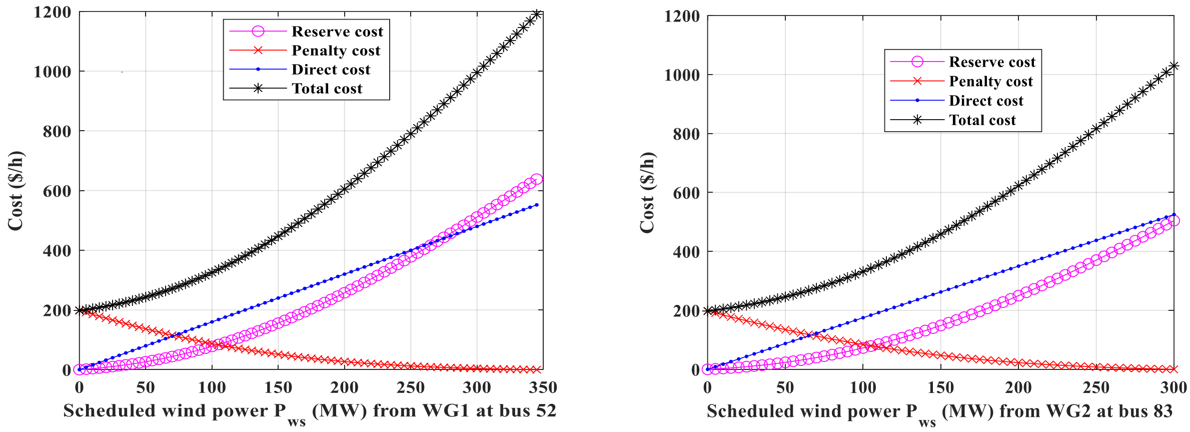

(a) WG1(bus 52) **(b)** WG2(bus 83)

Fig. 6.44: Variation of wind power cost vs scheduled power for wind generator (a) WG1(52), (b) WG2(83).

A.2. Scenario 2: Probability density function parameter vs cost: modified DZA-114 bus

Here, the scale (α) of Weibull distribution is varied while the shape parameters is constant ($\beta = 2$). Our goal was to see how it affects any changes in costs to the costs of wind power generator for a predetermined arbitrarily chosen schedule power. A scheduled power with value of 345 MW is fixed on the WG1 (52), while for the WG2 (83) was a 300MW. **figures (6.45 (a) and (b)),** illustrate the cost-to-scale factor curves for wind farm 1 and 2. The overall minimum cost is around the middle range of scale parameters. With a rising in the scale parameter, the wind speeds probability also increases at their higher value. If scheduled power is maintained, the penalty costs increase, resulting in an increase in the overall power cost. After a certain value of scale parameter, the reserve cost won't go down as much is not significant.

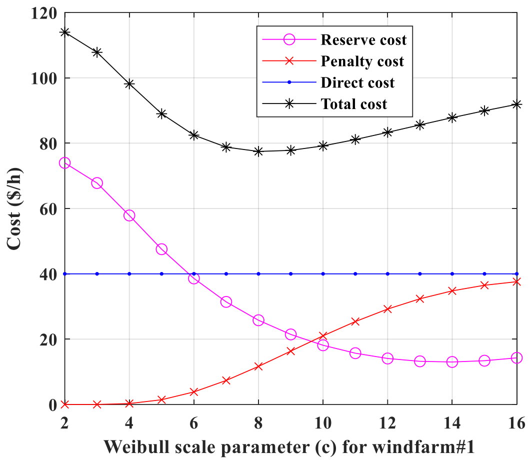

(a) windfarm#1 (bus 52)

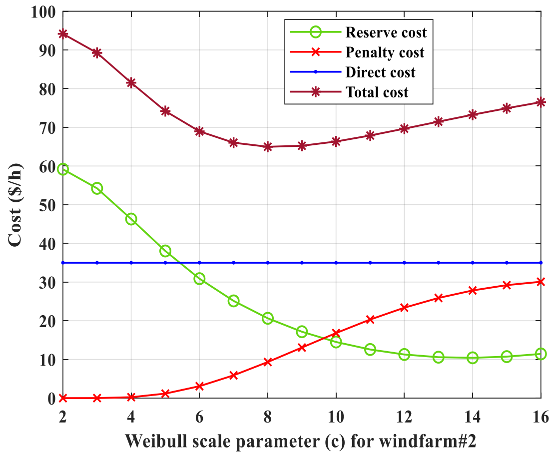

(**b)** windfarm#2 (bus 83)

Fig. 6.45: Variation of wind power cost vs Weibull scale parameter (α)

(a) windfarm#1(52), (b) windfarm#2(83).

Similar to wind power, cost variations of solar power over/ under-estimation are plotted against schedule power in **figures (6.46, and 6.47).** Yearly operating and maintenance cost for solar PV power plant is almost in similar range of that of onshore wind power plant [37]. Therefore, for our study purpose the direct, penalty and reserve cost coefficients for solar PV are assumed to be $h_s =$ 1.6 , $K_{Rs,k} = 3$, and $K_{PS,k}$=1.5, respectively. Other related solar PV parameters are discussed in **Section 3.1**. With the selected PDF parameters for solar irradiance, the total solar power cost is not monotonically increasing. Indeed, the minimum cost is reported somewhere around 15 MW of scheduled power.

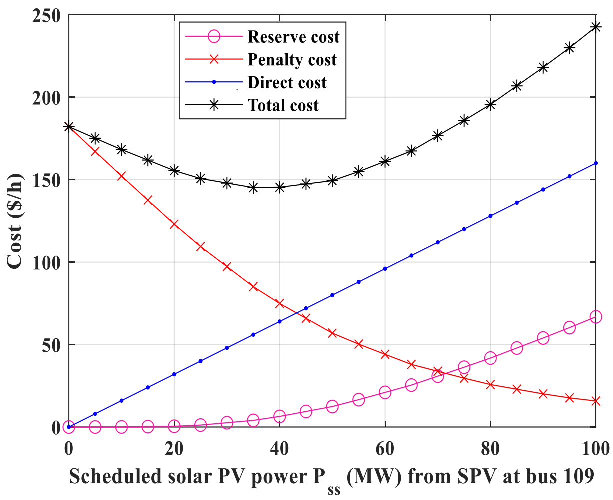

Fig. 6.46: Variation of solar power cost vs scheduled power for solar generator SG:109.

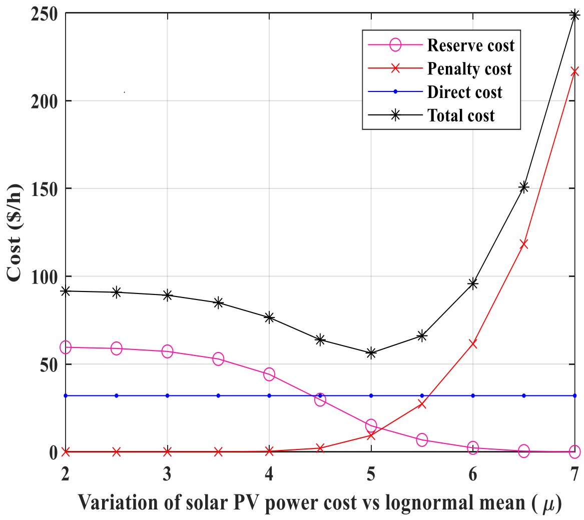

Fig. 6.47: Variation of solar power cost vs lognormal mean for solar generator SG:109.

6.4.2.2. Optimization Results of Modified DZA-114 bus Power System

This section presents the simulation results obtained by applying the proposed algorithm FDB-AOA to the Algerian electrical network DZA-114 bus. It is subdivided into two subsections, detailed as follows:

A. Subsection One: Experimental Results for the proposed FDB-AOA

As a first, we start by the study of the effectiveness of the presence of renewable energy and FACTS devices in the electrical network Algerian DZA-114 bus, for all cases there are three scenarios. By applying the proposed algorithm FDB-AOA the simulation results of the presented technique. The basic case refers to the scenario where renewable energy sources are not taken into account; that is, all power generation is sourced from traditional power plants. In this scenario, the lowest recorded values of active power at bus locations #52, #83, and #109 are 34.5 MW, 30 MW, and 10 MW, respectively [10].

- **B. Scenario 1: without renewable energy and FACTS Devices**
- **C. Scenario 2: with presence of renewable energy sources**
- **D. Scenario 3: with presence of renewable energy and FACTS Devices**

In the following resents the optimization of the Algerian electricity network.

- **Case-1: Generation Cost (C_{gen})**:

this case selected the **Generation Cost (C_{gen} (\$/h))** as a fitness function. the simulation results of the presented technique. for three scenarios, the simulation results of the presented technique. for all scenarios, by applying the proposed metaheuristic Approach have been represent in the **table (6.52)**. The convergence behaviors comparison of FDB-AOA with other methods are illustrated in **figure (6.48)** for the three scenarios.

Table. 6.52: Solution of optimal power flow case 1 for DZA-114 bus system: Case-1.

Control variables	Min	Max	scenario 1	scenario 2	scenario 3	Parameters	Min	Max	scenario 1	scenario 2	scenario 3
P_{TG5}(MW)	135	1350	556.1998	465.9248	461.9142	P_{TG1} (MW)	135	1350	374.24865	474.42740	518.48258
P_{TG11}(MW)	10	100	93.8256	99.9910	99.5614	Q_{TG4} (MVAr)	-20	400	345.53355	232.37749	335.88404
P_{TG15}(MW)	30	300	291.5430	228.0022	238.1138	Q_{TG5} (MVAr)	-20	200	165.86197	198.64986	144.92563
P_{TG17}(MW)	135	1350	424.1314	508.9761	358.7840	Q_{TG11} (MVAr)	-50	100	97.08369	91.17042	56.34043
P_{TG19}(MW)	34.5	345	147.5310	80.2968	148.5362	Q_{WG15}(MVAr)	0	100	23.02280	50.95361	86.54041
P_{TG22}(MW)	34.5	345	266.7542	200.3255	198.7597	Q_{TG17} (MVAr)	0	400	389.76445	396.78095	365.17593
P_{WG52}(MW)	0	345	228.4193	233.8165	249.7531	Q_{TG19} (MVAr)	0	60	30.37808	51.51982	54.99395
P_{TG80}(MW)	34.5	345	274.9511	129.4540	125.2871	Q_{TG22} (MVAr)	0	50	42.75701	49.93567	45.88815
P_{WG83}(MW)	0	300	196.9859	299.9909	299.1754	Q_{WG52}(MVAr)	0	50	40.76992	49.73146	37.09840

P_{TG98}(MW)	30	300	103.2280	116.5992	166.0966	Q_{TG80} (MVAr)	0	60	41.82416	59.05195	56.98448
P_{TG100}(MW)	60	600	510.8764	599.9638	595.6483	Q_{WG83}(MVAr)	-50	200	171.56755	97.84903	152.74855
P_{TG101}(MW)	20	200	191.7231	199.9889	191.6375	Q_{TG98} (MVAr)	0	50	20.38886	48.51327	39.19980
P_{SG109}(MW)	0	100	92.3840	99.9916	99.1559	Q_{TG100} (MVAr)	0	270	200.59274	269.57622	203.49547
P_{TG111}(MW)	10	200	57.4832	63.9715	57.9883	Q_{TG101} (MVAr)	-50	200	110.52414	40.19253	45.64993
V_4(p.u)	0.90	1.10	1.0218	1.0396	1.0407	Q_{SG109} (MVAr)	-50	100	44.41023	24.58844	33.25297
V_5(p.u)	0.90	1.10	1.0138	1.0346	1.0321	Q_{TG111} (MVAr)	-50	155	51.85276	41.05474	68.95389
V_{11}(p.u)	0.90	1.10	1.0108	1.0337	1.0053						
V_{15}(p.u)	0.90	1.10	1.0088	1.0334	1.0458						
V_{17}(p.u)	0.90	1.10	1.0188	1.0616	1.0231						
V_{19}(p.u)	0.90	1.10	0.9877	1.0380	0.9743	**C_{gen} ($/h)**			**17512.661**	**16661.1543**	**16630.4160**
V_{22}(p.u)	0.90	1.10	1.0014	1.0223	1.0010	**P_{loss} (MW)**			83.2848	74.7202	81.8940
V_{52}(p.u)	0.90	1.10	1.0195	1.0427	1.0004	**C_{gross} ($/h)**			25841.1395	24133.17627	24819.8208
V_{80}(p.u)	0.90	1.10	0.9879	1.0239	0.9969	**VD (p.u)**			3.00517	3.16939	3.42089
V_{83}(p.u)	0.90	1.10	1.0297	1.0618	1.0436	**Emission (ton/h)**			3.90787	5.49336	5.27087
V_{98}(p.u)	0.90	1.10	1.0163	1.0690	1.0333	**stability index**			0.351785	0.330046	0.343555
V_{100}(p.u)	0.90	1.10	1.0406	1.0949	1.0557	**Thermal gen cost ($/h)**			17383.60353	15661.8799	15508.59516
V_{101}(p.u)	0.90	1.10	1.0252	1.0489	1.0195	**Valveff cost ($/h)**			129.05748	66.057318	77.188664
V_{109}(p.u)	0.90	1.10	1.0526	1.0341	1.0264	**Fuelvlv cost ($/h)**			17512.6610	15727.9372	15585.7838
V_{111}(p.u)	0.90	1.10	1.0173	1.0528	1.0976	**Tgen cost ($/h)**			17383.60352	16595.0969	16553.22729
T_{80-88}(p.u)	0.90	1.10	0.9060	0.9286	0.9073	**Wind cost ($/h)**				761.8061	889.9099
T_{81-90}(p.u)	0.90	1.10	0.9429	1.0427	1.0209	**Solar cost ($/h)**				171.4110	154.7223
T_{86-93}(p.u)	0.90	1.10	0.9506	0.9411	0.9474						
T_{42-41}(p.u)	0.90	1.10	0.9426	0.9326	1.0246						
T_{58-57}(p.u)	0.90	1.10	0.9886	0.9877	0.9816						
T_{44-43}(p.u)	0.90	1.10	0.9480	1.0288	0.9707						
T_{60-59}(p.u)	0.90	1.10	0.9157	0.9623	0.9777						
T_{64-63}(p.u)	0.90	1.10	0.9148	0.9812	0.9335						
T_{72-71}(p.u)	0.90	1.10	0.9387	0.9769	0.9654						
T_{17-18}(p.u)	0.90	1.10	1.0011	1.0323	0.9706						
T_{21-20}(p.u)	0.90	1.10	0.9261	0.9995	0.9331						
T_{27-26}(p.u)	0.90	1.10	0.9487	0.9111	1.0332						
T_{28-26}(p.u)	0.90	1.10	1.0072	0.9511	1.0122						
T_{31-30}(p.u)	0.90	1.10	1.0305	1.0699	1.0667						
T_{48-47}(p.u)	0.90	1.10	0.9606	1.0103	0.9604						
T_{76-74}(p.u)	0.90	1.10	1.0383	0.9256	1.0199						
FACTS rating						FACTS location					**scenario 3**
$\tau_{TCSC\ 1}$(%)	0	50%			20.31	TCSC1 branch, (con. buses):					99 (73-67)
$\tau_{TCSC\ 2}$(%)	0	50%			17.58	TCSC2 branch, (con. buses):					148 (93-91)
Φ_{TCPS1} (deg)	- 5°	5°			4.5384	TCPS1 branch, (con. buses):					142 (99-102)
Φ_{TCPS2} (deg)	- 5°	5°			4.0411	TCPS2 branch, (con. buses):					122(87-99)
Q_{SVC1} (MVAr)	- 10	10			9.0334	SVC1 bus no:					89
Q_{SVC2} (MVAr)	- 10	10			6.2498	SVC2 bus no:					57

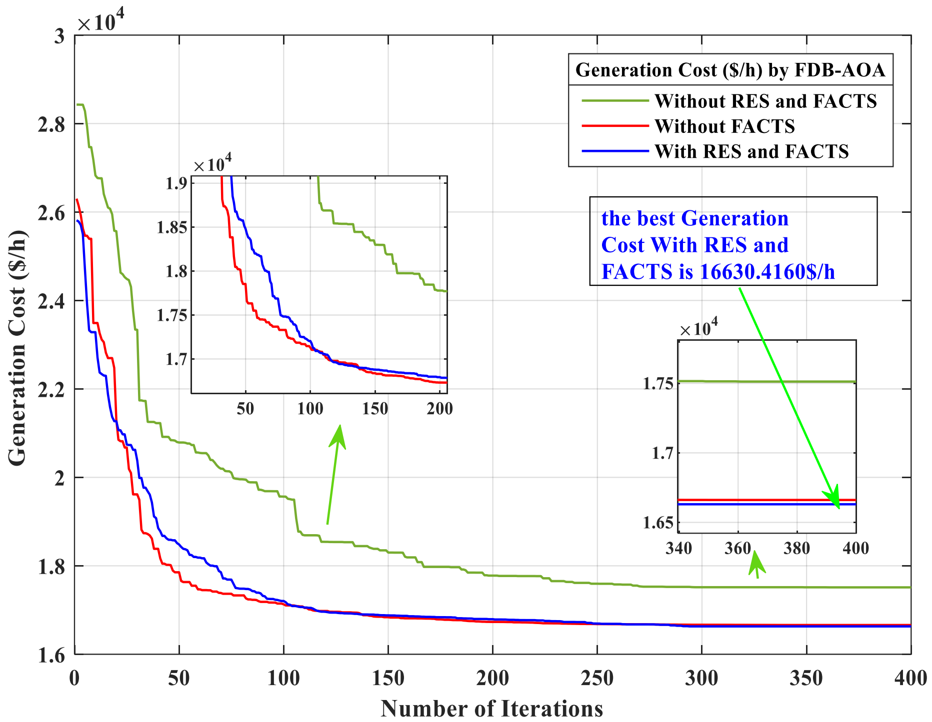

Fig. 6.48: Convergence behaviors comparison: Case-1: modified DZA-114 bus.

Case-2: Real power losses (P_{loss} (MW)):

The fitness function selected in this case is the **Real power losses (Ploss (MW))**. The **table (6.53)** shows the simulation results of the presented technique FDB-AOA without renewable energy, with renewable energy, and with renewable energy and Facts devices attained the most favorable P_{loss} **(MW)** value, reaching (**62.9773 MW**). The convergence behaviors comparison providing by FDB-AOA are illustrated in **figure (6.49).**

Table. 6.53: The optimized results of FDB-AOA: Case-2: DZA-114 bus.

Control variables	Min	Max	scenario 1	scenario 2	scenario 3	Parameters	Min	Max	scenario 1	scenario 2	scenario 3
P_{TG5}(MW)	135	1350	227.6195	366.8473	402.8842	P_{TG1} (MW)	135	1350	776.94508	554.07576	548.31218
P_{TG11}(MW)	10	100	97.1474	99.8166	99.9092	Q_{TG4} (MVAr)	-20	400	276.40207	293.14102	239.08457
P_{TG15}(MW)	30	300	179.4398	186.1784	190.5300	Q_{TG5} (MVAr)	-20	200	187.91008	155.12602	192.84516
P_{TG17}(MW)	135	1350	468.5123	605.3354	622.8335	Q_{TG11} (MVAr)	-50	100	87.45018	77.27976	97.36909
P_{TG19}(MW)	34.5	345	137.1819	154.8844	112.6113	Q_{WG15} (MVAr)	0	100	37.27993	79.23104	84.72056
P_{TG22}(MW)	34.5	345	204.5337	178.8048	165.3513	Q_{TG17} (MVAr)	0	400	375.94974	397.13757	359.40523
P_{WG52}(MW)	0	345	213.3829	187.7838	170.6650	Q_{TG19} (MVAr)	0	60	51.63688	60.21428	59.30509
P_{TG80}(MW)	34.5	345	306.8478	284.3871	272.0978	Q_{TG22} (MVAr)	0	50	36.30840	48.74670	49.30335
P_{WG83}(MW)	0	300	223.5767	202.3720	217.5344	Q_{WG52} (MVAr)	0	50	39.85477	47.64316	48.75215
P_{TG98}(MW)	30	300	207.5762	224.2241	233.4851	Q_{TG80} (MVAr)	0	60	53.29295	57.08695	59.46096
P_{TG100}(MW)	60	600	406.9653	359.1122	353.8170	Q_{WG83} (MVAr)	-50	200	94.84307	152.42058	185.75001
P_{TG101}(MW)	20	200	199.8173	194.1877	199.9756	Q_{TG98} (MVAr)	0	50	35.43100	45.24280	37.24732

P_{SG109}(MW)	0	100	49.5848	96.8825	99.9767	Q_{TG100} (MVAr)	0	270	251.87183	159.30657	94.50227
P_{TG111}(MW)	10	200	95.4606	97.2468	99.9941	Q_{TG101} (MVAr)	-50	200	50.16684	31.08290	41.19205
V_4(p.u)	0.90	1.10	1.0649	1.0263	1.0734	Q_{SG109} (MVAr)	-50	100	47.78152	22.48069	31.47764
V_5(p.u)	0.90	1.10	1.0554	1.0168	1.0687	Q_{TG111} (MVAr)	-50	155	15.94389	49.71556	41.05888
V_{11}(p.u)	0.90	1.10	1.0547	1.0122	1.0709						
V_{15}(p.u)	0.90	1.10	1.0481	1.0242	1.0763						
V_{17}(p.u)	0.90	1.10	1.0656	1.0539	1.0609						
V_{19}(p.u)	0.90	1.10	1.0168	1.0216	1.0281						
V_{22}(p.u)	0.90	1.10	1.0184	1.0264	1.0217	**C_{gen} (\$/h)**			22819.4358	19968.7342	19992.0372
V_{52}(p.u)	0.90	1.10	1.0168	1.0457	1.0237	**P_{loss} (MW)**			**67.5911**	**65.1388**	**62.9773**
V_{80}(p.u)	0.90	1.10	1.0425	1.0073	1.0151	**C_{gross} (\$/h)**			29578.55070	26482.61763	26289.76718
V_{83}(p.u)	0.90	1.10	1.0666	1.0406	1.0522	**VD(p.u)**			3.73560	2.45509	3.35010
V_{98}(p.u)	0.90	1.10	1.0750	1.0365	1.0380	**Emission (ton/h)**			6.92042	5.22653	5.34579
V_{100}(p.u)	0.90	1.10	1.0966	1.0486	1.0440	**stability index**			0.3202137	0.3479633	0.3315744
V_{101}(p.u)	0.90	1.10	1.0602	1.0187	1.0320	**Thermal gen cost (\$/h)**			22685.22184	17928.24419	17954.18881
V_{109}(p.u)	0.90	1.10	1.0821	0.9975	1.0461	**Valveff cost (\$/h)**			134.213933	106.25916	106.82048
V_{111}(p.u)	0.90	1.10	1.0109	1.0880	1.0719	**Fuelvlv cost (\$/h)**			22819.4358	18034.5034	18061.0093
T_{80-88}(p.u)	0.90	1.10	1.0025	0.9005	0.9841	**Tgen cost (\$/h)**			22685.22184	19862.47507	19885.21670
T_{81-90}(p.u)	0.90	1.10	0.9630	0.9003	0.9495	**Wind gen cost (\$/h)**				1643.0102	548.31218
T_{86-93}(p.u)	0.90	1.10	0.9824	0.9018	0.9304	**Solar gen cost (\$/h)**				291.2207	239.08457
T_{42-41}(p.u)	0.90	1.10	0.9232	0.9133	0.9572						
T_{58-57}(p.u)	0.90	1.10	1.0025	0.9160	0.9696						
T_{44-43}(p.u)	0.90	1.10	0.9967	0.9563	0.9900						
T_{60-59}(p.u)	0.90	1.10	1.0181	0.9299	0.9747						
T_{64-63}(p.u)	0.90	1.10	1.0101	0.9407	0.9122						
T_{72-71}(p.u)	0.90	1.10	0.9489	0.9069	0.9625						
T_{17-18}(p.u)	0.90	1.10	1.0126	0.9965	1.0278						
T_{21-20}(p.u)	0.90	1.10	0.9988	0.9853	1.0148						
T_{27-26}(p.u)	0.90	1.10	0.9963	1.0652	0.9870						
T_{28-26}(p.u)	0.90	1.10	0.9932	0.9121	0.9702						
T_{31-30}(p.u)	0.90	1.10	1.0846	1.0352	1.0938						
T_{48-47}(p.u)	0.90	1.10	0.9371	0.9391	0.9844						
T_{76-74}(p.u)	0.90	1.10	1.0208	1.0557	1.0655						
FACTS rating						FACTS location					**scenario 3**
$\boldsymbol{\tau_{TCSC\ 1}}$(%)	0	50%			38.50	TCSC1 branch, (con. buses):					75 (29-39)
$\boldsymbol{\tau_{TCSC\ 2}}$(%)	0	50%			49.27	TCSC2 branch, (con. buses):					21 (9-3)
$\boldsymbol{\Phi_{TCPS1}}$ **(deg)**	- 5°	5°			3.8151	TCPS1 branch, (con. buses):					134 (98-97)
$\boldsymbol{\Phi_{TCPS2}}$ **(deg)**	- 5°	5°			3.0398	TCPS2 branch, (con. buses):					101 (29-26)
$\boldsymbol{Q_{SVC1}}$ **(MVAr)**	- 10	10			9.9608	SVC1 bus no:					34
$\boldsymbol{Q_{SVC2}}$ **(MVAr)**	- 10	10			5.6624	SVC2 bus no:					81

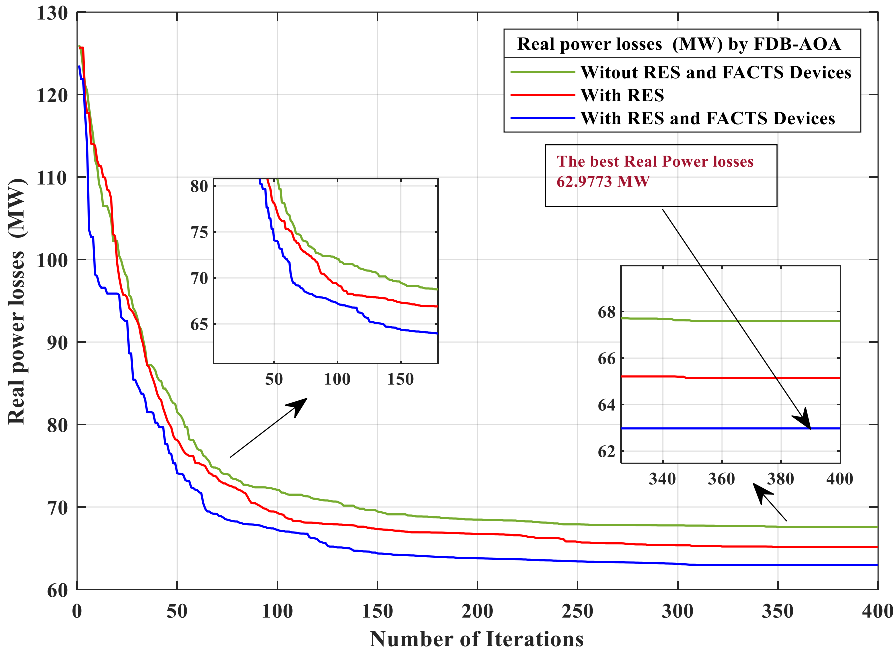

Fig. 6.49: Convergence behaviors comparison: Case-2: modified DZA-114 bus

Case 3: Gross cost (C_{gross} ($/h)):

The third case selected the **Gross cost (C_{gross} ($/h))** as a fitness function. The **table (6.54)** displays the optimized results of the presented method FDB-AOA achieved the best **C_{gross} (23784.4379 $/h)** compared to the obtained results with the presence and absence of RES. The convergence behaviors comparison of the three scenarios for the third case by FDB-AOA are depicted in **figure (6.50).**

Table. 54: The optimized results by FDB-AOA: Case-3: modified DZA-114 bus.

Control variables	Min	Max	scenario 1	scenario 2	scenario 3	Parameters	Min	Max	scenario 1	scenario 2	scenario 3
P_{TG5}(MW)	135	1350	785.1830	447.1735	473.2426	P_{TG1} (MW)	135	1350	298.07441	472.56968	482.15441
P_{TG11}(MW)	10	100	77.2254	98.5127	99.0198	Q_{TG4} (MVAr)	-20	400	334.59475	380.89797	314.50688
P_{TG15}(MW)	30	300	121.6791	215.0994	195.0887	Q_{TG5} (MVAr)	-20	200	162.74499	92.13344	134.80142
P_{TG17}(MW)	135	1350	628.9116	461.8681	513.7074	Q_{TG11} (MVAr)	-50	100	60.27126	96.93216	89.83804
P_{TG19}(MW)	34.5	345	105.7152	156.2468	79.5261	Q_{WG15} (MVAr)	0	100	67.28885	22.13463	85.84978
P_{TG22}(MW)	34.5	345	188.4839	190.5059	201.8655	Q_{TG17} (MVAr)	0	400	404.30547	393.81528	391.55670
P_{WG52}(MW)	0	345	198.9683	227.8482	228.4906	Q_{TG19} (MVAr)	0	60	56.10315	58.56292	57.18597
P_{TG80}(MW)	34.5	345	248.5958	135.3215	139.0835	Q_{TG22} (MVAr)	0	50	44.39879	45.67603	32.02381
P_{WG83}(MW)	0	300	242.4486	299.6609	299.8989	Q_{WG52} (MVAr)	0	50	45.90259	48.14397	47.81613
P_{TG98}(MW)	30	300	89.2866	125.0556	105.7301	Q_{TG80} (MVAr)	0	60	27.86978	58.19586	57.02977
P_{TG100}(MW)	60	600	494.1318	596.8551	598.1138	Q_{WG83} (MVAr)	-50	200	174.12187	192.50057	123.92047
P_{TG101}(MW)	20	200	138.8126	199.1522	199.1147	Q_{TG98} (MVAr)	0	50	9.85596	41.34431	49.45380
P_{SG109}(MW)	0	100	86.4573	99.3665	99.5515	Q_{TG100} (MVAr)	0	270	230.09519	152.12191	145.12235
P_{TG111}(MW)	10	200	98.8897	76.5413	83.3527	Q_{TG101} (MVAr)	-50	200	16.27542	42.15751	50.77294
V_4(p.u)	0.90	1.10	1.0458	1.0135	1.0790	Q_{SG109} (MVAr)	-50	100	60.63561	47.20379	32.84909
V_5(p.u)	0.90	1.10	1.0411	0.9968	1.0703	Q_{TG111} (MVAr)	-50	155	40.26622	52.33044	53.07069
V_{11}(p.u)	0.90	1.10	1.0122	1.0104	1.0706						
V_{15}(p.u)	0.90	1.10	1.0361	0.9900	1.0810						

V_{17}(p.u)	0.90	1.10	1.0429	1.0368	1.0585				
V_{19}(p.u)	0.90	1.10	0.9912	0.9833	1.0346				
V_{22}(p.u)	0.90	1.10	1.0065	1.0002	1.0211	**C_{gen} (\$/h)**	16424.8653	16527.1571	16690.3918
V_{52}(p.u)	0.90	1.10	1.0333	1.0207	1.0737	**P_{loss} (MW)**	75.8633	74.7775	70.9405
V_{80}(p.u)	0.90	1.10	0.9815	1.0152	0.9854	**C_{gross} (\$/h)**	**24011.1955**	**24004.9105**	**23784.4379**
V_{83}(p.u)	0.90	1.10	1.0300	1.0634	1.0258	**VD (p.u)**	3.00685	3.03252	3.33075
V_{98}(p.u)	0.90	1.10	1.0146	1.0378	1.0326	**Emission (ton/h)**	3.41392	5.21041	5.52862
V_{100}(p.u)	0.90	1.10	1.0426	1.0582	1.0429	**stability index**	0.3376246	0.3576617	0.3106125
V_{101}(p.u)	0.90	1.10	1.0016	1.0270	1.0312	**Fuelvlv cost (\$/h)**	16424.8653	15515.9205	16690.3918
V_{109}(p.u)	0.90	1.10	1.0887	1.0651	1.0489	**Thermal gen cost (\$/h)**	16296.91091	15416.79127	15623.1771
V_{111}(p.u)	0.90	1.10	1.0226	1.0814	1.0851	**Tgen cost (\$/h)**	16424.8655	16428.02788	16622.3903
T_{80-88}(p.u)	0.90	1.10	0.9066	0.9122	0.9003	**Valveff cost (\$/h)**	127.954593	99.129267	68.001462
T_{81-90}(p.u)	0.90	1.10	0.9683	0.9115	0.9067	**Wind gen cost (\$/h)**		797.7281	761.5114
T_{86-93}(p.u)	0.90	1.10	0.9220	0.9098	0.9030	**Solar gen cost (\$/h)**		213.5085	237.7017
T_{42-41}(p.u)	0.90	1.10	0.9266	0.9482	1.0075				
T_{58-57}(p.u)	0.90	1.10	1.0219	0.9045	0.9165				
T_{44-43}(p.u)	0.90	1.10	0.9080	1.0866	0.9385				
T_{60-59}(p.u)	0.90	1.10	0.9221	0.9687	0.9279				
T_{64-63}(p.u)	0.90	1.10	0.9615	0.9494	0.9166				
T_{72-71}(p.u)	0.90	1.10	0.9619	0.9779	0.9790				
T_{17-18}(p.u)	0.90	1.10	1.0022	1.0085	1.0299				
T_{21-20}(p.u)	0.90	1.10	1.0006	0.9973	1.0072				
T_{27-26}(p.u)	0.90	1.10	0.9932	0.9810	0.9421				
T_{28-26}(p.u)	0.90	1.10	1.0201	1.0782	0.9664				
T_{31-30}(p.u)	0.90	1.10	1.0517	1.0586	1.0091				
T_{48-47}(p.u)	0.90	1.10	0.9439	0.9657	0.9473				
T_{76-74}(p.u)	0.90	1.10	0.9471	1.0990	0.9965				
FACTS rating						**FACTS location**			**scenario 3**
$\tau_{TCSC\ 1}$(%)	0	50%			47.45	TCSC1 branch, (con. buses):			73 (26-34)
$\tau_{TCSC\ 2}$(%)	0	50%			44.120	TCSC2 branch, (con. buses):			133 (100-97)
Φ_{TCPS1} **(deg)**	- 5°	5°			4.4120	TCPS1 branch, (con. buses):			88 (52-30)
Φ_{TCPS2} **(deg)**	- 5°	5°			4.0727	TCPS2 branch, (con. buses):			90 (40-41)
Q_{SVC1} **(MVAr)**	- 10	10			7.6360	SVC1 bus no:			96
Q_{SVC2} **(MVAr)**	- 10	10			8.7643	SVC2 bus no:			81

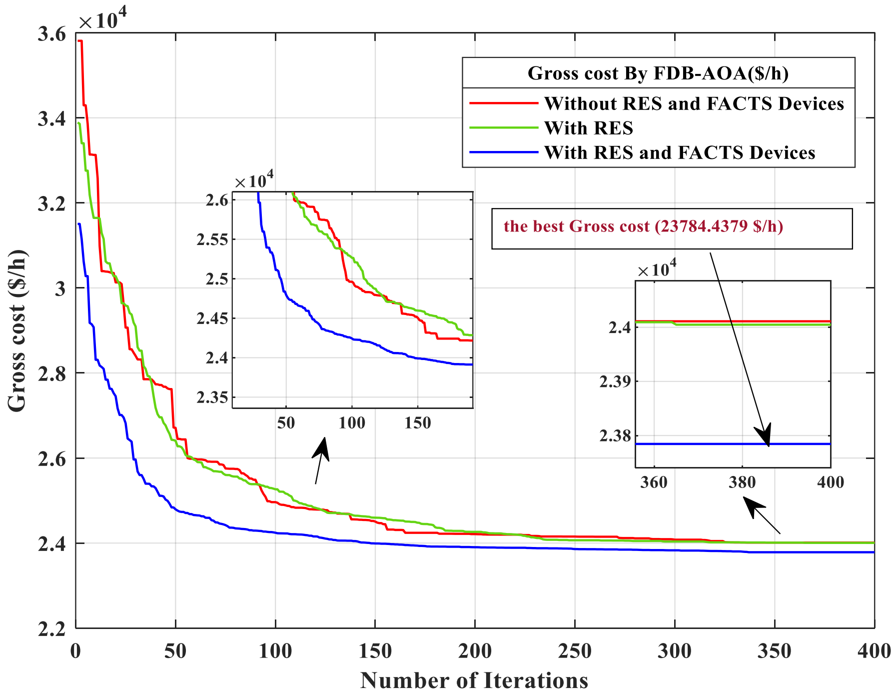

Fig. 6.50: convergence behaviors comparison: Case-3: modified DZA-114 bus.

Analysis of the results with presence of RESs and FACTS devices: modified DZA-114 bus.

This part is dedicated to confirming and evaluating the efficiency of the reported approach, FDB-AOA in solving OPF problems on the modified Algerian electric transmission network DZA-114 bus. The optimization results of all cases studied are summarized, explanted, discussed and analyzed are provided in the **table (6.55).** As well as the details of the parameters that resulted in the optimization of the adopted network, for each objective function. Which including the optimized results of control variables, including the locations and sizing of FACTS device optimized, as well as the busses and branch numbers where connections are specified as means, the buses where connected the SVCs, and branch numbers where connection are designated for TCSC and TCPS, all these are mentioned in the **table (6.55).**

In Case-1, wherein the aim is to optimize the fitness function generation cost ($\boldsymbol{C_{\text{gen}}}$ **($/h)** in **eq. (2.27)),** the reported algorithm can be successful favorable results with a cost value of **16630.4160 $/h**. The Bus 89 and bus 57 are identified as the optimal locations for the two SVCs in this case. The branches numbers for TCSC and TCPS, as applicable in this optimization case are 99,148, 142, and 122, respectively, that are frequently certainly operating at or near in their middle capabilities. FACTS devices are often installed in networks to enhance loading capability.

In Case-2, wherein the objective is the minimization of real power loss ($\boldsymbol{P_{\text{loss}}}$ **(MW) in eq. (2.28))**, both the FACTS devices allocation and rating is optimized in a way to enhance loading capacity a maximum of network. Due to that, the proposed algorithm can be attained a favorable result with a real power loss of **62.9773 MW**. The scheduling outcomes of wind generators are commonly more than the thermal units due to their less cost.

The optimal locations for the two SVCs in in this case are the buses 34 and 81. While the best favorable branches numbers for connecting the TCSC and TCPS in this optimization case are 75, 21, 134, and 101, respectively, FACTS devices are frequently utilized in power systems to enhance their loading capacity.

In **Case-3**, where the primary objective is to minimize the gross cost ($\boldsymbol{C_{\text{gross}}}$ **($/h) (eq.(2.33))**). This objective highlights the crucial importance of combining both cost and loss considerations into a single objective function. One of a simple way to achieve this is the creating a cost model that incorporates the converted energy cost equivalent of the loss.

The best optimum value of the gross cost achieved by the proposed method is **23784.4379 $/h**. It is well-established that in case 3, the optimal cost of generation, when combined with the cost of losses, depends on the price coefficients for both wind and thermal power generator units, as well as the unit price of energy. Nevertheless, when both objectives are considered together, it results in a reduced gross cost (**C_{gross}**). The optimal locations for the two SVCs in in this case are the buses 96 and 81. Also The best favorable branches numbers for connecting the TCSC and TCPS in this optimization case are 73, 133, 88, and 90, respectively.

Table. 6.55: the optimized results of the adopted test system for all cases utilizing FBD-AOA for the scenario three: modified DZA-114 bus.

Control variables	**Min**	**Max**	**Case1**	**Case 2**	**Case 3**	**Parameters**	**Min**	**Max**	**Case1**	**Case 2**	**Case 3**
P_{TG5}(MW)	135	1350	461.9142	402.8842	473.2426	P_{TG1} (MW)	135	1350	518.48258	548.31218	482.15441
P_{TG11}(MW)	10	100	99.5614	99.9092	99.0198	Q_{TG4} (MVAr)	-20	400	335.88404	239.08457	314.50688
P_{TG15}(MW)	30	300	238.1138	190.5300	195.0887	Q_{TG5} (MVAr)	-20	200	144.92563	192.84516	134.80142
P_{TG17}(MW)	135	1350	358.7840	622.8335	513.7074	Q_{TG11} (MVAr)	-50	100	56.34043	97.36909	89.83804
P_{TG19}(MW)	34.5	345	148.5362	112.6113	79.5261	Q_{WG15} (MVAr)	0	100	86.54041	84.72056	85.84978
P_{TG22}(MW)	34.5	345	198.7597	165.3513	201.8655	Q_{TG17} (MVAr)	0	400	365.17593	359.40523	391.55670
P_{WG52}(MW)	0	345	249.7531	170.6650	228.4906	Q_{TG19} (MVAr)	0	60	54.99395	59.30509	57.18597
P_{TG80}(MW)	34.5	345	125.2871	272.0978	139.0835	Q_{TG22} (MVAr)	0	50	45.88815	49.30335	32.02381
P_{WG83}(MW)	0	300	299.1754	217.5344	299.8989	Q_{WG52} (MVAr)	0	50	37.09840	48.75215	47.81613
P_{TG98}(MW)	30	300	166.0966	233.4851	105.7301	Q_{TG80} (MVAr)	0	60	56.98448	59.46096	57.02977
P_{TG100}(MW)	60	600	595.6483	353.8170	598.1138	Q_{WG83} (MVAr)	-50	200	152.74855	185.75001	123.92047
P_{TG101}(MW)	20	200	191.6375	199.9756	199.1147	Q_{TG98} (MVAr)	0	50	39.19980	37.24732	49.45380
P_{SG109}(MW)	0	100	99.1559	99.9767	99.5515	Q_{TG100} (MVAr)	0	270	203.49547	94.50227	145.12235
P_{TG111}(MW)	10	200	57.9883	99.9941	83.3527	Q_{TG101} (MVAr)	-50	200	45.64993	41.19205	50.77294
V_4(p.u)	0.90	1.10	1.0407	1.0734	1.0790	Q_{SG109} (MVAr)	-50	100	33.25297	31.47764	32.84909
V_5(p.u)	0.90	1.10	1.0321	1.0687	1.0703	Q_{TG111} (MVAr)	-50	155	68.95389	41.05888	53.07069
V_{11}(p.u)	0.90	1.10	1.0053	1.0709	1.0706						
V_{15}(p.u)	0.90	1.10	1.0458	1.0763	1.0810						
V_{17}(p.u)	0.90	1.10	1.0231	1.0609	1.0585						
V_{19}(p.u)	0.90	1.10	0.9743	1.0281	1.0346						
V_{22}(p.u)	0.90	1.10	1.0010	1.0217	1.0211	**C_{gen} ($/h)**			**16630.4160**	19992.0372	16690.3918
V_{52}(p.u)	0.90	1.10	1.0004	1.0237	1.0737	**P_{loss} (MW)**			81.8940	**62.9773**	70.9405
V_{80}(p.u)	0.90	1.10	0.9969	1.0151	0.9854	**C_{gross} ($/h)**			24819.82080	26289.76718	**23784.4379**
V_{83}(p.u)	0.90	1.10	1.0436	1.0522	1.0258	**Thgen cost ($/h)**			15508.59516	17954.18881	15623.1771
V_{98}(p.u)	0.90	1.10	1.0333	1.0380	1.0326	**Valveff cost ($/h)**			77.188664	106.8204807	68.0014615
V_{100}(p.u)	0.90	1.10	1.0557	1.0440	1.0429	**Wind cost ($/h)**			889.9099	1628.5291	761.5114
V_{101}(p.u)	0.90	1.10	1.0195	1.0320	1.0312	**Solar cost($/h)**			154.7223	302.4988	237.7017
V_{109}(p.u)	0.90	1.10	1.0264	1.0461	1.0489	**Fuelvlv cost ($/h)**			15585.7838	18061.0093	16690.3918
V_{111}(p.u)	0.90	1.10	1.0976	1.0719	1.0851	**VD (p.u)**			3.42089	3.35010	3.33075
T_{80-88}(p.u)	0.90	1.10	0.9073	0.9841	0.9003	**Emission (ton/h)**			5.27087	5.34579	5.52862
T_{81-90}(p.u)	0.90	1.10	1.0209	0.9495	0.9067	**stability index**			0. 3435543	0.3315744	0.3106125
T_{86-93}(p.u)	0.90	1.10	0.9474	0.9304	0.9030	**tgen cost ($/h)**			**16553.22730**	19885.21670	16622.3903
T_{42-41}(p.u)	0.90	1.10	1.0246	0.9572	1.0075						
T_{58-57}(p.u)	0.90	1.10	0.9816	0.9696	0.9165						
T_{44-43}(p.u)	0.90	1.10	0.9707	0.9900	0.9385						
T_{60-59}(p.u)	0.90	1.10	0.9777	0.9747	0.9279						
T_{64-63}(p.u)	0.90	1.10	0.9335	0.9122	0.9166						
T_{72-71}(p.u)	0.90	1.10	0.9654	0.9625	0.9790						
T_{17-18}(p.u)	0.90	1.10	0.9706	1.0278	1.0299						
T_{21-20}(p.u)	0.90	1.10	0.9331	1.0148	1.0072						
T_{27-26}(p.u)	0.90	1.10	1.0332	0.9870	0.9421						
T_{28-26}(p.u)	0.90	1.10	1.0122	0.9702	0.9664						
T_{31-30}(p.u)	0.90	1.10	1.0667	1.0938	1.0091						
T_{48-47}(p.u)	0.90	1.10	0.9604	0.9844	0.9473						
T_{76-74}(p.u)	0.90	1.10	1.0199	1.0655	0.9965						

FACTS rating						FACTS location	Case1	Case 2	Case 3
$\tau_{TCSC\ 1}$(%)	0	50%	20.31	38.50	47.45	TCSC1 branch, (con. buses):	99 (73-67)	75 (29-39)	73 (26-34)
$\tau_{TCSC\ 2}$(%)	0	50%	17.58	49.27	44.120	TCSC2 branch, (con. buses):	148 (93-91)	21 (9-3)	133 (100-97)
Φ_{TCPS1} (deg)	- 5°	5°	4.5384	3.8151	4.4120	TCPS1 branch, (con. buses):	142 (99-102)	134 (98-97)	88 (52-30)
Φ_{TCPS2} (deg)	- 5°	5°	4.0411	3.0398	4.0727	TCPS2 branch, (con. buses):	122(87-99)	101 (29-26)	90 (40-41)
Q_{SVC1} (MVAr)	- 10	10	9.0334	9.9608	7.6360	SVC1 bus no:	89	34	96
Q_{SVC2} (MVAr)	- 10	10	6.2498	5.6624	8.7643	SVC2 bus no:	57	81	81

The bar chart graph illustrated in the **figure (6.51)**, represents the active power of the generators, excluding the slack generator, for scenario three (with presence of renewable energy and facts devices) for each case (1 to 3).

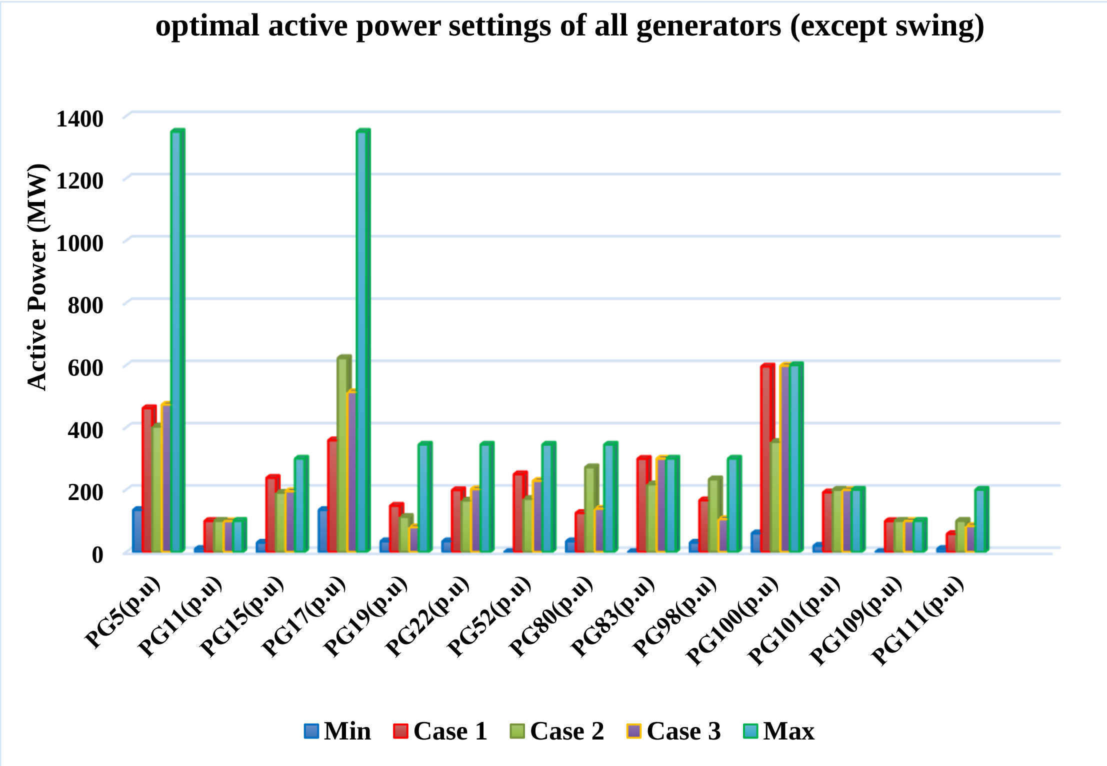

Fig. 6.51: Optimal real power for all generators (excluding slack) for Cases 1 to 3: modified DZA-114 bus.

Additionally, bar chart graph illustrates in the **figures 6.52 (a) and (b)** represent the generator bus voltages and taps transformer (in p.u) for each case, also depicts the permissible intervals of control variables and their corresponding values for achieving optimal solutions for each objective function.

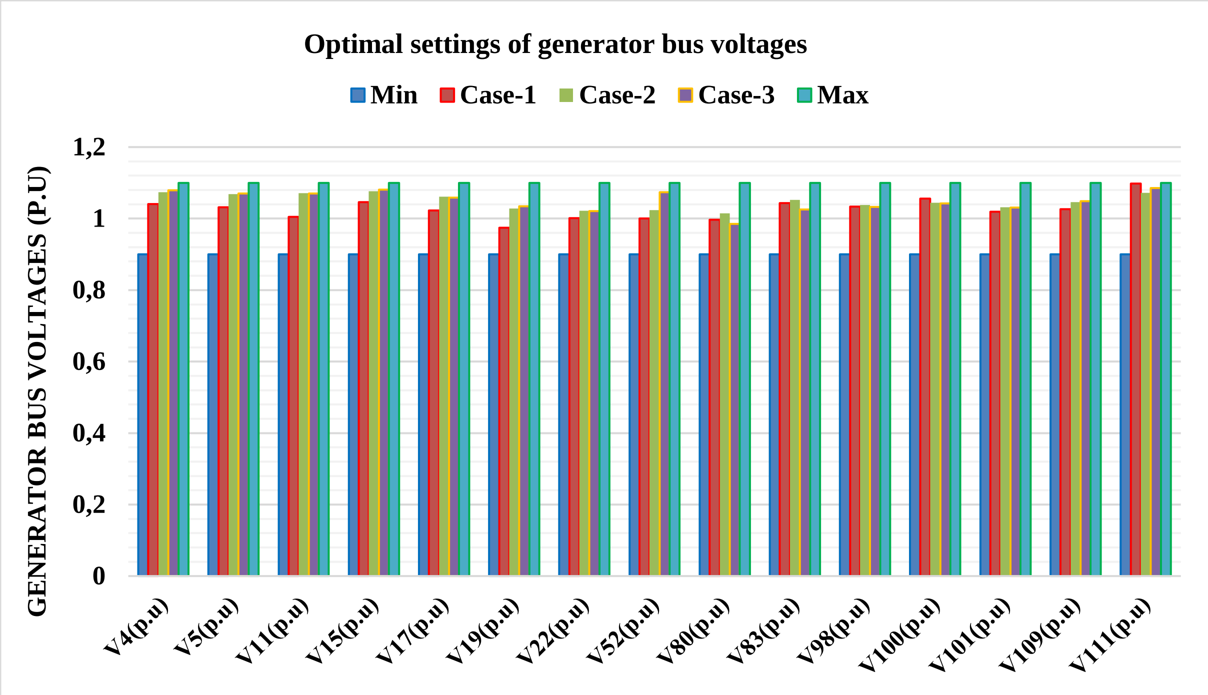

(a)

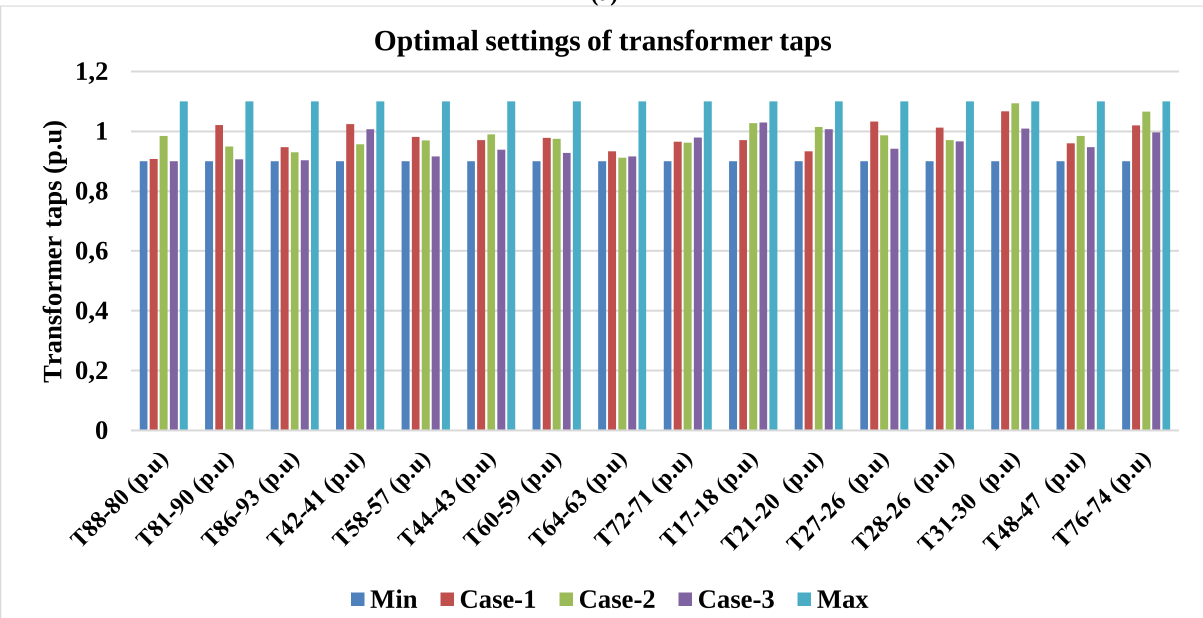

(b)

Fig. 6.52: Optimal voltage of generators bus (a), and taps transformer (b) for Cases 1 to 3: DZA-114 bus.

Breakdown of several costs for all cases (1 to 3) (modified DZA-114 bus)

The bar-chart graph presented in **figure (6.53)** displays the breakdown of different costs. It should be noted that the penalty cost is the lowest cost in all instances of the wind's energy generators. The increased scheduled power from the wind and solar power plants generators results in higher reserve costs for overestimating power plants in the cases 2 and 3. As the direct costs are related to the scheduled output power from the wind generator, they increase with the scheduled power. The total cost of wind or solar power plants generators is the total of direct, penalty, and reserve costs. As illustrated in the **table (6.56)**, owing to the lowest scheduled power of the thermal generators in first case.

Table. 6.56: Breakdown of several prices for each case (modified DZA-114 bus).

Cost	Case 1	Case 2	Case 3
Direct cost wind	491,128394	843,955385	407,561285
Reserve cost wind	293,118927	764,512962	216,661296
Penalty cost wind	105.662542	20,0607665	137.28885
Wind power cost	889,9099	1628,5291	761,5114
Direct cost Solar	92,781251	159,9906	133,36426
Reserve cost solar	38,472212	134.729515	91,97931
Penalty cost solar	23,4688098	7,7786593	12,35812
Solar power cost	154,7223	302,4988	237,7017
Loss cost	8189,4	6297,73	7094,05
Thermal cost	15508,59516	17954,18881	15623,1771
Valve cost	77,188664	106,8204807	68,0014615
Generation Cost	16630,416	19885,2167	16690,3918
Tgen cost	16553,2273	19992,0372	16622,3903
Gross cost	24819,8208	26289,76718	23784,4379

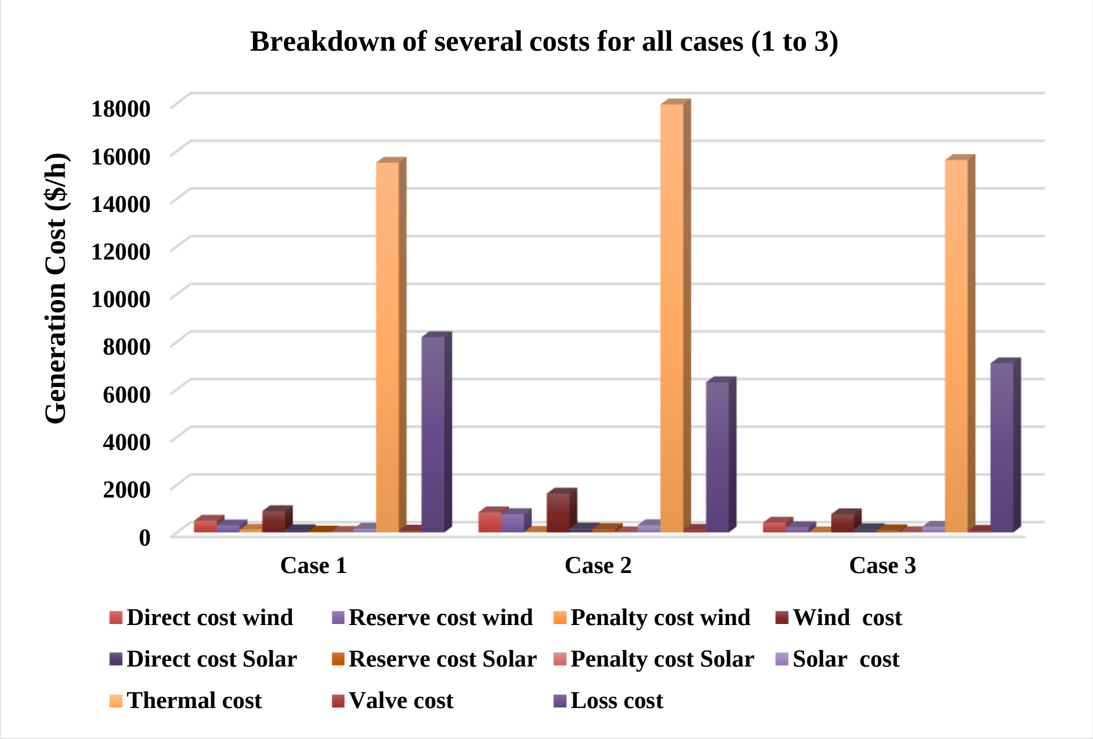

Fig. 6.53: Breakdown of several prices for all Cases-(1 to 3): modified DZA-114 bus.

The voltage profiles of load bused of all the case studies conducted on the modified system are illustrated in **figure (6.54).** The purpose of showcasing the profiles is to demonstrate that the algorithm has successfully adhered to the boundaries to critical constraints. Additionally, it is noteworthy that the generator's active and reactive power limitations have been met in all cases.

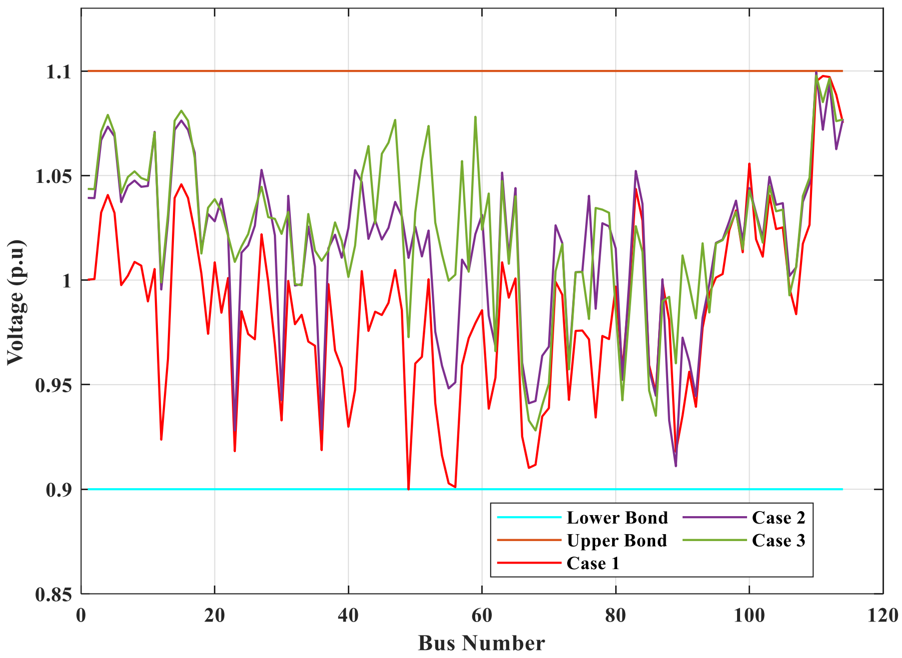

Fig. 6.54: Voltage profiles buses of the modified DZA-114 bus for test cases (Cases-1 to 3) by FBD-AOA.

A. Subsection Two: A comparative studied between the FDB-AOA and other methods

This subsection conducted a comprehensive experimental study to evaluate the performance of the presented metaheuristic algorithm FDB-AOA with several other optimization algorithms such as SHADE-SF, MSA-SF, and ABC-SF. To achieve a rational comparison, the fourth algorithms are compared under the same parameters, 400 iterations, 60 population size. The rest internal parameters considered for these algorithms are mentioned in **table. (6.49)** The optimizations results are given in below.

Case.1: Generation Cost (C_{gen} (\$/h))

The **Generation Cost (C_{gen} (\$/h))** is selected as a fitness function for this case. The **table (6.57)** displays the results of the presented technique compared with other techniques**.** It is confirmed that the FDB-AOA achieved the best C_{gen} with a value of **16747.7449 \$/h** compared to other techniques (SHADE-SF, MSA-SF; ABC-SF). The convergence behaviors comparison of FDB-AOA with other methods are illustrated in **figure (6.55).**

Table. 6.57: The optimized results of the FDB-AOA and other methods: Case.1 (modified DZA-114 bus).

Control variables	Min	Max	FDB-AOA	SHADE	ABC	MSA	Parameters	Min	Max	FDB-AOA	SHADE	ABC	MSA
P_{TG5}(MW)	135	1350	461.9142	538.9198	490.0732	473.5571	P_{TG1} (MW)	135	1350	518.48258	477.49608	476.82729	596.30831
P_{TG11}(MW)	10	100	99.5614	99.9389	99.9014	93.6510	Q_{TG4} (MVAr)	-20	400	335.88404	309.85633	289.21022	368.36070
P_{TG15}(MW)	30	300	238.1138	224.0488	239.0153	228.0677	Q_{TG5} (MVAr)	-20	200	144.92563	195.19286	190.09565	135.33789

P_{TG17}(MW)	135	1350	358.7840	434.4517	503.7204	352.1022
P_{TG19}(MW)	34.5	345	148.5362	80.3767	80.6871	102.9520
P_{TG22}(MW)	34.5	345	198.7597	204.7490	200.7788	194.3059
P_{WG52}(MW)	0	345	249.7531	240.9844	232.0702	254.9589
P_{TG80}(MW)	34.5	345	125.2871	132.0247	134.3207	150.2361
P_{WG83}(MW)	0	300	299.1754	299.9546	299.9946	294.5519
P_{TG98}(MW)	30	300	166.0966	126.5678	119.5938	106.4810
P_{TG100}(MW)	60	600	595.6483	599.6502	599.6821	586.0254
P_{TG101}(MW)	20	200	191.6375	199.9482	199.9422	189.7541
P_{SG109}(MW)	0	100	99.1559	99.9987	99.9529	96.3634
P_{TG111}(MW)	10	100	57.9883	51.4510	33.3685	90.2828
V_4(p.u)	0.90	1.10	1.0407	1.0520	1.0622	1.0349
V_5(p.u)	0.90	1.10	1.0321	1.0469	1.0565	1.0244
V_{11}(p.u)	0.90	1.10	1.0053	1.0387	1.0450	0.9909
V_{15}(p.u)	0.90	1.10	1.0458	1.0382	1.0521	1.0290
V_{17}(p.u)	0.90	1.10	1.0231	1.0260	1.0571	1.0156
V_{19}(p.u)	0.90	1.10	0.9743	0.9837	1.0080	0.9706
V_{22}(p.u)	0.90	1.10	1.0010	0.9784	1.0162	0.9597
V_{52}(p.u)	0.90	1.10	1.0004	1.0141	1.0222	1.0361
V_{80}(p.u)	0.90	1.10	0.9969	1.0077	1.0064	0.9892
V_{83}(p.u)	0.90	1.10	1.0436	1.0534	1.0451	1.0322
V_{98}(p.u)	0.90	1.10	1.0333	1.0343	1.0500	1.0396
V_{100}(p.u)	0.90	1.10	1.0557	1.0630	1.0726	1.0659
V_{101}(p.u)	0.90	1.10	1.0195	1.0306	1.0558	1.0398
V_{109}(p.u)	0.90	1.10	1.0264	1.0249	1.0613	0.9986
V_{111}(p.u)	0.90	1.10	1.0976	1.0968	1.0852	1.0556
T_{80-88}(p.u)	0.90	1.10	0.9073	0.9178	0.9416	0.9699
T_{81-90}(p.u)	0.90	1.10	1.0209	0.9396	0.9501	0.9290
T_{86-93}(p.u)	0.90	1.10	0.9474	0.9104	0.9770	0.9496
T_{42-41}(p.u)	0.90	1.10	1.0246	1.0227	0.9139	0.9301
T_{58-57}(p.u)	0.90	1.10	0.9816	0.9088	0.9780	0.9335
T_{44-43}(p.u)	0.90	1.10	0.9707	0.9973	0.9378	0.9315
T_{60-59}(p.u)	0.90	1.10	0.9777	0.9687	0.9860	0.9268
T_{64-63}(p.u)	0.90	1.10	0.9335	0.9298	0.9163	0.9116
T_{72-71}(p.u)	0.90	1.10	0.9654	0.9311	1.0218	0.9357
T_{17-18}(p.u)	0.90	1.10	0.9706	1.0489	1.0254	1.0465
T_{21-20}(p.u)	0.90	1.10	0.9331	1.0055	1.0137	0.9624
T_{27-26}(p.u)	0.90	1.10	1.0332	1.0457	0.9887	0.9641
T_{28-26}(p.u)	0.90	1.10	1.0122	0.9019	0.9871	0.9757
T_{31-30}(p.u)	0.90	1.10	1.0667	1.0496	1.0785	0.9792
T_{48-47}(p.u)	0.90	1.10	0.9604	1.0444	1.0648	1.0441
T_{76-74}(p.u)	0.90	1.10	1.0199	1.0731	0.9182	0.9635
FACTS rating						
$\tau_{TCSC\ 1}$(%)	0	50%	20.31	32.37	32.30	31.29
$\tau_{TCSC\ 2}$(%)	0	50%	17.58	40.78	31.79	07.35
Φ_{TCPS1} **(deg)**	- 5°	5°	4.5384	4.2979	4.3875	3.8571

Q_{TG11} (MVAr)	-50	100	56.34043	92.59276	78.25370	52.11805
Q_{WG15}(MVAr)	0	100	86.54041	29.79417	37.21500	60.33796
Q_{TG17} (MVAr)	0	400	365.17593	352.25180	397.40099	389.03531
Q_{TG19} (MVAr)	0	60	54.99395	47.05665	41.89765	34.94793
Q_{TG22} (MVAr)	0	50	45.88815	35.39275	49.51342	15.46222
Q_{WG52}(MVAr)	0	50	37.09840	49.88547	34.97520	49.97637
Q_{TG80} (MVAr)	0	60	56.98448	51.39960	54.42825	27.95688
Q_{WG83}(MVAr)	-50	200	152.74855	159.38383	105.75656	108.16399
Q_{TG98} (MVAr)	0	50	39.19980	17.74394	20.94143	49.78633
Q_{TG100} (MVAr)	0	270	203.49547	217.30301	225.06597	269.33981
Q_{TG101} (MVAr)	-50	200	45.64993	70.85441	89.04905	105.52876
Q_{SG109} (MVAr)	-50	100	33.25297	30.61340	31.86033	20.67804
Q_{TG111} (MVAr)	-50	155	68.95389	68.01699	68.01100	38.73528

C_{gen} **($/h)**	**16630.4160**	**16753.9977**	**16880.2514**	**16919.2878**
P_{loss} **(MW)**	81.8940	83.5606	82.9285	82.5977
C_{gross} **($/h)**	24819.82080	25110.0601	25173.09738	25179.05623
thgencost	15508.59516	15742.4560	15909.54576	15790.5721
Valveff cost	77.188664	80.5606	80.23501	72.07355
Wind cost	889.9099	793.1042	781.4825	793.7280
Solar cost	154.7223	137.8773	108.9881	262.9141
Fuelvlv cost	15585.7838	15823.0162	15989.78077	15862.6457
VD (p.u)	3.42089	3.24299	3.50660	3.38145
Emission (ton/h)	5.27087	5.60252	5.62912	5.68678
stability index	0. 3435543	0.32203	0.325409	0.35514
Tgen cost ($/h)	**16553.22730**	**16673.43709**	**16800.01638**	**16847.21424**

FACTS location	**FDB-AOA**	**SHADE**	**ABC**	**MSA**
TCSC1 branch, (con. buses):	99 (73-67)	27 (17-27)	145 (94-82)	22 (13-12)
TCSC2 branch, (con. buses):	148 (93-91)	73 (26-34)	16 (10-11)	27 (17-27)
TCPS1 branch, (con. buses):	142 (99-102)	19 (6-3)	102(73-66)	51 (18-37)

Φ_{TCPS2} (deg)	- 5°	5°	4.0411	4.8353	2.7084	3.7475	TCPS2 branch, (con. buses):	122(87-99)	129 (80-84)	142 (99-102)	104 (63-65)
Q_{SVC1} (MVAr)	- 10	10	9.0334	9.4969	7.6969	5.4119	SVC1 bus no:	89	18	102	93
Q_{SVC2} (MVAr)	- 10	10	6.2498	7.1977	7.0490	9.3457	SVC2 bus no:	57	89	84	54

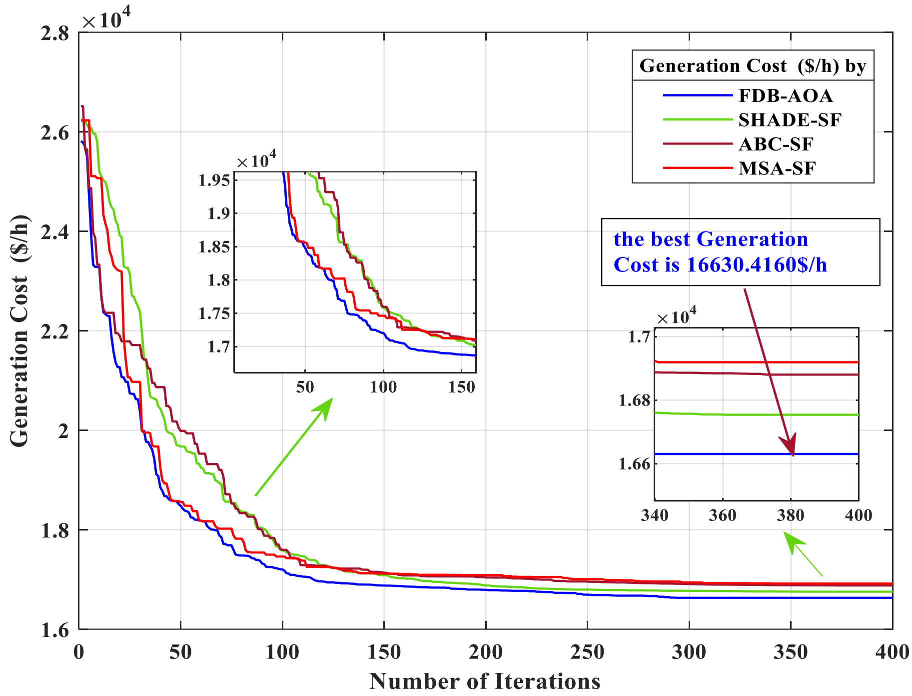

Fig. 6.55: convergence behaviors comparison of FDB-AOA with other methods: Case.1: DZA-114 bus.

Case.2: Real power losses (P_{loss} (MW))

The second case selected the P_{loss} **(MW)** as a fitness function. The **table (6.58)** displays the simulation results of the presented technique compared with other techniques**.** It is confirmed that the FDB-AOA achieved the best P_{loss} **(62.9773 MW)** compared to other techniques (SHADE-SF, MSA-SF; ABC-SF). The convergence behaviors comparison of FDB-AOA with other methods are illustrated in **figure (6.56)**.

Table. 6.58: The optimized results of the FDB-AOA other methods: Case.2: modified DZA-114 bus.

Control variables	Min	Max	FDB-AOA	SHADE	ABC	MSA	Parameters	Min	Max	FDB-AOA	SHADE	ABC	MSA
P_{TG5}(MW)	135	1350	402.8842	216.5239	487.0914	480.4214	P_{TG1} (MW)	135	1350	548.31218	767.03375	484.22350	459.69134
P_{TG11}(MW)	10	100	99.9092	99.9935	99.7103	96.2446	Q_{TG4} (MVAr)	-20	400	239.08457	340.29247	305.19403	298.71951
P_{TG15}(MW)	30	300	190.5300	171.5344	162.1131	221.9652	Q_{TG5} (MVAr)	-20	200	192.84516	117.38470	144.37988	161.85600
P_{TG17}(MW)	135	1350	622.8335	519.7239	633.2669	560.4151	Q_{TG11} (MVAr)	-50	100	97.36909	98.18325	87.20060	98.08329
P_{TG19}(MW)	34.5	345	112.6113	97.9139	79.8163	98.8742	Q_{WG15} (MVAr)	0	100	84.72056	59.44041	82.20170	45.33002
P_{TG22}(MW)	34.5	345	165.3513	196.9078	170.9805	200.7081	Q_{TG17} (MVAr)	0	400	359.40523	398.56038	378.98776	389.66075
P_{WG52}(MW)	0	345	170.6650	199.2492	208.7638	214.2172	Q_{TG19} (MVAr)	0	60	59.30509	56.33806	55.72201	36.24781
P_{TG80}(MW)	34.5	345	272.0978	286.8486	244.5910	253.1673	Q_{TG22} (MVAr)	0	50	49.30335	42.31354	44.65099	40.59195
P_{WG83}(MW)	0	300	217.5344	189.0960	257.4898	255.4150	Q_{WG52} (MVAr)	0	50	48.75215	47.16564	44.09602	48.96663
P_{TG98}(MW)	30	300	233.4851	228.5471	208.0473	171.0998	Q_{TG80} (MVAr)	0	60	59.46096	49.08598	52.01037	49.70409

P_{TG100}(MW)	60	600	353.8170	422.8559	388.9435	420.9639	Q_{WG83} (MVAr)	-50	200	185.75001	176.70218	149.13659	202.52337
P_{TG101}(MW)	20	200	199.9756	199.4018	198.5795	198.5371	Q_{TG98} (MVAr)	0	50	37.24732	29.25648	38.63531	25.19186
P_{SG109}(MW)	0	100	99.9767	98.9315	99.8342	98.1511	Q_{TG100} (MVAr)	0	270	94.50227	71.72491	126.05650	99.37776
P_{TG111}(MW)	10	200	99.9941	97.8332	71.6467	65.6489	Q_{TG101} (MVAr)	-50	200	41.19205	65.45632	62.10014	72.90781
V_4(p.u)	0.90	1.10	1.0734	1.0733	1.0807	1.0808	Q_{SG109} (MVAr)	-50	100	31.47764	38.34423	25.68086	21.58998
V_5(p.u)	0.90	1.10	1.0687	1.0585	1.0727	1.0732	Q_{TG111} (MVAr)	-50	155	41.05888	50.83579	51.35409	46.79738
V_{11}(p.u)	0.90	1.10	1.0709	1.0700	1.0723	1.0780							
V_{15}(p.u)	0.90	1.10	1.0763	1.0614	1.0790	1.0719							
V_{17}(p.u)	0.90	1.10	1.0609	1.0636	1.0700	1.0713	C_{gen} **($/h)**			19992.0372	20797.1811	18961.1326	18434.5115
V_{19}(p.u)	0.90	1.10	1.0281	1.0611	1.0348	1.0281	P_{loss} **(MW)**			**62.9773**	**65.3943**	**68.0976**	**68.5202**
V_{22}(p.u)	0.90	1.10	1.0217	1.0537	1.0304	1.0351	C_{gross} **($/h)**			26289.76718	27336.61321	25770.88824	25286.52957
V_{52}(p.u)	0.90	1.10	1.0237	1.0679	1.0503	1.0526	**Thermal gen cost**			17954.18881	18741.23330	17225.93154	16843.11680
V_{80}(p.u)	0.90	1.10	1.0151	0.9867	1.0027	1.0236	**Valveff cost**			1.068204807	92.7313118	117.06180	8.83950321
V_{83}(p.u)	0.90	1.10	1.0522	1.0253	1.0421	1.0689	**Wind cost ($/h)**			1628.5291	1670.0712	1421.3127	1326.5574
V_{98}(p.u)	0.90	1.10	1.0380	1.0236	1.0445	1.0480	**Solar cost ($/h)**			302.4988	293.1453	196.8266	176.4423
V_{100}(p.u)	0.90	1.10	1.0440	1.0243	1.0502	1.0581	**Fuelvlve cost ($/h)**			18061.0093	18833.9646	17342.9933	16931.5118
V_{101}(p.u)	0.90	1.10	1.0320	1.0318	1.0419	1.0492	**VD (p.u)**			3.35010	3.97003	3.45029	3.64093
V_{109}(p.u)	0.90	1.10	1.0461	1.0639	1.0397	1.0333	**Emission (ton/h)**			5.34579	6.34547	5.34734	5.05545
V_{111}(p.u)	0.90	1.10	1.0719	1.0907	1.0774	1.0656	**stability index**			0.3315744	0.327453	0.327141	0.321904
T_{80-88}(p.u)	0.90	1.10	0.9841	0.9122	0.9288	0.9458	**Tgen cost ($/h)**			19885.21670	20704.44978	18844.07084	18346.11651
T_{81-90}(p.u)	0.90	1.10	0.9495	0.9019	0.9817	1.0017							
T_{86-93}(p.u)	0.90	1.10	0.9304	0.9506	0.9533	0.9391							
T_{42-41}(p.u)	0.90	1.10	0.9572	0.9471	1.0280	0.9646							
T_{58-57}(p.u)	0.90	1.10	0.9696	0.9135	0.9588	0.9401							
T_{44-43}(p.u)	0.90	1.10	0.9900	0.9365	0.9847	0.9564							
T_{60-59}(p.u)	0.90	1.10	0.9747	0.9332	0.9675	0.9782							
T_{64-63}(p.u)	0.90	1.10	0.9122	0.9187	0.9535	0.9778							
T_{72-71}(p.u)	0.90	1.10	0.9625	0.9215	1.0024	1.0066							
T_{17-18}(p.u)	0.90	1.10	1.0278	0.9869	1.0166	1.0074							
T_{21-20}(p.u)	0.90	1.10	1.0148	0.9892	0.9907	1.0218							
T_{27-26}(p.u)	0.90	1.10	0.9870	0.9072	1.0210	1.0060							
T_{28-26}(p.u)	0.90	1.10	0.9702	0.9673	0.9235	0.9655							
T_{31-30}(p.u)	0.90	1.10	1.0938	1.0443	1.0420	1.0398							
T_{48-47}(p.u)	0.90	1.10	0.9844	0.9390	0.9997	0.9554							
T_{76-74}(p.u)	0.90	1.10	1.0655	0.9991	0.9750	1.0557							
FACTS rating							**FACTS location**			**FDB-AOA**	**SHADE**	**ABC**	**MSA**
$\tau_{TCSC\ 1}$(%)	0	50%	38.50	48.31	43.51	45.32	TCSC1 branch, (con. buses):			75 (29-39)	105(63-65)	43 (42-48)	58 (20-24)
$\tau_{TCSC\ 2}$(%)	0	50%	49.27	48.38	47.94	36.64	TCSC2 branch, (con. buses):			21 (9-3)	83 (52-59)	118 (85-86)	146 (92-93)
Φ_{TCPS1} **(deg)**	- 5°	5°	3.8151	2.5214	4.8841	3.1110	TCPS1 branch, (con. buses):			134 (98-97)	151 (90-93)	104 (63-65)	139 (86-81)
Φ_{TCPS2} **(deg)**	- 5°	5°	3.0398	4.3985	3.3182	4.1016	TCPS2 branch, (con. buses):			101 (29-26)	98 (73-62)	57 (20-24)	120 (87-106)
Q_{SVC1} **(MVAr)**	- 10	10	9.9608	9.3775	7.2050	8.1585	SVC1 bus no:			34	53	67	23
Q_{SVC2} **(MVAr)**	- 10	10	5.6624	7.1792	7.7152	6.9602	SVC2 bus no:			81	70	97	38

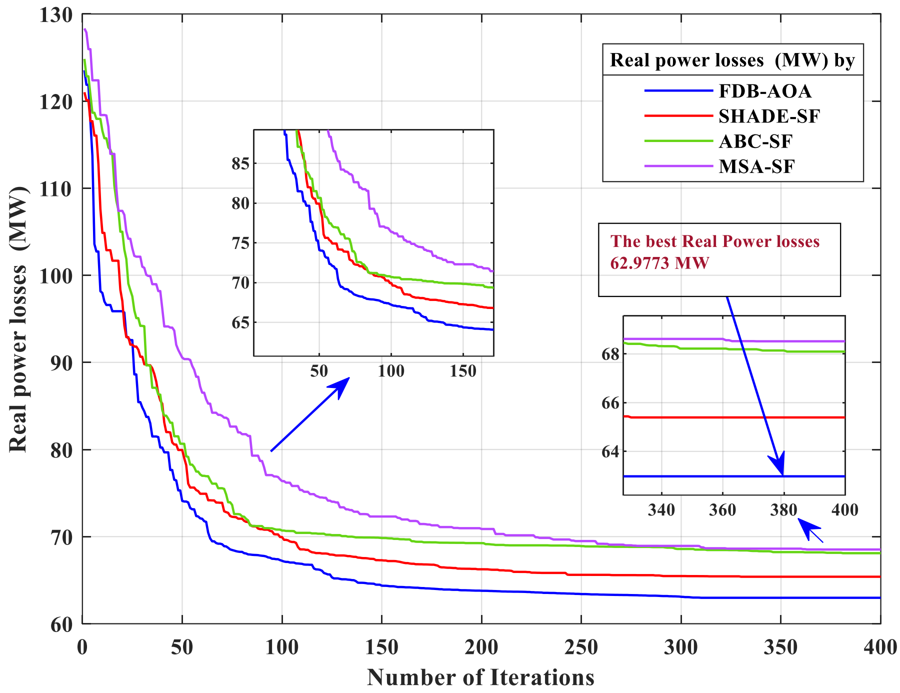

Fig. 6.56: convergence behaviors comparison of FDB-AOA with other methods: Case.2: DZA-114 bus.

Case 3: Gross cost (C_{gross} ($/h))

The third case selected the **Gross cost (C_{gross} ($/h))** as a fitness function. The **table 6.59** displays the optimized results of the presented method in comparison to other techniques**.** The results confirm that the FDB-AOA achieved the best C_{gross} (**23784.4379 $/h**) compared to other techniques. The convergence behaviors comparison of FDB-AOA with others methods are depicted in **figure (6. 66)**

Table. 6.59: The optimized results of FDB-AOA and other methods: Case. 3: modified DZA-114 bus.

Control variables	Min	Max	FDB-AOA	SHADE	ABC	MSA	Parameters	Min	Max	FDB-AOA	SHADE	ABC	MSA
P_{TG5}(MW)	135	1350	473.2426	476.5727	443.0489	467.4584	P_{TG1} (MW)	135	1350	482.15441	477.56039	492.58392	473.89319
P_{WG11}(MW)	10	100	99.0198	99.7445	96.2477	99.9737	Q_{TG4} (MVAr)	-20	400	314.50688	265.20673	331.84960	262.58356
P_{TG15}(MW)	30	300	195.0887	180.1873	208.0076	194.6639	Q_{TG5} (MVAr)	-20	200	134.80142	154.88931	166.37637	198.56899
P_{TG17}(MW)	135	1350	513.7074	493.1712	481.5080	501.1064	Q_{TG11} (MVAr)	-50	100	89.83804	100.84045	27.54206	80.68442
P_{TG19}(MW)	34.5	345	79.5261	127.4308	131.1930	79.7581	Q_{WG15} (MVAr)	0	100	85.84978	87.75769	89.60024	64.35724
P_{TG22}(MW)	34.5	345	201.8655	199.1092	203.4023	218.6722	Q_{TG17} (MVAr)	0	400	391.55670	399.04556	364.92110	340.57340
P_{TG52}(MW)	0	345	228.4906	224.5311	222.1924	231.0796	Q_{TG19} (MVAr)	0	60	57.18597	54.91076	57.25248	59.61231
P_{TG80}(MW)	34.5	345	139.0835	158.8363	153.4486	123.7811	Q_{TG22} (MVAr)	0	50	32.02381	42.94807	48.82714	49.93701
P_{TG83}(MW)	0	300	299.8989	299.3286	299.2134	299.8456	Q_{TG52} (MVAr)	0	50	47.81613	45.05219	35.70953	49.04622
P_{TG98}(MW)	30	300	105.7301	102.4363	96.9475	138.0027	Q_{WG80} (MVAr)	0	60	57.02977	55.12649	45.04753	59.54183
P_{TG100}(MW)	60	600	598.1138	589.6002	595.6271	599.9839	Q_{TG83} (MVAr)	-50	200	123.92047	189.90921	145.09359	165.11487
P_{TG101}(MW)	20	200	199.1147	198.3855	198.8700	199.9860	Q_{TG98} (MVAr)	0	50	49.45380	25.15690	36.47609	48.99188
P_{WG109}(MW)	0	100	99.5515	99.0812	98.8367	99.9918	Q_{TG100} (MVAr)	0	270	145.12235	120.39054	147.90570	168.26670
P_{TG111}(MW)	10	200	83.3527	72.4732	77.5456	71.4464	Q_{TG101} (MVAr)	-50	200	50.77294	62.91134	73.96189	56.48094
V_4(p.u)	0.90	1.10	1.0790	1.0574	1.0650	1.0231	Q_{WG109} (MVAr)	-50	100	32.84909	21.45933	47.72023	39.59099
V_5(p.u)	0.90	1.10	1.0703	1.0501	1.0584	1.0182	Q_{TG111} (MVAr)	-50	155	53.07069	54.87773	50.65877	53.01622
V_{11}(p.u)	0.90	1.10	1.0706	1.0574	1.0173	1.0092							

V_{15}(p.u)	0.90	1.10	1.0810	1.0593	1.0695	1.0186					
V_{17}(p.u)	0.90	1.10	1.0585	1.0614	1.0551	1.0298					
V_{19}(p.u)	0.90	1.10	1.0346	1.0399	1.0380	1.0125					
V_{22}(p.u)	0.90	1.10	1.0211	1.0313	1.0428	1.0188	**C_{gen} ($/h)**	16690.3918	16643.5552	16660.0668	16670.7031
V_{52}(p.u)	0.90	1.10	1.0737	1.0641	1.0535	1.0378	**P_{loss} (MW)**	70.9405	71.4485	71.6728	72.6431
V_{80}(p.u)	0.90	1.10	0.9854	1.0025	0.9917	1.0098	**C_{gross} ($/h)**	**23784.4379**	**23788.4049**	**23827.344**	**23935.0162**
V_{83}(p.u)	0.90	1.10	1.0258	1.0530	1.0361	1.0556	**VD(p.u)**	3.33075	3.10562	3.08080	2.49612
V_{98}(p.u)	0.90	1.10	1.0326	1.0332	1.0353	1.0419	**Emission (ton/h)**	5.52862	5.39482	5.36394	5.45689
V_{100}(p.u)	0.90	1.10	1.0429	1.0487	1.0488	1.0608	**stability index**	0.3106125	0.322490	0.325193	0.351117
V_{101}(p.u)	0.90	1.10	1.0312	1.0334	1.0418	1.0328	**Fuelvlv cost ($/h)**	16690.3918	16571.05277	15661.71471	15671.2293
V_{109}(p.u)	0.90	1.10	1.0489	1.0137	1.0886	1.0531	**Wind cost ($/h)**	761.5114	809.5844	782.2763	803.0148
V_{111}(p.u)	0.90	1.10	1.0851	1.0846	1.0795	1.0807	**Solar cost ($/h)**	237.7017	198.9534	216.0758	196.4590
T_{160}(p.u)	0.90	1.10	0.9003	0.9009	0.9271	0.9060	**Thermal cost ($/h)**	15623.1771	15635.0174	15567.5389	15586.15500
T_{161}(p.u)	0.90	1.10	0.9067	1.0068	0.9083	0.9233	**Valveff cost ($/h)**	68.0014615	72.50239	94.1761243	85.0742719
T_{162}(p.u)	0.90	1.10	0.9030	0.9438	0.9018	0.9250	**Tgen cost ($/h)**	16622.3903	16498.55038	16565.8907	16585.62881
T_{163}(p.u)	0.90	1.10	1.0075	0.9530	0.9506	1.0028					
T_{164}(p.u)	0.90	1.10	0.9165	0.9282	0.9164	0.9429					
T_{165}(p.u)	0.90	1.10	0.9385	0.9702	1.0215	0.9276					
T_{166}(p.u)	0.90	1.10	0.9279	0.9489	0.9323	0.9477					
T_{167}(p.u)	0.90	1.10	0.9166	0.9645	1.0219	0.9886					
T_{168}(p.u)	0.90	1.10	0.9790	0.9640	0.9539	0.9634					
T_{169}(p.u)	0.90	1.10	1.0299	1.0234	0.9882	0.9716					
T_{170}(p.u)	0.90	1.10	1.0072	0.9568	0.9568	0.9706					
T_{171}(p.u)	0.90	1.10	0.9421	0.9283	0.9603	0.9372					
T_{172}(p.u)	0.90	1.10	0.9664	1.0154	0.9781	0.9518					
T_{173}(p.u)	0.90	1.10	1.0091	1.0153	1.0139	1.0299					
T_{174}(p.u)	0.90	1.10	0.9473	0.9283	1.0154	0.9700					
T_{175}(p.u)	0.90	1.10	0.9965	1.0551	1.0764	1.0067					
FACTS rating							**FACTS location**	**FDB-AOA**	**SHADE**	**ABC**	**MSA**
$\tau_{TCSC\ 1}$(%)	0	50%	0.0778	0.1293	0.3425	49.41	TCSC1 branch, (con. buses):	73 (26-34)	18 (11-42)	148 (93-91)	96 (54-55)
$\tau_{TCSC\ 2}$(%)	0	50%	0.4745	0.1293	0.2945	35.90	TCSC2 branch, (con. buses):	133(100-97)	98 (73-62)	121 (87-82)	48 (96-98)
Φ_{TCPS1} **(deg)**	- 5°	5°	4.4120	4.9337	4.6378	4.5334	TCPS1 branch, (con. buses):	88 (52-30)	146 (92-93)	42 (44-42)	20 (9-2)
Φ_{TCPS2} **(deg)**	- 5°	5°	4.0727	3.3507	4.2100	2.5304	TCPS2 branch, (con. buses):	90 (40-41)	40 (75-74)	91 (40-50)	136 (87-100)
Q_{SVC1} **(MVAr)**	- 10	10	7.6360	7.2551	7.1167	9.3509	SVC1 bus no:	96	34	38	53
Q_{SVC2} **(MVAr)**	- 10	10	8.7643	5.4359	9.9745	8.8460	SVC2 bus no:	81	68	68	67

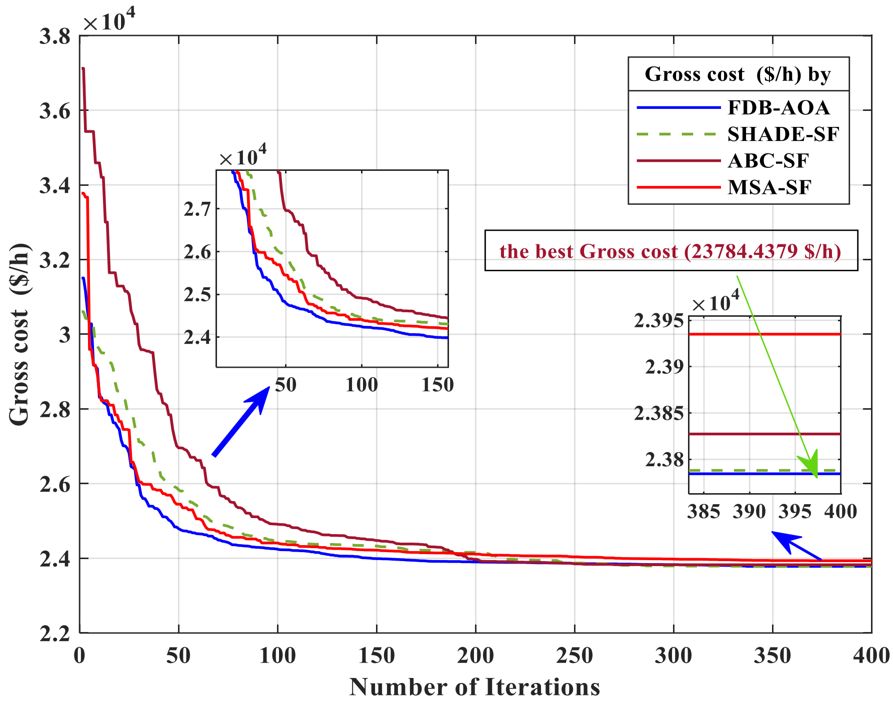

Fig. 6.57: Convergence behaviors comparison of FDB-AOA and other methods: Case.3: DZA-114 bus.

Discussion of the results

The **tables (6.57, 6.58, 6.59),** show the findings of the study conducted on the modified DZA-114 bus for various cases. According to the optimization results mentioned in those tables, it can be observed that the FDB-AOA algorithm has achieved the most satisfactory results while complying with all constraints. However, it is important to note that comparing the apparent numerical results of a constrained optimization problem is not a reliable method. Hence, it is crucial to verify the feasibility of the solutions.

These simulation results clearly demonstrated the superiority of the presented method (FBD-AOA) when compared to the three other population metaheuristic algorithms. It can be observed that this technique could solve the single-objective OPF problem involved both the wind power generators, and multi-types of FACTS devices, with high efficiency. It also provides considerably lower value for the majority of test cases analyzed, without forgetting the competitive computational times of the FBD-AOA compared to other algorithms. It should be mentioned that the best results have been achieved by FBD-AOA among the comparative methods. As seen, the FBD-AOA has the best performance in terms of optimal solution, convergence, and efficiency with a minimum execution time.

The **figures (Figs. 6.55, 6.56, 6.57)**, illustrate the convergence behaviors of the FBD-AOA method in comparison to other metaheuristic algorithms for cases 1 to 3, respectively. These diagrams indicate that the FBD-AOA algorithm exhibits faster convergence, following a uniform and systematic pattern. SHADE-SF converges also rapidly when seeking the optimal solution, it could be a good competitor in finding of the optimum solution, as well as convergence and precision to the FBD-AOA. It has been shown to have regular and superior performance in all cases when compared to other algorithms. Of the other algorithms, specifically MSA-SF and ABC-SF, exhibit irregular and erratic convergence, often requiring the longest time to reach the final solution (the best optimum). They stagnate at various stages for extended periods while searching for viable and superior candidates. The scheduling outcomes of wind power plants generators are more than the thermal units for the case 2 and 3 for all algorithms, the best favorable locations and rating for all uses FACTS devices are mentioned in are detailed in the corresponding tables related for each case.

- **Comparison between literature review**

Comparison between the results obtained by the proposed method with those of the Slim Mould Optimizer method from the literature review [10].

Table. 6.60: Comparison between the results obtained by the proposed method with literature revue for the modified DZA-114 bus.

	generators cost without valve ($/h)	Total generation cost ($/h)	Power losses (MW)
FDB-AOA with renewable energy	16595.0969	16661.1543	62.9773
FDB-AOA with renewable energy and FACTS devices	16553.22730	16630.4160	65.1388
Slim Mould Optimizer Method [10]	16693.11		65.90

6.5. Conclusion

This chapter present the application and results of our work, a recent robust optimization algorithm-inspired from the algorithm has been suggested for provide an optimization problem related to the electrical fields, like firstly we applied on the estimation of the PV parameters of PV panels as a first Part, in the second part, a recent robust optimization algorithm-inspired from the algorithm has been suggested for provide optimal-solution of the OPF problem in the modified IEEE 30-bus test system and Algerian electrical network DZA-114 bus. Uncertainty nature of both solar and wind energy sources has been modelled based on the Weibull and lognormal PDFs distribution. Numerical results of FDB-AOA are compared with the obtained results by others algorithm like the SHADE, ABC, and MSA technique with the superiority of feasible solutions method. The results revealed that the FDB-AOA significantly gives a superior solution, while ensuring the feasibility of solutions, where outperformed the others methods in the base case and other sub-cases whatever the constraints of test system. The results suggest that the proposed FDB-AOA can be successfully applied to solve highly nonlinear problems. The findings of this document are likely to be beneficial to researchers.

Therefore, the proposed algorithm-based FDB-AOA is an excellent and highly recommended technique for the stochastic OPF problem, since it more Recent even in the case of practical electrical network.

General Conclusion

General conclusion

The primary objective of this thesis is to improve the efficiency of electrical networks by integrating various Flexible AC Transmission Systems (FACTS) using intelligent optimization method like metaheuristic methods. The first objective of this thesis is the solving of the single and multi-objective optimization of optimal power flow (OPF) using a recent intelligent optimization approach. To achieve this goal, a robust optimization method so called thermal exchange optimization approach is used for solve these challenges The optimization is conducted by using FDB-AOA, FDB-AEO, SSA, PSO, and GA algorithms. The simulation was carried out on the IEEE 30-bus test system. Before testing the multi- objective version of the proposed metaheuristic method (TEO), the OPF problem was compared with other powerful multi-objective methods. This comparison showed that the proposed method quickly converges, for the majority of cases, by obtained a best value of the fitness function, with a reduced execution time. After than the SSA algorithm was conducted to solve the OPF with both types is large scale which is the reel Algerian electric transmission network DZA-114 bus. The results confirmed their efficiency in solving the single and multi-objective OPF in large scale. The second objective, which represent the contribution of this thesis, where applied a recent hybrid optimization algorithm named FDB-AOA for solving the single objective of OPF problems in the hybrid electrical network, with consideration of the integration of stochastic renewable energy and intelligent compensation system which are the FACTS devices. Optimization approaches have been successfully applied to find the best location and sizing of FACTS devices, with a best optimal control variables of the medium-sized (IEEE 30-bus) with stochastic wind power plants, also in large-scale test systems as well the practical power system which is the reel electric transmission network Algerian DZA-114 bus incorporate stochastic wind and solar power plants. From the results found, it can be seen that metaheuristic methods are well suited for determining the optimal values of the powers generated by the interconnected plants to achieve the lowest possible cost as well as the best profit. A critical analysis on the both obtained and reported results was presented, and approved the feasibility of solutions. The application of some optimization methods has given encouraging results as they allow improving the efficiency of electrical networks in terms of production cost reduction, emission gas reduction, loss reduction, and reduction of voltage deviation at the load bus levels.

As perspectives, we propose:

1. To extend this study to consider the modeling and integration of the FACTS devices system to improve the security of transport networks, especially in case of overload and fault.

2. To consider the techno-economic impact of the integration of renewable sources, namely, solar energy and wind energy on the quality of the electrical energy of the Algerian eclectic network.

3. To consider the effect of the integration of renewable sources on electrical network stability.

4. To apply recent metaheuristic algorithms for solving the OPF with both types (single and multi-objectives OPF) on the recent version of the Algeria electrical transmission network, with integration of renewable energies and FACTS Devices.

REFERENCES

References

[1] Khan, I. U., Javaid, N., Gamage, K. A., Taylor, C. J., Baig, S., & Ma, X. (2020). Heuristic algorithm based optimal power flow model incorporating stochastic renewable energy sources. IEEE Access, 8, 148622-148643.

[2] Nkan, I. E., Okpo, E. E., & Okpura, N. I. (2023). Optimum location of shunt FACTS devices for enhancement of power system loadability using continuation power flow. International Multilingual Journal of Science and Technology (IMJST), 8(9), 6666-6674.

[3] Mouassa, S. (2021). Optimisation de l'écoulement de puissance par les méthodes non-conventionnelles dans les réseaux électriques intelligents (Smart Grid) (Doctoral dissertation, Universidad de Jaén).

[4] Ilyas, M. A., Abbas, G., Alquthami, T., Awais, M., & Rasheed, M. B. (2020). Multi-objective optimal power flow with integration of renewable energy sources using fuzzy membership function. IEEE Access, 8, 143185-143200.

[5] Mahdad, B. (2020). Improvement optimal power flow solution considering SVC and TCSC controllers using new partitioned ant lion algorithm. Electrical Engineering, 102(4), 2655-2672.

[6] B. Mahdada, K. Srairia, T. Bouktirb, "Optimal power flow for large-scale power system with shunt FACTS using efficient parallel GA" International Jour of Elecr Power & Energ Syst, Volume 32, Issue 5, June 2010, Pages 507–517

[7] Mahdad, B., & Srairi, K. (2022). Interactive artificial ecosystem algorithm for solving power management optimizations. Electrical Engineering & Electromechanics, (6), 53-66.

[8] Biswas, P. P., Suganthan, P. N., & Amaratunga, G. A. (2017). Optimal power flow solutions incorporating stochastic wind and solar power. Energy conversion and management, 148, 1194-1207.

[9] Biswas, P. P., Arora, P., Mallipeddi, R., Suganthan, P. N., & Panigrahi, B. K. (2021). Optimal placement and sizing of FACTS devices for optimal power flow in a wind power integrated electrical network. Neural computing and Applications, 33, 6753-6774.

[10] Mouassa, S., Althobaiti, A., Jurado, F., & Ghoneim, S. S. (2022). Novel design of slim mould optimizer for the solution of optimal power flow problems incorporating intermittent sources: A case study of algerian electricity grid. IEEE Access, 10, 22646-22661.

[11] HELD, Lukas, MUELLER, Felicitas, STEINLE, Sina, et al. An optimal power flow algorithm for the simulation of energy storage systems in unbalanced three-phase distribution grids. Energies, 2021, vol. 14, no 6, p. 1623.

[12] Adjoudj, L. (2018). Contribution à l'étude de l'OPF du réseau Algérien basée sur les énergies renouvelables et les FACTS (Doctoral dissertation).

[13] MOMOH, J. A., EL-HAWARY, M. E., et ADAPA, R. A review of selected optimal power literature to 1993. Part planning in large scale power systems. IEEE Trans. Power Syst, 1999, vol. 9, no 2, p. 668-676.

[14] Sun, D. I., Ashley, B., Brewer, B., Hughes, A., & Tinney, W. F. (1984). Optimal power flow by Newton approach. IEEE Transactions on Power Apparatus and systems, (10), 2864-2880.

[15] Pudjianto, D., Ahmed, S., & Strbac, G. (2002). Allocation of VAR support using LP and NLP based optimal power flows. IEE Proceedings-Generation, Transmission and Distribution, 149(4), 377-383.

[16] Castronuovo, E. D., Campagnolo, J. M., & Salgado, R. (2001). New versions of interior point methods applied to the optimal power flow problem. Optmization [Online] Digest, 128.

[17] Herbadji, O. (2019). Contribution à l'optimisation des réseaux électriques en présence des Multi-FACTS par des méthodes métaheuristiques hybrides (Doctoral dissertation).

[18] Osman, M. S., Abo-Sinna, M. A., & Mousa, A. A. (2004). A solution to the optimal power flow using genetic algorithm. Applied mathematics and computation, 155(2), 391-405

[19] [Bakirtzis, A. G., Biskas, P. N., Zoumas, C. E., & Petridis, V. (2002). Optimal power flow by enhanced genetic algorithm. IEEE Transactions on power Systems, 17(2), 229-236.],

[20] Abido, M. A. (2002). Optimal power flow using particle swarm optimization. International Journal of Electrical Power & Energy Systems, 24(7), 563-571

[21] Varadarajan, M., & Swarup, K. S. (2008). Differential evolutionary algorithm for optimal reactive power dispatch. International Journal of Electrical Power & Energy Systems, 30(8), 435-441.

[22] Adaryani, M. R., & Karami, A. J. I. J. (2013). Artificial bee colony algorithm for solving multi-objective optimal power flow problem. International Journal of Electrical Power & Energy Systems, 53, 219-230.

[23] Duman, S., Güvenç, U., Sönmez, Y., & Yörükeren, N. (2012). Optimal power flow using gravitational search algorithm. Energy conversion and management, 59, 86-95.

[24] Abido, M. A. (2002). Optimal power flow using tabu search algorithm. Electric power components and systems, 30(5), 469-483.

[25] Thitithamrongchai, C., & Eua-Arporn, B. (2007). Self-adaptive differential evolution based optimal power flow for units with non-smooth fuel cost functions. Journal of Electrical Systems, 3(2), 88-99.

[26] Sayah, S., & Zehar, K. (2008). Modified differential evolution algorithm for optimal power flow with non-smooth cost functions. Energy conversion and Management, 49(11), 3036-3042.

[27] Kumar, A. R., & Premalatha, L. (2015). Optimal power flow for a deregulated power system using adaptive real coded biogeography-based optimization. International Journal of Electrical Power & Energy Systems, 73, 393-399.

[28] El-Fergany, A. A., & Hasanien, H. M. (2015). Single and multi-objective optimal power flow using grey wolf optimizer and differential evolution algorithms. Electric Power Components and Systems, 43(13), 1548-1559.

[29] Mohamed, A. A. A., Mohamed, Y. S., El-Gaafary, A. A., & Hemeida, A. M. (2017). Optimal power flow using moth swarm algorithm. Electric Power Systems Research, 142, 190-206.

[30] MOHAMED, Al-Attar Ali, MOHAMED, Yahia S., EL-GAAFARY, Ahmed AM, et al. Optimal power flow using moth swarm algorithm. Electric Power Systems Research, 2017, vol. 142, p. 190-206.

[31] Pulluri, H., Naresh, R., & Sharma, V. (2018). A solution network based on stud krill herd algorithm for optimal power flow problems. Soft Computing, 22, 159-176.

[32] Abdo, M., Kamel, S., Ebeed, M., Yu, J., & Jurado, F. (2018). Solving non-smooth optimal power flow problems using a developed grey wolf optimizer. Energies, 11(7), 1692.

[33] Abd El-sattar, S., Kamel, S., Ebeed, M., & Jurado, F. (2021). An improved version of salp swarm algorithm for solving optimal power flow problem. Soft Computing, 25, 4027-4052.

[34] Swief, R. A., Hassan, N. M., Hasanien, H. M., Abdelaziz, A. Y., & Kamh, M. Z. (2021). AC&DC optimal power flow incorporating centralized/decentralized multi-region grid control employing the whale algorithm. Ain Shams Engineering Journal, 12(2), 1907-1922

[35] Ali, M. H., El-Rifaie, A. M., Youssef, A. A., Tulsky, V. N., & Tolba, M. A. (2023). Techno-Economic Strategy for the Load Dispatch and Power Flow in Power Grids Using Peafowl Optimization Algorithm. Energies, 16(2), 846

[36] Meng, A., Zeng, C., Wang, P., Chen, D., Zhou, T., Zheng, X., & Yin, H. (2021). A high-performance crisscross search based grey wolf optimizer for solving optimal power flow problem. Energy, 225, 120211.

[37] Le, P. M., Duong, T. L., Vo, D. N., Le, T. T., & Nguyen, S. Q. (2020). An Efficient Hybrid Method for Solving Security-Constrained Optimal Power Flow Problem. International Journal on Electrical Engineering and Informatics, 12(4), 933-955.

[38] Radosavljević, J., Klimenta, D., Jevtić, M., & Arsić, N. (2015). Optimal power flow using a hybrid optimization algorithm of particle swarm optimization and gravitational search algorithm. Electric Power Components and Systems, 43(17), 1958-1970.

[39] Sonmez, Y., Duman, S., Kahraman, H. T., Kati, M., Aras, S., &Guvenc, U. (2022). Fitness-distance balance based artificial ecosystem optimisation to solve transient stability constrained optimal power flow problem. Journal of Experimental & Theoretical Artificial Intelligence, 1-40.

[40] [Guvenc, U., Duman, S., Kahraman, H. T., Aras, S., & Katı, M. (2021). Fitness–Distance Balance based adaptive guided differential evolution algorithm for security-constrained optimal power flow problem incorporating renewable energy sources. Applied Soft Computing, 108, 107421

[41] Hassan, M. H., Elsayed, S. K., Kamel, S., Rahmann, C., & Taha, I. B. (2022). Developing chaotic Bonobo optimizer for optimal power flow analysis considering stochastic renewable energy resources. International Journal of Energy Research, 46(8), 11291-11325.

[42] You, L., Ma, H., & Saha, T. K. (2023). A CVaR-constrained optimal power flow model for wind integrated power systems considering Transmission-side flexibility. International Journal of Electrical Power & Energy Systems, 150, 109087.

[43] Riaz, M., Hanif, A., Masood, H., Khan, M. A., Afaq, K., Kang, B. G., & Nam, Y. (2021). An optimal power flow solution of a system integrated with renewable sources using a hybrid optimizer. Sustainability, 13(23), 13382.

[44] Singh, R. P., Mukherjee, V., & Ghoshal, S. P. (2015). Particle swarm optimization with an aging leader and challengers algorithm for optimal power flow problem with FACTS devices. International Journal of Electrical Power & Energy Systems, 64, 1185-1196.

[45] Aras, S., Gedikli, E., & Kahraman, H. T. (2021). A novel stochastic fractal search algorithm with fitness-distance balance for global numerical optimization. Swarm and Evolutionary Computation, 61, 100821

[46] Wirmond, V. E., Fernandes, T. S., & Tortelli, O. L. (2011). TCPST allocation using optimal power flow and Genetic Algorithms. International Journal of Electrical Power & Energy Systems, 33(4), 880-886.

[47] Sebaa, K., Bouhedda, M., Tlemcani, A., & Henini, N. (2014). Location and tuning of TCPSTs and SVCs based on optimal power flow and an improved cross-entropy approach. International Journal of Electrical Power & Energy Systems, 54, 536-545.

[48] Naderi, E., Pourakbari-Kasmaei, M., & Abdi, H. (2019). An efficient particle swarm optimization algorithm to solve optimal power flow problem integrated with FACTS devices. Applied Soft Computing, 80, 243-262

[49] Shafik, M. B., Chen, H., Rashed, G. I., & El-Sehiemy, R. A. (2019). Adaptive multi objective parallel seeker optimization algorithm for incorporating TCSC devices into optimal power flow framework. IEEE Access, 7, 36934-36947.

[50] Inkollu, S. R., & Kota, V. R. (2016). Optimal setting of FACTS devices for voltage stability improvement using PSO adaptive GSA hybrid algorithm. Engineering science and technology, an international journal, 19(3), 1166-1176.

[51] Benabid, R., Boudour, M., & Abido, M. A. (2009). Optimal location and setting of SVC and TCSC devices using non-dominated sorting particle swarm optimization. Electric Power Systems Research, 79(12), 1668-1677.

[52] Mohamed, A. A. A., Mohamed, Y. S., El-Gaafary, A. A., & Hemeida, A. M. (2017). Optimal power flow using moth swarm algorithm. Electric Power Systems Research, 142, 190-206.

[53] Nusair, K., Alasali, F., Hayajneh, A., & Holderbaum, W. (2021). Optimal placement of FACTS devices and power-flow solutions for a power network system integrated with stochastic renewable energy resources using new metaheuristic optimization techniques. International Journal of Energy Research, 45(13), 18786-18809

[54] Ebeed, M., Mostafa, A., Aly, M. M., Jurado, F., & Kamel, S. (2023). Stochastic optimal power flow analysis of power systems with wind/PV/TCSC using a developed Runge Kutta optimizer. International Journal of Electrical Power & Energy Systems, 152, 109250

[55] Neelamkavil Pappachan, S. (2023). Development of optimal placement and sizing of FACTS devices in power system integrated with wind power using modified krill herd algorithm. COMPEL-The international journal for computation and mathematics in electrical and electronic engineering

[56] Hassan, M. H., Daqaq, F., Kamel, S., Hussien, A. G., & Zawbaa, H. M. (2023). An enhanced hunter-prey optimization for optimal power flow with FACTS devices and wind power integration. IET Generation, Transmission & Distribution

[57] Mohamed, A. A., Kamel, S., Hassan, M. H., & Domínguez-García, J. L. (2024). Optimal Power Flow Incorporating Renewable Energy Sources and FACTS Devices: A Chaos Game Optimization Approach. IEEE Access

[58] Mokhtaria, Z. E. R. O. U. A. L. (2015). Optimisation et contrôle de l'écoulement des puissances actives par système FACT. Mémoire de Magister, Université Mohamed Boudiaf-Oran.

[59] Kamel, S., Abokrisha, M., Selim, A., & Jurado, F. (2021). Power flow control of power systems based on a simple TCSC model. Ain Shams Engineering Journal, 12(3), 2781-2788.

[60] ZOBEIDI, M. (2021). Amélioration de la sécurité des systèmes électriques à travers l'approche de sensibilité pour l'emplacement optimal des dispositifsFACTS (Doctoral dissertation).

[61] Long, W., & Nilsson, S. L. (2020). Introduction to flexible AC transmission systems (FACTS) controllers: a chronology. Flexible AC Transmission Systems: FACTS, 3-12.

[62] Gadal, R., Oukennou, A., El Mariami, F., Belfqih, A., & Agouzoul, N. (2023). Voltage Stability Assessment and Control Using Indices and FACTS: A Comparative Review. Journal of Electrical and Computer Engineering, 2023.

[63] Marouani, I., Guesmi, T., Alshammari, B. M., Alqunun, K., Alshammari, A. S., Albadran, S., ... & Rahmani, S. (2023). Optimized FACTS Devices for Power System Enhancement: Applications and Solving Methods. Sustainability, 15(12), 9348.

[64] Sulaiman, M. H., & Mustaffa, Z. (2022). Optimal placement and sizing of FACTS devices for optimal power flow using metaheuristic optimizers. Results in Control and Optimization, 8, 100145.

[65] Abdullah, M. K., Hassan, L. H., & Moghavvemi, M. (2022). Voltage stability assessment of grid connected PV systems with FACTS devices. Scientific reports, 12(1), 22279.

[66] Benyekhlef, L, July (2018), Gestion optimale d'un réseau d'énergie électrique avec incorporation des systèmes FACTS, Université Kasdi Merbah Ouargla.

[67] Ahmad, A. A., & Sirjani, R. (2020). Optimal placement and sizing of multi-type FACTS devices in power systems using metaheuristic optimisation techniques: An updated review. Ain Shams Engineering Journal, 11(3), 611-628

[68] Nadeem, M., Imran, K., Khattak, A., Ulasyar, A., Pal, A., Zeb, M. Z., ... & Padhee, M. (2020). Optimal placement, sizing and coordination of FACTS devices in transmission network using whale optimization algorithm. Energies, 13(3), 753.

[69] Hafeez, A., Ali, A., Keerio, M. U., Mugheri, N. H., Abbas, G., Khan, A., ... & Bouzguenda, M. (2023). Optimal site and size of FACTS devices with the integration of uncertain wind generation on a solution of stochastic multi-objective optimal power flow problem. Frontiers in Energy Research, 11, 1293870.

[70] Zellagui, M., & Chaghi, A. (2013). Impact of apparent reactance injected by TCSR on distance relay in presence phase to earth fault. Advances in Electrical and Electronic Engineering, 11(3), 156-168.

[71] Mansouri, M. M., & Nayeripour, M. (2019). DC offset removal of thyristor switched series capacitor and in a novel and simple method. International Journal of Advanced Science and Research

[72] Fawzy, I. Y., Mossa, M. A., Elsawy, A. M., & Diab, A. A. Z. (2024). Enhancing the Performance of Power System under Abnormal Conditions Using Three Different FACTS Devices. International

Journal of Robotics and Control Systems, 4(1), 1-32.

[73] Kalpaktsoglou, D., Tsiakalos, A., Pouros, S., & Roumeliotis, M. (2021). Comparison between thyristor switched series capacitors and thyristor switched parallel capacitors for wind power systems-a simulation study. WSEAS Trans Power Syst, 15, 257.

[74] Amrr, S. M., Asghar, M. J., Ashraf, I., & Meraj, M. (2020). A comprehensive review of power flow controllers in interconnected power system networks. IEEE Access, 8, 18036-18063.

[75] Ding, C., Li, X., Li, B., Jiang, Q., Wen, M., & Liu, T. (2023). Research on IPFC-Based Dynamic Droop Control Strategy. Energies, 16(14), 5400.

[76] Ewaoche, O. J., & Nwulu, N. (2018, December). Modelling and Simulation of Interline Power Flow Controller for Improved Transmission System Security. In 2018 International Conference on Computational Techniques, Electronics and Mechanical Systems (CTEMS) (pp. 250-255). IEEE.

[77] Hardas, A. V., & Rajderkar, V. (2017). Impact of Thyristor controlled phase angle regulator on power flow. International journal of electrical engineering & technology (IJEET), 8(2), 01-07.

[78] Okampo, E. J., Nwulu, N., & Bokoro, P. N. (2022). Optimal placement and operation of FACTS technologies in a cyber-physical power system: Critical review and future outlook. Sustainability, 14(13), 7707.

[79] Duman, S., Akbel, M., &Kahraman, H. T. (2021). Development of the multi-objective adaptive guided differential evolution and optimization of the MO-ACOPF for wind/PV/tidal energy sources. Applied Soft Computing, 112, 107814.

[80] Long, W., Jiao, J., Liang, X., Xu, M., Tang, M., & Cai, S. (2022). Parameters estimation of photovoltaic models using a novel hybrid seagull optimization algorithm. Energy, 249, 123760. 651

[81] Haddi, S. E. B. A. A. (2019). Contribution à l'optimisation de l'insertion des énergies renouvelables dans un réseau électrique intelligent (Smart Grid) (Doctoral dissertation, thèse de doctorat en sciences option: Réseaux électriques, université de Setif 1).

[82] Boukaroura, A., & Slimani, L. (2021). Contribution à la modélisation et à l'optimisation des réseaux de distribution sous incertitudes.

[83] Wang, L. (2008). Integration of renewable energy sources: reliability-constrained power system planning and operations using computational intelligence (Vol. 70, No. 02).

[84] McINTYRE, R. A. (2010). State of the art of photovoltaic technologies. Science Progress, 93(4), 361-392.

[85] Jiang, L. L. (2014). Modeling and optimization of photovoltaic systems under partially shaded and rapidly changing conditions (Doctoral dissertation).

[86] Rawa, M., Abusorrah, A., Al-Turki, Y., Calasan, M., Micev, M., Ali, Z. M., ... & Aleem, S. H. A. (2022). Estimation of parameters of different equivalent circuit models of solar cells and various photovoltaic modules using hybrid variants of honey badger algorithm and artificial gorilla troops optimizer. Mathematics, 10(7), 1057.

[87] Babaa, S., Armstrong, M., & Pickert, V. (2014). Overview of maximum power point tracking control methods for PV systems. Journal of Power and Energy Engineering.

[88] Bourzami, A. (2019). Contribution à l'étude de la stabilité des grands réseaux électriques dans un marché de l'électricité dérégulé en présence des sources d'énergie renouvelable par la logique floue (Doctoral dissertation).

[89] Houam, A. (2022). Optimisation de l'intégration des énergies renouvelables dans les réseaux de distribution par la commande MPPT (Doctoral dissertation, Université Larbi-Tébessi. Tebessa).

[90] Kouadri, R. (2021). Contribution à l'optimisation de l'intégration des énergies renouvelables au réseau électrique en présence des dispositifs FACTS-HVDC (Doctoral dissertation).

[91] Alabdali, Q. A., Bajawi, A. M., Fatani, A. M., & Nahhas, A. M. (2020). Review of recent advances of

Wind Energy. Sustain. Energy, 8(1), 12-19.

[92] Tahaguas, W. (2023, April). Modeling and simulation of power system dynamics for studying the impacts of increasing wind power in a weak grid system. In Res Electricae Magdeburgenses. Magdeburger Forum zur Elektrotechnik (Vol. 94).

[93] Sjökvist, E. (2023). Improvement of Wind Power Forecasting and Prediction of Production Losses Caused by Ice Formation on Wind Turbine Blades:-A Machine Learning Approach.

[94] Nappu, M. B., Arief, A., & Ajami, W. A. (2023). Energy Efficiency in Modern Power Systems Utilizing Advanced Incremental Particle Swarm Optimization–Based OPF. Energies, 16(4), 1706.

[95] Farhat, M., Kamel, S., Atallah, A. M., Hassan, M. H., & Agwa, A. M. (2022). ESMA-OPF: Enhanced slime mould algorithm for solving optimal power flow problem. Sustainability, 14(4), 2305.

[96] Liu, S., Wu, C., & Zhu, H. (2022). Topology-aware graph neural networks for learning feasible and adaptive AC-OPF solutions. IEEE Transactions on Power Systems.

[97] Souag, S. (2016). Contribution à l'étude de l'analyse des contingences par la méthode de dc load flow sous labview (Doctoral dissertation).

[98] YAHIAOUI, M. (2014). Contrôle optimal des puissances réactives et des tensions dans un réseau d'énergie électrique par dispositifs FACTS (Doctoral dissertation, Thèse de doct).

[99] Abdellah, D. (2016). Répartition optimale des puissances utilisant les techniques de l'intelligence artificielle. Université des Frères Mentouri Constantine, Faculté des Sciences De l'Ingénieur, Département d'Electrotechnique.

[100] S. Duman, H. T. Kahraman, and M. Kati, "Economical operation of modern power grids incorporating uncertainties of renewable energy sources and load demand using the adaptive fitness-distance balancebased stochastic fractal search algorithm," Eng. Appl. Artif. Intell., vol. 117, p. 105501, 2023.

[101] Kullampalayam Murugaiyan, N., Chandrasekaran, K., Manoharan, P., & Derebew, B. (2024). Leveraging opposition-based learning for solar photovoltaic model parameter estimation with exponential distribution optimization algorithm. Scientific Reports, 14(1), 528

[102] Daqaq, F., Kamel, S., Ouassaid, M., Ellaia, R., & Agwa, A. M. (2022). Non-dominated sorting Manta ray foraging optimization for multi-objective optimal power flow with wind/solar/small-hydro energy sources. Fractal and Fractional, 6(4), 194.

[103] Nappu, M. B., Arief, A., & Ajami, W. A. (2023). Energy Efficiency in Modern Power Systems Utilizing Advanced Incremental Particle Swarm Optimization–Based OPF. Energies, 16(4), 1706.

[104] Avvari, R. K., & DM, V. K. (2022). Multi-Objective Optimal Power Flow including Wind and Solar Generation Uncertainty Using New Hybrid Evolutionary Algorithm with Efficient Constraint Handling Method. International Transactions on Electrical Energy Systems, 2022.

[105] Kahraman, H. T., Akbel, M., & Duman, S. (2022). Optimization of optimal power flow problem using multi-objective manta ray foraging optimizer. Applied Soft Computing, 116, 108334.

[106] Sulaiman, M. H., & Mustaffa, Z. (2022). Optimal placement and sizing of FACTS devices for optimal power flow using metaheuristic optimizers. Results in Control and Optimization, 8, 100145,

[107] Hassan, M. H., Daqaq, F., Kamel, S., Hussien, A. G., & Zawbaa, H. M. (2023). An enhanced hunter-prey optimization for optimal power flow with FACTS devices and wind power integration. IET Generation, Transmission & Distribution.

[108] Pennada, V. S. T. (2020). Solving Multiple Objective Optimization Problem using Multi-Agent Systems: A case in Logistics Management.

[109] GANDIBLEUX, Xavier, SEVAUX, Marc, SÖRENSEN, Kenneth, et al. (ed.). Metaheuristics for multiobjective optimisation. Springer Science & Business Media, 2012.

[110] BOUZIDI Boumediene; 2013. Optimisation de la production et du transport de l'énergie par les

techniques d'évaluation de performance » Mémoire de Magister option: Réseaux Electriques; Université d'Oran.

[111] GACEM, Abdelmalek. Commande Robuste d'un Dispositif FACTS par les Méthodes Métaheuristiques pour la Stabilité de Tension d'un Réseau Electrique. 2019. Thèse de doctorat. Université Mohamed Khider-Biskra.

[112] BETKA, Abir. Estimation de mouvement par les techniques métaheuristiques. 2019. Thèse de doctorat. Université Mohamed Khider-Biskra.

[113] LABBI, Yacine. Gestion et contrôle optimale de l'énergie électrique sur les sites de production. 2016. Thèse de doctorat. Université Mohamed Khider-Biskra.

[114] BOUCHEKARA, Houssem. Solution of the optimal power flow problem considering security constraints using an improved chaotic electromagnetic field optimization algorithm. Neural Computing and Applications, 2020, vol. 32, no 7, p. 2683-2703.

[115] Ebeed, M., Kamel, S., & Jurado, F. (2018). Optimal power flow using recent optimization techniques. In Classical and recent aspects of power system optimization (pp. 157-183). Academic Press

[116] Bouchekara, H. R. E. H., Chaib, A. E., & Abido, M. A. (2018). Optimal power flow using GA with a new multi-parent crossover considering: prohibited zones, valve-point effect, multi-fuels and emission. Electrical Engineering, 100(1), 151-165.

[117] Adaryani, M. R., & Karami, A. (2013). Artificial bee colony algorithm for solving multi-objective optimal power flow problem. International Journal of Electrical Power & Energy Systems, 53, 219-230.

[118] Eid, A., Kamel, S., & Houssein, E. H. (2022). An enhanced equilibrium optimizer for strategic planning of PV-BES units in radial distribution systems considering time-varying demand. Neural Computing and Applications, 34(19), 17145-17173

[119] Bo, Y. A. N. G., Junting, W. A. N. G., Lei, Y. U., Pulin, C. A. O., Hongchun, S. H. U., & Tao, Y. U. (2022). Peafowl Optimization Algorithm Based Bi-Level Multi-Objective Optimal Allocation of Energy Storage Systems in Distribution Network. Journal of Shanghai Jiaotong University, 56(10), 1294.

[120] Bouchekara, H. R., Chaib, A. E., Abido, M. A., & El-Sehiemy, R. A. (2016). Optimal power flow using an Improved Colliding Bodies Optimization algorithm. Applied Soft Computing, 42, 119-131.

[121] Zerigat, D. H., Benasla, L., Belmadani, A., & Rahli, M. (2013). Solution of combined economic and emission dispatch problems using galaxy-based search algorithm. Journal of Electrical Systems, 9(4), 468-480.

[122] Gao, M., Yu, J., Yang, Z., & Zhao, J. (2023). A physics-guided graph convolution neural network for optimal power flow. IEEE Transactions on Power Systems.

[123] DJEBLAHI, Zahia, MAHDAD, Belkacem, et SRAIRI, Kamel. Solving the Energy Management Problems Using Thermal Exchange Optimization. 2024.

[124] Daryani, N., Hagh, M. T., & Teimourzadeh, S. (2016). Adaptive group search optimization algorithm for multi-objective optimal power flow problem. Applied soft computing, 38, 1012-1024.

[125] Akbari, E., Ghasemi, M., Gil, M., Rahimnejad, A., & Andrew Gadsden, S. (2022). Optimal power flow via teaching-learning-studying-based optimization algorithm. Electric Power Components and Systems, 49(6-7), 584-601.

[126] Eappen, G., & Shankar, T. J. P. C. (2020). Hybrid PSO-GSA for energy efficient spectrum sensing in cognitive radio network. Physical Communication, 40, 101091.

[127] Reddy, S. S. (2019). Optimal power flow using hybrid differential evolution and harmony search algorithm. International Journal of Machine Learning and Cybernetics, 10(5), 1077-1091.

[128] Birogul, S. (2019). Hybrid harris hawk optimization based on differential evolution (HHODE)

algorithm for optimal power flow problem. IEEE Access, 7, 184468-184488.

[129] Shaheen, M. A., Hasanien, H. M., & Alkuhayli, A. (2021). A novel hybrid GWO-PSO optimization technique for optimal reactive power dispatch problem solution. Ain Shams Engineering Journal, 12(1), 621-630.

[130] Elgebaly, A. E., Taha, I. B., Azmy, A. M., & Abd El-Ghany, H. A. (2021). Optimal design and control of SSSCs for TLs considering technical and economic indices using GA and SAMPE-JAYA algorithms. IEEE Access, 9, 38907-38919.

[131] Muangkhiew, P., & Chayakulkheeree, K. (2021, March). Unified Optimal Power Flow Incorporating Full AC Control Variables. In 2021 9th International Electrical Engineering Congress (iEECON) (pp. 177-180). IEEE.

[132] ABUSHAWISH, Abdallah et JARNDAL, Anwar. Hybrid PSO-GWO optimization based parameter extraction method applied to GaN devices. In : 2021 4th International Conference on Circuits, Systems and Simulation (ICCSS). IEEE, 2021. p. 38-44.

[133] SAIF, Ahmed. Multi-Objective Optimization of Hybrid Solar-Wind-Battery Power Generation System. Thèse de doctorat. Masdar Institute of Science and Technology.

[134] Zhao, S., Zhang, T., Ma, S., & Chen, M. (2022). Dandelion Optimizer: A nature-inspired metaheuristic algorithm for engineering applications. Engineering Applications of Artificial Intelligence, 114, 105075.

[135] Ali, T., Malik, S. A., Daraz, A., Aslam, S., & Alkhalifah, T. (2022). Dandelion Optimizer-Based Combined Automatic Voltage Regulation and Load Frequency Control in a Multi-Area, Multi-Source Interconnected Power System with Nonlinearities. Energies, 15(22), 8499.

[136] Islam, M. Z., Wahab, N. I. A., Veerasamy, V., Hizam, H., Mailah, N. F., Guerrero, J. M., & Mohd Nasir, M. N. (2020). A Harris Hawks optimization based single-and multi-objective optimal power flow considering environmental emission. Sustainability, 12(13), 5248.

[137] Khodadadi, N., Talatahari, S., & Dadras Eslamlou, A. (2022). MOTEO: a novel multi-objective thermal exchange optimization algorithm for engineering problems. Soft Computing, 26(14), 6659-6684.

[138] Khodadadi, N., Talatahari, S., & Dadras Eslamlou, A. (2022). MOTEO: a novel multi-objective thermal exchange optimization algorithm for engineering problems. Soft Computing, 26(14), 6659-6684.

[139] Sonmez, Y., Duman, S., Kahraman, H. T., Kati, M., Aras, S., &Guvenc, U. (2022). Fitness-distance balance based artificial ecosystem optimisation to solve transient stability constrained optimal power flow problem. Journal of Experimental & Theoretical Artificial Intelligence, 1-40.

[140] Hashim, F. A., Hussain, K., Houssein, E. H., Mabrouk, M. S., & Al-Atabany, W. (2021). Archimedes optimization algorithm: a new metaheuristic algorithm for solving optimization problems. Applied Intelligence, 51, 1531-1551.

[141] Yenipinar, B., Şahin, A., Sönmez, Y., Yilmaz, C., & Kahraman, H. T. (2021, October). Design optimization of induction motor with FDB-based Archimedes optimization algorithm for high power fan and pump applications. In The International Conference on Artificial Intelligence and Applied Mathematics in Engineering (pp. 409-428). Cham: Springer International Publishing.

[142] Zhang, J., Wang, S., Tang, Q., Zhou, Y., & Zeng, T. (2019). An improved NSGA-III integrating adaptive elimination strategy to solution of many-objective optimal power flow problems. Energy, 172, 945-957.

[143] Zaro, F. R., &Abido, M. A. (2011, November). Multi-objective particle swarm optimization for optimal power flow in a deregulated environment of power systems. In 2011 11th International Conference on Intelligent Systems Design and Applications (pp. 1122-1127). IEEE.

[144] Duman, S., Akbel, M., &Kahraman, H. T. (2021). Development of the multi-objective adaptive guided differential evolution and optimization of the MO-ACOPF for wind/PV/tidal energy

sources. Applied Soft Computing, 112, 107814.

[145] Kahraman, H. T., Akbel, M., & Duman, S. (2022). Optimization of optimal power flow problem using multi-objective manta ray foraging optimizer. Applied Soft Computing, 116, 108334.

[146] Zahia, D., Belkacem, M., & Kamel, S. (2023, May). Dandelion Optimizer (DO) algorithm for Parameters Extraction of Photovoltaic Solar Cell. In 2023 1st International Conference on Renewable Solutions for Ecosystems: Towards a Sustainable Energy Transition (ICRSEtoSET) (pp. 1-6). IEEE.

[147] Singla, M. K., & Nijhawan, P. (2022). Triple diode parameter estimation of solar PV cell using hybrid algorithm. International Journal of Environmental Science and Technology, 19(5), 4265-4288.

[148] Ahmad, H. K. (2022). Ac Power Flow Analysis Using Fast Decoupled Newton-Raphson Algorithm Compared with Gaussian-Seidel Approach. Journal of Optoelectronics Laser, 41(3), 2022.

[149] Ministère de l'énergie : https://www.energy.gov.dz/?rubrique=electricite-et-gaz (22/ 01/2020).

[150] ARIF, Salem, DUVEAU, Jean, HELLAL, Abdelhafid, et al. Optimisation par essaim de particules appliquée à l'écoulement optimal de puissance réactive. Revue internationale de génie électrique, 2007, vol. 10, p. 6-2007.

[151] Djeblahi, Z., Mahdad, B., & Srairi, K., Solving the energy management problem of the Algerian Electrical Network 114-node using the Salp Swarm Algorithm. under review in the International Journal of Applied Power Engineering (IJAPE), 2024.

[152] Djeblahi, Z., Mahdad, B., & Srairi, K., Optimized the locations and sizes of FACTS devices on electrical network involving wind power using a new hybrid stochastic algorithm. *Engineering Research Express*, 2024, *6*(3), 035339.

[153] Djeblahi, Z., Mahdad, B., & Srairi, K., Optimal Locations and sizing of FACTS Devices on the Algerian electrical network involving stochastic renewable energy Using a New Hybrid Stochastic Algorithm.

Annex

Annex A: Data of IEEE 30-bus test system

Table (A.1): node data (IEEE 30- bus test system)

N° du JB	V_{Module} (pu)	V_{Angle} (Deg)	PG (MW)	QG (MVAR)	PD (MW)	QD (MVAR)	Qmin	Qmax
1	1.06	0	176.8535	0	0	0	0	0
2	1.043	0	48.4212	50	21.7	12.7	-40	50
3	1	0	0	0	2.4	1.2	0	0
4	1	0	0	0	7.6	1.6	0	0
5	1.01	0	21.756	37	94.2	19	-40	40
6	1	0	0	0	0	0	0	0
7	1	0	0	0	22.8	10.9	0	0
8	1.01	0	22.7234	37.3	30	30	-10	40
9	1	0	0	0	0	0	0	0
10	1	0	0	19	5.8	2	0	0
11	1.082	0	11.9796	16.2	0	0	-6	24
12	1	0	0	0	11.2	7.5	0	0
13	1.071	0	11.3208	10.6	0	0	-6	24
14	1	0	0	0	6.2	1.6	0	0
15	1	0	0	0	8.2	2.5	0	0
16	1	0	0	0	3.5	1.8	0	0
17	1	0	0	0	9	5.8	0	0
18	1	0	0	0	3.2	0.9	0	0
19	1	0	0	0	9.5	3.4	0	0
20	1	0	0	0	2.2	0.7	0	0
21	1	0	0	0	17.5	11.2	0	0
22	1	0	0	0	0	0	0	0
23	1	0	0	0	3.2	1.6	0	0
24	1	0	0	4.3	8.7	6.7	0	0
25	1	0	0	0	0	0	0	0
26	1	0	0	0	3.5	2.3	0	0
27	1	0	0	0	0	0	0	0
28	1	0	0	0	0	0	0	0
29	1	0	0	0	2.4	0.9	0	0
30	1	0	0	0	10.6	1.9	0	0

Table (A.2): line data (IEEE 30-bus test system)

N° of line	Line designation	Resistance (pu)	Reactance (p.u.)	Susceptance (p.u.)	Tap
1	1 -2	0.0192	0.0575	0.0264	1
2	1 -3	0.0452	0.1652	0.0204	1
3	2 -4	0.057	0.1737	0.0184	1
4	3 -4	0.0132	0.0379	0.0042	1
5	2 -5	0.0472	0.1983	0.0209	1
6	2 -6	0.0581	0.1763	0.0187	1

7	4 -6	0.0119	0.0414	0.0045	1
8	5 -7	0.046	0.116	0.0102	1
9	6 -7	0.0267	0.082	0.0085	1
10	6 -8	0.012	0.042	0.0045	1
11	6 -9	0	0.208	0	0.978
12	6 -10	0	0.556	0	0.969
13	9 -11	0	0.208	0	1
14	9 -10	0	0.11	0	1
15	4 -12	0	0.256	0	0.932
16	12 -13	0	0.14	0	1
17	12 -14	0.1231	0.2559	0	1
18	12 -15	0.0662	0.1304	0	1
19	12 - 16	0.0945	0.1987	0	1
20	14 -15	0.221	0.1997	0	1
21	16 -17	0.0824	0.1923	0	1
22	15 -18	0.1073	0.2185	0	1
23	18 -19	0.0639	0.1292	0	1
24	19 - 20	0.034	0.068	0	1
25	10 -20	0.0936	0.209	0	1
26	10 -17	0.0324	0.0845	0	1
27	10 -21	0.0348	0.0749	0	1
28	10 -22	0.0727	0.1499	0	1
29	21 -23	0.0116	0.0236	0	1
30	15 -23	0.1	0.202	0	1
31	22 -24	0.115	0.179	0	1
32	23 -24	0.132	0.27	0	1
33	24 -25	0.1885	0.3292	0	1
34	25 -26	0.2544	0.38	0	1
35	25 - 27	0.1093	0.2087	0	1
36	28 -27	0	0.396	0	0.968
37	27 -29	0.2198	0.4153	0	1
38	27 -30	0.3202	0.6027	0	1
39	29 - 30	0.2399	0.4533	0	1
40	8 -28	0.0636	0.2	0.0214	1
41	6 -28	0.0169	0.0599	0.065	1

Annex B: The Algerian electrical transmission network

The following tables provide an overview of the state of the Algerian electricity transmission network (lines, power transformers, and substations) in service of the GRTE electrical network by region up to December 31, 2018.

Table (B.1): The State of the Algerian Electricity Transmission Network

	Alger Capital	**Alger Centre**	**Annaba**	**Oran**	**Sétif**	**Hassi messaoud**	**TOTAL**
Overhead lines							
400 kV	0	1084,97	833,46	640,55	568,47	998,80	4126,25
400 kV exploits on 220 kV	0	0	0	316	98	217,5	631,5
220kV	147,93	2247,62	1619,01	3287,23	2958,57	3502,11	13762,47
150 kV	0	0	22,05	0	50,33	0	72,38
90 kV	0	0	566,71	/	0	0	566,21
60 kV	256,57	2092,5	1407,71	3264,07	2041,49	773,12	9835,46
Total lines	**404,50**	**5426,59**	**4448,44**	**7518,25**	**5716,49**	**5663,03**	**29177,72**
Underground cables							
400 kV	0	0	0	0	3,16	0,76	3,92
220 kV	38,43	15,11	7,17	12,35	2,10	3,35	78,51
60 kV	189,47	47,65	38,44	85,01	22,82	0,90	387,29
Total Cables	227,90	62,76	45,61	97,36	28,08	4,92	466,63
Total General	**632,40**	**650489,35**	**4594,05**	**7615,61**	**5744,94**	**5668**	**29644,35**

Table (B.2): Inventory of lines in (Km) by voltage level

	Alger Capital	**Alger Centre**	**Annaba**	**Oran**	**Setif**	**Hassi Messaoud**	**Total**
Transformer							
400/220 kV	0	10	6	5	6	5	33
220/30 kV	0	0	1	0	3	26	30
220/60/11 kV	23	39	33	45	43	14	197
60/30 kV	69	96	80	136	109	32	522
HT/MT/MT kV	8	8	3	15	1	0	35

Total TR	100	153	123	201	162	78	817

Table (B.3): Numbers of power transformer

	Alger Capital	Alger Centre	Annaba	Oran	Setif	Hassi Messaoud	Total
Mobile Cabin							
220/30 kV	/	1	2	3	7	15	28
60/30 et 60/10 kV	15	16	17	17	21	6	92
Total CM	**15**	**17**	**19**	**20**	**28**	**21**	**120**

Table (B.4): Numbers of mobile Cabin

		Alger Capital	Alger Centre	Annaba	Oran	Setif	Hassi Messaoud	Total
Posts								
400/220 kV		**0**	**4**	**3**	**2**	**3**	**4**	**16**
220/60 kV		**0**	**6**	**5**	**7**	**11**	**3**	**39**
220/30 kV		**0**	**0**	**2**	**0**	**2**	**14**	**18**
220/60/30kV		**4**	**10**	**9**	**12**	**9**	**4**	**48**
60/30 et 60/10 kV		**27**	**31**	**30**	**51**	**38**	**12**	**189**
HT/MT/MT		**1**	**5**	**1**	**5**	**1**	**0**	**13**
60 kV	**400 kV**	**0**	**1**	**0**	**0**	**2**	**0**	**3**
	220 kV	**0**	**2**	**1**	**2**	**1**	**3**	**9**
Total		**39**	**59**	**51**	**79**	**67**	**40**	**335**

Annex C: Data of Algerian Network 114 bus system

Table (C.1): Node data (Algerian Network 114 bus system)

Bus N°	Magnitude (pu)	Angle (Deg)	PD (MW)	QD (MVAR)
1	1	0	0	0
2	1	0	36	17
3	1	0	64	31
4	1.0773	0	125	94
5	1	0	335	250
6	1	0	78	37
7	1	0	55	26
8	1	0	50	24
9	1	0	40	19
10	1	0	42	21
11	1	0	96	47

12	1	0	31	15
13	1	0	13	6
14	1	0	0	0
15	1	0	136	65
16	1	0	0	0
17	1.0682	0	0	0
18	1	0	0	0
19	1	0	11	5
20	1	0	14	9
21	1	0	70	52
22	1	0	42	25
23	1	0	23	11
24	1	0	60	36
25	1	0	17	8
26	1	0	55	26
27	1	0	0	0
28	1	0	0	0
29	1	0	37	18
30	1	0	30	15
31	1	0	0	0
32	1	0	40	24
33	1	0	29	14
34	1	0	29	14
35	1	0	33	16
36	1	0	17	8
37	1	0	11	5
38	1	0	20	10
39	1	0	20	10
40	1	0	21	10
41	1	0	53	32
42	1	0	0	0
43	1	0	31	18
44	1	0	0	0
45	1	0	12	6
46	1	0	0	0
47	1	0	21	10
48	1	0	0	0
49	1	0	13	6
50	1	0	4	2
51	1	0	1	1
52	1	0	56	27
53	1	0	16	8
54	1	0	21	10
55	1	0	18	9
56	1	0	33	20
57	1	0	35	21
58	1	0	0	0
59	1	0	36	17
60	1	0	0	0

61	1	0	27	13
62	1	0	22	11
63	1	0	49	29
64	1	0	0	0
65	1	0	11	5
66	1	0	35	21
67	1	0	10	5
68	1	0	11	5
69	1	0	20	10
70	1	0	7	3
71	1	0	36	22
72	1	0	0	0
73	1	0	36	22
74	1	0	0	0
75	1	0	0	0
76	1	0	12	6
77	1	0	7	3
78	1	0	13	7
79	1	0	14	7
80	1	0	157	107
81	1	0	0	0
82	1	0	75	36
83	1	0	70	51
84	1	0	46	34
85	1	0	45	22
86	1	0	0	0
87	1	0	32	15
88	1	0	46	22
89	1	0	34	17
90	1	0	18	9
91	1	0	44	21
92	1	0	10	5
93	1	0	0	0
94	1	0	48	23
95	1	0	35	17
96	1	0	0	0
97	1	0	42	20
98	1	0	13	6
99	1	0	105	50
100	1.0773	0	33	16
101	1.0818	0	50	24
102	1	0	34	16
103	1	0	66	32
104	1	0	18	9
105	1	0	0	0
106	1	0	64	31
107	1	0	65	37
108	1	0	22	11
109	1.0818	0	37	18

110	1	0	13	6
111	1.0909	0	94	56
112	1	0	24	12
113	1	0	23	11
114	1	0	24	12

Table (C.2): Node data (Algerian Network 114 bus system)

N° of line	Line designation		Resistance (Ω)	Reactance (Ω)	Susceptance (mΩ)	Tap
	from	to				
1	2	1	4.1140	19.5050	0.0626	1.0000
2	6	1	5.9050	27.9750	0.0901	1.0000
3	2	6	6.7760	24.1030	0.0733	1.0000
4	4	42	13.2620	62.6780	0.2017	1.0000
5	4	42	6.7280	5.8830	0.3045	1.0000
6	4	3	1.5970	7.6470	0.0996	1.0000
7	5	3	1.3550	9.1480	0.0607	1.0000
8	5	4	0.8710	6.0980	0.0407	1.0000
9	4	7	6.9700	32.8150	0.1058	1.0000
10	15	16	1.8390	6.5340	0.0200	1.0000
11	16	3	1.9840	6.9700	0.0213	1.0000
12	16	14	0.6290	2.1780	0.0066	1.0000
13	8	42	8.2760	30.4440	0.0938	1.0000
14	8	4	8.9060	42.1080	0.1357	1.0000
15	10	7	7.2600	34.3160	0.1105	1.0000
16	10	11	11.0350	52.0780	0.1676	1.0000
17	7	6	7.5990	35.8160	0.1153	1.0000
18	11	42	8.2280	39.0100	0.1256	1.0000
19	6	3	13.9390	48.9810	0.1508	1.0000
20	9	2	2.0330	13.7460	0.0913	1.0000
21	9	3	4.2590	29.0400	0.1928	1.0000
22	13	12	24.2480	114.4660	0.3686	1.0000
23	10	13	22.4580	105.9960	0.3413	1.0000
24	17	21	3.1460	11.8100	0.0364	1.0000
25	17	21	3.5330	13.4550	0.0417	1.0000
26	17	72	9.5350	35.4290	0.1095	1.0000
27	17	27	2.2260	11.4710	0.2072	1.0000
28	17	31	2.9520	15.0520	0.1275	1.0000
29	31	28	0.8230	4.2590	0.1541	1.0000
30	17	64	9.5830	35.1870	0.1085	1.0000
31	21	44	11.6160	41.6720	0.1271	1.0000
32	60	31	1.7910	12.2450	0.0812	1.0000
33	21	60	2.7100	12.7290	0.0409	1.0000
34	60	44	5.9050	27.9750	0.0901	1.0000
35	58	44	5.8560	27.5400	0.0886	1.0000
36	72	101	10.3090	48.7390	0.1570	1.0000
37	72	58	8.8570	41.7690	0.1345	1.0000
38	58	75	7.1630	33.9280	0.1091	1.0000
39	75	107	8.9540	42.3980	0.1364	1.0000

40	75	74	0.2900	1.2580	0.0054	1.0000
41	44	42	12.0030	43.7050	0.1341	1.0000
42	44	42	8.8570	41.8180	0.1345	1.0000
43	42	48	3.5820	24.4900	0.1624	1.0000
44	48	44	1.2100	7.6470	0.0506	1.0000
45	107	101	16.1660	76.3270	0.2457	1.0000
46	64	97	8.6150	31.6540	0.0971	1.0000
47	72	96	7.3570	26.1360	0.0798	1.0000
48	96	98	9.8250	34.8480	0.1064	1.0000
49	96	95	0.7260	3.3880	0.0110	1.0000
50	18	22	1.0440	5.0290	0.0472	1.0000
51	18	37	0.9220	4.4390	0.0417	1.0000
52	37	22	0.6160	2.9590	0.0278	1.0000
53	19	26	0.2090	0.2770	0.0472	1.0000
54	19	26	0.2090	0.2770	0.0472	1.0000
55	19	34	0.0680	0.4540	0.0028	1.0000
56	20	18	4.8530	10.5980	0.0361	1.0000
57	20	24	1.3540	5.0040	0.0167	1.0000
58	20	24	1.3250	4.9000	0.0167	1.0000
59	20	29	1.1480	4.2410	0.0139	1.0000
60	20	35	1.5410	5.5010	0.0167	1.0000
61	35	29	1.6490	5.9000	0.0194	1.0000
62	20	32	2.5490	8.5140	0.0278	1.0000
63	22	32	1.2310	4.1110	0.0139	1.0000
64	22	24	0.8600	2.8760	0.0083	1.0000
65	22	24	0.8600	2.8760	0.0083	1.0000
66	23	30	0.8600	2.8760	0.0083	1.0000
67	23	36	0.4900	1.6450	0.0056	1.0000
68	36	30	0.9830	3.2870	0.0111	1.0000
69	33	18	0.7380	2.4660	0.0083	1.0000
70	32	33	0.8600	2.8760	0.0083	1.0000
71	26	25	0.5000	1.8610	0.0056	1.0000
72	24	25	0.5900	2.1890	0.0083	1.0000
73	26	34	0.1760	1.1450	0.0056	1.0000
74	29	26	0.4280	0.5690	0.0944	1.0000
75	29	39	0.4540	2.9520	0.0111	1.0000
76	38	34	0.1690	1.1050	0.0056	1.0000
77	18	73	5.6050	12.3370	0.0417	1.0000
78	18	73	3.0740	10.9010	0.0333	1.0000
79	62	18	1.8290	6.9880	0.0222	1.0000
80	20	52	3.1430	7.7830	0.0306	1.0000
81	20	52	3.1500	7.8010	0.0306	1.0000
82	54	59	4.2770	11.0270	0.0417	1.0000
83	52	59	1.2960	3.6500	0.0139	1.0000
84	57	51	4.4170	14.7530	0.0500	1.0000
85	57	77	4.9180	16.4380	0.0556	1.0000
86	52	53	3.3730	6.4370	0.0194	1.0000
87	53	54	3.3730	6.4370	0.0194	1.0000
88	52	30	2.5990	6.4400	0.0250	1.0000

89	71	70	5.7560	11.3330	0.0361	1.0000
90	40	41	2.1100	5.8430	0.0222	1.0000
91	40	50	4.8350	13.1220	0.0444	1.0000
92	71	69	3.9350	13.1510	0.0444	1.0000
93	70	68	4.3340	7.8480	0.0250	1.0000
94	43	46	3.6900	12.3300	0.0417	1.0000
95	51	43	7.4410	12.8020	0.0417	1.0000
96	54	55	4.3060	14.3860	0.0500	1.0000
97	55	43	6.1490	20.5490	0.0694	1.0000
98	73	62	1.4760	4.9320	0.0167	1.0000
99	73	67	1.0490	25.2250	0.0861	1.0000
100	68	67	5.9330	12.8480	0.0417	1.0000
101	29	26	0.4280	0.5690	0.0944	1.0000
102	73	66	5.8430	20.7070	0.0639	1.0000
103	63	66	2.4590	8.2190	0.0278	1.0000
104	63	65	2.0050	6.7000	0.0222	1.0000
105	63	65	2.0050	6.7000	0.0222	1.0000
106	56	54	3.6900	12.3300	0.0417	1.0000
107	57	56	4.3060	14.3860	0.0500	1.0000
108	57	56	4.3060	14.3860	0.0500	1.0000
109	47	50	4.3060	14.3860	0.0500	1.0000
110	47	46	1.2310	4.1110	0.0139	1.0000
111	67	66	4.0610	10.0580	0.0389	1.0000
112	49	41	4.5540	15.2100	0.0528	1.0000
113	19	78	0.1510	0.1980	0.0333	1.0000
114	19	79	0.3780	0.5000	0.0833	1.0000
115	59	61	1.8470	6.5380	0.0194	1.0000
116	45	46	0.6160	2.1780	0.0056	1.0000
117	85	87	7.6470	36.0580	0.1161	1.0000
118	85	86	6.7280	31.7990	0.1023	1.0000
119	85	81	4.7920	22.6030	0.0727	1.0000
120	87	106	5.0820	23.9580	0.0771	1.0000
121	87	82	2.7100	12.8740	0.0413	1.0000
122	87	99	15.5850	60.4520	0.1878	1.0000
123	103	105	6.2920	29.6690	0.0955	1.0000
124	105	101	8.2760	39.0100	0.1256	1.0000
125	105	104	0.7260	3.3880	0.0110	1.0000
126	103	106	10.0670	47.5770	0.1531	1.0000
127	81	82	14.6650	52.0300	0.1587	1.0000
128	80	82	15.4400	54.6440	0.1667	1.0000
129	80	84	9.2440	32.7180	0.0998	1.0000
130	84	83	2.4680	8.7120	0.0267	1.0000
131	82	83	9.2440	32.7180	0.0998	1.0000
132	100	98	4.9370	28.9430	0.1558	1.0000
133	100	97	5.3720	36.7360	0.2436	1.0000
134	98	97	5.8560	21.6830	0.0671	1.0000
135	99	100	11.1800	52.7080	0.1696	1.0000
136	87	100	4.9370	33.5900	0.0217	1.0000
137	100	84	3.1460	21.3930	0.1419	1.0000

138	84	80	3.5820	24.4900	0.1624	1.0000
139	86	81	2.6620	18.3440	0.1217	1.0000
140	98	99	7.8890	28.0720	0.0855	1.0000
141	101	102	5.6140	26.4750	0.0853	1.0000
142	99	102	5.6140	26.4750	0.0853	1.0000
143	99	101	5.3720	36.7360	0.2436	1.0000
144	98	94	17.2790	61.7100	0.1897	1.0000
145	94	82	2.7100	12.7290	0.0409	1.0000
146	92	93	13.1540	33.1090	0.1225	1.0000
147	93	91	2.4620	8.6990	0.0257	1.0000
148	93	91	3.0700	10.8700	0.0335	1.0000
149	90	89	6.2860	19.4400	0.0639	1.0000
150	88	89	10.9670	33.2100	0.1099	1.0000
151	90	93	15.0010	25.8280	0.0837	1.0000
152	103	110	8.9540	42.3980	0.1364	1.0000
153	110	112	8.9540	42.3980	0.1364	1.0000
154	103	114	20.2800	95.7840	0.3085	1.0000
155	109	108	7.1630	33.9280	0.1091	1.0000
156	109	107	18.7790	88.7170	0.2855	1.0000
157	112	114	9.1960	43.3660	0.1395	1.0000
158	112	111	14.3750	67.8570	0.2184	1.0000
159	113	111	8.0830	38.0910	0.1256	1.0000
160	80	88	5.9530	151.9760	0	1.0300
161	81	90	3.0010	70.2770	0	1.0300
162	86	93	0.5810	35.9130	0	1.0300
163	42	41	0.5810	35.9130	0	1.0300
164	58	57	0.5810	35.9130	0	1.0300
165	44	43	1.4040	50.9650	0	1.0300
166	60	59	0.6780	24.9740	0	1.0300
167	64	63	0.9200	33.8800	0	1.0300
168	72	71	0.5810	35.9130	0	1.0300
169	17	18	0.6780	24.9740	0	1.0300
170	21	20	0.7740	25.4100	0	1.0300
171	27	26	1.1620	71.8260	0	1.0300
172	28	26	1.1620	71.8260	0	1.0300
173	31	30	0.3390	23.9580	0	1.0300
174	48	47	0.5810	35.9130	0	1.0300
175	76	74	4.308	161.656	0	1.0300